DEVELOPMENT OF ALL-SOLID-STATE MODELOCKED LASER SOURCES AT 1.55 MM

Gareth J. Valentine

A Thesis Submitted for the Degree of PhD
at the
University of St Andrews

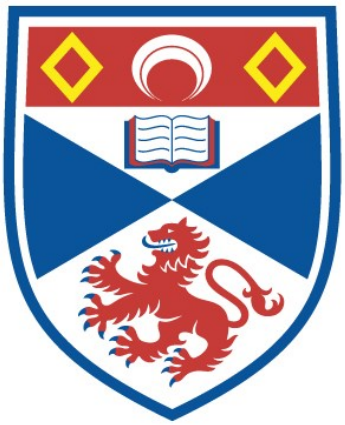

1999

Development of All-solid-state Modelocked Laser Sources at 1.55 μm

Thesis submitted for the degree of Doctor of Philosophy
to the University of St. Andrews

Gareth J. Valentine B.Sc.

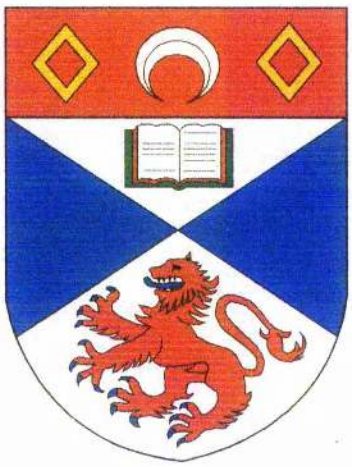

J.F. Allen Physics Research Laboratories
School of Physics and Astronomy
University of St. Andrews
North Haugh
St. Andrews
Fife KY16 9SS
Scotland

October 1998

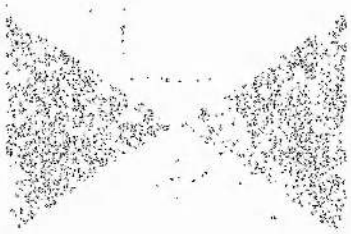

Declarations

I, Gareth John Valentine, hereby certify that this thesis, which is approximately sixty thousand words in length, has been written by me, that it is the record of work carried out by me and that it has not been submitted in any previous application for a higher degree.

I was admitted as a research student and as a candidate for the degree of Doctor of Philosophy in October 1993; the higher study for which this is a record was carried out at the University of St. Andrews between 1993 and 1998.

In submitting this thesis to the University of St. Andrews I understand that I am giving permission for it to be made available for use in accordance with the regulations of the University Library for the time being in force, subject to any copyright vested in the work not being affected thereby. I also understand that the title and abstract will be published, and that a copy of the work may be made and supplied to any bona fide library or research worker.

Date 14th October '98 Signature of candidate

I hereby certify that the candidate has fulfilled the conditions of the Resolution and Regulations appropriate for the degree of Doctor of Philosophy in the University of St. Andrews and that the candidate is qualified to submit this thesis in application for that degree.

Date Signature of supervisor

14/10/98

Abstract

This thesis concerns the generation of tunable ultrashort pulses near the 1.55 μm telecommunications window. Two principal laser systems are considered: i) the NaCl:OH^- colour-centre laser, which employs the technique of synchronously-pumped modelocking to generate tunable picosecond pulses and ii) the self-modelocked Cr^{4+}:YAG laser to generate femtosecond pulses tunable from 1.5-1.56 μm.

Details are given for an all-solid-state cw and cw-modelocked pump source for Cr^{4+}:YAG and colour-centre lasers based on Nd:YAG. Fibre-coupled AlGaAs laser diodes are employed as the solid-state pump source to this laser. When operated cw, up to 8.5 W of linearly polarised output power in a TEM_{00} beam is obtained. A compact cw actively-modelocked Nd:YAG laser is described having a pulse repetition rate of 194 MHz. Pulse durations down to 34 ps and output powers up to 6.0 W are obtained from this system. An 82 MHz Nd:YVO_4 laser is also detailed producing pulsewidths down to 75 ps and average output powers up to 3.5 W.

The intrinsic noise source associated with the synchronous modelocking technique is discussed and a simple passive stabilisation scheme, coherent-photon-seeding (CPS), is described and applied to the synchronously-modelocked NaCl:OH^- laser. Results of a simulation of this laser are reported and a comparison is made with the practical observations of the stabilised laser. For the first time, theoretical and experimental evidence for the presence of high frequency pulse jitter in synchronously-pumped-modelocked (SPML) lasers is presented and the coherent photon seeding technique is shown to eliminate this noise.

Details are also given for the construction of a compact, all-solid-state, femtosecond Cr^{4+}:YAG laser. A design prescription for laser resonators having a high propensity for self-modelocking is presented and an unconventional 3-mirror resonator is adopted for optimised self-modelocked operation. Using this design, modelocked output powers up to 300 mW with 120 fs pulses from a compact, regeneratively initiated laser having a pulse repetition rate of 320 MHz is reported for 4.7W incident pump power. Self-modelocking is demonstrated for pump powers down to ~1W with this cavity design.

A compact cavity design for self-modelocking is also assessed, with a footprint of just 20 X 25 cm, which places a prism in each cavity arm. 470 fs pulses at 220 mW average output power are reported.

Contents

1 Introduction

1.1 Overview

1998 is the 40th anniversary of Schawlow and Townes' proposition for a source of 'extremely monochromatic and coherent light'[1]. Since the first practical demonstration of the 'optical maser'[2], lasers have found countless applications ranging from those which exploit the coherent nature of laser light (e.g. producing holograms), to those that utilise their ability to create highly intense focused spots (e.g. industrial machining and laser surgery). However, it is the lesser-well-known ability of certain lasers to generate exceptionally high peak power light pulses of amazingly brief durations which this work describes. These 'ultrafast' lasers have been justly described as 'the Cadillacs of research tools'[3]. It has been desirable to measure events of ever shorter duration throughout history and currently, the fastest man-made events are pulses obtained from mode-locked lasers (~6.5 fs[4] recently reported) which may be used to study ultrafast phenomena especially those occurring in chemistry, biology, physics and optoelectronics.

One particular area of interest of ultrafast lasers is in the characterisation of semiconductor materials with emphasis on research into devices operating at 1550 nm. This region is attractive as it corresponds to the low-loss wavelength window for silica-based optical-fibres (~0.2 dB/km) and hence is important for optical telecommunications. For complete characterisation of these optoelectronic devices (such as laser diodes, diode amplifiers, modulators, switches and detectors), it is necessary to have access to ultrafast sources with broad wavelength tunability, reasonably high output powers and pulse durations down to ~100 fs.

Until recently, the only laser sources capable of fulfilling all these requirements were based on colour-centre gain media. These unfortunately require cryogenic cooling during operation adding to the bulk and expense of the overall system. Much current laser physics research is directed towards reducing the cost and size of laser systems[5]. This essentially involves using solid-state gain media pumped by high efficiency laser diodes. In the 1.55 μm region, Cr^{4+}:YAG has been the most promising medium for the

realisation of a compact, low-cost all-solid-state replacement for colour-centre lasers and much of the work presented here was aimed towards developing such a system.

Fundamental to reducing the cost of ultrafast laser systems is reducing the pump power requirement. This involves maximising the efficiency of the modelocked laser whilst reducing the threshold for cw and modelocked operation permitting the deployment of smaller and cheaper pump lasers.

In chapter 2, details of the construction of an all-solid-state Nd^{3+}:YAG pump laser are given, capable of pumping both Cr^{4+}:YAG lasers (when operated cw) and modelocked colour-centre lasers (when actively modelocked). This is more compact and cheaper to run than the mainframe arc-lamp pumped system which it was designed to replace.

Chapter 3 describes a simple, but highly effective technique for stabilising a synchronously-modelocked NaCl:OH^- colour-centre laser. This dramatically improves the stability of the modelocked pulse sequence and permits 'tuning' of the pulse duration by simply adjusting the laser cavity length.

The Cr^{4+}:YAG laser is introduced in chapter 4, and in chapter 5 the considerations to be made in designing a femtosecond laser system with minimal pump power requirements are described.

1.2 Modelocking Techniques

In general, unless some specific mode selective element is designed into a laser cavity, the emission from a laser will not be monochromatic but will consist of a number of closely spaced longitudinal modes. The mode spacing, $\Delta\nu$, depends on the effective optical length, $\mathbf{L_{eff}}$, of the laser resonator ($\Delta\nu = c/2L_{eff}$) and in general each mode will oscillate independently and out of phase resulting in an output with a chaotic temporal profile. The technique of modelocking[6,7,8] (also called 'phaselocking') involves, as expected, locking the phases of all the oscillating longitudinal modes together, which results in a regular sequence of pulses whose temporal spacing is equal to the round trip time of the laser cavity. The duration of the pulses is inversely proportional to the spectral bandwidth of the modelocked laser because the time and

frequency dependence of the amplitude and phase of light form a Fourier transform pair.

Several techniques have been developed to achieve modelocking, but all these methods fall under one of two categories, namely active or passive modelocking. For a comprehensive early review on modelocking techniques see reference 8.

1.2.1 Active modelocking

Active modelocking involves modulating either the overall laser loss or gain with an external frequency source. Applying amplitude modulation at a frequency equal to the longitudinal mode spacing forces each mode to acquire sidebands and hence by transferring power from each mode to its nearest neighbours, the phases of the oscillating modes are locked together. The pulse repetition frequency of actively modelocked lasers is governed by an external signal independent of the laser cavity.

Amplitude modulation

This conceptually simple technique essentially involves placing an optical shutter at one end of the laser cavity which is opened at the same rate as the cavity period. The light approaching the modulator when the modulator loss is minimum will see most gain, outside this region the light will experience net loss leading to the formation (after many round trips) of an optical pulse.

In practice the loss modulator is an acousto-optic device driven with a sinusoidal signal obtained from an external signal generator. An acoustic standing wave is induced in the modulator block whose magnitude depends on the amplitude of the applied RF-signal. A phase grating is generated by the local refractive index change induced by the acoustic standing wave. Intracavity power is diffracted outside the cavity at all points where the applied signal is non-zero, hence the cavity losses are minimum twice during each cycle of the RF-signal and so the pulse repetition frequency is twice the frequency of the electrical drive signal. The laser cavity period must be set to be equal to the period of the modelocked pulse sequence for the generation of the shortest pulses[9].

Amplitude modulation is the most common modelocking technique deployed in commercial Nd^{3+}:YAG lasers (such as the Spectra-Physics SP3800) and it is the method described in chapter 2 used to modelock an all-solid-state mini-Nd^{3+}:YAG laser.

Frequency modulation

An alternative active modelocking technique involves placing an electro-optic modulator at one of the cavity driven by a synthesised RF-signal. The refractive index of the electro-optic material is modulated by the applied RF-signal via the Pockels effect. This frequency shifts the circulating laser light except at the points where the applied rate of change of field is zero. Loss modulation effectively results when the circulating light is frequency shifted outside the gain bandwidth of the laser. Hence a pulse train develops at the two turning points of the RF-signal where the induced rate of change of phase shift is zero. The RF-signal is therefore applied at half the laser cavity repetition frequency. Note that two pulse trains are effectively formed at the two extremes of the RF electrical drive cycle (i.e. 180 degrees out of phase). These two sequences are independent and can exhibit individual characteristics and can lead to an instability in the modelocked pulse train. One advantage FM modulators have over AM modulators is the resonant frequency is not limited by the physical design of the device to the same extent as acousto-optic modulators, hence much higher repetition rates (and therefore more compact laser cavities) can be realised by employing FM modelocking. From the Kuizenga-Siegman[9] theory, the pulse duration from an actively modelocked laser is inversely proportional to the square root of the pulse repetition frequency, hence a compact FM-modelocked laser should produce pulses of shorter duration than an AM-modelocked laser. An additional advantage of FM-modulators is the absence of a temperature dependence of the resonant frequency, thus no active stabilisation is necessary to maintain efficient modulation as may be required with AM-modulation (see chapter 3).

Gain modulation

This modelocking technique is applicable both to electrically pumped semiconductor lasers and lasers pumped by a second laser which is modelocked. In the latter case it is termed 'synchronously-pumped modelocking (SPML)', (described in detail in chapter 3 applied to the NaCl:OH^- laser).

Gain modulation is a convenient technique to actively modelock semiconductor lasers: an RF signal with a period equal to the round trip time of the semiconductor laser cavity is applied with the DC bias to the gain section of the laser. To reduce the required frequency of the RF modelocking signal, it is usual to have the semiconductor laser in

an extended cavity by anti-reflection coating one of the diode facets (the other being HR coated) and using an external mirror to complete the resonator[10,11,12,13]. An alternative scheme is to place a laser diode, with both facets AR coated, in the centre of a resonator and applying RF power at a frequency twice that of the cavity repetition rate.

Synchronous-modelocking is most suited for systems based on gain media having upper-state lifetimes of the order of the laser cavity round trip times and large gain cross-sections such as dye and colour-centre lasers. The optical lengths of the pumped (slave) laser and the master laser must be matched to within ~5 μm for optimum modelocking. Dynamic gain saturation shortens the trailing edge of the SPML pulse, which results in an asymmetric pulse with a duration significantly shorter (by ~1 order of magnitude) than the pulse duration of the pumping laser.

1.2.2 Passive modelocking

In contrast to active modelocking, where the pulse period is governed by a frequency source external to the laser cavity, passive modelocking techniques rely on the circulating laser field to induce a modelocking mechanism.

A nonlinear element is included in the laser resonator which possesses an intensity-dependent loss: high power components (e.g. noise) of the circulating laser field experience the least loss. The maximum emission principle[14,15] (MEP) states that for given mode amplitudes, the phases of the individual modes adjust themselves to maximise the rate of stimulated emission inside the gain medium. In the case of passive modelocking, the MEP favours modelocked operation over free running cw operation, as high intensities experience least loss.

Since the pulse shortening in passive modelocking techniques is driven by the circulating laser field itself, significantly shorter pulse durations can be obtained compared to active modelocking schemes. Currently the shortest pulse duration to be obtained directly from a laser (~6 fs [4]) was generated by a passive modelocking technique.

Regenerative modelocking

Although technically speaking regenerative modelocking[16,17] should be classed as a passive technique because the driving signal is derived from the laser field itself, it has

more in common with active modelocking as active modelocking electronics are used with no nonlinear element.

A photodiode having a bandwidth ~300 MHz, detects the weak longitudinal mode beating of the cw un-modelocked laser. After filtering and dividing the frequency of the electrical signal to half the mode spacing frequency, the signal is amplified and used to drive a modulator (either acousto-optic or electro-optic) placed at one end of the laser cavity. Provided that the phase of the RF-signal thus derived is set correctly, a modelocked pulse will develop inside the cavity. Any environmentally induced fluctuations in the laser cavity length will be linked to a change in the frequency of the modulator drive signal thus ensuring immunity to cavity length/drive frequency mismatches.

This technique is often used to generate a high intensity modelocked pulse to initiate a second passive modelocking mechanism, especially self-modelocking, as it is essentially self-starting.

Passive modelocking using fast saturable absorbers

This is conceptually the most straightforward form of passive modelocking. An absorbing element which saturates on instantaneous intensity, is placed inside the cavity. After switching on the laser, the most intense noise feature will be preferentially amplified as this will saturate the absorber greatest and hence will experience the least loss. Because it is only the instantaneous intensity of the laser field which modulates the absorber, this is termed self-amplitude modulation (SAM). After many round trips, this noise feature develops into a modelocked pulse sequence. Because the only pulse shaping mechanism is saturation of the loss, the final pulse duration is limited to the recovery time of the absorber usually ~10 ps.

Passive modelocking using slow saturable absorbers

Provided that certain conditions are satisfied, it is possible to obtain modelocked pulses of significantly shorter duration than the recovery time of the saturable absorber[18]. The leading edge of the pulse is shaped by the absorber which is subsequently bleached, hence the remaining pulse is unaffected by the presence of the absorber[19]. Dynamic gain saturation may then sharpen the trailing edge of the pulse if the gain cross section is sufficiently high (as is the case with dye and colour-centre

lasers). A narrow gain window results if the saturation energy and recovery time of the absorber are less than those of the gain medium.

By carefully positioning the absorbing medium in a bi-directional ring cavity, a grating is established by two counter-propagating pulses inside the absorber leading to enhanced loss saturation. This technique called colliding-pulse modelocking[20] (CPM) has enabled sub 20 fs pulses to be obtained directly from a dye laser[21] (with suitable dispersion compensation).

Hybrid modelocking

In certain cases when modelocking with a slow saturable absorber is desirable, it may be more practicable to pump the laser using a modelocked pump source. This may be due to the fact that the recovery time of the gain is less than that of the absorber medium making passive modelocking impossible. In these instances, hybrid modelocking may be adopted where gain modulation by synchronous-pumping is assisted by a weak saturable absorber[22]. But this is really an active modelocking technique as the pulse repetition frequency is controlled by the master (pump) laser frequency.

Passive modelocking using synthetic fast saturable absorbers

It is possible to obtain modelocking using artificial saturable absorbers based on fast reactive (as opposed to resistive) nonlinearities. The laser must be configured so that the effects of the nonlinearity induce amplitude modulation of the circulating laser field. The nonlinearity is then behaving as a saturable absorber with an almost instantaneous recovery time permitting the generation of pulses of exceptionally short duration.

Five methods of simulating fast saturable absorber action using non-resonant reactive nonlinearities have been demonstrated to date. Coupled-cavity modelocking, polarisation rotation modelocking and self- (Kerr-lens) modelocking all rely on third-order ($\chi^{(3)}$ based) nonlinear effects. Also second-order nonlinear effects have been exploited in nonlinear-mirror modelocking using second-harmonic generation and cascaded $\chi^{(2)}$ modelocking.

Coupled cavity modelocking

Self-phase modulation (SPM) may be successfully employed to obtain passive modelocking by constructing the laser as an interferometer with the nonlinear element placed in one arm. Fabry-Perot, Michelson and Sagnac interferometers have been used for modelocking. An intense noise feature will experience an intensity-dependent phase shift on propagating through the nonlinear element (often monomode optical fibre). If the two interferometer arms are suitably aligned, it is possible after recombining the nonlinear arm with the main cavity, for constructive interference to occur at the centre of the noise feature thus enhancing the peak intensity, whilst destructive interference suppresses the wings of the noise feature. After many round trips, a modelocked pulse sequence results[23].

This modelocking technique termed 'coupled-cavity modelocking' (CCM) (also called 'additive-pulse modelocking' (APM)) was first demonstrated with a synchronously-modelocked $KCl:Tl^{(0)}$ colour-centre laser[24] where the synchronous-pumping merely served to initiate this passive modelocking mechanism. It was subsequently applied to other solid-sate laser systems including Nd^{3+}:YAG[25], Nd^{3+}:YLF[26], Nd^{3+}:glass[27], Ti:sapphire[28], $NaCl:OH^{-}$[29] and Cr^{4+}:Forsterite[30] although in most cases it has been superseded by the simpler self-modelocking technique. One major drawback of this technique is the necessity to maintain interferometrical matching of the linear and nonlinear arm lengths. This often requires the addition of some form of electronic active stabilisation scheme[31] which adds to the overall complexity of the laser.

Self-modelocking

In 1990 it was observed by Spence et al.[32] that passive modelocking could be established in a Ti:sapphire laser cavity with no apparent modelocking element. Initially the pulses were strongly chirped and ~2 ps in duration suggesting the presence of uncompensated self-phase modulation. The inclusion of an intracavity prism pair to provide anomalous group-velocity dispersion (GVD) permitted the generation of pulses as short as 60 fs from a self-modelocked (SML) laser.

Initially the modelocking mechanism was unclear. Although the pulse shaping in the dispersion-compensated cavity was solitonic with the SPM induced by the high intensities in the gain medium balanced by the negative GVD provided by the prism

pair, this is insufficient in itself to establish modelocking. Some form of discrimination is required to favour modelocked operation above normal cw-operation (to satisfy the maximum emission principle). At first it was thought that self-amplitude modulation resulted from interference between two transverse modes of the laser resonator, similar to the coupled-cavity modelocking scheme, as it seemed essential for the laser to operate multimode before modelocking could be achieved. Later, theoretical work[33,34,35] established that self-amplitude modulation (SAM) was provided by self-focusing via the optical Kerr-effect in the gain medium itself, which induced beam shaping in the laser cavity. By configuring the laser cavity in a suitable fashion, the laser field may experience greater gain for stronger self-focusing thus enhancing the high intensity noise components of the circulating field at the expense of the low intensity cw background. After many round trips a modelocked pulse develops whose final duration depends on the intracavity dispersion.

Herrmann[36] suggested three mechanisms by which self-amplitude modulation may be present in a self-modelocked laser. Conceptually, the simplest method is termed 'hard-aperture self-modelocking', and involves placing a physical constriction to the intracavity laser field somewhere in the resonator. Often this is a slit placed in front of one of the end-mirrors of the laser cavity slightly clipping the beam in one plane (usually the tangential). The laser cavity is then aligned in such a way that the spot size at the constriction reduces for stronger nonlinear lensing in the gain medium, hence high intensities experience less round trip loss compared to a low intensity cw signal and are enhanced.

'Soft-aperture modelocking' relies on the enhanced extraction of the pumped volume of the gain medium by the re-shaped intracavity beam in the presence of stronger nonlinear lensing. Whereas hard-aperture modelocking depends on a 1-dimensional change in the beam somewhere in the cavity, soft-aperture modelocking results from a 3-dimensional change inside the gain medium without the addition of a beam restricting element. In practice it is often much easier to align a laser for soft-aperture modelocking than for operation with a 'hard-aperture' although this technique requires a well defined pump beam (i.e. near diffraction-limited). For lasers pumped with poor beam quality broad-stripe laser diodes, it is preferable to decouple the modelocking from the pump mode, hence hard-aperture modelocking is usually adopted.

A third mechanism involved in self-modelocked lasers is termed 'gain-guiding'[37]. This is a transverse redistribution of the intracavity field inside the gain element induced by the inverted gain medium, resulting in a change in the beam shape throughout the resonator. This phenomenon affects both hard and soft aperture modelocked lasers and has been shown by modelling to change the stability limits of the laser resonator.

A simple design procedure for self-modelocked laser cavities has been developed by Cerullo et al.[38,39,40,41,42] which will be described in detail in chapter 5. Even though this model neglects gain-guiding and gain-saturation and only considers a 2-dimensional plane inside the laser resonator, it allows a laser designer to assess the suitability of a novel cavity design for self-modelocking. This was employed during the design of the unconventional three-mirror and four-mirror laser designs in chapter 5.

In most instances, self-modelocking is not self-starting. This is especially true when the laser is operating close to the cw threshold and to initiate SML a mechanism is usually required to introduce a noise feature inside the laser cavity. This could be a weak saturable absorber element[43], an extracavity moving mirror[44] a semiconductor saturable absorber mirror structure[4] (SESAM) or simply physically tapping or translating a cavity end-mirror[32]. An alternative, convenient technique is to deploy regenerative modelocking[17] as described above in section 1.2.2.1. Synchronous-pumping has also been deployed to initiate self-modelocking in several systems[45] but the active nature of this scheme can cause problems once passive modelocking is established: the repetition rate of the pump laser and the passively-modelocked laser may be different leading to a modulation of the laser output. Recently, it has been shown that with careful cavity design and alignment, that it is possible to achieve self-start self-modelocking[41] which uses the weak noise features present within a free-running cw laser to initiate the self-modelocking mechanism.

Self-modelocking is presently the most successful passive modelocking technique. Several commercial laser systems are currently available[46] which employ this scheme and it has been responsible for the generation of the shortest pulse directly from a laser[4]. It has been applied to lasers based on the following gain media: Ti:sapphire[32], various Cr^{3+}:Colquiriites[47,48], Nd:YAG[49], Nd:YLF[50], Cr^{4+}:forsterite[51], Cr^{4+}:YAG[52], NaCl:OH^-[53], and Rh6G[54] dye laser. The last two systems have gain media with large gain cross-sections which implies that gain-saturation will have a considerable effect on

the modelocking mechanism. Also a second nonlinear element was included in both these systems in a tightly focusing part of the cavity to act as the Kerr-medium as there was insufficient self-focusing in the gain medium alone for self-modelocking to be successful. The low output power obtained from both systems implies that this is not an appropriate modelocking technique for lasers based on organic dyes and colour-centre gain media.

Further details of self-modelocking with specific information on designing laser resonators which are optimised for this technique, will be given in chapter 5.

Polarisation rotation modelocking

$\chi^{(3)}$ nonlinearities can also be exploited via the Kerr induced polarisation rotation effect. Quarter wave plates are placed either side of a bulk Kerr medium in which there is a tight cavity focus. For a polarised laser (e.g. one with Brewster-angled elements) careful adjustment of the two waveplates will create a synthetic fast saturable absorber: high intensities experience less round trip loss than a cw signal. This technique was successfully demonstrated with a Ti:sapphire laser in 1991[55], but, self-modelocking is a simpler modelocking scheme for this laser. Nevertheless, this modelocking scheme might be more appropriate in laser systems which would require a separate nonlinear Kerr element to the gain medium for successful self-modelocking e.g. the NaCl:OH^- laser.

Nonlinear mirror modelocking via second-harmonic generation

A neat technique to achieve passive modelocking is to exploit second-harmonic generation (SHG) and subsequent down-conversion via three-wave mixing in a crystal with a non-zero $\chi^{(2)}$. This was first demonstrated in an Nd:YAG laser by Stankov et al.[56] A SHG crystal was incorporated into the laser cavity and the output coupler replaced with a mirror which had a relatively low reflectivity at the 1.064 μm fundamental wavelength but was highly reflecting at the second harmonic at 532 nm. If the phase-matching condition between the unconverted fundamental and the second-harmonic signal reflected from the dichroic end-mirror, is optimised for a high conversion efficiency back to the fundamental wavelength, high intensity noise bursts will experience less loss at the end-mirror and SHG crystal assembly than a cw signal. Phase matching can be achieved by adjusting the separation of the SHG crystal from the dichroic end-mirror. Pulse durations as short as 5.1 ps have been obtained from

Nd:YLF lasers modelocked using this technique once the group-velocity mismatch between the fundamental and second-harmonic signal was compensated for using a birefringent plate[57].

Modelocking with cascaded $\chi^{(2)}$ nonlinearities

This technique is similar to hard-aperture self-modelocking because it relies on a decrease in loss at an intracavity aperture due to the beam re-shaping induced for high intensities but this is achieved by SHG and subsequent down-conversion in a nonlinear crystal[58]. In practice, the layout is similar to that for nonlinear mirror modelocking described in section 1.2.2.5.4 but the dichroic end-mirror is high-reflecting both for the second-harmonic and the fundamental signal. Modelocking is accomplished by suitably positioning an intracavity slit, and by adjustment of the SHG crystal position and cavity alignment, as with aligning a hard-aperture self-modelocked laser. Cascading $\chi^{(2)}$ nonlinearities in this way simulates a nonlinear crystal with an extremely large $\chi^{(3)}$ and hence may be useful in modelocking laser systems with low peak powers (i.e. lasers based on gain media with narrow linewidths and hence long pulse durations). Pulse durations as short as 5.9 ps have been obtained from an Nd:YAG laser modelocked using this method[57].

1.3 Ultrashort Pulse Characterisation

1.3.1 Linear pulse measurement techniques

The most straightforward method of measuring an optical pulse is with a broadband photodiode and a fast oscilloscope. Unfortunately, while photodiodes with bandwidths as broad as 100 GHz have been developed, the real-time oscilloscopes are limited to bandwidths <1 GHz. Thus for pulses less than ~1 ns in duration, this direct detection method merely serves to monitor the amplitude noise of the individual pulses in the modelocked sequence, no information about the actual pulse duration may be inferred from this measurement.

Sampling oscilloscopes with effective bandwidths greater than 100 GHz are useful for repetitive signals (such as those obtained from a modelocked laser) and may resolve pulses down to ~20 ps. A 9.5 GHz InGaAs detector with a Tektronix 7603 sampling scope could resolve the shape of pulses down to 50 ps in duration. For

resolving pulses shorter than ~20 ps, an electron-optical streak camera is suitable.

The electron-optical streak camera

For the typical pulses obtained from a synchronously-modelocked NaCl:OH^- laser (chapter 3) and the actively-modelocked diode-pumped Nd:YAG laser described in chapter 2, a Photochron II synchroscan streak camera with an S1 photocathode was used (figure 1.1). Modern S1 photocathodes have useful sensitivity to light at wavelengths out to ~1.5 μm.

The streak camera is essentially an imaging tube with electrostatic deflector plates to sweep the image across the phosphor screen[59]. Light incident on the slit is imaged onto the photocathode which converts the photons into an electron beam. This electron beam may be swept across the phosphor screen creating a streaked image of the entrance slit. If an optical pulse is incident on the slit, a packet of electrons is liberated corresponding to the temporal pulse profile. When this packet is swept across the screen, an intensity profile of the pulse is created as a streak of light, provided that the static image (before the deflection signal is applied) is sufficiently smaller than the streaked image.

For optimum temporal resolution, the electrons liberated by the photocathode should have identical energies (and hence velocities) to minimise transit-time dispersion. This is optimal when the energy of the incident light is close to the long-wavelength cut-off of the photocathode: the long-wavelength cut-off depends upon the work-function of the photocathode material. For photon energies greater than the photocathode work-function, the emitted photelectrons are not monoenergetic due to the electron-hole generation mechanism and lattice scattering processes. This results in a distribution of initial photoelectron energies between zero and $\mathbf{h}\nu$-ε (where ε is the photocathode work function) causing a distribution in the transit time of electrons from the photocathode to the phosphor screen. A positively biased electron extraction grid placed close (~0.5 mm) to the photocathode, creating a large electric field (**E**~20 kV/cm), helps to reduce the electron velocity spread by accelerating the photoelectrons to high energies over a very short period to make the initial energy spread insignificant[59].

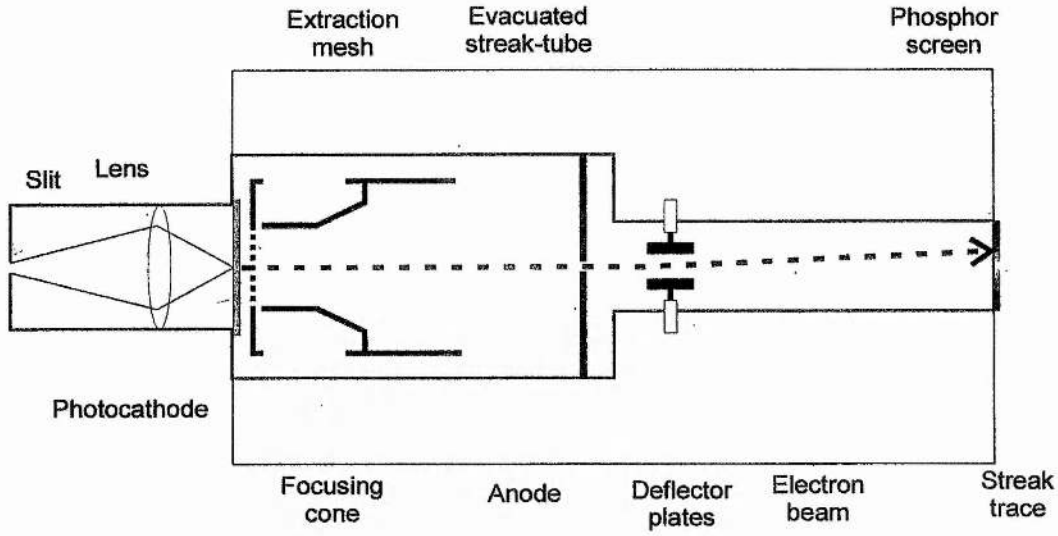

FIGURE 1.1: *Schematic of the Photochron II streak camera*

With periodic pulse sequences, such as those obtained from cw modelocked lasers, it is convenient to operate the streak camera with the deflector plates driven repetitively in synchronisation with the modelocked pulses enabling a real-time trace of the pulse profile to be displayed on an optical multichannel analyser (OMA) or equivalent. This mode of operation, termed 'synchroscan'[60] increases the dynamic range of the streak camera but unfortunately, because the trace results from an integration over thousands of modelocked pulses, the temporal resolution is limited to ~1 ps (in the case of a Photochron IV streak tube[61]) due to optical pulse jitter and jitter in the deflector drive electronics.

Figure 1.2 outlines the standard layout for operating a synchroscan streak camera as was used to characterise the SPML NaCl:OH$^-$ laser in chapter 3. The fast photodiode signal drives a tunnel-diode oscillator circuit at the pulse repetition frequency of ~82 MHz which reduces the translation of optical amplitude noise into jitter in the electronic drive signal. The signal is then frequency-doubled to 164 MHz to increase the maximum sweep speed of the streak tube. After amplification to a few watts, the RF signal is coupled into a high Q resonance circuit driving the deflector plates. This ensures a high electrostatic sweep voltage is applied to the plates.

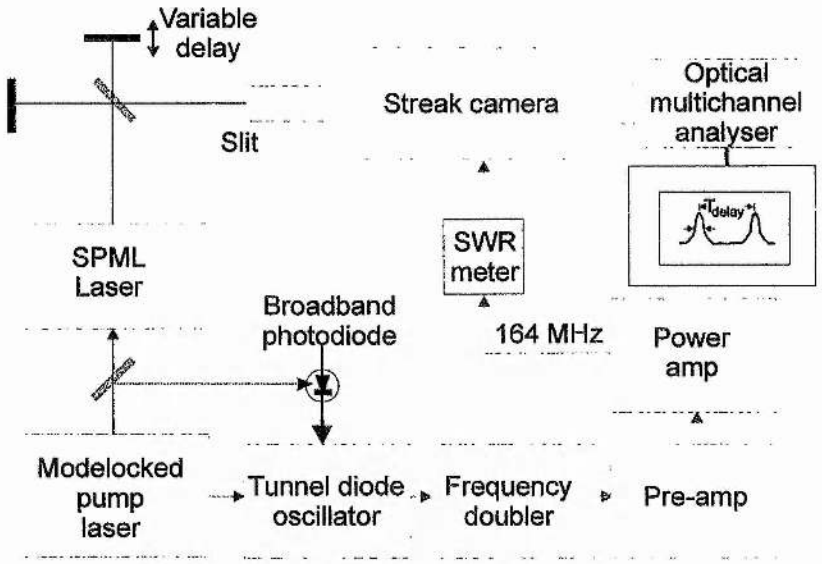

FIGURE 1.2: *Schematic of the synchroscan drive electronics, as used with the SPML laser described in chapter 3. The variable delay permits calibration of the OMA.*

1.3.2 Nonlinear pulse measurement techniques

The second-harmonic generation autocorrelator

The dilemma with creating very short events, such as the ultrashort pulses obtained from self-modelocked lasers, is that an even shorter event is required to characterise them. Since modelocked pulses are the shortest man-made events possible, the ultrashort pulse must be used to measure itself. One approach to achieving this utilises the second-order autocorrelation function of the modelocked pulse generated by a second-harmonic generation autocorrelator, first reported in the mid 1960's[62]. This effectively translates the problem of measuring a small time interval into one of measuring the distance a pulse propagates in that time interval, which is straightforward given the speed of light.

There are essentially three types of SHG autocorrelator which have the same basic layout as in figure 1.3. The most straightforward, and used throughout this work, employs a collinear type I phasematched arrangement, that is, the two beams from the interferometer have the same polarisation and propagate on a common path through the SHG crystal. This has the useful capability of generating an interferometric autocorrelation trace allowing the degree of chirp present on the modelocked pulse to be estimated. Unfortunately, there is always a second-harmonic generated signal for both

pulses so the autocorrelation trace is superimposed on a non-zero background signal resulting in poor contrast. Background-free intensity autocorrelation traces are possible using either collinear type II phasematching, where the two delayed pulses are of orthogonal polarisation, or non-collinear type I phasematching, where the two beams are laterally displaced but cross over in the SHG crystal. For both of these cases, a second-harmonic signal is only generated when an optical signal is present simultaneously in both beams, thus making it easier to determine if the modelocked pulse is superimposed on a pedestal or cw background.

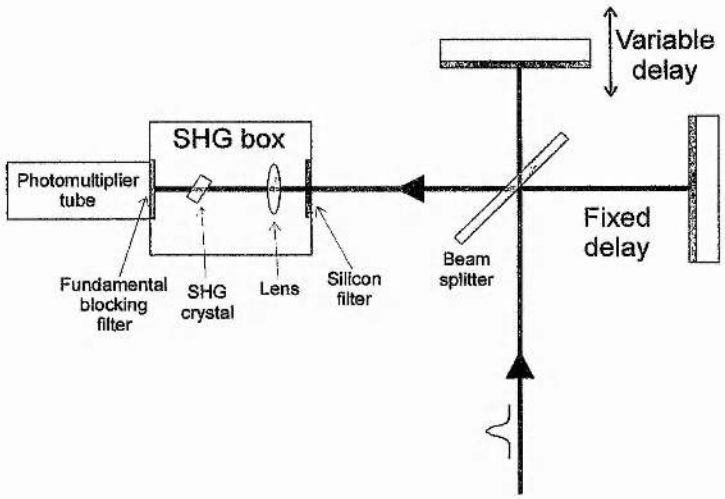

FIGURE 1.3: *Schematic of the second-harmonic generation (SHG) autocorrelator (collinear with type I phasematching).*

Figure 1.3 illustrates a typical type I collinear SHG-autocorrelator, as used to characterise the modelocked lasers described in this thesis. The pulse is first divided in intensity into two with a ~50 % beamsplitter. The two components are then recombined in a Michelson interferometer arrangement. A variable delay is introduced between the two pulses before recombination in a second-harmonic generating crystal. The output of the SHG crystal has a quadratic dependence on the incident intensity, which allows the second-order autocorrelation function $G^2(\tau)$ in equation 1.1 to be constructed by varying the delay between the two pulses. Normally, the autocorrelator has a low-frequency response and cannot resolve the individual optical cycles in the pulse. Thus the autocorrelation function is constructed from the pulse envelope only and is termed an 'intensity' autocorrelation:

$$G^2(\tau) = 1 + 2\frac{\int_{-\infty}^{\infty} I(t)\cdot I(t-\tau)\cdot dt}{\int_{-\infty}^{\infty} I^2(t)\cdot dt} \qquad \text{Equation (1.1)}$$

τ is the delay between the two pulses and **I(t)** describes the temporal intensity profile of a pulse in the modelocked pulse sequence. From equation 1.1 it can be seen that for delays outwith the extent of the modelocked pulse duration τ_p, $\mathbf{G^2(\tau>>\tau_p)=1}$ because $\mathbf{I(\tau>>\tau_p)=0}$, whereas if the two pulses overlap, $\mathbf{G^2(0)=3}$. Thus the autocorrelation trace for a completely modelocked laser has a value of 3:1 from the peak of the outline to the background level (figure 1.4(a)). For a free-running multiple longitudinal mode (cw, not modelocked) laser, $\mathbf{G^2(0)=3}$ as the cw light will correlate with itself at zero delay. However, for delays greater than the coherence time of the light, the autocorrelation trace will result from a time averaging of the incoherent light: $\mathbf{G^2(\tau>>\tau_p)=2}$ given that $\mathbf{I(\tau>>\tau_p)\neq 0}$. Thus a cw multi-axial-mode laser has an autocorrelation trace with a ratio of 3:2 (figure 1.4(b)). The width of the coherence spike corresponds to the coherence time of the laser light. In the case of a partially modelocked pulse or noise burst, the trace will have a broad pedestal of ratio 2:1 corresponding to the width of the noise burst envelope. Superimposed on top of this will be a coherence spike whose width corresponds to the coherence time of the substructure of the noise burst (figure 1.4(c)). This type of trace is typically seen with unstabilised synchronously-modelocked lasers which operate with excessive bandwidth. Often, a modelocked laser may exhibit multiple pulsing, which may occur when the intracavity dispersion compensation is not optimised for the high intracavity power. This results in an autocorrelation trace with 2N-1 peaks where N corresponds to the number of output pulses per round trip (shown in figure 1.4(d) for N=2).

The autocorrelator used throughout this thesis used a crystal of Li:NbO_3 of either 1 mm or 200 μm thickness, for SHG. This does not restrict the measurement to pulses with bandwidths less than the phasematching bandwidth of the crystal, provided that the pulses are unchirped[63]: only the central carrier frequency is required for second-harmonic generation and as this is constant throughout the envelope of an unchirped pulse, the phasematching bandwidth can be quite narrow.

In practice, to eliminate problems with feedback into the laser, gold corner-cube

retroreflectors were used as the two mirrors in the Michelson interferometer. To obtain a real-time autocorrelation trace, the variable-delay reflector was mounted on a moving-coil loudspeaker driven with a triangular-waveform at a frequency ~20 Hz. The autocorrelator delay is calibrated by translating the second mirror (mounted on a micrometer translation stage) by a known distance and measuring the time shift of the autocorrelation trace on the oscilloscope.

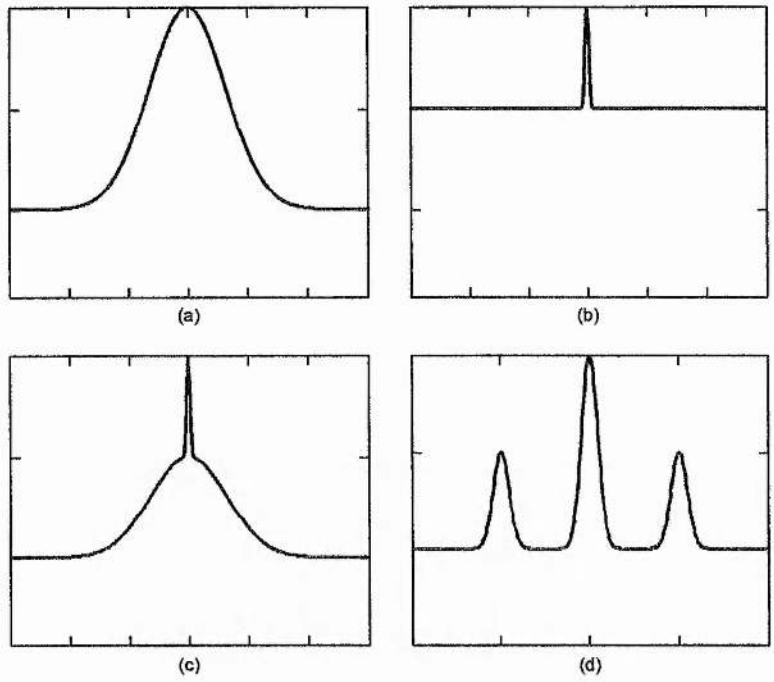

FIGURE 1.4: *Intensity autocorrelations obtained for different laser operating conditions.* **(a)** *Completely modelocked laser.* **(b)** *free-running cw-laser with multiple longitudinal modes oscillating out-of-phase.* **(c)** *Partially modelocked laser/noise burst.* **(d)** *Modelocked laser operating with multiple pulses.*

One drawback of the second-harmonic autocorrelation technique is that no precise information about the pulse shape is available from the symmetrical trace. The pulse duration may be deduced from an intensity autocorrelation trace (as in figure 1.4(a)) by assuming a pulse shape and dividing the autocorrelation full-width at half-maximum (FWHM) by a factor, 'κ', corresponding to that pulse shape (in table 1.1). After measuring the spectral width FWHM, the duration-bandwidth product is calculated and compared to the theoretical value relevant to the assumed pulse shape as listed in table 1.1. If the calculated value differs from the theoretical limit, either the assumed pulse shape was incorrect or the pulse is chirped.

I(t) (pulse shape)	$\Delta\nu\Delta\tau_p$	κ $(\Delta\tau/\Delta\tau_p)$
e^{-t^2} **(Gaussian)**	0.441	1.414
$\sec h^2(t)$ **(sech²)**	0.315	1.543 (1.897 for interferometric)
$\frac{1}{(e^t+e^{-rt})^2}$ (r=3) **(asymmetric sech²)**	0.278	1.549
$\frac{1}{1+t^2}$ **(Lorentzian)**	0.221	2.000
$e^{-2\lvert t\rvert}$ **(double-sided exponential)**	0.142	2.421
$\begin{cases} e^{-t} & ;t \geq 0 \\ 0 & ;t < 0 \end{cases}$ **(single-sided exponential)**	0.11	2.000

TABLE 1.1: *Theoretical time-bandwidth products and correction factors for intensity autocorrelation measurements for different pulse-shapes.*

By increasing the frequency response of the photomultiplier detector shown in figure 1.3, it is possible to resolve the interference between the individual optical cycles of the modelocked pulses as the delay is varied. A 'fringe resolved' autocorrelation takes the form of the second-order autocorrelation function given by:

$$g_2(\tau) = \int_{-\infty}^{\infty} \left| \xi(\omega_0, t) + \xi(\omega_0, t-T) \right|^4 .dt \qquad \text{Equation (1.2)}$$

where the electric field of the pulse is described by:

$$\xi(\omega_0, t) = E(t).e^{i\omega_0 t} . \qquad \text{Equation (1.3)}$$

This results in an 'interferometric' autocorrelation trace with an 8:1 contrast ratio,

which conveys additional information regarding the frequency chirp present on a pulse. This is because a variation of the instantaneous phase over the duration of the pulse will reduce interference of the delayed pulses and hence reduce fringe visibility at the wings or centre of the interferometric trace. An additional advantage of an interferometric trace is that it is self calibrating: the fringe separation corresponds to one optical cycle at the centre wavelength of the pulse. Unfortunately, erroneous pulse duration measurements will be deduced from this type of autocorrelation if chirp is present. Note that the factor 'κ' for deducing the pulse duration from the autocorrelation trace is different for interferometric traces (table 1.1). In practice, interferometric autocorrelation traces were obtained by impedance-matching the photomultiplier-tube with the oscilloscope using a terminating resistor of ~5 kΩ.

Recently, there have been several impressive demonstrations of the exploitation of the two-photon absorption effect in a light detector, to replace both the second-harmonic generating crystal and the photomultiplier tube[64,65,66]. Detection devices as inexpensive and simple as a light-emitting diode[67] (LED) have been demonstrated to produce interferometric autocorrelation traces with a collinear style Michelson interferometer. InGaAs[68] and silicon photodiodes[69] have also been utilised in such a scheme. The basic requirement is that the bandgap energy of the semiconductor is greater than wavelength of the light emitted by the laser. The photodetector is used photovoltaically so any potential difference appearing across the junction of the diode must arise from a two-photon absorption effect (TPA). This involves exciting the valence band electrons to a virtual energy level with one photon of the laser light. A second photon is required to promote this electron into the conduction band. The response of this effect has a quadratic dependence on the intensity of the incident light, hence its ability to replace the SHG crystal and photodetector in a second-order autocorrelator.

Advanced pulse characterisation techniques

The combination of the intensity and interferometric autocorrelation traces with a measurement of the spectral bandwidth of the modelocked pulses reveals considerable information regarding the status of a modelocked laser: linear-chirp present on a modelocked pulse may be observed as reduced fringe visibility in the wings of an interferometric autocorrelation trace. For an unchirped pulse, it is easy to deduce some information regarding the pulse shape by calculation of the time-bandwidth product for the different possible pulse shapes listed in table 1.1. In practice, a $sech^2$ pulse is usually

produced from lasers in which self-phase-modulation is a major pulse shaping mechanism (e.g. self-modelocked systems) as this pulse shape is a solution to the nonlinear Schrödinger equation[70]. Nevertheless, advanced diagnostic systems have been demonstrated which allow complete characterisation of ultrashort pulses.

Normally a nonlinear optical element is used to act as a time-gate to sample segments of the optical pulse. This can involve second-harmonic generation or Kerr-based effects. Because a nonlinear process is involved, recovery of the original pulse requires an iterative algorithm which can be computationally intense.

An example of such a diagnostic technique, called frequency-resolved optical-gating[71] (FROG), involves a nonlinear autocorrelator (such as the SHG system in figure 1.3) which acts as a time-gate. The resulting (e.g. SHG) signal is passed through a spectrometer, which allows a sonogram of the pulse to be constructed, by taking the variable delay of the autocorrelator into account. Using a suitable iterative algorithm, the complete pulse phase and spectral information can be reconstructed.

1.3.3 Spectral analysis of the modelocked pulse sequence

The optical spectrum of a modelocked laser provides useful information regarding the operating status of the laser. The spectral bandwidth is useful in determining the pulse shape, and whether the modelocked pulse is duration-bandwidth limited. In addition, it immediately shows whether the modelocked pulse is superimposed on a cw background signal by the presence of a cw spike.

Two basic techniques were employed for spectral analysis. For broad bandwidth femtosecond pulses obtained from self-modelocked systems, a fibre-coupled Anritsu-Wiltron MS96A optical spectrum analyser was used. This was basically a scanning monochromator with a resolution of 0.1 nm. The much narrower bandwidth picosecond pulses produced by the synchronously-modelocked NaCl:OH^- laser in chapter 3 required a high-finesse scanning Fabry-Perot interferometer for measurement. This comprised two plane 95% reflecting dielectric mirrors, one of which was mounted on a micrometer translation stage while the other was on a piezoelectric transducer driven with a ramped signal. Calibration of the free-spectral-range was accomplished by moving one mirror until the two mirrors touched, then translating the mirror back a measured distance to give the required resolution. For small separations, a correction

factor of 16 μm would be necessary to account for the finite thickness of the dielectric coatings[72]. The free-spectral-range is given by:

$$FSR(\nu) = \frac{c}{2 \cdot d} \qquad \text{Equation (1.4)}$$

and hence the bandwidth FWHM of the pulse can be measured from a storage oscilloscope.

1.4 Ultrashort Pulse Propagation

In designing laser sources capable of producing the shortest optical pulses, it is important that both the broad optical spectra associated with the modelocked pulses, and their strong peak electric field strength are given careful consideration as both give rise to interesting phenomena.

1.4.1 Pulse propagation in linear dielectric media

An ultrashort pulse propagating in a linear dielectric medium will become distorted owing to the frequency dependence of the linear electrical-susceptibility tensor $\chi^{(1)}(\omega)$. This results in a frequency dependence of the velocity of light propagating in the medium, which causes a modelocked pulse with a broad optical spectrum to stretch.

One way of expressing the frequency dependence of the refractive index of a medium is with an empirical Sellmeier equation:[6]

$$n^2(\omega) - 1 = \frac{A\omega_e^{\,2}}{\omega_e^{\,2} - \omega^{\,2}} \qquad \text{Equation (1.5)}$$

ω_e is an effective resonant frequency of the material of relative strength **A**.

The material dispersion may be expressed by a Taylor expansion of the propagation constant $\beta(\omega)$ defined by:

$$\beta(\omega) = \frac{\omega}{c} \cdot n(\omega) \qquad \text{Equation (1.6)}$$

about the central carrier frequency ω_0:[6]

$$\beta(\omega) = \beta(\omega_0) + \beta'(\omega_0)\cdot(\omega-\omega_0) + \frac{1}{2!}\beta''(\omega_0)\cdot(\omega-\omega_0)^2 + \frac{1}{3!}\beta'''(\omega_0)\cdot(\omega-\omega_0)^3$$

Equation (1.7)

where the apostrophe signifies differentiation with respect to ω.

The terms in equation 1.7 have the following physical significance:

$$\beta(\omega_0) = \frac{\omega_0}{c}\cdot n(\omega_0) \qquad \frac{1}{v_\phi} = \frac{1}{\text{phase velocity}}$$ Equation (1.8)

$$\beta'(\omega_0) = \frac{1}{c}\cdot\left(n(\omega_0) + \omega_0\cdot n'(\omega_0)\right) \qquad \frac{1}{v_g} = \frac{1}{\text{group velocity}}$$ Equation (1.9)

$$\beta''(\omega_0) = \frac{1}{c}\cdot\left(2\cdot n'(\omega_0) + \omega_0\cdot n''(\omega_0)\right)$$ group-velocity dispersion (GVD) Equation (1.10)

$$\beta'''(\omega_0) = \frac{1}{c}\cdot\left(3\cdot n''(\omega_0) + \omega_0\cdot n'''(\omega_0)\right)$$ third-order dispersion (TOD) Equation (1.11)

The central carrier frequency, ω_0, of a modelocked pulse propagates at the phase velocity, $\mathbf{v_\phi}$, through the medium, but the pulse envelope itself propagates at the group velocity $\mathbf{v_g}$. For an ultrashort pulse with a broad bandwidth propagating in a medium with a non-zero group-velocity dispersion, implying that the group velocity changes with frequency, the pulse envelope will change shape (broaden or compress). It is more usual to express GVD as a function of the wavelength derivative of the material's refractive index:

$$\beta''(\omega_0) = \frac{4\pi^2 c_0}{\omega^3}\cdot\frac{d^2 n(\lambda_0)}{d\lambda_0{}^2}$$ Equation (1.12)

For an initially unchirped Gaussian pulse, the pulse duration (τ_{p0}) will be increased by a factor of $\sqrt{2}$ on propagation through the medium for a distance of: [6]

$$z_D = \frac{\tau_{p0}^2}{(4\ln 2)\beta''}$$ Equation (1.13)

This 'dispersion length' term is similar to the Rayleigh range expression for a focussed Gaussian beam and an expression for the pulse duration after propagating for a distance '**z**' through a medium is,

$$\tau_p^{\,2}(z) = \left[1 + \left(\frac{z}{z_D}\right)^2\right] \cdot \tau_{p0}^{\,2}. \qquad \text{Equation (1.14)}$$

From equation 1.13 and using values pertinent to fused silica, it is apparent that the dispersion length is of the order of 1 m for 1 ps pulses but just 1 cm for pulses of ~100 fs in duration. The gain medium in a laser is often of this length and so for lasers to produce sub-picosecond pulses it is important to compensate for this intracavity material GVD. For the even shorter pulse durations currently being reported by some research groups[4] (<20 fs), the third-order dispersion (TOD) becomes increasingly important and must be taken into account.

1.4.2 Non-resonant Optical Nonlinearities

The high optical intensities available since the development of the laser have enabled certain nonlinear phenomena associated with optical materials to be accessed. These phenomena may be classified into resonant nonlinearities, which occur in materials exhibiting absorption at or close to the applied optical signal (e.g. incident radiation having a photon energy equal to the bandgap of a semiconductor sample), or non-resonant nonlinearities which are present in all transparent dielectric optical materials. An example of the former type is the gain experienced by a synchronously-modelocked laser pulse in the SPML NaCl:OH$^-$ laser described in chapter 3, however, in general these are not important in the understanding of self-modelocked lasers where gain saturation does not play an important role. Non-resonant nonlinearities are important as they give rise to a number of effects which are crucial to the understanding and optimisation of a femtosecond laser.

For applied optical signals having strong electric fields, higher-order terms for the electrical susceptibility tensor must be included in the expression for the polarisation induced in a transparent dielectric medium (defined as net electric dipole moment per unit volume)[6]:

$$p = \varepsilon_0 \chi_{(1)} \cdot \mathrm{E} + \chi_{(2)} \cdot \mathrm{E}^2 + \chi_{(3)} \cdot \mathrm{E}^3 \qquad \text{Equation (1.15)}$$

The χ terms are in fact tensors, but for simplicity only a magnitude for χ is considered. $\chi_{(1)}$ is the linear susceptibility, responsible for the refractive index of the material:

$$n^2 = \Re e\left(1 + \chi_{(1)}\right) \qquad \text{Equation (1.16)}$$

The second-order nonlinearity term ($\chi_{(2)}$) is non-zero only for materials based on a crystal structure which does not possess inversion symmetry i.e. those materials which are also piezoelectric e.g. urea. This is responsible for second-harmonic generation (SHG) and for three-wave mixing in optical parametric oscillators. Apart from the use of the SHG effect to provide the auxiliary light for the NaCl:OH^- laser (see chapter 3) second-order nonlinearities were not exploited for this work.

The third-order nonlinearity term is non-zero for all dielectric materials but it becomes significant only for light beams with extremely strong electric fields such as those obtained by a tightly focussed beam from a modelocked laser. It is responsible for a number of phenomena including: third-harmonic generation, Raman scattering, Brillouin scattering and the Kerr-effect. This last effect is exploited in modelocked lasers resulting in spectral and spatial modification of the intracavity beam.

The Kerr-effect

If a sufficiently strong DC electric field is applied to a transparent dielectric medium, the non-zero $\chi_{(3)}$ value in equation 1.15 results in a dependence of the refractive index of the material on the electric field strength[6]:

$$n = n_0 + n_{2E} \cdot E_0^2 \qquad \text{Equation (1.17)}$$

$\mathbf{E_0}$ describes the applied electric field and $\mathbf{n_{2E}}$ is the Kerr coefficient (typically $\mathbf{n_{2E}} \sim 10^{-22}$ m^2V^{-2}). For a material with a positive $\mathbf{n_{2E}}$, the electric field causes an increase in the refractive index for optical fields polarised parallel to the applied DC field $\mathbf{E_0}$, but a decrease in the refractive index for fields polarised perpendicular to $\mathbf{E_0}$. Thus a birefringence is induced in the material which may be used with crossed polarisers in a Kerr-cell modulator to induce an amplitude modulation on the optical field.

Normally the electric fields required to achieve appreciable modulation are very high (~100's kV/cm^2) but if the applied optical signal is of sufficient strength, the electric field associated with the optical signal itself may incite a change in the refractive index of the material. This is termed the 'optical Kerr-effect'. Equation 1.17 is then expressed as:

$$n = n_0 + n_{2I} \cdot I \qquad \text{Equation (1.18)}$$

$\mathbf{n_{2I}}$ is typically $\sim 10^{-20}$ m^2W^{-1}; **I** is optical intensity, related to the time averaged

electric field strength of the optical signal by:

$$I = \sqrt{\varepsilon / \mu} \cdot \langle E^2 \rangle . \qquad \text{Equation (1.19)}$$

This has an important effect both in the spatial and temporal domains for a femtosecond laser pulse propagating in a transparent dielectric medium.

Self-focusing of high intensity Gaussian beams

The smooth transverse profile of a Gaussian beam induces a spatial variation in the refractive index of a dielectric medium, according to equation 1.16: for a positive $\mathbf{n_{2I}}$, the refractive index will be greater in the centre (peak) of the beam than in the wings of the beam profile thus creating a graded-index lens whose strength depends on the intensity of the overall beam. For the special case of an optical pulse propagating through a medium, the induced nonlinear-lens will have a time dependence, being strongest at the peak of the pulse and weakest in the wings. It will be shown later that this time-dependent lens is exploited in self-modelocked lasers to create a synthetic fast saturable absorber.

Self-phase modulation (SPM)

For an ultrashort pulse propagating inside a dielectric medium having a positive $\mathbf{n_{2I}}$, the refractive index of the material will gradually increase, reaching a maximum at the peak of the pulse before decaying back to its original value after the trailing edge. The material effectively becomes optically longer during the leading edge of the pulse, thus the arrival of the optical cycles is delayed. Conversely, during the trailing edge of the pulse, the material becomes gradually optically shorter hence the arrival of the optical cycles is advanced. Consequently, for a pulse propagating through a medium of length **L**, a net phase shift results which is given by[6]:

$$\phi(t) = \frac{2\pi(n_0 + n_{2I} I) \cdot L}{\lambda} . \qquad \text{Equation (1.20)}$$

A positively chirped pulse results if $\mathbf{n_{2I}}$ is positive –that is- the pulse leading edge is red-shifted whereas the trailing edge is blue shifted. If the initial pulse has a smooth envelope, and neglecting any effects due to chromatic dispersion in the nonlinear medium, SPM induces a linear frequency chirp across the central region of the pulse, such as would result if the pulse had propagated through a medium with positive group-velocity dispersion, but the overall pulse shape would remain unchanged. Note that this

results in a broadening of the optical spectrum of the pulse: the time-bandwidth product increases by a factor of $\sqrt{2}$ on propagating through a length L of material, if its peak intensity satisfies:

$$I_0 = \frac{\lambda}{2\pi \cdot n_{2I} L}. \qquad \text{Equation (1.21)}$$

In the special case of a pulse propagating in a nonlinear material and experiencing negative (anomalous) GVD, the positive chirp induced by the spectral broadening effect of SPM could be compensated by the anomalous GVD of the material; hence a shorter, duration-bandwidth limited pulse may result from an initially broader pulse by the interplay of SPM and GVD in a nonlinear medium. This enables solitons to propagate inside optical fibres possessing anomalous group-velocity dispersion: the initial pulse coupled into the fibre is continually broadened spectrally by SPM and subsequently compressed by negative GVD until a final steady-state pulse shape is attained, limited only by higher-order dispersive and nonlinear effects. The resulting pulse does not then change shape on further propagation in the optical fibre provided that there is no loss[70]. This final pulse shape depends on the initial pulse energy where higher energies result in shorter pulse durations.

1.4.3 Ultrashort Pulse Propagation in a Resonator

In an actual laser resonator, both self-phase modulation (SPM) and group-velocity dispersion (GVD) co-exist, and together control the final pulse duration obtained from the laser[73].

The intracavity elements contribute to the overall cavity GVD –that is- the gain medium, any modelocking devices (e.g. acousto-optic modulators) and the dielectric mirror coatings. In general, this GVD will be positive. Additionally, the tight focus present inside the vibronic gain medium of a tunable laser induces considerable self-phase modulation which effectively generates the equivalent phase shift as would be produced by positive GVD. Without any compensation for this excessive positive GVD, the modelocked pulse durations would be severely limited by equation 1.11 to the order of 1 ps.

In 1984, Fork et al.[74,75] demonstrated that negative group-velocity dispersion could be artificially introduced into a laser cavity using a sequence of Brewster-angled

prisms with very low insertion loss. Such an arrangement is illustrated in figure 1.5. Chromatic dispersion at prism 1 causes the incident beam to spread by an angle θ. This results in a path difference, before reconstruction by prism 2, dependent on the wavelength of the light component. Consideration of the geometry of figure 1.5 allows an expression for the effective GVD contribution to be derived: the second derivative of the optical path length of the prism sequence with wavelength is:

$$\frac{d^2P}{d\lambda^2} = 2\ell\left\{\left[\frac{d^2n}{d\lambda^2} + \left(2n - \frac{1}{n^3}\right)\left(\frac{dn}{d\lambda}\right)^2\right]\sin\theta - 2\left(\frac{dn}{d\lambda}\right)^2\cos\theta\right\} \quad \text{Equation (1.22)}$$

ℓ is the prism apex separation, **n** is the index of refraction of the prism material, λ is the wavelength and **P** is the optical path length. The GVD contributed by the geometry of this system may be calculated with (from re-arranging equation 1.10):

$$\beta''(\lambda_0) = \frac{\lambda_0^3}{2\pi c^2}\frac{d^2P}{d\lambda^2}. \quad \text{Equation (1.23)}$$

Similarly, the material GVD contribution of the prisms and other intracavity elements, may be calculated as:

$$\beta''(\lambda_0) = \frac{\lambda_0^3}{2\pi c^2}\frac{d^2n}{d\lambda^2}\cdot L. \quad \text{Equation (1.24)}$$

Here **L** refers to the physical length of material through which the beam passes.

Equation 1.22 is simplified by making the assumption that **cos** θ is unity, and ℓ **sin** θ is approximated to twice the spot size at the first prism.

The overall material contribution to intracavity GVD may be calculated using equation 1.24, and hence the prism separation required to compensate for this is found using equations 1.22-1.23. Generally, an excess of anomalous intracavity GVD is required to compensate for the effective positive group-velocity dispersion contribution by the SPM inside the gain medium.

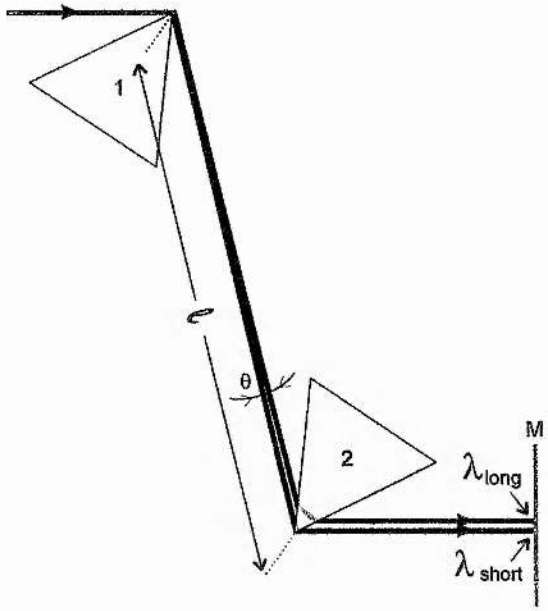

FIGURE 1.5: *Prism sequence having negative overall group-velocity dispersion.*

For the generation of the shortest pulses, third-order dispersion (TOD) becomes important. In a prism GVD compensated cavity this has two sources: the material contribution by all the intracavity elements and the geometrical contribution by the prism separation. Careful selection of the prism material is essential to minimise total TOD: by balancing the intraprism path length of the intracavity beam with the prism separation, overall TOD and GVD may be set to zero, provided that both contributions are of opposite signs[76,77].

A simple model to describe how the GVD and SPM balance to produce a modelocked pulse of a certain duration is based on a soliton propagating inside an optical fibre[70]. In the soliton model both the dispersion and the nonlinearity are considered to occur simultaneously inside the resonator. Of course, this is not physically realistic: the SPM occurs only inside the gain/nonlinear medium whereas the dispersion appears principally between the compensating prisms. However, this assumption is valid provided that the total cavity round-trip length within the dispersive (L_D) and nonlinear lengths (L_{NL}) defined by:

$$L_D = \frac{\tau_{p0}^2}{|\beta''|} \qquad \text{Equation (1.25)}$$

$$L_{NL} = \frac{1}{P_0 \gamma} = \frac{\tau_{p0} \cdot \lambda \cdot w_{eff}^2}{E \cdot n_{2I}}. \qquad \text{Equation (1.26)}$$

E is the pulse energy, $\mathbf{w_{eff}}$ refers to the effective beam radius inside the nonlinear medium. This model is only strictly valid for pulse durations ~100 fs or greater as for pulses considerably shorter than this, the discrete nature of the separate SPM and GVD sources becomes important. The possible $\mathbf{N^{th}}$ order solitons from this model are given by the relationship:

$$N^2 = \frac{L_D}{L_{NL}} \qquad \text{Equation (1.27)}$$

Hence for the lowest order (N=1) soliton, a relationship between dispersion, pulse energy and pulse duration can be derived:

$$\tau_{p0} = \lambda \cdot w_{eff}^2 \cdot \frac{|\beta_2|}{E \cdot n_{2I}} \qquad \text{Equation (1.28)}$$

From this expression, it can be seen that the pulse duration is inversely proportional to the pulse energy. Additionally, it is proportional to the square of the effective beam waist, hence a small reduction in the beam waist should have a considerable effect on the modelocked pulse duration. This is important in reducing the modelocking threshold of a laser, discussed in chapter 5.

1.5 Summary

The basic techniques appropriate to the design and operation of active and passive modelocked lasers have been outlined in this chapter. The key procedures employed throughout the work discussed in this thesis to characterise ultrashort pulses, have also been described. The effects of chromatic dispersion on ultrashort pulse propagation and the nonlinear effects associated with high peak optical powers, have been discussed in the context that is relevant to the behaviour of a modelocked laser cavity.

In chapter 2, an all-solid-state laser pump source, suitable for pumping a modelocked laser, is described. Chapter 3 provides a description for the application of a simple, yet efficacious, stabilisation technique, to an actively-modelocked colour-centre laser, for improved modelocking performance. In chapter 4 the novel and unusual vibronic solid-state gain medium Cr^{4+}:YAG is introduced, with cw and modelocked performance and limitations discussed. The design of a compact laser cavity specifically aimed at overcoming some of the drawbacks associated with Cr^{4+}:YAG is

described in chapter 5, and results for a compact system with repetition rates up to 400 MHz are presented.

References

1 A.L. Schawlow and C.H. Townes, *Phys. Rev.* **112**, 1940 (1958)

2 T.H. Maiman, *Nature* **187**, 493 (1960)

3 H.W. Messenger, *Laser Focus World* **30 No. 10**, Editorial p5 (1994)

4 I.D. Jung, F.X. Kärtner, N. Matuschek, D.H. Sutter, F. Morier-Genoud, Z. Shi, V. Scheuer, M. Tisch, T. Tschudi and U. Keller, *Appl. Phys. B* **65**, 137 (1997)

5 P.M.W. French, private communication at LEOS meeting on ultrafast physics, Glasgow 1997

6 A.E. Siegman in *Lasers*, (University Science Books, Mill Valley, California) 1986

7 H.A. Haus, *J. Appl. Phys* **46**, 3049 (1975)

8 G.H.C. New, *Rep. Prog. Phys.* **46**, 877 (1983)

9 D. J. Kuizenga and A. E. Siegman, *IEEE J. Quantum Electron.* **QE-6**, p694 (1970)

10 P.T. Ho, L.A. Glasser, E.P. Ippen, H.A> Haus, *Appl. Phys. Lett.* **33**, 241 (1978)

11 L.A. Glasser, *Electron. Lett.* **14**, 725 (1978)

12 H. Kawaguchi and A.K. Sarwar, *Appl. Phys. Lett.* **62**, 2164 (1993)

13 P. Langlois, D. Gay, N. McCarthy and M. Piché, *Opt. Lett.* **23** , 114 (1998)

14 H. Statz and C.L. Tang, *J. Appl. Phys.* **36**, 3923 (1965)

15 G.H.C. New, *Rep. Prog. Phys* **46**, 877 (1983)

16 G.R. Huggett, *Appl. Phys. Lett.* **13**, 186 (1968)

17 D.E. Spence, J.M. Evans, W.E. Sleat and W. Sibbett, *Opt. Lett.* **17**, 1762 (1991)

18 E.P. Ippen, C.V. Shank and A. Dienes, *Appl. Phys. Lett.* **21**, 348 (1972)

19 G.H.C. New, *Opt. Commun.* **6**, 188 (1972)

20 R.L. Fork, B.I. Greene and C.V. Shank, *Appl. Phys. Lett.* **38**, 671 (1981)

21 A. Finch, G. Chen, W.E.D. Sleat and W. Sibbett, *J. Mod. Opt.* **35**, 345 (1988)

22 J.Q. Bi, W. Hodel and H.P. Weber, *Opt. Commun.* **89**, 240 (1992)

23 K.J. Blow and D. Wood, *J. Opt. Soc. Am. B* **5**, 629 (1988)

24 L.F. Mollenauer and R.H. Stolen, *Opt. Lett.* **9**, 13 (1984)

25 J.R.M. Barr and D.W. Hughes, *Appl. Phys. B* **49**, 323 (1989)

26 C. Speilmann, F. Krausz, E. Wintner and A.J. Schmidt in *Digest of the Topical Meeting on Ultrafast Phenomena* (Optical Society of America, Washington, D.C., 1990), paper PD10

27 J.K. Chee, E.C. Cheung, M.N. Kong and J.M. Liu in *Digest of the Topical Meeting on Ultrafast Phenomena* (Optical Society of America, Washington, D.C., 1990), paper MA2

28 P.M.W. French, J.A.R. Williams and J.R. Taylor, *Opt. Lett.* **14**, 686 (1989)

29 C.P. Yakymyshyn, J.F. Pinto and C.R. Pollock, *Opt. Lett.* **14**, 621 (1989)

30 A. Sennaroglu, T.J. Carrig and C.R. Pollock, *Opt. Lett.* **17**, 553 (1992)

31 F.M. Mitschke and L.F. Mollenauer, *IEEE J. Quantum Electron.* **QE-22**, 2242 (1986)

32 D.E. Spence, P.N. Kean and W. Sibbett, *Opt. Lett.* **16**, 42 (1991)

33 D.K. Negus, L. Spinelli, N. Goldblatt and G. Feugnet in *Advanced Solid-State Lasers Topical Meeting Vol. 10 OSA Proceedings Series* (Optical Society of America, Washington, D.C., 1991) p120

34 F. Salin, J. Squier and M. Piché, *Opt. Lett.* **16**, 1674 (1991)

35 M. Piché, *Opt. Commun.* **86**, 156 (1991)

36 J. Herrmann, *J. Opt. Soc. Am. B*, **11** , 498, (1994)

37 F. Salin and J. Squier, *Opt. Lett.* **17**, 1352 (1992)

38 V. Magni, G. Cerullo and S. De Silvestri, *Opt. Commun.* **96**, 348 (1993)

39 V. Magni, G. Cerullo and S. De Silvestri, *Opt. Commun.* **101**, 365 (1993)

40 G. Cerullo, S. De Silvestri, V. Magni, and L. Pallaro, *Opt. Lett.* **19**, 807 (1994)

41 G. Cerullo, S. De Silvestri and V. Magni, *Opt. Lett.* **19**, 1040 (1994)

42 V. Magni, G. Cerullo S. De Silvestri and A. Monguzzi, *J. Opt. Soc. Am. B* **12**, 476 (1995)

43 N. Sarukura, Y. Ishida, T. Yanagawa and N. Nakano, *Appl. Phys. Lett.* **57**, 229 (1990)

44 N.H. Rizvi, P.M.W. French and J.R. Taylor, *Opt. Lett.* **17**, 279 (1992)

45 C. Spielman, F. Krausz, T. Brabec, E. Wintner and A.J. Schmidt, *Opt. Lett.* **16**, 1180 (1991)

46 Examples of commercial self-modelocked Ti:Sapphire systems are the Tsunami system from Spectra-Physics, Mountain View, CA USA, and the Mira from Coherent, Santa Clara, CA USA

47 A. Miller, P. Li Kam Wa, B.H.T. Chai and E.W. Van Stryland, *Opt. Lett.* **17**, 195 (1992)

48 V.P. Yanovsky, F.W. Wise, A. Cassanho and H.P. Jensenn, *Opt. Lett.* **20**, 1304 (1995)

49 K.X. Liu, C.J. Flood, D.R. Walker and H.M. van Driel, *Opt. Lett.* **17**, 1361 (1992)

50 G.P.A. Malcolm and A.I. Ferguson, *Opt. Lett.* **16**, 1967 (1991)

51 A. Seas, V. Petricevic and R.R. Alfano, *Opt. Lett.* **17**, 937 (1992)

52 A. Sennaroglu, C. R. Pollock, and H. Nathel, *Opt. Lett.* **19**, p390 (1994)

53 G.T. Kennedy, R.S. Grant and W. Sibbett, *Opt. Lett.* **18**, 1736 (1993)

54 Y.-F. Chou, K.-L. Deng and J. Wang, *Opt. Lett.* **18**, 1247 (1993)

55 G. Gabetta, D. Huang, J. Jacobson, M. Ramaswammy, H.A. Haus, E.P. Ippen and J. Fujimoto, in *Technical Digest of Conference on Lasers and Electro-Optics* (Optical Society of America, Washington D.C. 1991) paper CPDP8

56 K.A. Stankov and J. Jethwa, *Opt. Commun.* **66**, 41 (1988)

57 G. Cerullo, V. Magni and A. Monguzzi, *Opt. Lett.* **17**, 1785 (1995)

58 R. DeSalvo, D.J. Hagan, M. Sheik-Bahae, G. Stegeman and E.W. Van Stryland, *Opt. Lett.* **17**, 28 (1992)

59 D.J. Bradley, B. Liddy, W.E. Sleat, *Opt. Commun.* **2**, 391 (1971)

60 W. Sibbett, *Proc. XVth international conference on high speed photography and photonics, SPIE* **21**, 226 (1982)

61 A. Finch, Y. Liu, W.E. Sleat, W. Sibbett and G. Chen, *Proc XVIIIth international conference on high speed photography and photonics, SPIE* **1032**, 97 (1988)

62 H.P. Weber, *J. Appl. Phys.* **38**, 2231 (1967)

63 A.M. Weiner, *IEEE J. Quantum Electron.* **QE-19**, 1276 (1983)

64 F.R. Laughton, J.H. Marsh, D.A. Barrow and E.L. Portnoi, *IEEE J. Quantum Electron.* **QE-30**, 838 (1994)

65 H.K. Tsang, L.Y. Chan, J.B.D. Soole, H.P. Leblanc, M.A. Koza and R. Bhat, *Electron. Lett.* **31**, 1773 (1995)

66 A.M. Georgievski and S.V. Zaitsev, *Instrum. & Exper. Techniques* **39**, 117 (1996)

67 D.T. Reid, M. Padgett, C. McGowan, W.E. Sleat and W. Sibbett, *Opt. Lett.* **22**, 233 (1997)

68 C. McGowan, D.T. Reid, M. Ebrahimzadeh and W. Sibbett, *Opt. Commun.* **134**, 186 (1997)

69 L.P. Barry, P.G. Bollond, J.M. Dudley, J.D. Harvey and R. Leonhardt, *Electron. Lett.* **32**, 1922 (1996)

70 G.P. Agrawal in *Nonlinear Fiber Optics* (Academic Press, London 1995)

71 D.J. Kane and R. Trebino, *IEEE J. Quantum Electron.* **29**, 571 (1993)

72 R.S. Grant, Ph.D. Thesis, University of St. Andrews (1991)

73 O.E. Martinez, R.L. Fork and J.P. Gordon, *Opt. Lett.* **9**, 156 (1984)

74 R.L. Fork, O.E. Martinez and J.P. Gordon, *Opt. Lett.* **9**, 150 (1984)

75 J.P. Gordon and R.L. Fork, *Opt. Lett.* **9**, 153 (1984)

76 B.E. Lemoff and C.P.J. Barty, *Opt. Lett.* **17**, 1367 (1992)

77 B.E. Lemoff and C.P.J. Barty, *Opt. Lett.* **18**, 57 (1993)

2. Construction Of An All-solid-state Nd:YAG Pump Laser

2.1 Introduction

The tunable 1.5 μm laser sources discussed in this thesis, viz, the NaCl:OH^- colour-centre laser described in chapter 3, the older colour-centre KCl:Tl^0 laser, and their prospective room temperature replacement, the Cr^{4+}:YAG laser, possess broad absorption bands around 1 μm. In the case of Cr^{4+}:YAG the absorption peak is at 1.030 μm[1] whereas the peak for NaCl:OH^- is closer to 1.1 μm[2]. Until relatively recently, the only high power pump lasers available for excitation purposes in this wavelength region have been mainframe Nd^{3+}:YAG systems using side-pumped arc-lamp pumping, operating at the strongest Nd^{3+}:YAG line at 1.064 μm. For pumping Cr^{4+}:YAG, >6W stable cw output power was required for self-modelocked femtosecond operation[3]. In the case of the synchronously pumped modelocked (SPML) colour-centre laser, the pump laser is required to be actively modelocked. This produces pulses of ~5 ps from a synchronously modelocked NaCl:OH^- laser[4], and initiates modelocking in a femtosecond, coupled-cavity modelocked colour-centre laser[5].

Relying on commercial mainframe lasers as a pump source has its drawbacks, not least of which are the considerable running costs. Neodymium, being a rare earth element, has transitions that are purely electronic in behaviour giving rise to an absorption spectrum consisting of a series of sharp lines (figure 2.1)[6]. Using the light emitted by a krypton arc-lamp for optical pumping is therefore inefficient because the broadband emission from a krypton arc does not readily match the absorption lines in the Nd^{3+}:YAG medium[7]. As a consequence, most of the power consumed in driving the arc-lamp is wasted. In the case of the Spectra-Physics SP3800 for example, a 4.1 kW arc-lamp is required, yielding just 12W cw in a TEM_{00} mode. This inefficiency inevitably leads to undesirable heating, and mains water-cooling is essential.

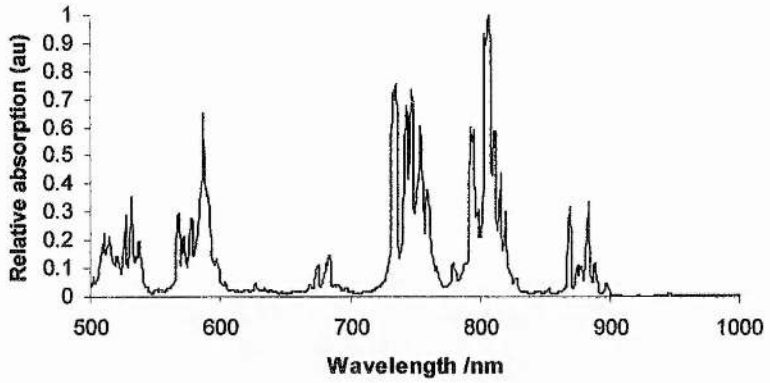

FIGURE 2.1: *Absorption spectrum of Nd:YAG.*

A more efficient approach is to optically pump the Nd^{3+}:YAG at a wavelength corresponding to one of the absorption peaks in figure 2.1. Fortunately, high power AlGaAs laser diodes are now commercially available which are designed to operate at the wavelength of the largest Nd^{3+}:YAG peak at 808 nm. Replacing the arc-lamp with laser diodes not only reduces running costs, but eliminates the dependence on mains water cooling and large three-phase power supplies opening up the possibility of the construction of a compact laser system. Recently, this has been demonstrated by the replacement of expensive and inefficient argon ion lasers with the Spectra-Physics 'Millennia,'[8] and Coherent's air-cooled 'Verdi'[9] lasers, both highly compact, intracavity frequency-doubled Nd^{3+}:YVO_4 lasers operating with up to 5W output power at 532 nm.

In this chapter, I will detail the design and operation of high power laser diode pumped Nd^{3+}:YAG laser sources. From early experience gained while using Cr^{4+}:YAG with mainframe Nd:YAG laser pumping (see chapter 5), it was apparent that ~6W of linearly polarised cw laser power at ~1 μm was necessary to drive a self-modelocked Cr^{4+}:YAG system. As discussed in the following section, practically any laser source would be superior to the arc-lamp pumped Nd:YAG laser used early on in this work, however, as a benchmark, it was expected that amplitude noise of <10% rms over a one minute period and negligible beam pointing stability would be achieved by opting for an all-solid-state pump laser (in line with other reported all-solid-state Nd based lasers[8]).

As a replacement of the modelocked mainframe laser, the all-solid-state alternative should generate pulses of ~100 ps duration at a repetition frequency of

~80 MHz. Average output power is required to be ~3W for pumping the colour-centre laser, however, since a green light source is also required for NaCl:OH^- pumping (see chapter 3), average output powers of ~5W are desirable to generate an additional second-harmonic 532 nm signal in an anisotropic doubling crystal. Again the amplitude and beam pointing stability of this laser would be superior to the mainframe laser it replaces.

With cw performance, the all-solid-state laser described in this chapter achieves 8.3W output power with considerably improved stability over the mainframe laser. Modelocked performance of different laser systems having a range of pulse repetition rates (192MHz and 82MHz) is reported with average output powers up to 6.5W.

2.2 The Mainframe SP3800 Nd^{3+}:YAG Laser

2.2.1 Design And Construction

To gain some insight into the advantages obtained in opting to use a laser diode pumped Nd^{3+}:YAG system as opposed to the mainframe arc-lamp pumped lasers (e.g. the Spectra Physics SP3800 and SP3000 systems), it is useful to study some of the features of the SP3800 laser with the intention to use it as a pump source for the modelocked laser in mind.

The SP3800, in common with all arc-lamp pumped lasers, relies on a side-pumped geometry. This takes the form of a closed, highly polished, gold-plated cylindrical chamber of elliptical cross-section, with a long, low-concentration Nd^{3+} doped YAG rod placed along one focus, and the arc-lamp of similar length parallel along the other[7]. This inevitably leads to pumping a greater volume of the gain medium than is depleted by a circulating TEM_{00} laser field. To suppress multiple transverse modes, it is therefore essential that an aperture be placed at a suitable location in the cavity thereby discriminating in favour of TEM_{00} operation but at a cost of reduced output power.

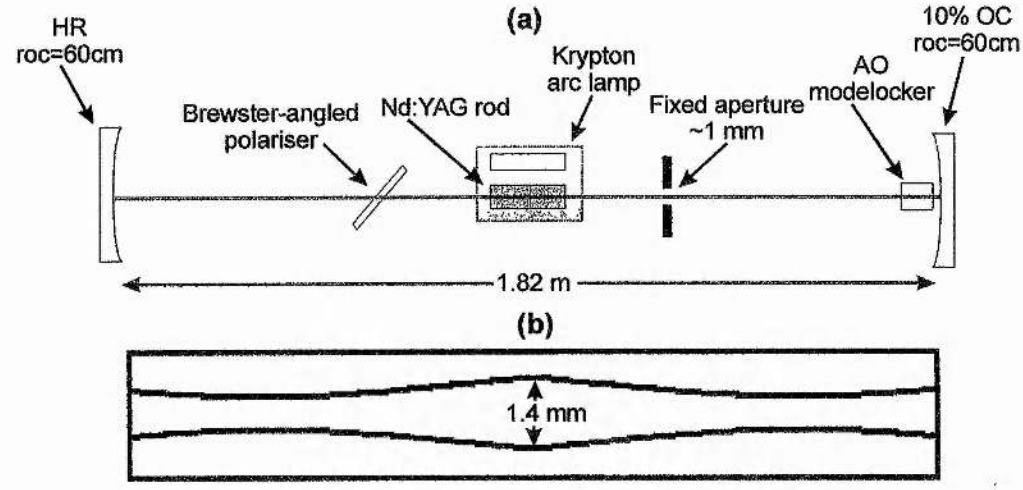

FIGURE 2.2 (a) *Cavity layout of the SP3800 laser* **(b)** *Beam inside the cavity during operation*

The designers of the SP3800 laser (and its lower power predecessor, the SP3000), have exploited the effect of thermal lensing in the Nd^{3+}:YAG rod to increase operational efficiency. The cavity has a symmetrical design, as shown in figure 2.2(a), with the two mirrors separated to a distance which is outside the stability range of an empty resonator. During lamp pumped operation, the 8 cm long cylindrical rod receives a circularly symmetrical heating effect causing it to act as a distributed spherical lens of focal length ~36 cm[10]. The addition of this lens to the cavity allows the resonator to reach stability with the laser mode inflated inside the gain medium (figure 2.2(b)) thus exploiting more of the lamp pumped region.

One major drawback of the SP3800 laser was the excessively noisy output beam. This manifested itself as two effects:

i) low frequency amplitude noise; the SP3800 had an active closed-loop 'light control' circuit which dramatically reduced the amplitude fluctuations on the output beam. Without this, the noise was in excess of +/- 5 %.

ii) beam pointing instability; observable as a random motion of the laser output beam on a similar timescale to the amplitude noise.

The SP3800 fitted with the SP3800 optics as supplied (i.e. with a 1.1 mm aperture and both mirrors having 50 cm radius of curvature (roc)) was too noisy for use as a solid-state pump source. This matter was partially resolved by fitting a smaller aperture (1.0 mm in this case) and mirrors from the SP3000 laser (both 60 cm roc). All the

experiments performed using this laser as a pump source used this arrangement, unless stated otherwise.

2.2.2 Characterisation Of The Noise

To illustrate the improvement in performance expected when replacing the mainframe Nd^{3+}:YAG laser with a laser diode pumped system, measurements were performed on the output power of the SP3800 laser aligned for low noise, high power cw pumping (i.e. with SP3000 optics and a 1.0 mm aperture) using a large area germanium photodiode with a linear amplifier.

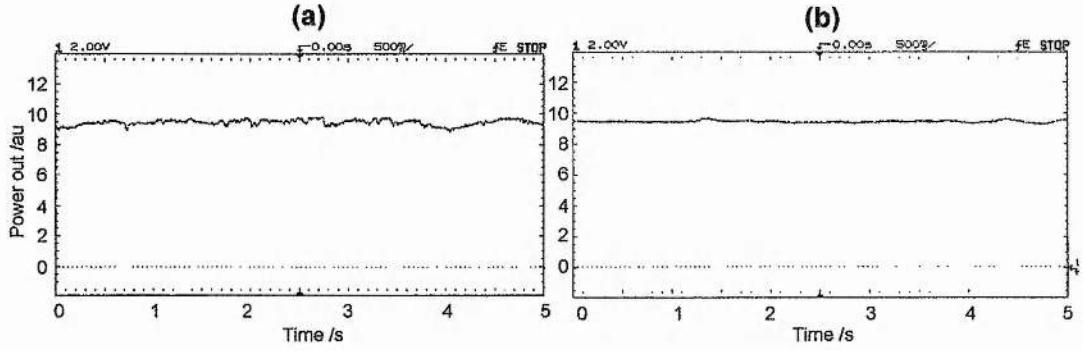

FIGURE 2.3: *Characterisation of the amplitude noise of the mainframe SP3800, (a) Without light control active stabilisation (noise=10.5% pk-pk), (b) With light control (noise=4.6% pk-pk)*

Figure 2.3 demonstrates the improvement in amplitude stability attained when the closed loop 'light control' circuit is implemented on the SP3800. Without active stabilisation, the ripple on the laser output (over a period of 5 seconds) is in excess of 10% (peak to peak) (figure 2.3 (a)). Applying light control reduces this noise to less than 4.6% (figure 2.3 (b))[11].

To characterise the beam pointing instability of the laser, a calibrated quadrant detector was used. This is a special photodiode split into four equally sized sectors. Two error signals derived from these four diodes fully describe the position of a light beam falling on the quadrant detector by a combination of magnitude and sign of the output voltage. This was calibrated by placing the detector on two orthogonally mounted translation stages with micrometer actuators controlling the X and Y directions, and recording the error voltages in the two planes as the detector was translated through a weakly focused spot (using a 30 cm focal length lens) from a HeNe laser. Using the same lens to focus the spot of the SP3800 laser onto the centre of the detector enabled

the motion of the laser beam waist to be monitored over a period of time using an X-Y plotter. The motion of the SP3800 with SP3000 optics and 1.0 mm aperture was recorded for one minute in figure 2.4. The detector was placed two metres away from the output coupler and a 30 cm lens focused a spot w_0~100 μm onto its centre. The beam was unexpectedly observed to be asymmetric in its movement; as much as 90 μm in the X plane but only 50 μm in the Y plane.

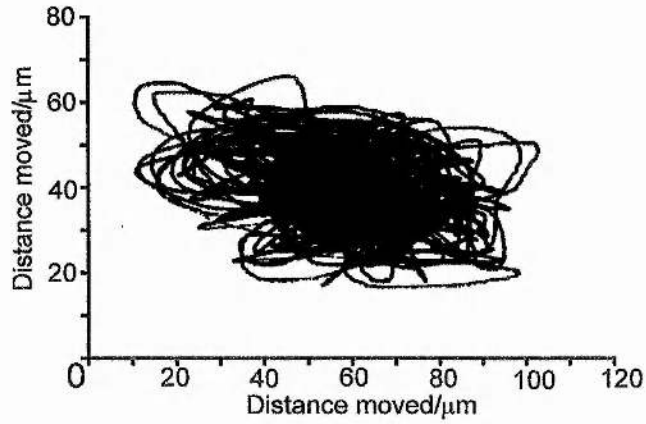

FIGURE 2.4: *Beam pointing instability of the mainframe laser SP3800 (fitted with SP3000 optics and a 1.0 mm aperture) recorded two metres away from the laser at a large beam waist over a period of one minute.*

It is worth pointing out that while figure 2.4 was recorded with the light control stabilisation on, a similar measurement performed on the laser with no active stabilisation applied showed beam motion to an identical extent, implying that light control stabilisation has no effect on beam pointing instability.

There was some uncertainty as to whether fitting a larger aperture to the laser might increase beam pointing stability (and output power) but at a cost of reduced amplitude stability. This reasoning was as a result of an earlier measurement taken without the lens to focus the beam onto the quadrant detector (i.e. the output beam was allowed to impinge on the detector with a large spot) which indicated significantly less motion from a laser fitted with a 1.3 mm aperture than one with a 1.0 mm aperture. However, repeating this measurement using a lens to form a waist at the detector suggested the beam motion was actually worse (as illustrated in figure 2.5), with the waist covering an area of 90μm x 160μm. The earlier contradictory result may be explained as an effect of a beam spot larger than the detector; increasing the size of the aperture expands the beam spot on the detector thus desensitising the quadrant detector

from measuring movement. Further evidence of this was the nonlinear behaviour noted from the error signals when translating the detector through a large, unfocussed HeNe laser beam, probably as a result of the Gaussian profile. Care is therefore needed when using quadrant detectors to compare laser performance, that the system is set up so that the laser spot size is sufficiently small compared to the size of the detector. In this case this was assured by the linear response of the detector when translating it through the focused beam.

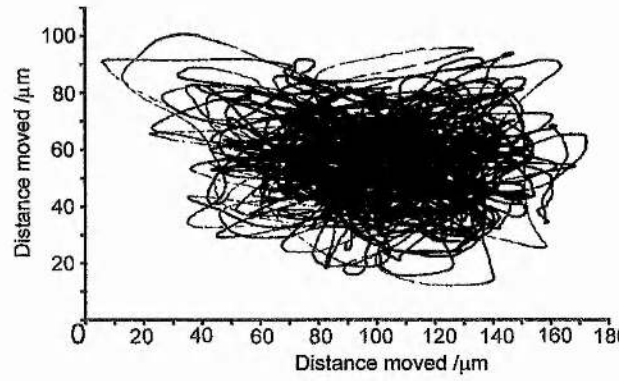

FIGURE 2.5: *Effect of increasing the intracavity aperture on the SP3800 beam pointing stability. All parameters identical to figure 2.4 except aperture=1.3 mm diameter.*

The beam pointing instability was not a great hindrance when the laser was employed as a pump source for the NaCl:OH^-, and KCl:Tl^0 colour-centre lasers; their gain media have a short length (~2 mm) and modelocking relies principally on the pump pulse shape, not on the stability of the pumped volume. However, using the mainframe laser as a pump source for the Cr^{4+}:YAG laser introduced problems: The gain medium has a low pump absorption coefficient (~1.5 cm^{-1}) and thus needs to be long (~20 mm) to absorb sufficient incident pump light for efficient operation. It therefore suffers more noticeably from pump beam motion than the colour-centre lasers. Attempting to operate this laser to produce femtosecond duration pulses, using self-modelocking with a soft aperture effect, exacerbated the issue. The modelocking mechanism requires that the modelocked laser mode experiences greater gain in the laser medium by better pump-laser mode overlap than the cw mode. If the gain region is constantly shifting in position due to beam pointing instability, stable modelocked operation is impossible to achieve.

2.3 AlGaAs Laser Diodes For Pumping Nd:YAG

Semiconductor laser diodes were first employed as a pump source for Nd^{3+}:YAG in 1968[12] but it has only been since the mid-1980's, with the development of high power AlGaAs laser diode bars, that the possibility of realising an all-solid-state replacement for high power, cw, arc-lamp pumped Nd^{3+}:YAG lasers became realistic.

2.3.1 Overview of diode-pumping approaches

Whilst it is inappropriate here to enter into detail concerning the construction and operation of semiconductor laser diodes (the subject has been dealt with extensively elsewhere[13]) it is useful to look at some of the characteristics of diode lasers which must be considered when designing an all-solid-state system.

Owing to the highly asymmetric nature of their construction i.e. ~20 emitters each ~80 μm x 1 μm, equally spaced on a 1cm wide semiconductor bar, the beam emitted from a bare diode bar has vastly differing divergences in the two planes, e.g. the 20 W SDL-3460-S laser diode bar has divergences of 5^{O} and 40^{O} in the planes parallel and perpendicular to the active region respectively. However, this inequality in divergences is not as important as the beam quality (or M^2)[14] of the light emitted from the laser diode bar. Whereas the light perpendicular to the active region is near diffraction limited (i.e. close in behaviour during focusing and subsequent propagation to an ideal laser source with an M^2~1), the light parallel to the active region is >1000 times diffraction-limited[15]. The effect of this is that focusing the beam equally in both planes results in an elliptical spot 1000 times larger in the parallel plane than the other plane- or alternatively, to focus down to an equal sized spot in both planes involves the parallel plane diverging 1000 times faster than the diffraction-limited plane. The significance of this imbalance depends on the laser diode pumping geometry employed.

Side-pumped laser geometries

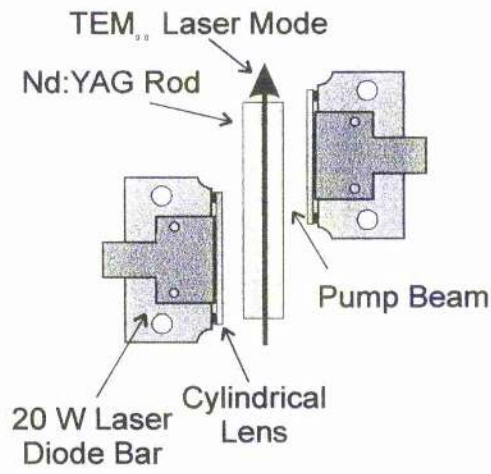

FIGURE 2.6: *Generalised schematic of side-pumped Nd:YAG laser geometries*

The principle of a side-pumped Nd^{3+}:YAG laser is very similar to that of an arc-lamp pumped system (figure 2.6)[16]. Usually several laser diode bars are placed parallel to a Nd^{3+}:YAG rod which has a highly polished AR coated barrel. A cylindrical lens is usually used to collimate the highly diverging diffraction limited plane, but no control is necessary of the non-diffraction-limited axis. Better coupling of the pump light into the Nd^{3+}:YAG laser's TEM_{00} mode is realised with this scheme than with an arc-lamp in an elliptical chamber mainly due to the higher brightness of the laser diode emission. Also the laser diode emits at a wavelength corresponding to the strongest absorption transition in Nd^{3+}:YAG in figure 2.1 at 808 nm. This enables much greater optical-optical conversion efficiencies (up to 25% recently demonstrated[17]) than is possible with an arc-lamp pumped laser. This pumping scheme has the advantage that only a small, distributed thermal load is imposed on the Nd^{3+}:YAG rod allowing this laser design to be scaled up to extraordinarily high output powers. (Recently a fibre-coupled laser diode side-pumped geometry was demonstrated giving up to 160 W multimode and 62 W TEM_{00}[17].) Unfortunately, for constructing lasers with up to 10 W output power, this relatively inefficient scheme is inappropriate, requiring the expense of several laser diode bars when, theoretically, just one could be used if optimally employed.

Longitudinally pumped laser geometries

Maximising the efficiency of any optically pumped laser system involves optimising the overlap of the circulating laser mode with the inverted (pumped) region. To this end, the most natural pumping scheme to employ is one where both pump and laser modes are collinear, involving pumping the gain medium along the optical axis (end pumping). It is when attempting to construct end pumped lasers using the currently available high power laser diode bars that the highly asymmetric nature of their beam quality becomes problematic. The near diffraction limited plane can easily be focused to overlap the circulating laser mode over the whole length of the gain medium, however the non-diffraction-limited plane allows mode matching over only very small distances. This leads to poor efficiency and excessive heating of the Nd^{3+}:YAG rod. One approach to increase pump mode overlap in the non-diffraction limited plane has been demonstrated recently with Cr^{3+}:LiSAF[18]; a cylindrical intracavity mirror was used to produce a highly elliptical mode in the gain medium. Unfortunately, the beam quality of the resulting Cr^{3+}:LiSAF laser was relatively poor in the corresponding plane (M^2~1.8). Another method involves internally folding the resonator mode at the pumped surface of the gain medium thus allowing the faster diverging non-diffraction-limited plane to overlap over a broader laser mode area.[15,19]

Techniques have been employed to 'reshape' the highly asymmetric laser diode mode into one more suitable for pumping a resonator having a circularly symmetric laser mode in the gain region. These have included stripe stacking devices, which reshape the beam in free space, e.g. Clarkson and Hanna's two mirror system[20] or Edwin's stripe stacker[21]. Beam reshaping has enabled efficiencies up to 42%[22] to be obtained in end-pumped Nd^{3+}:YAG lasers. An alternative, extremely rugged technique employed in commercial high power end-pumped laser systems involves fibre coupling of the laser diode bars[23], and was the method employed in this work

2.3.2 Fibre-coupled laser diodes

The fibre-coupled laser diode pump source was commercially obtained from Opto-Power Corporation (model no. OPC-B030-FC). This consisted of two standard OPC 20 W diode bars, each having 19 emitting facets (each ~80 μm wide) spaced ~400 μm apart. A fibre lens mounted in front of the bar served to collimate the fast

(perpendicular) axis. Each emitter was then coupled into an AR coated optical fibre (~100 μm core, NA=0.11) simply by positioning the fibre a suitable distance away from the diode bar. The 38 individual fibres from the two bars could then allow a symmetric source to be created by rearranging the fibres into a circular bundle of 1.55 mm diameter. Inevitable coupling losses allowed a maximum output power of 35 W to be obtained from the fibre bundle, with a total ~40 W emitted from the two bare bars. Using a commercially obtained optical converter (model no. OPC-OC-01) comprising two aspherical lenses, this fibre bundle could be subsequently coupled into a single core multimode fibre. Usually a fibre with a core size of 600 μm and 0.37 NA was used with 82 % coupling efficiency, but later experiments involved pumping with a 400 μm 0.37 NA fibre. The smaller fibre was a brighter pump source enabling better pump-mode overlap to be attained[15] but at the expense of much poorer coupling efficiency in the OPC converter (rated at 41 %). The uncoupled laser light leads to heating of the SMA fibre adapter. Note that fibre coupling the laser diodes does not increase the overall brightness of the laser diode (in fact it is reduced), it merely offers a straightforward means to reshape the asymmetric source and deliver the light conveniently to the application.

It is worth pointing out an advantage that fibre-coupling has over other beam reshaping techniques, which is of particular value in commercial laser diode pumped systems. Unlike standard free-space arrangements, which require that the laser diodes be placed alongside the gain medium in the laser head, fibre coupling allows the laser diodes to be placed well away from the actual laser; e.g. in the Millennia and Verdi intracavity doubled Nd^{3+}:YAG systems, the laser diodes (and their ancillary cooling requirements) are positioned in the laser power supply[24]. In the Verdi system in particular, this is applied to maximal advantage in enabling the fibre bundles to be simply detached from the laser diode bar to permit rapid replacement of failed laser diodes without necessitating any specialised realignment procedures.

The temperature of the laser diode arrays was controlled using a Peltier effect thermoelectric cooler mounted on a water cooled base. A commercial temperature controller (Marlowe R020) controlled the temperature to within +/- 0.05^{o}C. One temperature controller was used, running both Peltier coolers in series whilst monitoring the temperature of one diode with an internally mounted thermistor.

The drive current for both laser diode bars connected in series was supplied by a Kingshill constant current power supply. It was found that the wavelength of the emitted radiation varied dramatically depending on the drive current, and the rated operating wavelength of 810 nm at 25^{O}C was not attained unless operating the diodes at the maximum current of 30 A. The wavelength could be tuned by changing the temperature of the diode bars at a rate of 0.3 nm/^{O}C.

2.4 Design Of A High Power cw Nd:YAG Laser

A key consideration to be made when designing high power cw lasers is to maximise the overlap of the inverted (pumped) gain region with the laser field. In the past, several techniques have been developed to achieve this by inflating the laser mode in the gain element using e.g. intracavity telescopes[25], or exploiting the thermal lens in an otherwise unstable resonator[26] (as is the case with the Spectra-Physics lasers described earlier). On the whole, these methods, which were originally designed for arc-lamp pumped systems, are only applicable to side-pumped lasers. Attempting to build an end-pumped system applying these methods is hindered by the aberrated thermal lensing effect as the output power is scaled up.

The low brightness (i.e. high M^2) of the fibre-coupled diode pump source, imposes serious restrictions on the allowed size of the laser mode in the gain medium. Focussing the pump beam tightly to match the size of a small laser mode (such as is produced in e.g. four mirror Z-cavities for Ti:Sapphire) leads to a poor pump-mode overlap as the pump beam will diverge several hundred times faster than the laser beam. Ideally, the laser crystal would have a very high pump absorption coefficient, allowing all the pump to be absorbed within the small volume corresponding to where the pump and laser mode overlap. Unfortunately, Nd^{3+}:YAG cannot be doped with more than 1.1% Nd^{3+} without the upper state lifetime decreasing rapidly due to fluorescence quenching[27]. Thus the maximum possible pump absorption coefficient is limited.

2.4.1 Thermal induced effects

The thermal lens induced when a rod (or slab) of material is optically pumped with high incident powers, results from three effects:[28]

(i) Bulging of the pumped end of the laser rod due to thermal expansion of the laser material. This always forms a positive (converging) lens.

(ii) A radial change in the refractive index due to the steady state temperature gradient under intense pumping. The magnitude and sign of this depends on the laser material's **dn/dT**. For Nd^{3+}:YAG, this is also positive, but for certain materials (e.g. YLF) it is negative and thus forms a diverging lens- useful for counterbalancing the effect of the positive end-bulging lens.

(iii) A thermal stress induced bulk lensing effect.

Ideally, thermal lensing should not be a problem when constructing high power lasers operating on a single transverse mode (TEM_{00}), as any unaberrated positive lens can be taken into account and compensated for when designing the laser cavity. Unfortunately, the thermal lens also has an aberrated component[29] which becomes increasingly important as the pump power is scaled up. This effect cannot be compensated for generally by standard optical components (though several techniques have been proposed to partially compensate this[30]). This 'aberrated' thermal lens leads to an additional loss to the fundamental laser mode. Hence, as the pump power is increased, it becomes more difficult to maintain a single TEM_{00} laser mode oscillating in the cavity. To minimise losses to the TEM_{00} mode, it has been suggested that the laser mode size should be restricted so only the central portion of the pumped region is utilised[31,28], thus perversely wasting a substantial portion of the pump energy.

A second effect which is detrimental to efficient laser operation also occurs when imposing a high thermal load on a laser crystal through optical pumping. This is thermal-stress-induced birefringence, and its effect depends upon whether the laser includes polarisation selecting elements. In the case of Nd^{3+}:YAG, the host has a cubic structure and is therefore optically isotropic, exhibiting no intrinsic birefringence. Unfortunately, when the host is unevenly heated and therefore stressed (as occurs when end-pumping the rod), a degree of birefringence develops[32]. In the case of a plane polarised laser with Brewster-angled elements, the beam becomes slightly depolarised

on each pass through the gain medium, hence a slightly elliptically polarised beam circulates within the laser cavity. The depolarised fraction of the laser may be observed reflected off the Brewster-angled elements and hence an estimate of the degree of thermal-stress-induced birefringence may be made by measuring this power.

Thermal-stress-induced birefringence is a major drawback when scaling up the output powers of plane-polarised end-pumped Nd^{3+}:YAG lasers. The round-trip intracavity losses can be effectively increased by several percent thus wasting potentially useful output power. Side-pumping, with its more distributed thermal load, suffers much less from this effect. One successful method of avoiding the effect completely is to employ a gain medium which has a birefringent host such as Nd^{3+}:YLF or Nd^{3+}:YVO_4. Any additional thermally induced birefringence is insignificant compared to their natural birefringence and hence has no depolarising effect[7]. Unfortunately, these materials have their own problems, namely, lower thermal conductivity, and a tendency to fracture when heated.

2.4.2 Laser Cavity Design

To satisfy the criteria discussed, the final cavity layout employed for high power cw operation was an adaptation of the three-mirror 'dog-leg' design described by Yelland et al[33]. This cavity was optimised for intracavity doubling and the characteristics given below were specifically geared towards fulfilling that goal.

i) Minimum number of cavity elements which therefore minimises parasitic losses; very important to achieve the high intracavity fields necessary for efficient frequency doubling.

ii) Small spot size on the plane end-mirror. This allows very high intensities to be realised in a second harmonic generating (SHG) crystal placed next to this mirror, essential for nonlinear frequency conversion techniques.

iii) Intracavity $\lambda/4$ plate and etalons ensured stable SHG operation on two longitudinal modes using the scheme of Oka et al.[34]

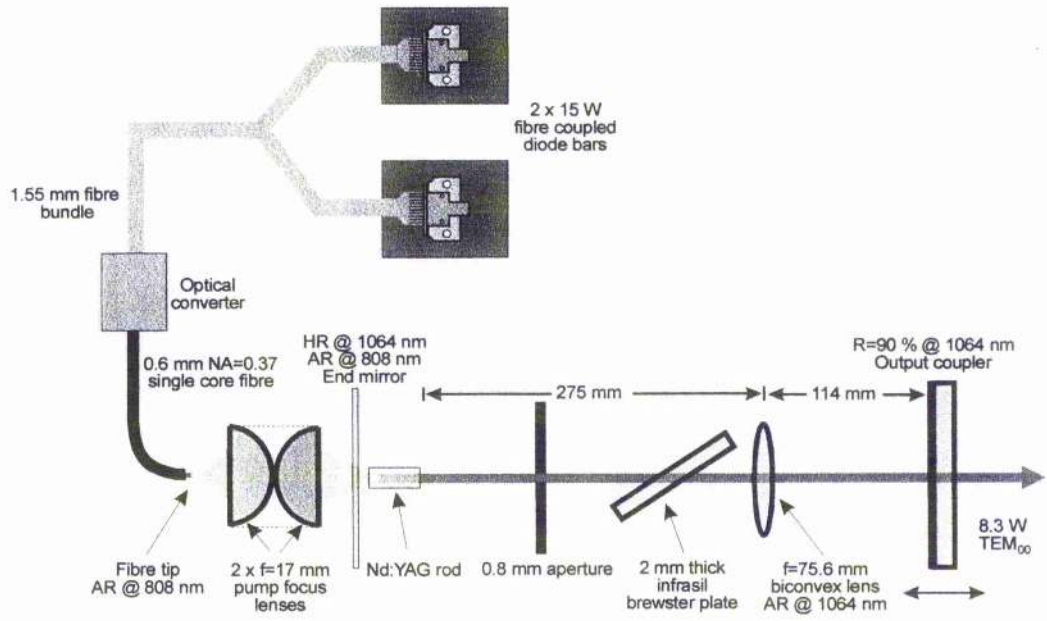

FIGURE 2.7: *Schematic of the 8.0 W cw Nd^{3+}:YAG laser built as a 1 μm pump source*

The cavity was also compact (~33 cm total length, ensuring broad mode spacing) and folded using a 10 cm radius of curvature (roc) mirror at near normal incidence. Compensation for thermal lensing was possible by adjusting the plane end-mirror to folding mirror separation. This laser had promising operation at the fundamental wavelength of 1.064 μm using a 10% output coupler as the plane end-mirror[15] and so was chosen as the starting point for the cw pump laser.

Figure 2.7 is a schematic of the final design built as a stable, reliable 8 W cw pump source. The etalon and λ/4 plate are not necessary for fundamental operation and hence are no longer included. The 10 cm roc folding mirror has been replaced with a 7.5 cm focal length broad-band-AR-coated biconvex lens. This eliminates the astigmatism associated with using the curved mirror slightly off-axis helping to ensure a spherically symmetric pump beam. The extra parasitic loss associated with using a lens can easily be tolerated in a Nd^{3+}:YAG laser designed for fundamental operation. The slightly longer focal length of the lens helps to ensure that TEM_{00} operation can be achieved for a broad range of thermal lens strengths.

Thermal lens estimation

A simple method for calculating the unaberrated thermal lens induced in an end-pumped laser rod was described by Innocenzi et al.[35] which was derived from the steady-state heat flow equation:

$$\nabla \cdot h(r,z) = Q(r,z) \qquad \text{Equation (2.1)}$$

where **h(r,z)** is the heat flux and Q is the power per unit volume deposited as heat. Note that only radial heat flow is considered, and the lensing effect calculated was just that component due to the refractive index change with temperature. An expression is derived, considering the steady state temperature distribution in the rod and the corresponding phase change induced by a change in the refractive index, for the total effective focal length of the thermal lens in the rod:

$$f = \frac{\pi . K_c . w_p^2}{P_{ph} \cdot \frac{dn}{dT}} \cdot \left(\frac{1}{1 - e^{-\alpha . l}} \right) \qquad \text{Equation (2.2)}$$

where $\mathbf{K_c}$ is the thermal conductivity of the rod, $\mathbf{w_p}$ is the spot size of the pump mode (assumed constant throughout the rod), $\mathbf{P_{ph}}$ is the incident pump power which contributes towards heating of the rod, $^{\mathbf{dn}}/_{\mathbf{dT}}$ is the temperature dependence of the refractive index, α is the differential absorption coefficient, and **l** is the rod length.

The model thus described is for a diffraction limited pump source with a Gaussian profile. To model the situation with the fibre-coupled diode pump source, it is necessary to adapt it slightly to account for the divergence of the pump beam as it propagates through the crystal[36]. This may be accomplished by simply slicing the laser rod many times, and calculating the dioptric power of each slice as the pump diverges and exponentially decreases in power due to absorption:

$$f_{eff} = \left\{ \sum_{z=0}^{l} \left[\frac{\pi . K_c . (w_0 + z . \tan(\vartheta))^2}{P_{h0} . e^{-\alpha . z} \cdot \frac{dn}{dT}} \cdot \left(\frac{1}{1 - e^{-\alpha . \delta z}} \right) \right]^{-1} \right\}^{-1} \qquad \text{Equation (2.3)}$$

Here w_0 is the size of the pump beam waist, P_{h0} is the incident pump power which will contribute to rod heating, θ is the divergence half angle of the pump mode (dependent on the etendue of the pump source) and δz is the thickness of each rod slice. This model assumes that the pump focus is placed on the pumped end of the rod.

Applying parameters suitable for the cw laser being designed in the above equation i.e. Nd^{3+}:YAG parameters[35]: $\mathbf{K_c}$=13 W/m.K, α~550 m^{-1}, $^{dn}/_{dT}$=7.3x10^{-6} K^{-1}, **l**=8 mm; for 1:1 imaging of the fibre inside the laser rod, $\mathbf{w_0}$~300 μm, θ~22°, and assuming the laser will operate with ~ 30% efficiency, the incident pump power which will contribute to heating for 8 W output power is $\mathbf{P_{ho}}$~19 W. The total effective focal length of the laser rod given by equation (2.3) due to bulk refractive index change alone is $\mathbf{f_{eff}}$=11.2 cm. The additional lensing effect introduced by bulging of the pumped surface of the rod should also be considered, in an attempt to include this, a stronger lens ($\mathbf{f_{eff}}$=10 cm) was estimated. This lens was positioned at the pumped end of the rod for the purpose of cavity design.

For the three-element cavity shown in figure 2.7, the change in spot size of the laser mode inside the Nd^{3+}:YAG gain medium as the various cavity elements are changed may be calculated using simple ABCD matrix analysis[37]. For the cavity without any thermal lens, this is plotted as the end mirror is translated away from the intracavity lens in figure 2.8, note that the rod to lens separation is kept fixed at 275 mm. The laser cavity only satisfies the stability criteria in the parameter space associated with the trace.

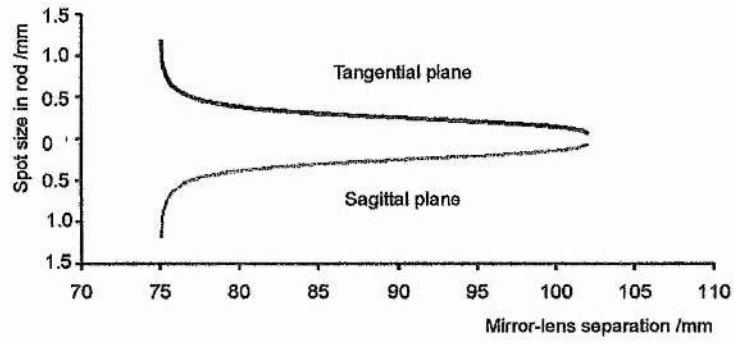

FIGURE 2.8: *Variation of laser spot size in the gain medium as the end mirror is translated away from the intracavity lens. No thermal lens in cavity.*

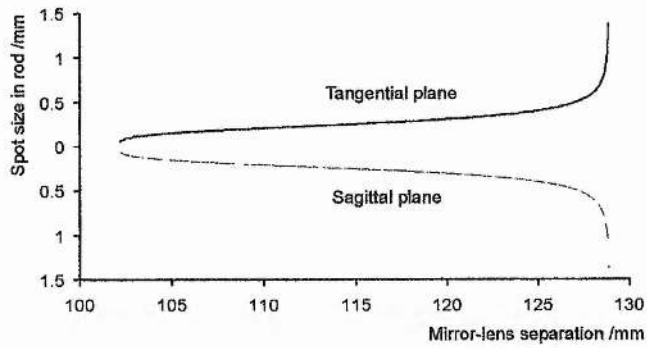

FIGURE 2.9: *Variation of laser spot size in the gain medium as the end mirror is translated away from the intracavity lens. f=10 cm thermal lens included in model.*

The inclusion of the predicted thermal lens on the pumped side of the rod gives the stability diagram in figure 2.9. From these two diagrams it can be seen that the spot size in the laser rod can easily be adjusted for optimum extraction of gain in a TEM_{00} mode simply by translating the end mirror from the focussing lens. This is true both for the cavity without the strong thermal lens (figure 2.8) and with the expected 10 cm lens in the laser rod (figure 2.9).

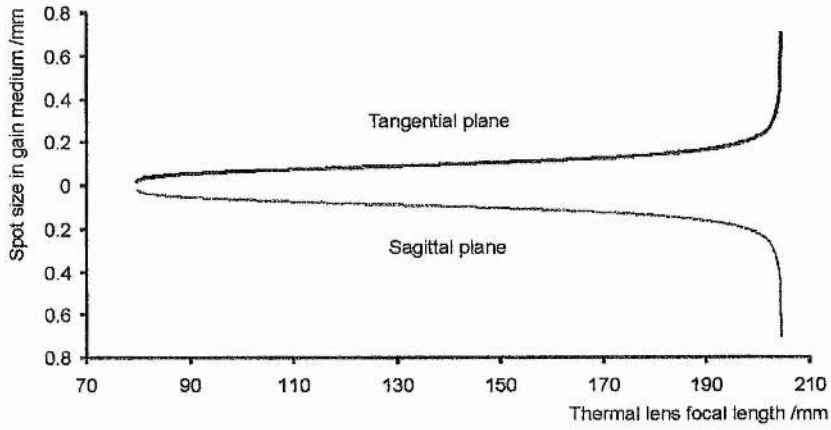

FIGURE 2.10: *Variation of laser spot size in rod with thermal lens strength*

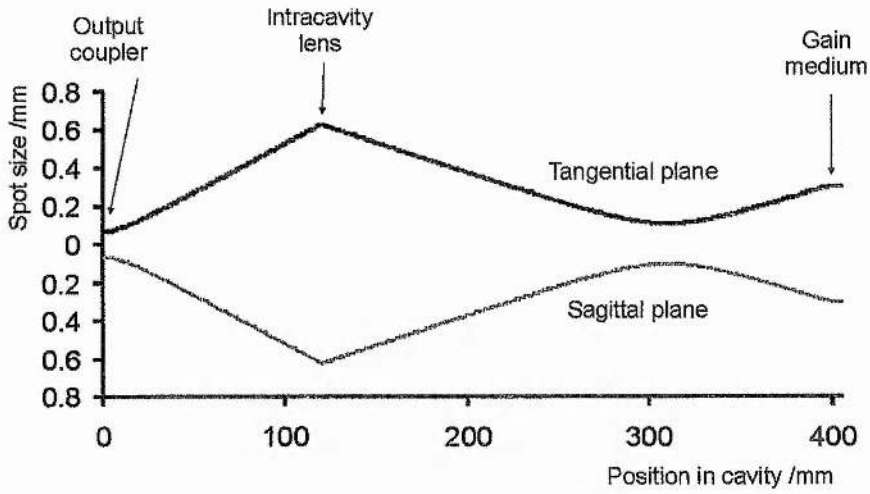

FIGURE 2.11: *'Fish shaped' laser mode inside the cw-laser cavity with a 10 cm thermal lens*

To assess the range of thermal lens focal lengths for which this cavity should be able to compensate, the mirror-lens separation was set to 12 cm giving a spot size of ~600 μm diameter in the gain crystal with a 10 cm thermal lens (figure 2.9). The spot size was recorded as the thermal lens was varied in the ABCD model. The result in figure 2.10 indicates the cavity can tolerate thermal lenses with focal lengths as short as 8 cm.

The profile of the laser mode as the beam propagates around the laser cavity (with 10 cm thermal lens) is simulated in figure 2.11. The thermal lens produces a beam waist ~9 cm behind the gain medium.

CW laser construction

As indicated on the laser schematic in figure 2.7, the pump light from the fibre must be focused into the Nd^{3+}:YAG rod through a thin (~1 mm thick) plane mirror. This was AR coated for the pump wavelength (808 nm) on the rear surface, and HR coated (R>99.9 %) on the front surface for the laser wavelength (1.064 μm). Owing to the highly divergent nature of the light emitted from the 600 μm fibre (~22^{O}), it was necessary to employ fast pump focusing optics if aperturing of the pump was to be avoided. Two AR-coated aspheric lenses (Melles-Griot 01 LAG 004/076) each of focal length f=17.5 mm and diameter ϕ=19 mm (f#=0.895) placed curved sides facing ~1 mm apart, were used to accomplish this. During the initial alignment, the axis of the pump was placed exactly in the centre of the laser rod aligned along the optical axis, helping

to ensure that the laser heating and cooling was circularly symmetric thus (hopefully) minimising aberrated thermal lensing effects which cannot be compensated in this simple cavity arrangement.

The plane-plane AR-AR coated Nd^{3+}:YAG rod (8 mm long x 3.5 mm diameter) obtained from VLOC (Virgo optics and Lightning Optical Corporation), was doped with 1.1 % Nd^{3+}. This was wrapped in indium and mounted in a copper heatsink. Initially, the copper mount was cooled directly with water from a closed cycle water cooler. Unfortunately, this exhibited excessive temperature swings (>5^{O} C) causing the output power of the Nd^{3+}:YAG laser to oscillate by as much as 10 %. To eradicate this effect, an electronically controlled thermoelectric cooler was used in conjunction with a water-cooled base to maintain the temperature of the mount at 8^{O}C.

To find the optimum operating temperature of the laser diodes for maximum pump absorption by Nd^{3+}:YAG, the transmitted pump power was monitored while changing the temperature and drive current of the laser diodes. For a drive current of 20 A, the laser diodes had to be operated at 28^{O}C. Throughout most of the early alignment stages, the diodes were run at this temperature. Only when the drive current exceeded 20 A was the temperature gradually lowered.

For initial alignment purposes, a plane-plane resonator was constructed using two thin, plane-parallel HR mirrors. It was while operating a Nd^{3+}:YAG laser with this cavity that it was observed that it was operating >50:1 plane-polarised at low pump powers, without the inclusion of any intracavity polarisation selecting elements. The plane of the polarisation was vertical with respect to the optical bench. At pump levels exceeding ~5 W, however, the output beam became randomly polarised. The probable cause of this apparent birefringent behaviour of a nominally isotropic host material, was mechanical stress induced birefringence resulting from clamping the rod tightly in the copper heatsink.

The complete cavity shown in figure 2.7 included an infrasil (low loss fused silica) window placed at Brewster's angle to select plane-polarised oscillation. An aperture of 0.8 mm diameter placed ~8 cm behind the laser rod (close to the intracavity beam waist in figure 2.11) helped to ensure that the cavity was operating TEM_{OO} during alignment for high power operation. Without this, it was easy to accidentally align with a 'doughnut' mode structure (mixture of TEM_{01} and TEM_{10} modes).

The cavity was first aligned for the lowest cw threshold, then the entire cavity repeatedly re-aligned (including the pump focusing optics) while increasing the pump power. The laser mode was checked periodically throughout this procedure to ensure that the output was TEM_{00}. TEM_{00} operation was straightforward to achieve providing sufficient care was taken during initial alignment that the pump mode was central in the laser rod and on-axis. The pump was increased up to 22 A drive current (=21.4 W incident pump power), producing a maximum output power of 8.5 W. At this current, the laser diodes were operated at 25.5^{O}C for optimum pump absorption. Attempting to pump the laser at powers higher than this was found to be counterproductive i.e. re-aligning the cavity for TEM_{00} operation led to a drop in actual output power.

2.4.3 CW Laser Characterisation

Power transfer characteristics

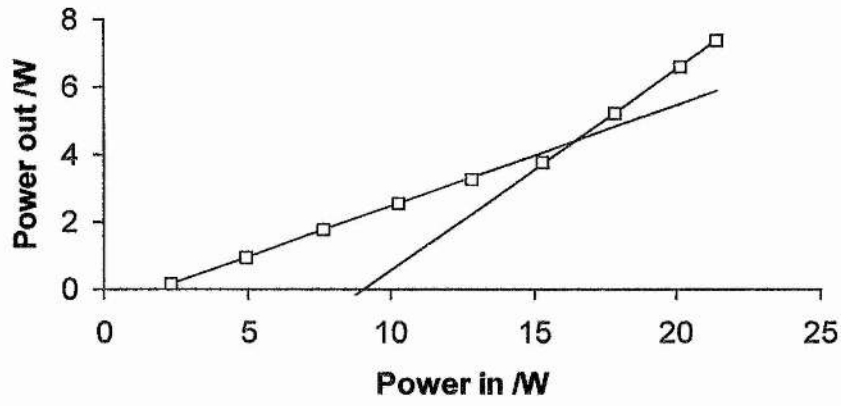

FIGURE 2.12: *Output power characteristics of the cw laser fitted with a 10% output coupler. See text for explanation.*

The output power characteristics of this simple cw laser are shown in figure 2.12. Note that no thermo-electric cooler was used to cool the Nd^{3+}:YAG (direct mains water cooling was employed) hence the highest output power here was only ~7.0 W. These measurements were taken for optimum alignment of the laser cavity for each input power, i.e. the end-mirror-lens separation was optimised for each measurement. Of significance are the two regions with different slope efficiencies. At low powers (less than 13 watts) the power in/power out was the expected straight line with a slope of

30% and the cavity did not require much re-alignment between measurements. However, as the power was increased, the cavity needed to be significantly re-aligned, and a new regime with a slope efficiency of ~60% was reached. This change in slope efficiencies represents a transition from operating in the stability region of figure 2.8, where the spot size in the laser crystal increases as the end-mirror is translated closer to the lens, to operation in the stability region of figure 2.9, where the converse is true due to the increasing strength of the thermal lens.

These transfer characteristics of the laser were measured with several different output couplers, however, due to the additional difficulties encountered with the varying thermal lens strength and accompanying cavity re-alignment, it was difficult to deduce anything useful from these. The 10% output coupler (employed during the measurement of figure 2.12) gave the maximum output power and was used when the diode pumped Nd^{3+}:YAG laser was implemented as a pump source for a Cr^{4+}:YAG laser.

Note that the maximum obtained output power of 8.5 W at 21.4 W incident pump power represents a total optical-optical conversion efficiency of ~40 % into a TEM_{00} mode, a notably high value. This is less than that claimed for the Millennia OEM laser diode pumped head running at the fundamental wavelength of 1.064 μm, which had an efficiency of ~50%[31], but this involved pumping Nd^{3+}:YVO_4 (which has a much greater pump absorption coefficient) from both ends of the gain medium (hence producing a more distributed thermal load). A different cavity arrangement was employed, which placed the gain medium in the centre of a near-confocal resonator.

Beam quality characterisation

An important laser parameter which must be considered when constructing a laser for use as a pump source for another laser is how close the beam is to the diffraction limit. This may be expressed using the parameter M^2, which can be used to describe how a non-diffraction limited beam behaves using standard equations for a diffraction limited beam[14], by scaling the laser's wavelength by a factor M^2, i.e.

$$w(z) = w_0 \cdot \sqrt{1 + \left[\frac{M^2 \lambda z}{\pi {w_0}^2}\right]^2} \qquad \text{Equation (2.4)}$$

$$\vartheta = \frac{\lambda M^2}{\pi w_0} \qquad \text{Equation (2.5)}$$

Equation 2.4 is an expression for the $1/e^2$ radius of a laser beam, w(z), at a position z away from the beam waist w_0[38]. For distances substantially greater than the Rayleigh range away from the beam waist, the spot size may be calculated from the expression for the far field divergence angle, θ, in equation 2.5. To end pump a long laser crystal with a low pump absorption coefficient in a laser resonating a diffraction limited beam, it is imperative that the pump laser has an M^2~1 for good pump and laser mode overlap.

During alignment, the laser mode was periodically studied with an infrared viewer and neutral density filter to ensure that the spot appeared to be Gaussian in form with no discernible substructure. Although this prevented higher order transverse modes becoming dominant, it was still possible for the laser beam to be non-diffraction limited. A measurement of the divergence of the beam from a known beam waist is therefore necessary for a complete assessment of beam quality.

The laser was weakly focused using a lens with a focal length of 30 cm. This ensured a relatively large beam waist which could be easily measured. A reverse-biased large area germanium photodiode with a 25 μm slit in front, enabled scanning of a small spot size. This was mounted on a stepper motor driven translation stage with a step size of 6.35 μm and a variable scanning speed. A flat-bed chart recorder was used to record the scanned profiles.

The beam waist was scanned which indicated a $1/e^2$ half width of 130 μm for both planes, however, the vertical waist was located ~1.5 cm in front of the horizontal waist indicating a source of astigmatism inside the laser cavity. This was probably the thermal lens. The M^2 was then deduced from equation 2.4 by taking a few further measurements of the spot size of the diverging laser beam at increasing distances from the beam waist. This suggested a value of the M^2 between 1.06 and 1.09 which is very close to the diffraction limit. A similar measurement made on the SP3800 mainframe laser, suggested an M^2 value closer to 1.2, although measurement of this was hampered by the beam pointing instability discussed in section 2.2.2.

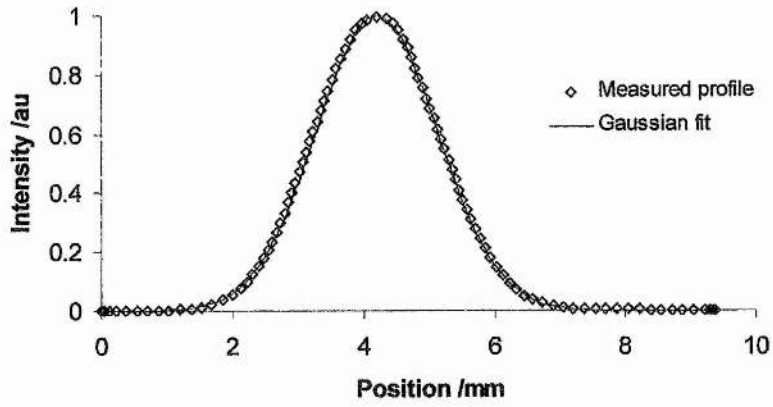

FIGURE 2.13: *Scanned profile of the 8 W Nd:YAG output beam.*

Figure 2.13 is a vertical scan taken during the M^2 measurement, of the beam 1m away from the beam waist. The solid red line is the best fitted line using the equation for a Gaussian profile:

$$I = \exp\left[-2\left(\frac{x}{w_0}\right)^2\right] \qquad \text{Equation (2.6)}$$

where w_0 is the beam waist (half width $1/e^2$ maximum).

Noise characteristics of the all-solid-state laser

The noise measurements made on the SP3800 mainframe laser in section 2.2.2 were repeated on the cw laser-diode-pumped Nd^{3+}:YAG to demonstrate its superiority as a low-noise pump source.

The amplitude noise measurement (figure 2.14) indicated less than 0.8% peak-peak noise, a significant improvement over the 4.6% measured with the actively stabilised SP3800. Power supply ripple at a frequency of 100 Hz was the only observable noise on the output.

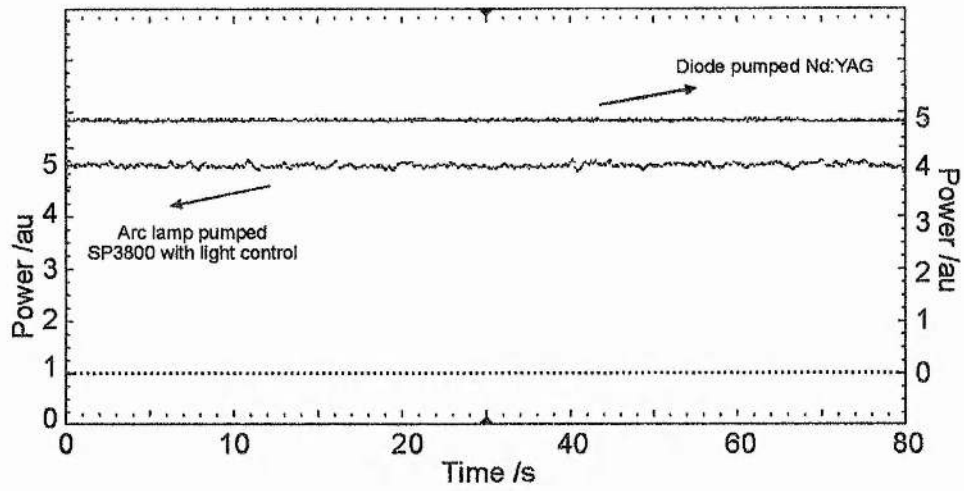

FIGURE 2.14: *Comparison of the amplitude noise of the all-solid-state laser with the mainframe SP3800.*

The beam pointing stability assessment, described in section 2.2., was carried out using the same 30 cm focal length lens placed 2 m away from the laser output coupler, to provide a spot ~100 μm in radius on the quadrant photodiode. The resulting trace in figure 2.15, recorded over a one minute interval, suggests an order of magnitude less movement than the mainframe arc-lamp-pumped system (figure 2.4).

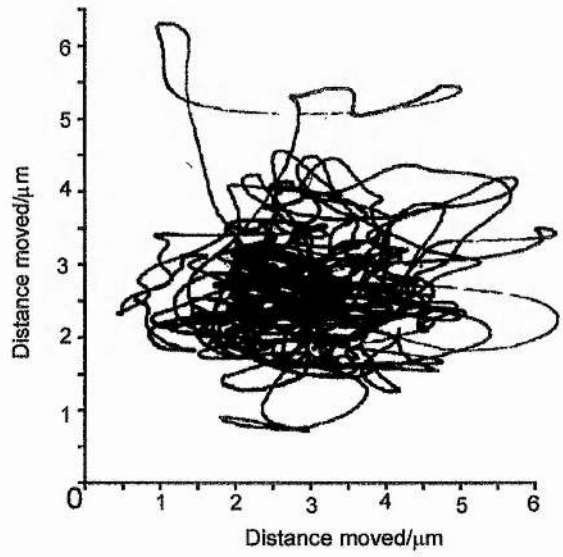

FIGURE 2.15: *Beam pointing instability of the 8 W cw all-solid-state Nd:YAG laser*

2.4.4 Thermal Lens Measurement

To directly replace the mode-locked SP3800 Nd^{3+}:YAG laser as a pump source for the NaCl:OH^- colour-centre laser, an actively modelocked laser-diode-pumped system would require similar pulse repetition rates to the mainframe laser. The main constraint on the repetition rates of acousto-optically modelocked lasers are the positions of the resonances of the modelocker. The modelocker fitted in the SP3800 laser had resonances around 41 MHz allowing pulse repetition rates of ~82 MHz, corresponding to a total laser cavity length of 1.83 m. To scale up the total length of the all-solid-state laser from ~40 cm to 182 cm, required more accurate knowledge of the thermally induced lens in the Nd^{3+}:YAG rod to enable it to be compensated.

Several techniques have been described to measure the lensing induced in a laser rod under intense optical pumping. A simple method, described by Neuenschwinder et al[39], involves calculating the spot size on the output coupler surface from a measurement made of the beam after focusing by an extracavity lens of known focal length (figure 2.16). The thermal lens may then be deduced by predicting the lens strength required to create the calculated beam waist on the output coupler. This technique allows the spherical unaberrated component of the thermal lens to be accurately determined with the laser configured as a stable resonator which is aligned for optimum operation.

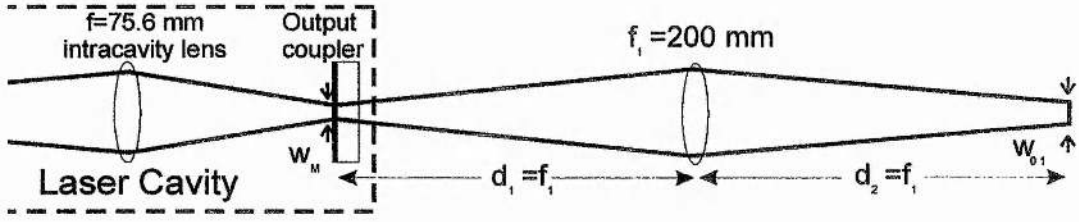

FIGURE 2.16: *Configuration for the measurement of the thermal lens.*

The far field spot size (w_{01} in figure 2.16), formed using a 20 cm biconvex lens positioned 20 cm from the front surface of the output coupler, was measured by translating a slit through the spot in the X and Y planes. From Neuenschwinder[39], the spot size on the output coupler was then deduced using the relation:

$$w_M = \frac{f_1}{w_{01}} \cdot \frac{\lambda}{\pi} \qquad \text{Equation (2.7)}$$

where the symbols are as defined in figure 2.16. The positions of the individual laser cavity elements must be accurately measured and the required thermal lens (placed on the pumped end of the laser rod) was then determined. The graph in figure 2.17(a), derived for the measured laser cavity (aligned for high power operation) using simple ABCD matrix analysis, allows the thermal lens focal length to be deduced from the measured spot size on the output coupler. The greatest source of error when employing this method is the measurement of the positions of the cavity elements, in particular the separation of the end mirror from the intracavity lens.

Several measurements were made for the thermal lens at different pump powers. For the lower powers, it was necessary to re-align the cavity slightly by placing the plane end mirror closer to the intracavity lens, allowing a stable laser resonator to be maintained with a weaker thermal lens. The spot-size vs. thermal lens graph for this arrangement is shown in figure 2.17(b).

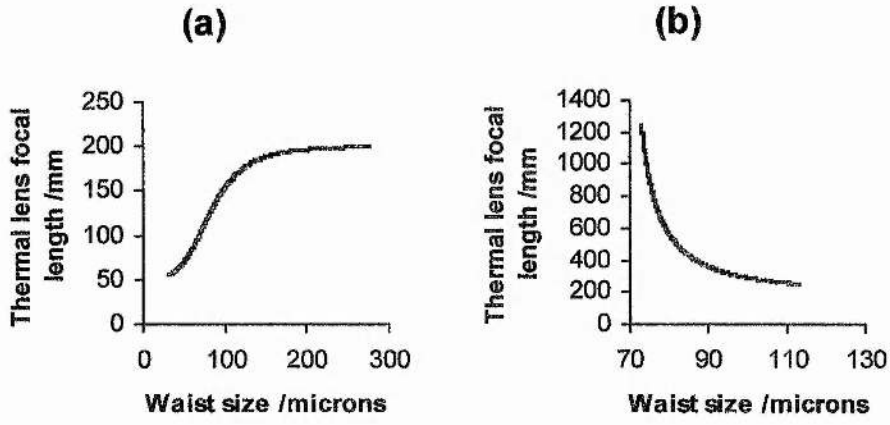

FIGURE 2.17: *Variation of spot size on plane output coupler with thermal lens for the cw laser cavity.* **(a)** *Aligned for high power operation (strong thermal lens).* **(b)** *Re-aligned for weak thermal lensing.*

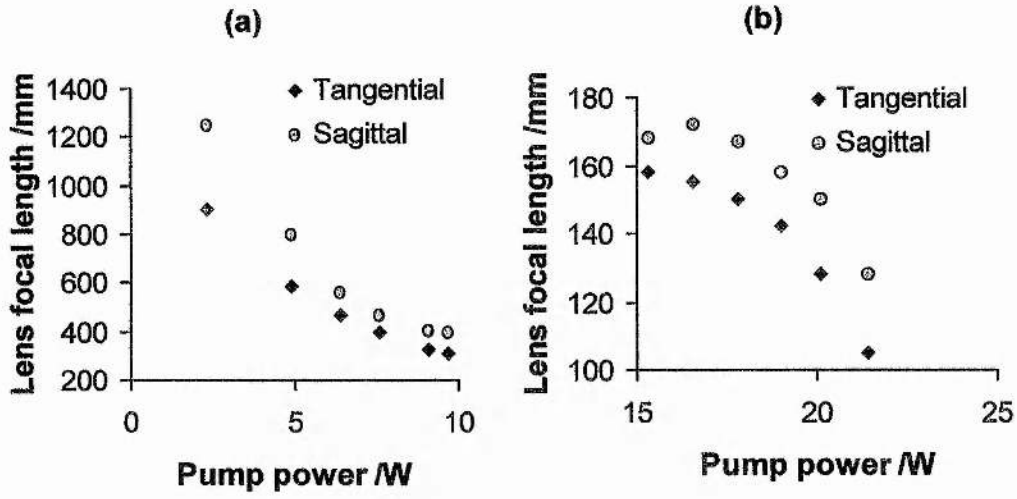

FIGURE 2.18: *Measured unaberrated thermal lens focal lengths* **(a)** *cavity aligned for low pump powers.* **(b)** *aligned for high pump powers (normal operation)*

The measured values for the thermal lens focal length are summarised in the graphs in figure 2.18. It is immediately apparent that the thermal lens has different strengths in the two planes (defined with respect to the Brewster plate). This is most likely due to asymmetric cooling of the Nd^{3+}:YAG rod in the mount. For weak thermal lensing, the curve has a hyperbolic dependence on pump power in agreement with Neuenschwinder and predicted by equation 2.3.

During normal operation (i.e. with 21W incident on the Nd^{3+}:YAG rod) the thermal lens was measured to be 10.5 cm and 12.8 cm in the tangential and sagittal planes respectively, close to the value of 11.2 cm predicted by equation 2.3.

2.5 Actively Modelocked All-Solid-State Nd^{3+}:YAG Laser

2.5.1 Introduction

Replacing the modelocked SP3800 laser with an all-solid-state system for synchronously pumping the NaCl:OH^- colour-centre laser affords fewer immediate benefits compared to those achieved in replacing the cw pump source for a Cr^{4+}:YAG laser. As I have already noted, the very short gain media length characteristic of colour-centre lasers, and the modelocking mechanisms normally employed, imply less dependence on the beam pointing stability of the pump source. The potential advantages

of an all-solid-state system are mainly of lower running costs (due to the higher efficiencies inherent in laser diode pumped systems) and the ability to slightly modify the cavity layout to satisfy certain requirements of NaCl:OH^- lasers (e.g. efficient intracavity doubling to produce the required auxiliary light for re-orientating the colour-centres).

Both the SP3000 and SP3800 lasers are reliable, robust systems when actively modelocked. Both laser cavities are constructed on invar rails providing some immunity to temperature induced length variations which would be detrimental to modelocked performance.

The noise characteristics of the modelocked pulse train depend principally on the stability of the signal generator providing the RF signal to the acousto-optic modulator. Considerable reduction of the phase noise from a modelocked SP3800 has been demonstrated by the replacement of the tunable signal generator with a temperature controlled fixed frequency crystal oscillator[40]. It follows that no significant reduction in the pulse jitter is expected from substituting the arc-lamp-pumped laser with an all-solid-state system, but the slight improvement in low frequency amplitude noise will be beneficial.

2.5.2 Design of an all-solid-state modelocked Nd:YAG laser

The first attempt to construct an all-solid-state replacement for the SP3800 achieved only partial success; high average output powers were obtained but the pulse durations were excessive (shortest were 500 ps). Later it was realised that the angle of the Nd^{3+}:YAG rod has a crucial effect on modelocking behaviour: Aligning exactly along the optical axis- (optimum for best cw performance), created a bandwidth limiting intracavity element. The laser should either be constructed with the Nd^{3+}:YAG rod angled slightly (limiting the cw operation) or, preferably, deploy a gain element with one end face wedged. Optimisation of the following cavity design by using a wedged rod should enable an all-solid-state replacement of the modelocked SP3800 to be realised.

Long cavity design

The 1.82m long laser cavity necessary for direct replacement of the modelocked SP3800 laser, with a pulse repetition rate of 82 MHz, is a challenge to construct when

the gain medium suffers thermal lensing with focal lengths as short as 11cm. Since a lower power was required to pump colour-centre lasers, the laser was designed to be pumped with the diodes operating at a lower power of 20W, hence the expected thermal lens was only ~13cm (from figure 2.18).

The basic resonator layout remained the same as in figure 2.7 but the focal length of the intracavity lens needed to be extended in line with the cavity length. Instead of employing a single lens, a combination of a positive and a negative lens of identical focal length (15 cm) were used. The effective focal length of this lens pair is given by:

$$f = \frac{f_1 \cdot f_2}{f_1 + f_2 - d} \qquad \text{Equation (2.8)}$$

The lens separation, d, was set to give the optimum focal length for operation. A fixed separation of 57mm was used which resulted in a focal length of approximately 400mm, suitable for use in a long cavity of this type. Using the ABCD matrix method, the required cavity dimensions for optimum operation may be estimated. The intracavity beam for this optimum position is shown in figure 2.19. The beam has expanded to a large spot (~6 mm diameter) at the point of the converging lens, it is important to ensure no aperturing occurs at this point. A tight waist (~90 μm) is formed on the plane output coupler. The tolerance of this cavity to varying thermal lens focal lengths is illustrated in figure 2.20. By comparing this with the equivalent for the short cw cavity in figure 2.10, it can be assumed that this laser should operate over a much wider range of pump powers without necessitating re-alignment.

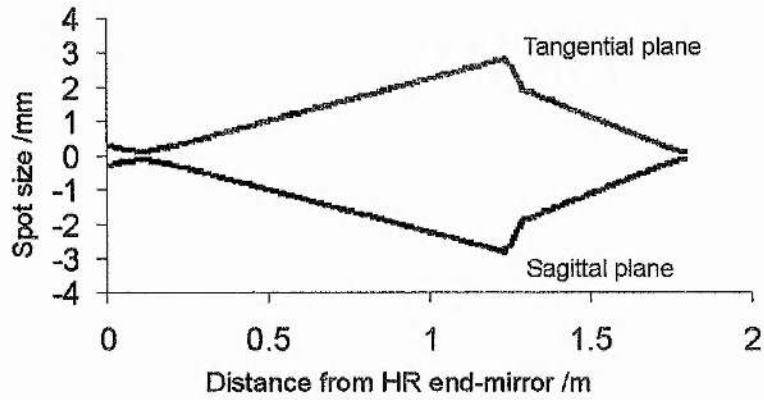

FIGURE 2.19: *Intracavity beam for 1.82m laser cavity*

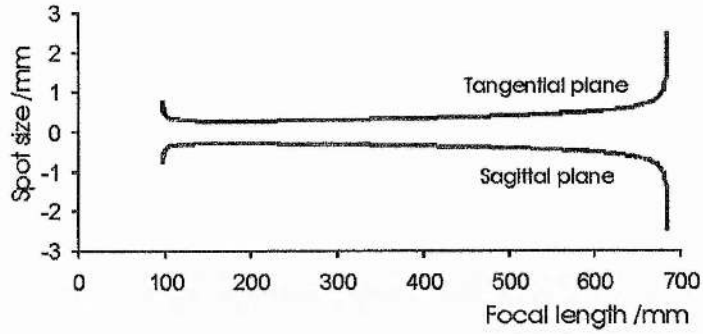

FIGURE 2.20: *Variation of laser spot size in rod with thermal lens strength*

The final design for the long modelocked laser is outlined in figure 2.21. The fixed separation lens pair assembly was mounted on a large translation stage which allowed optimisation of the cavity for maximum TEM_{00} cw operation. Additionally, simultaneous translation of the plane output coupler and lens assembly allowed the cavity length to be adjusted for modelocking without changing the effective laser stability condition. The resonator could be easily constructed from the short 8W cw laser by removing the output coupler and placing the additional optics in the positions indicated in figure 2.21. At a drive current of 21A, the long cw laser produced up to 6.1W TEM_{00}.

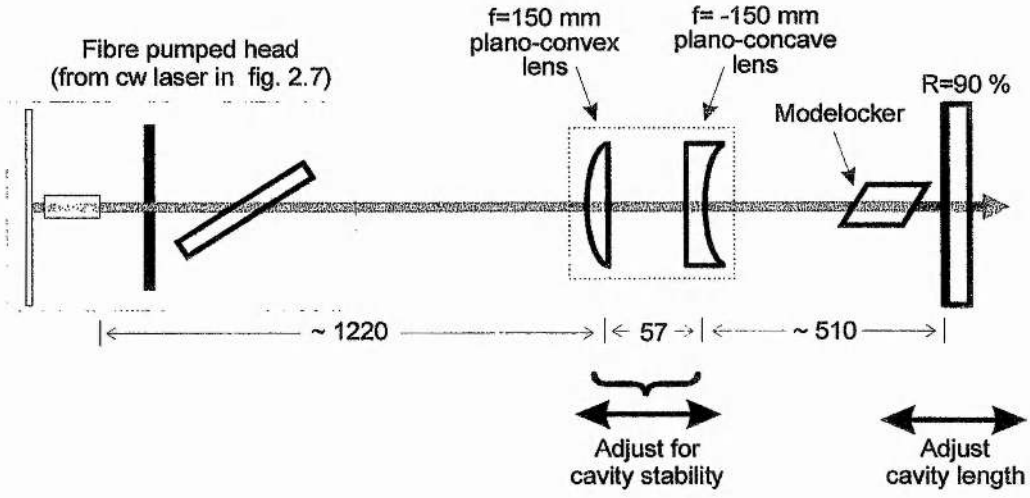

FIGURE 2.21: *Schematic of the 1.8m long laser cavity for active modelocking. (All dimensions in mm)*

For actively modelocked operation using amplitude modulation (AM), a Brewster-angled infrasil acousto-optic modulator of length 8mm (Newport Electro-Optic Systems model N12041-2) was placed immediately in front of the 10% output

coupler. Owing to the tight focusing of the beam on the plane output coupler, the addition of a Brewster-angled element introduces some astigmatism. This was compensated by slightly rotating one of the intracavity lenses.

The modelocked laser operated at a frequency of 82.53MHz with an average output power of 5.7W. The modelocker was driven with 700mW of RF power. The pulse duration, measured using an InGaAs photodiode with a 10GHz bandwidth and a sampling oscilloscope, was typically 500ps in duration- too long for use as a synchronous pump source. The cause of this excessively long pulsed behaviour was traced to etalon effects introduced by the plane-parallel laser rod. This could be partially rectified by rotating the rod mount by ~5^{O} which enabled modelocked pulses of 150ps to be realised. Unfortunately, this also misaligned the laser cavity for optimum cw operation and the average output power dropped to 3W.

The cw operation of this long-cavity laser when first assembled together with the modelocked operation of a shorter compact Nd^{3+}:YAG laser system described in the following section, suggest that substitution of the plane-parallel rod with a plane wedged crystal will enable sub 100ps pulses to be realised from an 82MHz AM-modelocked all-solid-state Nd^{3+}:YAG laser with average output powers exceeding 5W.

Design and construction of a compact modelocked Nd:YAG laser

An alternative acousto-optic modelocking device, the Spectra-Physics model-342 Brewster-prism modulator, originally designed to modelock argon ion lasers running at 82 MHz repetition rate, was found to have resonances at ~97 MHz. A modulation depth of 9.6% for 1W RF power was measured when operating on a resonance near this high drive frequency.

The high frequency resonance opened up the possibility of constructing a compact, all-solid-state modelocked Nd^{3+}:YAG laser, as the total cavity length would only need to be ~75 cm. Since this is approximately only twice the length of the short cw cavity, it was a straightforward modification to exchange the 75mm intracavity lens with one of 150mm focal length and double all the cavity dimensions in figure 2.7.

The entire cavity was rebuilt for optimum modelocked performance with a plane-parallel rod, i.e. the laser rod was angled >5^{O} but the optical fibre tip was imaged exactly in the centre of the pumped side of the rod. This helped to ensure that the end of

the rod with the greatest thermal load was symmetrically cooled. As with the long cavity, both the intracavity lens and the end mirror were mounted on translation stages.

Without any modelocking device, this extended cavity produced 6.5W TEM_{00} for just 19W pump power.

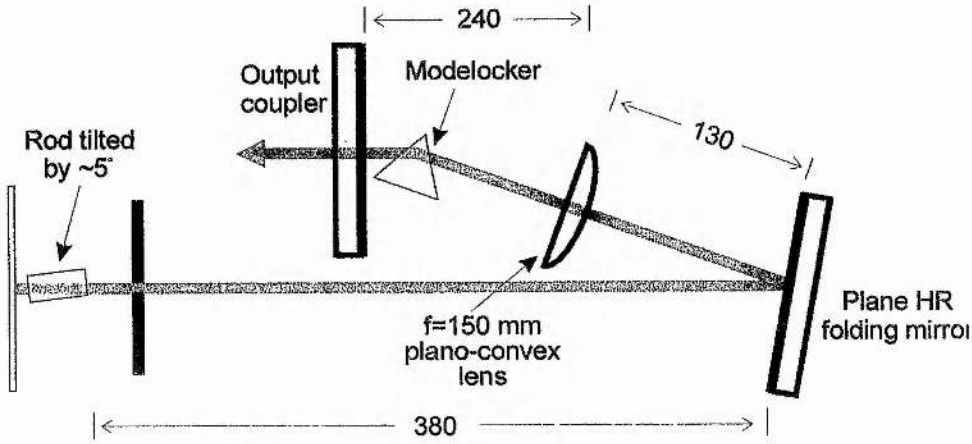

FIGURE 2.22: *Schematic of the compact, modelocked all-solid-state Nd:YAG laser. (All dimensions in mm)*

The entire laser cavity including the prism modulator is illustrated, with dimensions, in figure 2.22. Note that the Brewster-plate is no longer necessary as the Brewster-angled prism ensures plane-polarised operation. The cavity was folded upon itself using a plane HR mirror allowing the entire laser to be positioned upon a small portable breadboard. The 15cm lens was of a plano-convex design which was not optimum for a laser cavity such as this where the lens must image a highly diverging beam onto the output coupler. This introduced additional spherical aberration within the cavity[41] and further improvement in laser operation may be possible using a biconvex lens.

Modelocker stabilisation

Acousto-optic modulators have acoustic resonances located at frequencies depending upon their physical dimensions. Several closely spaced resonances normally occur. The Spectra-Physics 342 prism modulator has resonances spaced 600kHz apart between 94-98 MHz with the resonances around 96 MHz being the strongest. The normal procedure for running an acousto-optic modulator efficiently on a resonance is to approach the resonance from a lower frequency and gradually increase the drive frequency until a stable resonance is reached. When the modulator is running on a

resonance, the modulating element heats up and its resonant frequency increases, hence the modulator will no longer be running at its most efficient as a large proportion of the incident RF power will be reflected out from the modulator.

For efficient modelocking, the modulator must be maintained on a resonance regardless of environmental changes in temperature or RF induced heating of the modulator. To ensure this, the stabilisation scheme described by Klann et al.[42] was implemented. This is outlined in figure 2.23. This stabilisation method relies upon the phenomenon that the RF signal reflected from an acousto-optic modulator undergoes a phase change as the drive frequency is swept through a resonance. A DC error signal may thus be derived using a phase sensitive detector (PSD), the sign and magnitude of which indicate the location of the modulator resonance with respect to the driving RF frequency. Using this signal to suitably vary the RF amplitude allows the control of the temperature of the modulator and hence its resonant frequency. Once set

up correctly, this closed loop would maintain the modulator running at a constant voltage standing-wave-ratio (SWR) regardless of changes in ambient temperature etc.

A standing wave ratio meter placed in the RF line between the PSD and the modulator is necessary for setting up the closed loop circuit. The modulator is first driven with a low power RF signal (~200 mW). The gain control signal to the voltage controlled amplifier (VCA) is initially disconnected and a resonance close to the required operating frequency is located using the standard procedure. This involves slowly increasing the drive frequency from a point just below the resonance while observing the SWR meter. A rapid decrease in the SWR meter reading occurs once the resonant frequency is located. Without any stabilisation, the SWR reading would then slowly increase indicating more RF power reflected as the modulator heats up and the resonant frequency increases. It is at this point that the VCA signal is applied and the resonant frequency of the modulator is effectively locked to the RF drive signal.

Crucial to the correct operation of the stabilisation scheme is ensuring that the phase of the reflected signal at the PSD produces an error signal of the correct sign to lock on to the resonance. This involves varying the length of the cable from the PSD to the modelocker until the lowest SWR is maintained during stabilisation.

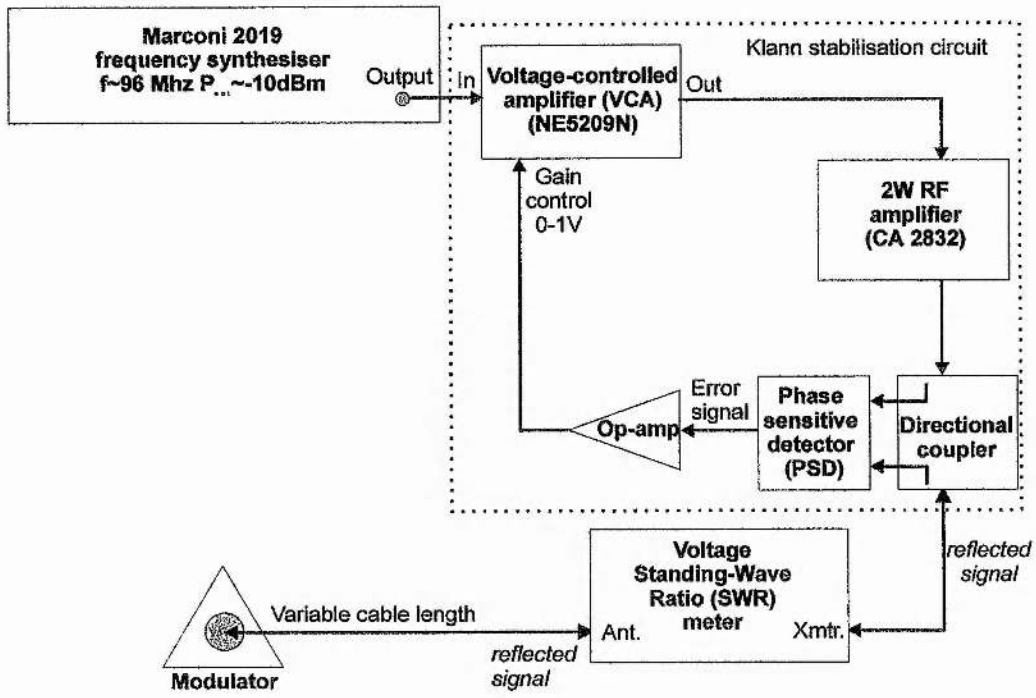

FIGURE 2.23: *Schematic of the stabilisation scheme used to lock the modelocker onto a resonance.*

Once stabilised, the RF power to the modulator could be increased by slowly increasing the drive frequency. To maintain operation on a resonance, the stabilisation loop raised the modulator temperature by increasing the RF incident power. For optimum operation, ~1.0W RF power was applied resulting in an SWR reading of just 1.2. This could be maintained indefinitely providing the VCA range was not exceeded by the control signal.

2.5.3 Characterisation of the compact, all-solid-state, actively modelocked Nd:YAG laser using amplitude-modulation

For complete characterisation of the modelocked mini-laser, the scheme outlined in figure 2.24 was implemented.

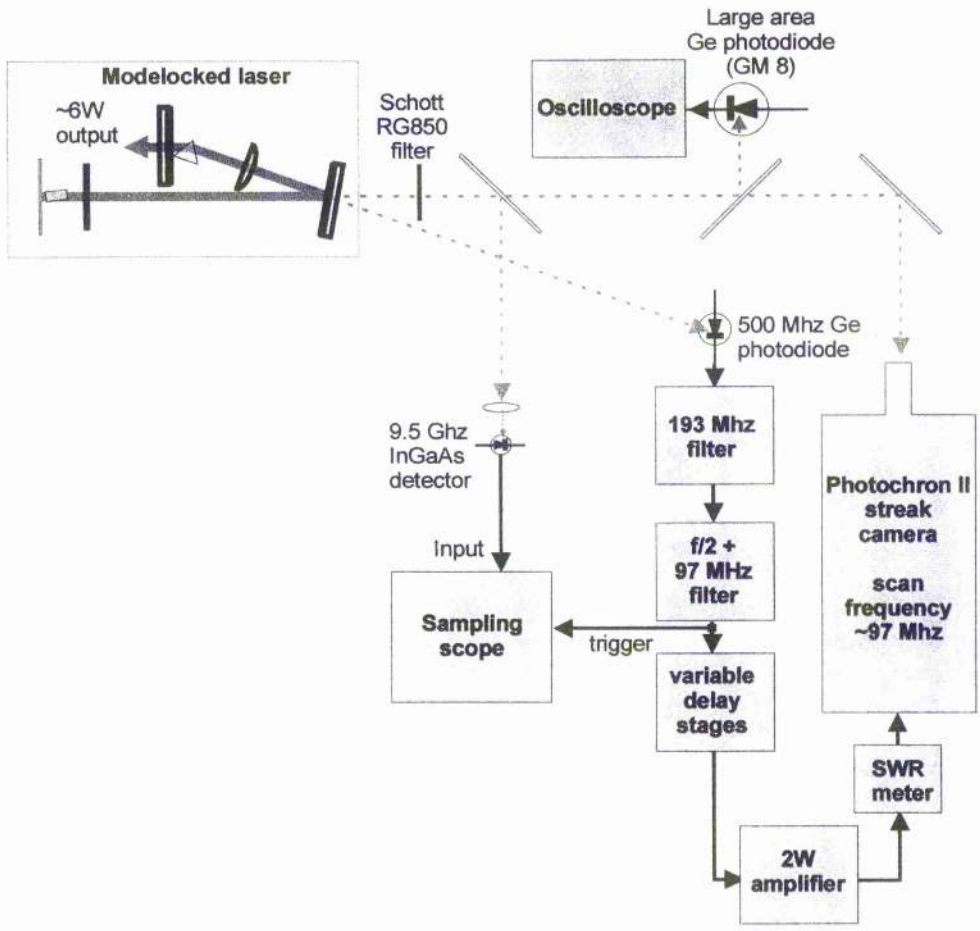

FIGURE 2.24: *Schematic of the diagnostics used for characterisation of modelocked operation*

The amplitude noise could be monitored throughout with a broad area germanium photodiode. This helped to ensure that the laser was not operating in a Q-switched regime when aligning for short pulse operation.

The sampling oscilloscope in conjunction with a 9.5 GHz bandwidth InGaAs detector could resolve pulse durations down to ~50 ps. For pulses shorter than this, a Photochron 2 synchroscan streak camera was employed. Calibration of the streak camera was achieved by adjusting the variable delay stage by a pre-measured delay and

measuring the shift in position of the pulse on the streak tube. An optical multichannel analyser (OMA) placed behind the streak tube, allowed a real-time trace of the pulse shape to be obtained.

The streak camera was modified to allow the deflector plates to be swept at 97 MHz i.e. half the cavity frequency. Because in practice, the VCA and frequency synthesiser were combined in one unit, the amplitude from the signal generator varied to permit modelocker stabilisation. Thus it was necessary for the drive signal for the streak camera to be taken from the modelocked laser itself using a small area germanium photodiode. A broad bandwidth divide-by-two circuit followed by a narrow band filter reduced the frequency to the required 97 MHz.

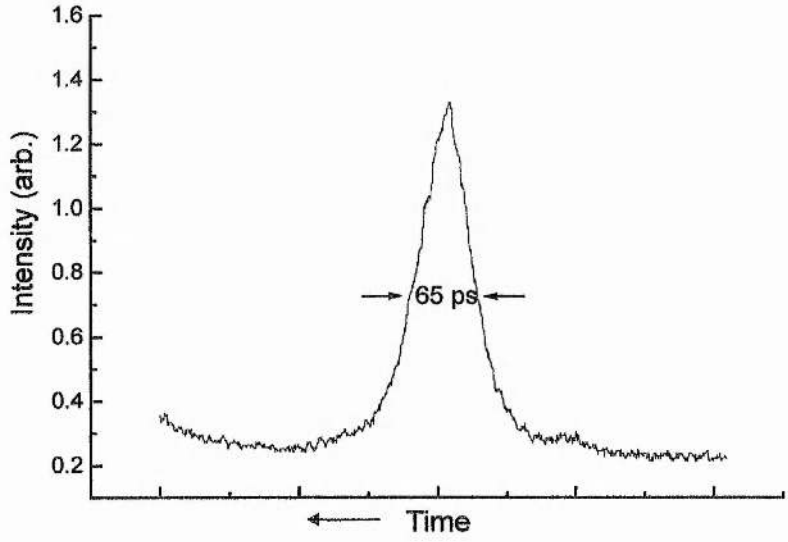

FIGURE 2.25: *Typical streak trace obtained from the compact, actively modelocked Nd:YAG laser*

With the prism modelocker driven with 800 mW RF power and placed immediately in front of the output coupler, this laser readily produced sub 100 ps pulses. An actuator with a differential drive controlling the positioning of the prism modelocker permitted precise adjustment of the effective cavity round-trip-time for optimum modelocked performance.

Figure 2.25 is the shortest synchroscan streak trace obtained at 5.5 W average output power with a 7% output coupler, indicating symmetric pulses of ~65 ps in duration.

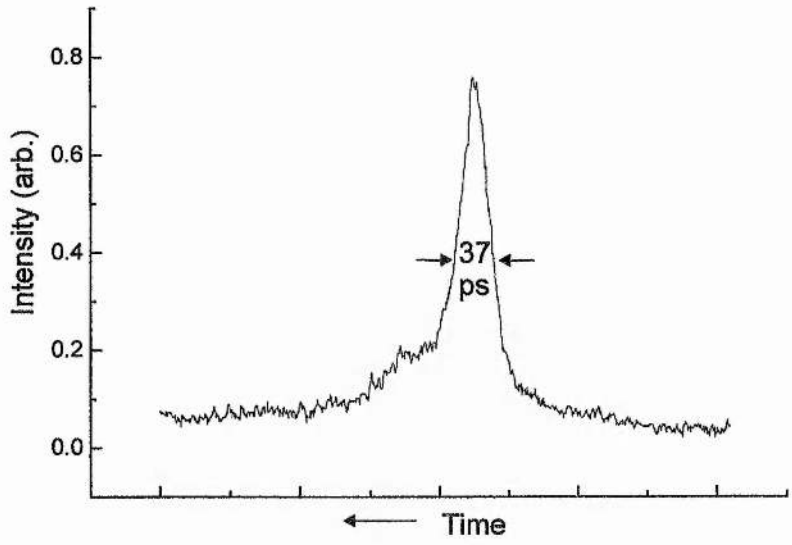

FIGURE 2.26: *Streak trace of pulses obtained from the laser with 8 mm gap between the modelocker and the end-mirror*

By translating the output coupler further away from the modelocking element to give an ~8 mm gap, shorter asymmetric pulses were easily obtained after precise adjustment of the cavity length. This is illustrated in figure 2.26 which shows a highly asymmetric 37 ps pulse. Note that this pulse has a large pedestal on its trailing edge. The average power obtained (using the optimum 10% output coupler) was 6.0 W.

By increasing the applied RF power to the modulator from 800 mW to 1.5 W (by increasing the drive frequency), and optimally positioning the modelocker in the intracavity beam, the pedestal in figure 2.26 could be reduced giving the cleaner asymmetric pulse in figure 2.27. However, this high level of RF power exceeded the manufacturer's specifications and was not maintained for long intervals to avoid inflicting damage to the modulator.

The pulses obtained from this modelocked laser (down to ~30 ps) are significantly shorter than those routinely generated by the commercial SP3800 when modelocked (normally >70 ps). Although the higher RF drive frequencies involved in modelocking a compact laser leads to a shorter duration transparency window in the modulator, an additional effect is probably helping to increase the oscillating bandwidth.

The Kuizenga-Siegman[43] theory provides a useful expression relating the approximate pulse duration expected from an actively AM modelocked laser to the modulation frequency:

$$\tau \sim 0.45 \cdot \left(\frac{\alpha_m \cdot p_m}{\Delta_m} \right)^{\frac{1}{4}} \cdot \left(\frac{1}{f_m \cdot \Delta f} \right)^{\frac{1}{2}} \qquad \text{Equation (2.9)}$$

τ is the expected pulse duration, α_m is the gain cross section of the laser medium, $\mathbf{p_m}$ is the path length in the gain medium, Δ_m is the modulation index, $\mathbf{f_m}$ is the modulation frequency, and $\Delta\mathbf{f}$ is the gain bandwidth. Thus, all other things being equal, the pulse duration should be reduced by a factor $\sqrt{f_1 / f_2}$ on increasing the modulation frequency from $\mathbf{f_1}$ to $\mathbf{f_2}$. This suggests a reduction to 65% of the pulse duration of a 1.82 m long laser (nominally ~75ps but can be less than 60ps) which is ~40-50ps. The additional reduction in pulse duration observed here is partially due to the higher RF power applied to the modulator ($\Delta_m \propto P_m^{\frac{1}{2}}$ for acousto-optic modulators[38] where $\mathbf{P_m}$ is the applied RF power), but is also explained by the phenomenon of enhanced spatial hole burning.

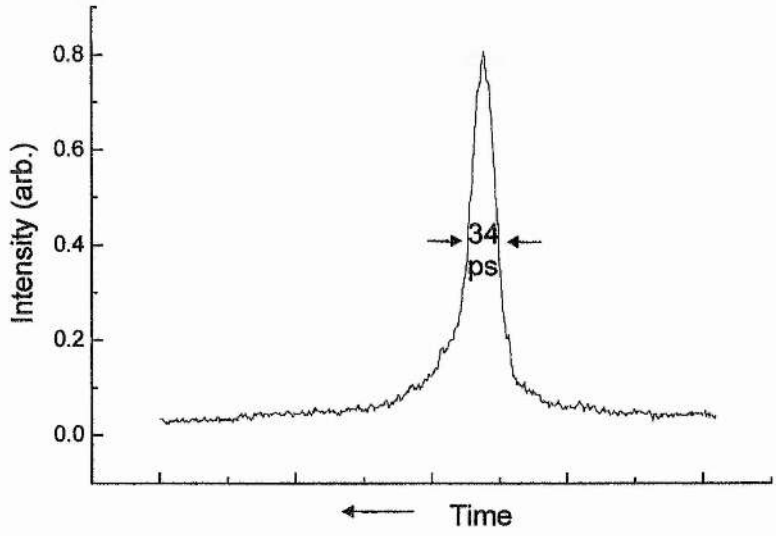

FIGURE 2.27: *Shorter 'clean' pulse obtained with higher RF power and optimal modelocker alignment.*

Ever since research started on laser-diode pumped actively modelocked lasers, it has been observed that the pulse durations obtained have often been considerably shorter than predicted by equation 2.9. Early on, it was suggested that spatial hole burning (SHB) could be playing an important role which the Kuizenga-Siegman theory neglects[44]. Later experimental[45] and theoretical[46] investigations concluded that enhanced SHB explained the broad-flattened bandwidth characteristic of actively modelocked diode pumped lasers. The enhanced SHB was only observed once laser-diode pumping became possible as the standard arrangement for diode-pumped lasers

is to have the gain medium at the end of the laser cavity, unlike arc-lamp-pumped lasers which require the gain medium to be located in the centre. Enhanced SHB is typically observed as a broad oscillating linewidth even in the absence of any modelocking element. Thus the modelocker is not required to increase the number of oscillating modes, only to bring the modes already oscillating into phase. Unfortunately, the linewidth of the laser for neither modelocked nor cw operation could be resolved on the scanning Fabry-Pérot interferometer available so an enhanced SHB spectrum was not recorded.

In the case of the laser in figure 2.22, the HR end-mirror is not on the actual gain medium as in reference 45. The gap between the plane end-mirror and the AR-coated rod implies that the SHB is not maximised for shortest pulse generation[47], and an HR-coated rod should produce yet shorter pulses. Using frequency-modulation active modelocking, enhanced SHB has permitted pulse durations as short as 12 ps in Nd^{3+}:YAG[44], 5 ps in Nd^{3+}:YLF[45] and 2.9 ps in Nd^{3+}:BEL[48]. Active amplitude-modulation (AM) modelocking, as employed here, has previously only produced pulses as short as 55 ps for an Nd^{3+}:YAG laser[49] (or 25 ps with the addition of a thin intracavity element[50]). The 34 ps pulse reported here is significantly short using simple AM modulation especially considering the high average output powers (5.5-6.0 W) possible with this arrangement.

With the prism modelocker driven with 800 mW RF power and placed immediately in front of the output coupler, this laser readily produced sub 100 ps pulses. An actuator with a differential drive controlling the positioning of the prism modelocker permitted precise adjustment of the effective cavity round trip time for optimum modelocked performance.

One observation made when detuning the length of this laser cavity away from the position for shortest pulse generation is that unlike the SP3800, there are several distinct locations where a single ultrashort pulse is obtained. This is illustrated in figure 2.28. Note that the detuning frequency shift Δf is only approximate due to temperature induced length fluctuations during the measurement as discussed later.

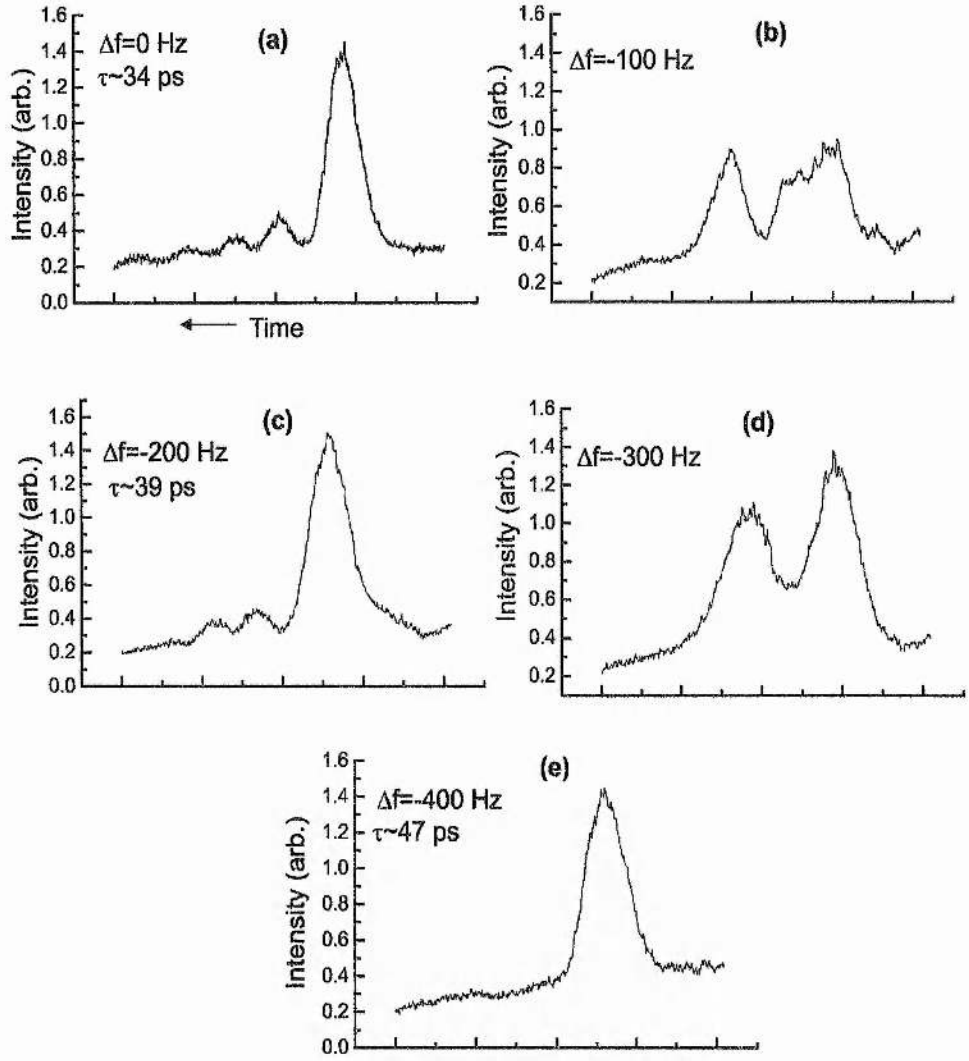

FIGURE 2.28: *Streak traces obtained from actively modelocked laser as the modelocker frequency is decreased (detuned) from the optimum for shortest pulse generation.*

One major drawback experienced with this compact actively modelocked laser was that the alignment for the shortest pulse generation was maintained for less than two minutes before temperature induced length variations detuned the cavity to operate with twin pulses as in figure 2.28(b). This necessitated constant re-adjustment of either the cavity length or the modelocker drive frequency rendering the laser unsuitable for use as a pump source. Detuning the cavity with the modelocker immediately adjacent to the output coupler to give the long pulse in figure 2.25 allowed stable short modelocked pulse operation to be maintained for ~12 minutes after which the cavity length had changed to give longer pulses (as shown in figure 2.29). The required frequency correction of 450 Hz to return to shorter pulse generation implied a cavity length contraction of ~3.5 μm. This was a major

inconvenience and suggested that it was not possible to construct an all-solid-state replacement for the commercial arc-lamp pumped systems. The Spectra-Physics SP3000 and SP3800 lasers are able to remain modelocked for several hours before re-alignment becomes essential. This is possible because the laser is constructed on Invar[51] alloy rails which provide immunity to temperature induced length fluctuations.

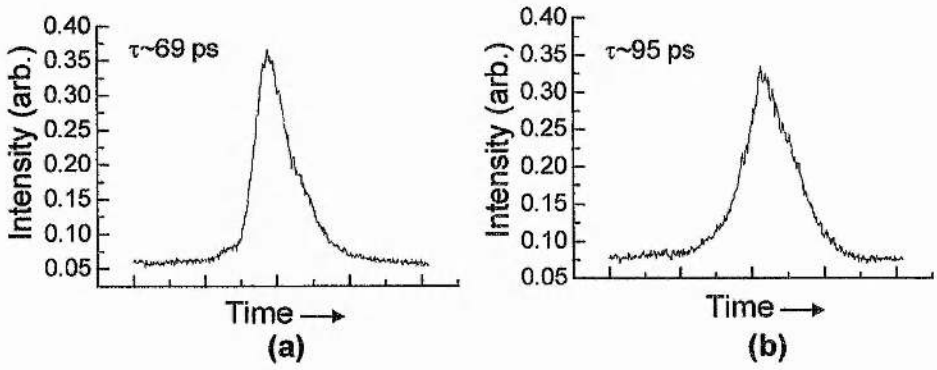

FIGURE 2.29: *Effect of temperature induced cavity length detuning on modelocked operation. Streak traces obtained:* **(a)** *Immediately after alignment* τ_{FWHM}*~69 ps.* **(b)** *After 12 minutes* τ_{FWHM}*~95 ps*

2.5.4 Active stabilisation of acousto-optic modelocked operation.

One possible method of controlling the modelocked condition of the laser to ensure that temperature induced variations of the laser cavity length do not detune the cavity round-trip time from the modelocker drive frequency, is to monitor the modelocked output of the laser and set up a closed feedback loop. This could then re-adjust the overall alignment of the laser system to compensate for any length fluctuations.

This proposal is conceptually identical to the stabilisation scheme employed by additive-pulse-modelocked (APM) aka coupled-cavity-modelocked (CCM) lasers to interferometrically match the length of the auxiliary non-linear cavity to the main laser cavity for stable CCM femtosecond pulse operation[52]. This scheme normally monitors the fundamental output of the CCM laser although sometimes the second harmonic is generated for monitoring using a non-linear crystal. The signal is compared to an empirically pre-set reference level and hence an error signal is derived. Subsequent integration and amplification of this produces a suitable voltage to drive a piezo-electric transducer thus allowing the laser or auxiliary cavity length to be controlled to maintain

a constant signal on the monitor photodiode. A simplified schematic of this CCM stabilisation circuit is in figure 2.30.

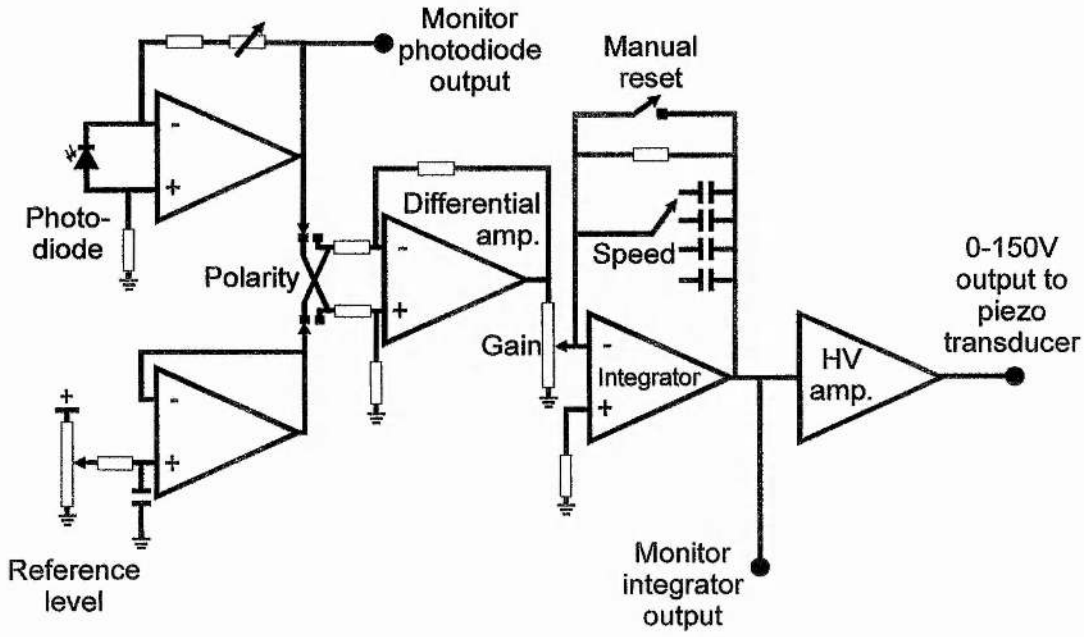

FIGURE 2.30: *Schematic diagram of the coupled cavity stabilisation circuit normally used to maintain interferometric matching of the coupled cavity lengths.*

Unfortunately, at the time the work was carried out on actively modelocking the diode pumped Nd^{3+}:YAG laser, some of the equipment necessary to implement this scheme was unavailable; a frequency synthesiser is required which permits a DC frequency modulation (FM) signal. Most synthesisers, including the Marconi 2019, have AC-coupled FM modulation inputs. The Anritsu model MG3633A is an example of a frequency synthesiser which does have a DC-coupled FM input. To assess the potential of this simple scheme for stabilising an actively modelocked laser against cavity length fluctuations, it was applied at a later date to the modelocked SP3800 mainframe laser. A KTP (potassium titanyl phosphate) second harmonic generating (SHG) crystal was used to frequency double a fraction of the modelocked laser output. The resulting 532 nm light was detected with a broad area germanium photodiode operating at the wings of its sensitivity bandwidth[53]. This signal was used as the monitor input for the CCM stabilisation circuit of figure 2.30. The loop was completed by using the integrator monitor output of the stabilisation circuit as the DC frequency modulation signal of the Anritsu MG3633A frequency synthesiser driving the acousto

optic modulator in the SP3800 laser. The complete stabilisation plan is illustrated in figure 2.31.

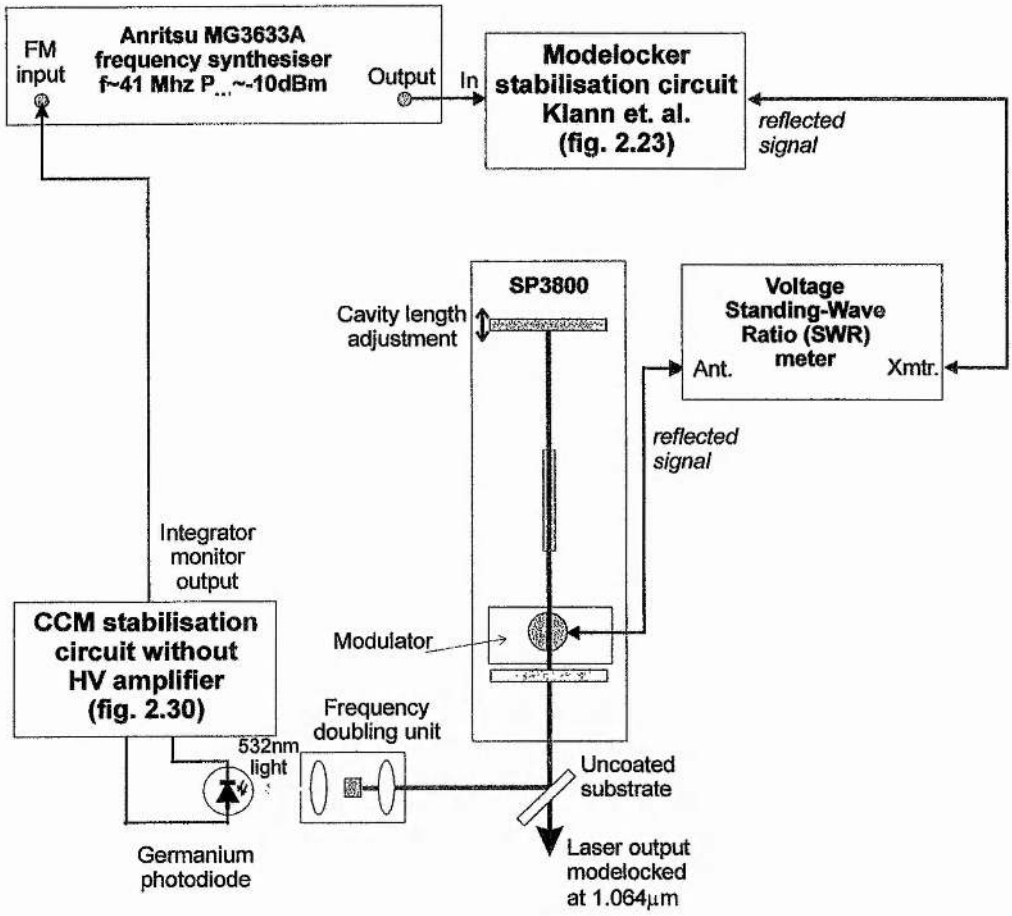

FIGURE 2.31: *Complete schematic of the scheme used to provide immunity to an actively modelocked laser from cavity length fluctuations*

Implementation of this scheme together with the acousto-optic modulator stabilisation system of Klann et al.[42] in figure 2.23 yielded promising preliminary results.

The pulse train was monitored using a 9.5 GHz InGaAs detector with a sampling oscilloscope and a small area germanium photodiode with a broad bandwidth real time oscilloscope (Tektronix 7603). Careful adjustment of the reference voltage and correct setting of the speed, gain and polarity of the CCM stabiliser were necessary to lock the SHG signal to a constant level. This helped to ensure a constant pulse duration regardless of fluctuations in cavity length.

To simulate the instabilities associated with the diode pumped Nd^{3+}:YAG laser on the SP3800, the pulse duration and SHG signal were recorded as the cavity length was

slightly detuned using the micrometer attached to the end HR mirror. This measurement was repeated both with and without stabilisation applied.

A few drawbacks, unique to the SP3800, were encountered when performing this assessment which would imply that the performance of this active stabilisation would be more successful when applied to the all-solid-state system. Most importantly was the intrinsic instability of the SP3800 as discussed in section 2.2.2. The amplitude noise, whilst reduced significantly by the light control circuit, was still significantly worse than that of the all-solid-state laser. Small fluctuations in the fundamental average output power were magnified after frequency doubling, and were interpreted by the stabilisation circuit as drifts in pulse duration. Similarly the beam pointing instability was translated to an amplitude noise and subsequently to a change in pulse duration. Other minor problems which were experienced when adjusting the length of the SP3800 cavity concerned the excessive backlash of the micrometer adjuster and coupling between the translation of the micrometer and the X and Y tilt adjustments of the end-mirror. This meant that the actual physical alignment of the laser was changed, as well as the cavity length, when the end-mirror was translated.

Figure 2.32 shows the pulse traces obtained from the SP3800 as the cavity is detuned. The shortest pulse duration of ~150 ps is quite excessive for this type of laser.

One drawback of using the SP3800 is that the light control stabilisation fails as soon as the cavity is detuned because average fundamental output power falls. Owing to the backlash associated with the micrometer and the coupling of the adjustments, it was necessary to re-optimise the modelocked laser when changing detuning direction hence the different SHG signals and modelocker drive frequencies for the zero-detuning measurements when changing detuning sign in figures 2.32 and 2.33.

The modelocker drive frequencies given in figure 2.32 were constant throughout the detuning. Detuning the cavity beyond +/- 20 μm resulted in a laser with so much amplitude noise as to make a measurement ineffectual.

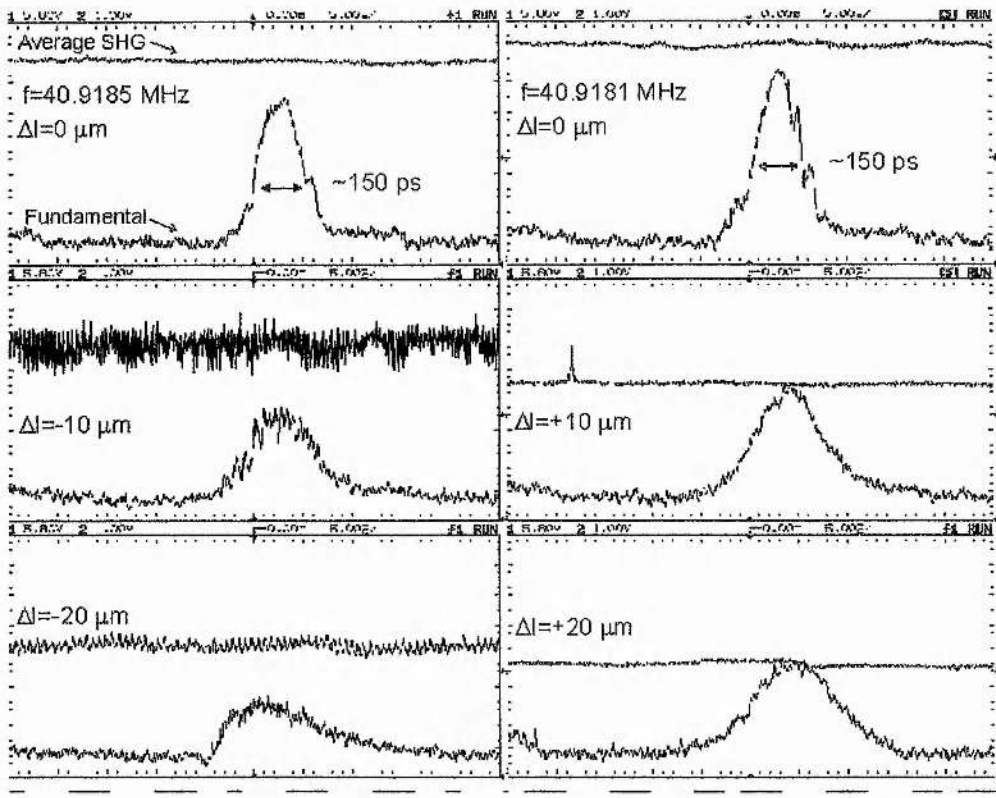

FIGURE 2.32: *Effect of cavity length detuning on modelocked performance. Sampling scope traces obtained without active stabilisation applied.*

The detuning performance of the laser once stabilisation was applied is shown in figure 2.33. The stabilisation circuit can be seen to adjust the modelocker drive frequency measured on an RF spectrum analyser, to compensate for the change in cavity round trip frequency.

The FM variation on the Anritsu frequency synthesiser was set to +/- 5.00 kHz throughout these measurements. A voltage of +/- 5V was required to obtain this full range.

For the stabilisation circuit to operate, it is necessary for the reference level to be set to lock the SHG signal to a value slightly less than the maximum which could be obtained from the laser. This is to permit the sign of the error voltage applied to the FM input to be deduced by the stabilisation circuit, and correct for any drift in SHG level.

From figure 2.33 it may be assumed that the duration of the modelocked pulses obtained from the laser are immune to cavity length expansions of over 40 μm. Unfortunately, the stabilisation appears less successful when the laser cavity is

contracted. The light control failed at a 20 μm contraction and the laser Q-switched once a 40 μm contraction was applied. This is possibly a result of reduced RF power being applied by the Klann stabilisation circuit to keep the acousto-optic modelocker on a resonance at a lower drive frequency, but is more likely to be a complication of the coupled adjustments on the SP3800 end-mirror misaligning the laser as the length is changed.

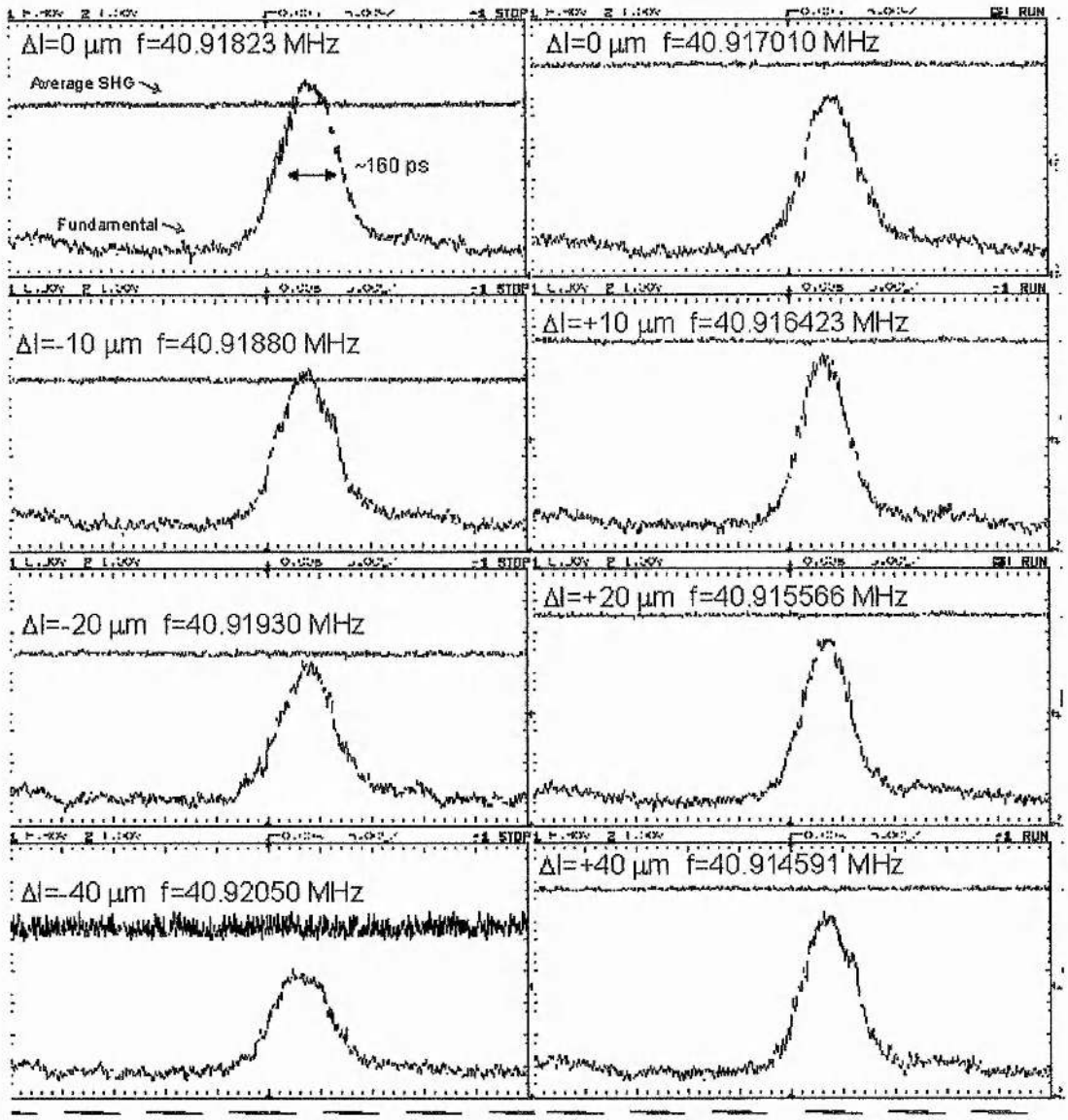

FIGURE 2.33: *Cavity length detuning with active stabilisation applied.*

Because this stabilisation scheme relies on locking the SHG signal to a constant predetermined level, it is useful to record the effect on SHG stability once this stabilisation is initiated. By a comparison of the SHG signals recorded during the small

time windows in figures 2.33, an appreciation cannot be made on how unstable the SHG signal normally is without this active stabilisation. Figure 2.34 shows a direct comparison of the stabilised and unstabilised SHG levels taken over an approximately five minute interval. The cavity length was kept constant throughout. Here it may be clearly seen that applying stabilisation causes the SHG level to drop. The improvement in stability appears dramatic with no ripples or glitches recorded. However, this measurement cannot resolve the very high frequency noise which may occasionally occur due to Q-switching etc. and in practice, the laser is not quite as stable as this measurement implies.

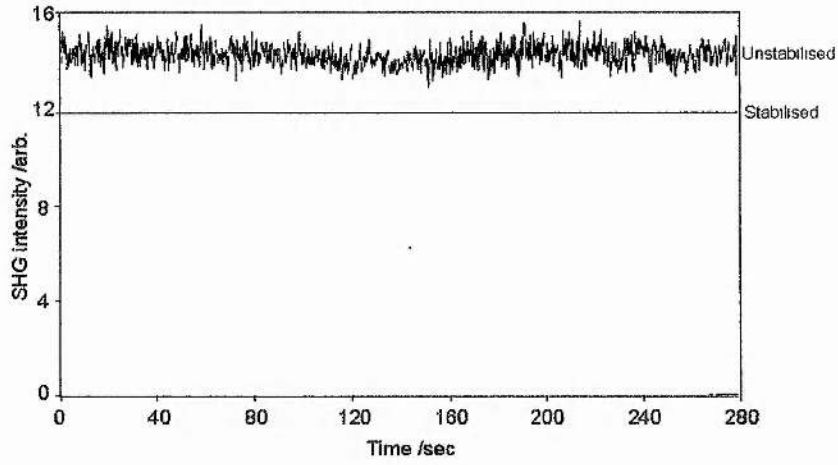

FIGURE 2.34: *Effect of active modelocking stabilisation on the second harmonic signal.*

A similar measurement performed on the fundamental intensity showed no discernible change in stability when this active stabilisation was applied. Likewise figure 2.35, which compares the modelocked pulse trains recorded over a two second interval obtained from the laser both before and after stabilisation was applied, shows no change in the stability of pulse peak power when applying modelocking stabilisation. It is therefore likely that this stabilisation just varies the pulse duration to compensate for amplitude fluctuations which would otherwise affect the SHG signal.

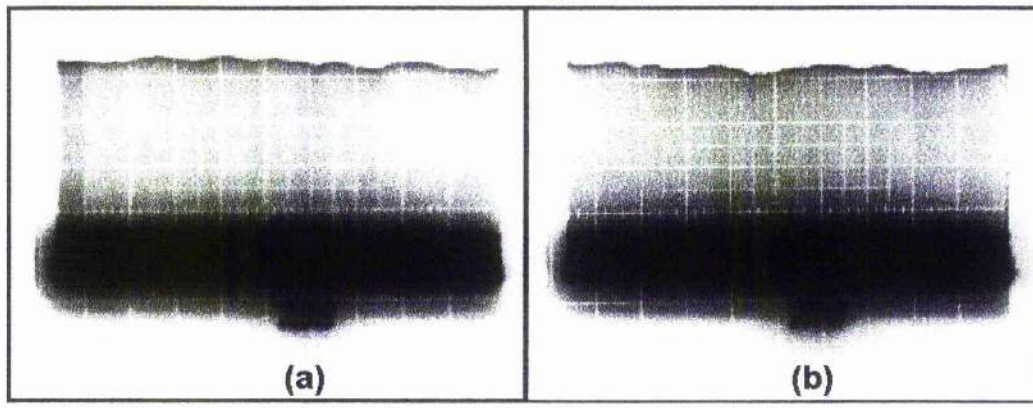

FIGURE 2.35: *Pulse train stability:* **(a)** *without stabilisation,* **(b)** *with stabilisation*

Considering the drawbacks discussed in using the SP3800 to assess this stabilisation technique, it is likely that this scheme would enable the all-solid-state actively modelocked Nd^{3+}:YAG laser to remain modelocked for suitably long intervals for it to find useful applications.

One drawback of using the stabilisation circuit to adjust the frequency of the modelocker is that the pulse repetition rate will be constantly drifting. This could be a problem if synchronously pumping a second laser when the cavity length mismatch will consequently change. An alternative is to revert to the APM stabilisation design and use a piezo-electric actuator mounted to a laser cavity mirror to counteract cavity length fluctuations.

A second drawback of this scheme is that the pulse jitter (phase noise) may be considerably increased as the cavity repetition rate changes. Again this disadvantage will be eliminated by using a piezo-actuated cavity mirror as used in APM stabilisation.

2.6 Construction of an Actively Modelocked Nd^{3+}:YVO_4 Laser Operating at 82 MHz

An alternative host for Nd^{3+} which has received considerable interest recently, particularly in microchip lasers, is yttrium vanadate (YVO_4)[54]. The recent commercial advances in high power all-solid-state lasers operating at 1.064 μm[31], and by intracavity frequency doubling to 532 nm[55], have relied upon using Nd^{3+}:YVO_4 as the gain medium pumped by fibre-coupled laser diodes.

Material	Pump wavelength (for peak absorption) (nm)	Gain bandwidth (GHz)	Peak absorption coefficient (cm^{-1})	dn/dT ($10^{-6}K^{-1}$)	Thermal conductivity ($Wm^{-1}K^{-1}$)
Nd:YAG	807.5	180	8	7	13
$Nd:YVO_4$:	808.5	210			5.2
π (E||c)			40.7	8.5	
σ (E||a)			10.5	2.9	

TABLE 2.1: *Comparison of some properties of Nd:YAG and Nd:YVO_4 (adapted from ref. 15)*

A comparison of some important optical and physical properties between Nd^{3+}:YAG and Nd^{3+}:YVO_4 is given in table 2.1. One important advantage Nd^{3+}:YVO_4 has over Nd^{3+}:YAG which has led to its application is the considerably higher pump absorption coefficient[56] (~five times greater). This enables a greater proportion of the diode pump light to be absorbed before diverging beyond the transverse spatial extent of the oscillating laser mode ensuring a greater extraction efficiency. Another feature of Nd^{3+}:YVO_4 is that it possesses natural birefringence so that unlike Nd^{3+}:YAG, a laser based on Nd^{3+}:YVO_4 will be plane polarised without including any polarisation selecting elements. Having natural birefringence has the added advantage that thermal stress induced birefringence is not a problem with this material[7]. Also, Nd^{3+}:YVO_4, unlike Nd^{3+}:YLF, has absorption peaks located around 808 nm (similar to Nd^{3+}:YAG) allowing the use of the same laser diodes to pump both materials. Unfortunately, the thermo-mechanical quality of Nd^{3+}:YVO_4 is much poorer than Nd^{3+}:YAG: it has lower thermal conductivity and a tendency to crack when thermally stressed.

A low power modelocked system was desired which could replace the SP3000 arc-lamp-pumped laser, and possibly by employing the technique of self-modelocking (or Kerr-lens-modelocking (KLM)) to produce ~10 ps pump pulses[57] for synchronously pumping a 1 ps colour-centre laser. Given the advantages of Nd^{3+}:YVO_4 listed above, plus the fact that it has a linewidth lying halfway between Nd^{3+}:YAG and Nd^{3+}:YLF for

possible shorter pulse generation, this material was employed in a 1.82 m all-solid-state actively modelocked laser.

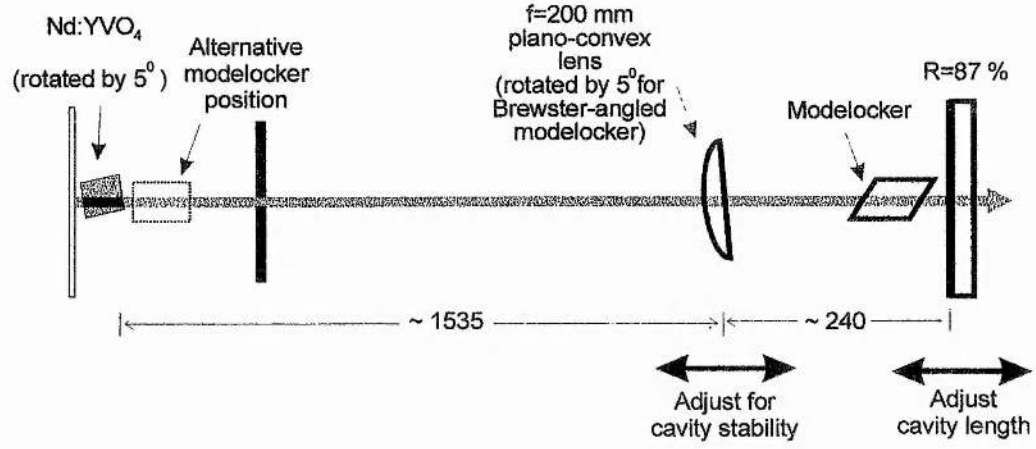

FIGURE 2.36: *Schematic of the actively modelocked Nd:YVO$_4$ laser.*

The laser was designed to give a maximum of 4 W average output power when modelocked. To ensure greater pump and laser mode overlap to maximise efficiency, the 600 μm fibre previously used was replaced with one having a 400 μm core (also 0.37 NA). Normally, the coupling efficiency of the 2 bar fibre bundle to the 400 μm fibre is rather low (~40%)[58], however, re-alignment of the coupling unit to match the particular fibre being used permitted coupling efficiencies of up to 65%. The laser was designed to be pumped with a maximum 12 W to prevent thermal induced fracturing of the Nd^{3+}:YVO_4.

The laser was first assembled using the scheme shown in figure 2.7 to assess cw operation. Unlike Nd^{3+}:YAG, it was found that a 13% output coupler afforded the greatest overall efficiency. For a total pump power of 11.6 W, 4.8 W cw was obtained from the short cavity.

The lower pump powers required for this laser implied weaker thermal lensing (~ 20 cm focal length expected) compared to the Nd^{3+}:YAG laser, hence extending the laser was simpler, requiring only a single 20 cm plano-convex lens to compensate for the thermal lens as shown in figure 2.36.

Two modelocker positions are shown. Initially a Brewster-angled Infrasil modulator was used, having resonances around 41 MHz. Because the intracavity beam undergoes tight focusing between the 200 mm lens and the output coupler, placing a Brewster-angled element here required that the lens be rotated by ~5^0 to compensate for

the resulting astigmatism. The plane AR-coated modelocker from the SP3800 laser was also used.

With the Brewster-angled modelocker placed in front of the output coupler, 110 ps pulses could be obtained with 3.8 W average output power. Shorter pulses (75 ps) were produced at 3.5W output using a 10% output coupler.

For possible self-modelocked operation, the plane-plane AR-coated modelocker was positioned behind the Nd^{3+}:YVO_4 rod. With active-modelocking, this enabled stable sub-100 ps pulses to be routinely obtained (at 3.3 W average output power) as measured on the streak camera in figure 2.37.

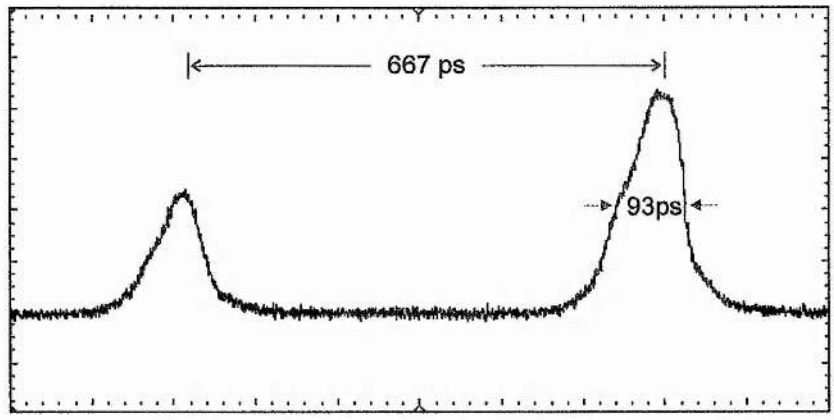

FIGURE 2.37: *Streak camera trace of pulses obtained from the actively modelocked Nd^{3+}:YVO_4 laser*

To attempt to obtain self-modelocked operation, the output coupler was reversed (its rear surface was AR coated for 1.064 μm) and a slit placed between the Nd^{3+}:YVO_4 rod and the HR end-mirror. It was anticipated that intensity dependent lensing in the substrate of the output coupler would cause a reduction in the spot size at the slit hence allowing hard aperture modelocking to be realised. Normally this would not be possible in a 3-mirror cavity design, but modelling this cavity using the methodology described by Magni et al[59] (discussed in chapter 4) suggested that the presence of a thermal lens in the gain medium would permit hard-aperture modelocking. Unfortunately, this was not observed and the shortest pulse obtained from the laser with this cavity remained at 75 ps.

For the production of pulses having durations ~10 ps, it is not actually necessary to resort to passive modelocking techniques. By exploiting the phenomenon of enhanced spatial hole burning, researchers have obtained pulses as short as 2.9 ps from

an actively modelocked Nd^{3+} laser[48]. The possibilities offered by this will be discussed in more detail in the following section.

2.7 Concluding Remarks

In this chapter I have detailed the design, construction and operation of an all-solid-state cw and cw-modelocked Nd^{3+}:YAG laser. The necessary criteria to be considered when designing a high power end-pumped system using a non-diffraction-limited pump source have been outlined together with an overview of cw laser alignment.

The cw laser described gave a maximum of 8.5 W, using a thermo-electric cooler to maintain the Nd^{3+}:YAG rod at 8^0 C. Without this temperature control, the maximum output power achieved was ~7.0 W.

A comparison was made of the amplitude noise and beam stability between the all-solid-state cw laser and the mainframe arc-lamp-pumped laser it was designed to replace. The diode-pumped laser was demonstrably superior in both regards with <0.8% peak-peak amplitude noise (compared to 4.6% peak-peak for the mainframe laser) and an order of magnitude improvement in beam-pointing stability.

The thermally induced lens in the Nd^{3+}:YAG of the cw laser was measured while the laser was operating at full power in a stable cavity. Focal lengths of 10.5 cm and 12.8 cm were measured for the thermal lenses in the tangential and sagittal planes respectively.

Three different actively mode-locked Nd^{3+} lasers were described, using amplitude-modulation (AM) as the modelocking mechanism. Initial results were disappointing with long pulse durations (~500 ps) measured, however high average output powers were obtained (5.7 W). Later it was realised that the plane-plane AR coated Nd^{3+}:YAG rod was seriously limiting the gain bandwidth of the laser by etalon effects hence accounting for the anomalously long pulse durations.

A compact actively-modelocked Nd^{3+}:YAG laser was constructed and characterised with the gain medium tilted by 5^0 to eliminate etalon effects. The compact cavity (~80 cm long) had a pulse repetition rate of ~193 MHz. This laser had high (6.0 W) average output powers and produced pulse durations as short as 34 ps, possibly

as a result of enhanced spatial hole burning. Unfortunately, these short pulse durations could only be maintained for very short periods (~ two minutes) before environmental temperature changes necessitated cavity length adjustment. An active stabilisation scheme was suggested which might permit the generation of short pulses to be maintained indefinitely. This was assessed on the mainframe Nd^{3+}:YAG laser and shown to maintain a constant pulse duration for cavity length expansions of over 40 μm, and contractions up to 20 μm. Stabilisation was achieved by varying the drive frequency of the modulator, but varying the cavity length using a piezo-transducer fixed to a mirror is also a possibility.

Finally, a lower power actively modelocked Nd^{3+}:YVO_4 laser was demonstrated. This had a repetition rate of 82 MHz, an average output power of up to 3.7 W and pulse durations down to 75 ps in duration. This was a potential replacement for the lower powered mainframe SP3000 laser.

It is highly desirable to construct a modelocked laser operating at ~1 μm with pulse durations of ~10 ps, a repetition rate of 82 MHz and average output powers of >3 W. This would serve as a useful pump source for synchronously pumping colour-centre lasers when pulse durations as short as 1 ps would be realised. In conjunction with coherent photon seeding[60] (described in chapter 3) this would create a useful tool giving bandwidth-limited pulses with durations tunable from 1 ps to ~20 ps at high average output powers.

Initially it was thought that a passive modelocking technique would be required to exploit sufficiently the narrow available bandwidth of Nd^{3+}:YAG for 10 ps pulse generation. Self-modelocking has been demonstrated in this material to produce pulses as short as 6.7 ps[61]. However, it has recently been established that enhanced spatial-hole-burning, possible when the gain medium is HR coated on one surface, can produce pulses of ~12 ps in conjunction with frequency-modulation (FM) modelocking[42].The most promising route to producing sub-10 ps pulses at high average output power is to employ a gain medium which has a slightly broader gain bandwidth than Nd^{3+}:YAG (e.g. Nd^{3+}:YVO_4 or Nd^{3+}:YLF), with an HR coating at 1.064 μm on one surface (the other surface being either Brewster-angled or AR-coated and wedged). FM modelocking should be deployed in preference to AM modelocking, or in conjunction with AM modelocking to allow lower repetition rates. This would represent a simple

laser arrangement without the alignment difficulties associated with self-modelocking or the necessity for an additional nonlinear element.

The high power cw all-solid-state Nd^{3+}:YAG laser described here proved itself to be invaluable as a pump source for the modelocked Cr^{4+}:YAG laser. Its superior low-noise performance permitted stable modelocked operation for long durations as will be described in chapter 5.

References

1 N.B. Angert, N. I. Borodin, V. M. Garmash, V. A. Zhitnyuk, A. G. Okhrimchuk, O. G. Siyuchenko, and A. V. Shestakov, *Sov. J. Quantum Electron.* **18**, p73 (1988)

2 G. Baldacchini,M. Cremona,M. Casalboni,D. Deviry,U. M. Grassano,A. Luci, M. Palummo,L. Casalis,P. Minguzzi,F. Pozzi, M. Tonelli, A. Scacco, *Physical Review B* **44**, p12189 (1991)

3 A. Sennaroglu, C. R. Pollock, and H. Nathel, *Opt. Lett.* **19**, p390 (1994)

4 K. R. German and C. R. Pollock, *Opt. Lett.* **12**, p474 (1986)

5 F. M. Mitschke and L. F. Mollenauer, *IEEE J. Quantum Electron.* **QE-22**, p2242 (1986)

6 Absorption spectrum measured in the laboratory using a scanning monochromator and high power heat lamp. Also located in ref. 7.

7 W. Koechner, *Solid-State Laser Engineering*, Springer-Verlag, Berlin (1996)

8 W. L. Nighan Jr., J. Cole, in Digest on *Conference on Advanced Solid-State Lasers*, (1996)

9 M. D. Selker, T. J. Johnston, G. Frangineas, J. L. Nightingale, D. K. Negas, in *Digest on Conference on Lasers and Electro-Optics* **1996**, paper CPD21, (1996)

10 R. Grant, Ph.D. Thesis, University of St. Andrews (1991)

11 The noise characteristics of the SP3800 were found to be dependent on a number of factors including the age and operating voltage of the arc-lamp in use. The higher the compliance voltage required for 30A, and the older the lamp, the greater the noise of the laser. The amplitude noise measured in ref. 10 is slightly less than reported here.

12 M. Ross, *Proc. IEEE* **56**, p196 (1968)

13 See e.g. G. P. Agarwal and N. K. Dutta, in *Long-Wavelength Semiconductor Lasers*, Van Nostrand Reinhold Company, New York (1986) and references therein

14 T. F. Johnston Jr., *Laser Focus World* **May 1990**, p173

15 C. Yelland, Ph.D. Thesis, University of St. Andrews (1996)

16 F. W. Ostermeyer, R. B. Allen, E. G. Dierschke, *App. Phys. Lett.* **19**, p289 (1971)

17 D. Golla, M. Bode, S. Knoke, W. Schöne, and A. Tünnermann, *Opt. Lett.* **21**, p210 (1996)

18 D. Kopf, G. Zhang, U. Keller, M. Moser, M. A. Emmanuel, R. J. Beach and J. A. Skidmore, in *Digest on Conference of Lasers and Electro-Optics* **1997**, Optical Society of America, Washington, D. C., paper CMC3 (1997)

19 C. Rahlff, Ph.D. Thesis, University of St. Andrews (1996)

20 W. A. Clarkson, D. C. Hanna, *Opt. Lett.* **21**, p375 (1996)

21 R. P. Edwin, *Opt. Lett.* **20**, p222 (1995)

22 W. A. Clarkson, D. C. Hanna, *Opt. Lett.* **21**, p869 (1996)

23 An early example of fibre coupling of laser diodes was: K. Kubodera and J. Noda, *Appl. Opt.* **21**, p3466 (1982). A more recent example demonstrating their advantages is in ref. 36

24 Millennia technical specification data sheet, Spectra-Physics Inc., (Mountain View, California) (1996)

25 D. C. Hanna, C. G. Sawyers, and M. A. Yuratchi, *Opt. & Quantum Electronics* **13**, p493 (1981)

26 V. Magni, *Appl. Opt.* **25**, p107 (1986)

27 V. Lupei, A. Lupei, S. Georgescu, and I. Ursu, *Appl. Phys. Lett.* **59**, p905 (1991)

28 J. K. Jabczynski, K. Kopczynski, and A. Szczesniak, *Opt. Eng.* **35**, p3572 (1996) See also ref. 35

29 S. C. Tidwell, J. F. Seamans, M. S. Bowers, A. K. Cousins, *IEEE J. Quantum Electron.* **QE-28**, p997 (1992)

30 R. Koch, *Opt. Commun.* **140**, p158 (1997)

31 W. L. Nighan Jr., D. Dudley, M. S. Keirstead, in Digest of *Conference on Lasers and Electro-Optics* **1995**, Optical Society of America, Washington, D.C. paper CMD4 (1995)

32 K. B. Steinbruegge, G. D. Baldwin, *Appl. Phys. Lett.* **25**, p220 (1972)

33 C. Yelland, and W. Sibbett, in Digest of *The Twelfth UK National Quantum Electronics Conference* **1995**, Institute of Physics, paper 2-4 (1995)

34 M. Oka and S. Kubota, *Opt. Lett.* **13**, 805 (1988)

35 M. E. Innocenzi, H. T. Yura, C. L. Fincher, R. A. Fields, *Appl. Phys. Lett.* **56**, p1831 (1990)

36 A. J. Alfrey, *IEEE J. Quantum Electron.* **QE-30**, p2350 (1994)

37 H. Kogelnik, *The Bell System Technical J.* **5**, p1550 (1966)

38 A. E. Siegman, in *Lasers*, University Science Books, California (1986)

39 B. Neuenschwinder, R. Weber, and H. P. Weber, *IEEE J. Quantum Electron.* **QE-31** p1082 (1995)

40 G. T. Kennedy, Ph.D. Thesis, University of St. Andrews (1993)

41 E. Hecht, in *Optics* (2nd edn.), Addison Wesley Publishing co. (Reading, Mass. USA) (1987)

42 H. Klann, J. Kuhl, and D. von der Linde, *Opt. Commun.* **38**, p390 (1981)

43 D. J. Kuizenga and A. E. Siegmann, *IEEE J. Quantum Electron.* **QE-6**, p694 (1970)

44 G. T. Maker and A. I. Ferguson, *Opt. Lett.* **14**, p788 (1989)

45 B. Braun, K.J. Weingarten, F.X. Kärtner, U. Keller, *App. Phys. B* **61**, p429 (1995)

46 F.X. Kärtner, B. Braun, U.Keller, *App. Phys. B* **61**, p569 (1995)

47 C. J. Flood, D. R. Walker, H. M. van Driel, *Opt. Lett.* **20**, p58 (1995)

48 A. A. Godil, A. S. Hou, B. A. Auld D. M. Bloom, *Opt. Lett.* **16**, p1765 (1991)

49 G. T. Maker, S. J. Keen, and A. I. Ferguson, *Appl. Phys. Lett.* **53**, p1675 (1988)

50 H. Roskas, T. Robl, and A. Seilmeier, *Appl. Phys. B* **40**, p59 (1986)

51 See e.g. M. Matsui, K. Adachi, and S. Chikazumi, *J. Appl. Phys.* **51**, p6319 (1980)

52 F. M. Mitschke and L. F. Mollenauer, *IEEE J. Quantum Electron.* **QE-22**, p2242 (1986)

53 Although a silicon photodiode would be more appropriate for detecting light at 532 nm, the germanium device was the only one correctly configured for operation with the APM stabilisation system.

54 A. A. Kaminskii, *Phys. Stat. Sol. A.* **1**, p573 (1968)

55 See references 8 and 9

56 Virgo-Optics commercial crystal data sheet, December 1993

57 K. X. Liu, C. J. Flood, D. R. Walker, and H. M. van Driel, *Opt. Lett.* **17**, p1361 (1992)

58 Data sheet for the OPC-OC-01 optical converter, Opto-Power-Corporation (Tucson, Arizona, USA) (1996)

59 V. Magni, G. Cerullo, S. De Silvestri and A. Monguzzi, *J. Opt. Soc. Am. B* **12**, p476 (1995)

60 G. J. Valentine, G. T. Kennedy, W. Sibbett, in in Digest of *Conference on Lasers and Electro-Optics* **1995**, Optical Society of America, Washington, D.C. paper CThI38 (1995)

61 B. Henrich and R. Beigang, *Opt. Commun.* **135**, p300 (1997)

3 Passive Stabilisation Of A Synchronously-modelocked NaCl:OH^- Colour-centre Laser

3.1 Introduction

Until the development of the Cr^{4+}:YAG laser[1], the most convenient high power, tunable, modelocked sources covering the important 1.55 μm telecommunications band, were lasers based on KCl:Tl^0(1) and NaCl:$OH^-(F_2^+)_H$ colour-centre gain media. These systems, whilst efficient and versatile, had the major inconvenience of requiring cooling to 77K necessitating a cryogenically engineered crystal mount cooled by liquid nitrogen. In addition, the KCl:Tl^0 laser crystals required periodic replacement (~6 months) due to bleaching of the colour-centres during use. Nonetheless, in the absence of any suitable alternative, they proved to be reliable sources of picosecond pulses when operated with synchronous modelocking[2], and femtosecond pulses with the technique of coupled-cavity-modelocking[3] (CCM) (also called 'additive-pulse-modelocking').

The synchronously-pumped-modelocked (SPML) NaCl:OH^- laser in particular has proved to be an invaluable tool for the study of optical non-linearities in various waveguide structures, when high peak powers may be required, but without the broad bandwidth associated with femtosecond pulses. Whereas the self-modelocked Cr^{4+}:YAG laser[4] is now a preferred alternative to the femtosecond CCM KCl:Tl^0 and NaCl:OH^- lasers, for high average power, versatility and stability, the SPML NaCl:OH^- laser is still probably the most suitable system to use for picosecond pulses at ~1.5 μm, especially when the simple technique of coherent-photon-seeding[5] (CPS) is deployed for enhanced stability.

In this chapter, the technique of modelocking by synchronous pumping is studied in considerable detail, with emphasis given to the noise characteristics of lasers that have been modelocked using this method. The SPML NaCl:OH^- laser is studied experimentally and modelled numerically, and the effects of deploying coherent-photon-seeding are examined.

3.1.1 Colour-Centres

A brief outline of colour centres is given. (For a more detailed description refer to reference 6.) Colour centres (or F-centres where 'F' stands for Farbe, 'colour' in German) are point defects in insulating crystals. Normally, the insulating crystal is an alkali-halide. The presence of an F-centre causes the normally transparent alkali-halide crystal to possess absorption bands in the visible part of the spectrum, hence the term 'colour-centre' crystal.

The simplest example of an F-centre is an anion vacancy in an alkali-halide lattice, occupied by a single electron to maintain an overall neutral charge. The energy levels of this F-centre may be modelled as a particle in a box. Strong interactions between the F-centre and vibrations in the crystal lattice (phonons) lead to considerable broadening of these energy levels, resulting in the broad absorption and fluorescence bands characteristic of colour-centres.

This simple F-centre is not laser active. The first demonstration of laser action in a colour-centre crystal was in flashlamp-pumped KCl:Li^+ in 1965[7] at 2.7 μm, and since then numerous different F-centres have been demonstrated spanning the spectral region from 800-4000 nm. The main drawback of colour-centre media is that they possess short operational lifetimes as the F-centres often 'migrate' through the crystal lattice to form aggregate F-centres which quench laser action. In addition, the cryogenic paraphernalia, which often accompanies colour-centre lasers, is inconvenient for many users. For these reasons, colour centres have been superseded in almost every application by vibronically broadened transition-metal-ion-doped solid-state crystals (e.g. Ti^{3+}:Al_2O_3) which operate at room temperature without fading.

The $(F_2^+)_H$ centre in NaCl:OH^-

Mollenauer et al. first examined the F_2^+ centre in NaCl as a possible colour-centre laser medium operating in the 1.5 μm region[8]. Unfortunately, the basic F_2^+ centre is naturally unstable and was found to fade within minutes of use. The centre consists of two adjacent F-centres in the <110> plane occupied by a single electron (hence the overall positive charge). During intense optical excitation, the centre can pivot around one of the vacancies changing orientation. Successive orientation effectively causes the

centre to 'migrate' through the lattice until it combines with other defects to form non-laser-active aggregate colour centres.

Several methods of stabilising F_2^+ -centres have been studied including radiation damage[9] and replacing a lattice alkali or halide ion with a substitutional ion to 'pin down' the location of the defect in the lattice[10]. Pinto et al.[11] first described the stabilised F_2^+-centre in NaCl, initially believing K^+ to be the stabilising ion. Later spectral analysis proved that O^{2-} was in fact the stabilising defect[12] (introduced into the host by contamination with OH^- ions.) The centre is thus identified as NaCl:OH^- $(F_2^+)_H$ where the 'H' denotes substitution of a halide ion for stabilisation.

Some important characteristics of the NaCl:OH^- gain medium are summarised in table 3.1.

Parameter	Value	Reference
Refractive index	1.53	
Absorption peak	1.09 μm	13
Emission peak	1.55 μm (1.59 μm)	13,14
Emission FWHM	33 THz (30 THz)	13,14
Tuning range	1.37-1.85 μm	15
Upper state lifetime (τ_{rad})	150 ns (75 ns)	13,16
Gain cross section (σ_{em})	8.5×10^{-17} cm^2	17
Quantum efficiency (η)	Approx. 100 %	13

TABLE 3.1: *Important optical characteristics of the $(F_2^+)_H$ centre in NaCl:OH^- at 77K*

During operation, the output power of the NaCl:OH^- laser gradually fades as the F^{2+} centres flip their orientation such that their dipole moments are perpendicular to the polarisation of the pump laser. The centres must be re-orientated by exciting them from the $1s\sigma_g$ ground state to a higher energy excited state using either F-band light (400-500 nm) or two-photon pumping using light from 500-650 nm in conjunction with the 1.064 μm pump light. Re-orientation then occurs during the non-radiative transitions to the first excited state ($2p\sigma_u$). In practice, light at 532 nm is normally used for centre

re-orientation as this can be simply derived by extracavity frequency-doubling a fraction of the Nd^{3+}:YAG pump light.

3.2 Actively Modelocked NaCl:OH^- Laser Using Synchronous Pumping

3.2.1 Synchronously-Pumped Modelocked Lasers

The technique of synchronously-pumped-modelocking (SPML) is simple and versatile. The wavelength range over which the modelocked pulses may be tuned is limited only by the gain bandwidth of the laser medium and the mirror coatings. SPML is an active-modelocking technique which relies upon gain modulation, accomplished by optically pumping the gain medium of the SPML laser (the 'slave' laser) with a modelocked pump laser (the 'master' laser). The optical length of the two laser cavities must be closely matched for optimum modelocked performance, (but as will be demonstrated later, the cavity lengths are not exactly equal).

Typically the pump laser is actively-modelocked (using either amplitude or frequency-modulation) so its repetition rate is governed by an external frequency source. An actively-modelocked Nd^{3+}:YAG laser normally has pulse durations of 75-100ps.

An important feature of synchronously-modelocked lasers is that their pulse durations can be significantly shorter than the duration of the original pump pulse. This is due to the combined effects of gain modulation (induced by the pump pulse) and dynamic gain saturation (by the SPML laser pulse). The latter effect shortens the trailing edge of the circulating laser pulse and requires a gain medium with a large emission cross-section such as dye and colour-centre lasers.

SPML was originally developed as a modelocking mechanism for dye lasers[18] e.g. rhodamine 6G, pumped by actively-modelocked frequency-doubled Nd^{3+}:glass lasers and modelocked argon-ion lasers. With the development of NaCl:OH^- colour-centre lasers, synchronous-modelocking was adopted allowing tunable pulses as short as 1.8 ps to be generated[19], using 60 ps pump pulses from an actively-modelocked Nd^{3+}:YLF

laser. Average output powers of over 1.7 W have been achieved at the peak of the gain at 1.6 μm.

Figure 3.1 shows the standard layout adopted when a synchronously-modelocked NaCl:OH^- laser was required. The NaCl:OH^- gain medium is placed in a cryostat maintained at 77 K with liquid nitrogen. Brewster-angled fused silica windows allow the polarised pump and circulating laser beams to access the Brewster-angled crystal with minimum loss.

About 30% of the available modelocked pump light was diverted to produce the required auxiliary 532 nm light for centre re-orientation. Up to 200 mW of green light was produced which was more than sufficient for maximum re-orientation. A zero-order, quarter-wave plate in the path of the 1.064 μm pump beam was required to produce an elliptically polarised pump for optimal colour-centre reorientation. The half-wave-plate in the 532 nm path created p-polarised green. Noncollinear pumping is normally employed (similar to dye lasers) though the performance sacrifice associated with this is minimal as the gain medium length is so short (~2.5 mm).

The cavity layout is a three-mirror geometry folded back on itself. The 1 m radius of curvature mirror in the long arm produces a cavity with a larger spot in the gain medium for better mode-matching with the pump beam and maintains a large stability region while matching the long length of the modelocked pump laser.

A 6.6 mm thick birefringent-filter (BRF) placed at Brewster's angle inside the laser cavity controlled the available oscillating bandwidth. For optimum synchronous-pumping, the length of the cavity was carefully controlled with a differential actuator on the end mirror M5.

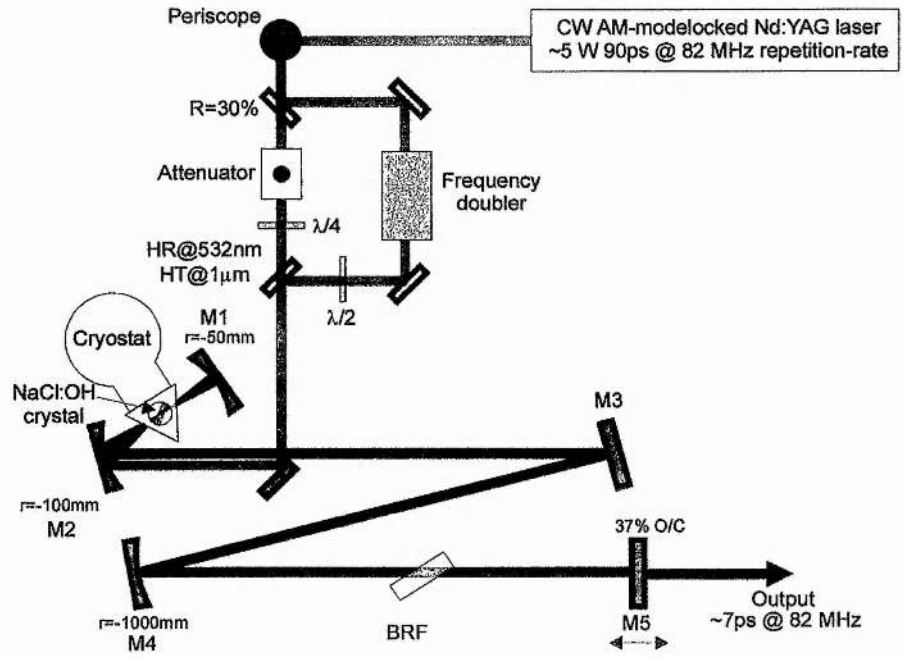

FIGURE 3.1: *Schematic of standard layout of the synchronously-modelocked NaCl:OH colour-centre laser*

One important characteristic of any synchronously-modelocked laser is the behaviour of detuning the slave laser cavity length with respect to the master pump laser length. This has been investigated both experimentally[20] and theoretically[21] for dye and colour-centre[22] gain media and will be presented in later sections of this chapter. The repetition rate of the SPML laser is identical to (or a submultiple of) that of the master laser, irrespective of the precise length of the slave laser. Changing the slave cavity length alters the modelocking dynamics inside the gain medium. This has the curious effect that when the slave laser length is longer than the length of the master laser, the SPML laser pulse effectively travels faster than the speed of light! How this occurs is clarified by the modelling in the next section.

A requirement of SPML lasers is that a bandwidth-limiting element must be used for complete modelocking to be achieved without excess bandwidth. The drawback of synchronously-modelocked lasers in the past is that even with this limiting element, modelocking is poor: the amplitude-noise of the modelocked pulse train is excessive and even slight detuning of the slave cavity results in pulses which are several times bandwidth limited. The noisy pulse train gives 'cusp shaped' autocorrelation traces which are characteristic of SPML lasers[23]. In addition, the RF spectrum of SPML lasers have a broad noise band centred at the harmonics of the pulse repetition frequency

indicating high frequency pulse energy fluctuations. The precise reason for this modelocking instability was unclear until a new method of modelling SPML lasers was developed. This demonstrated that as well as initiating the laser, the incoherent light emitted by spontaneous transitions in the gain medium (fluorescence) also plays a crucial role in the modelocking dynamics of synchronously-modelocked lasers[24]. This is described in the following section.

3.3 Numerical Modelling Of Synchronously-Modelocked Lasers

Early models of synchronously-modelocked lasers used the self-consistency method, originally developed to study AM actively-modelocked lasers[25]. This depends upon finding a pulse profile which remains unchanged following periodic modification by the different laser cavity elements. An initial pulse-shape must be assumed before the model is used. It was argued that this technique was not applicable to SPML lasers as the upper state lifetimes of the gain media normally employed in such arrangements are comparable to the cavity round-trip period such that the gain is significantly depleted during the transit of the circulating laser pulse through the gain medium[26]. Catherall et al.[27] developed a simple but powerful algorithm for modelling synchronously-modelocked lasers (the 'stepping model') which allowed the SPML laser pulse to develop over successive round trips; no assumptions about pulse-shape were made.

3.3.1 The 'Stepping Model' of SPML lasers

The model represents the circulating SPML pulse as a mesh of complex field values $\mathbf{V^{(k)}_{i,n}}$ within a small local time window of duration $\mathbf{T_{window}}$ centred on the peak of the pump pulse. The index **(k)** indicates the position of the time window within the laser cavity. The position within the local time window relative to the pump pulse peak is indicated by the suffix **i**:

$$t_i = i.\delta t - \frac{T_{window}}{2} \qquad \text{Equation (3.1)}$$

where $\delta\mathbf{t}$ is the mesh size. **n** is the cavity round trip number.

The model was first developed as a ring-cavity arrangement, as illustrated in figure 3.2 where the field experiences one pass through each pulse shaping element per

round trip. The field is subjected to different mathematical operations representing the laser cavity elements.

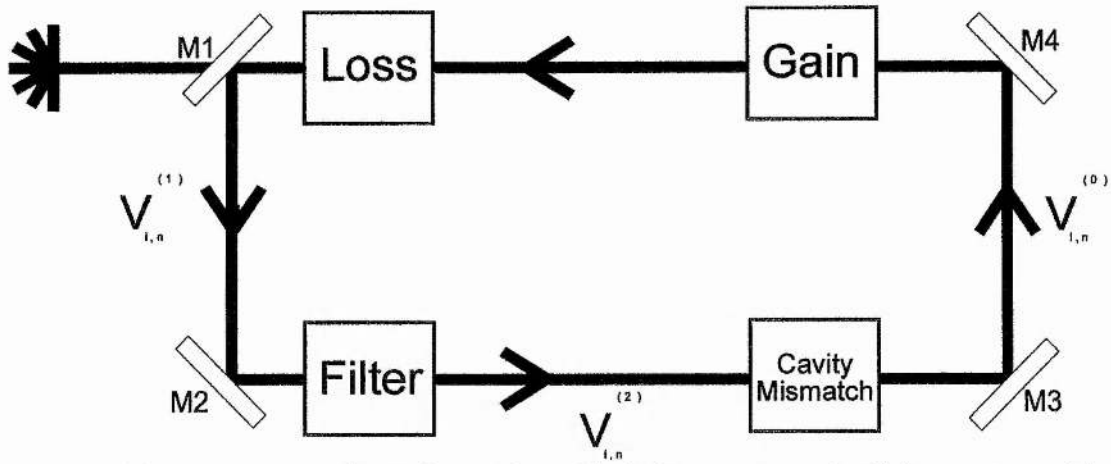

FIGURE 3.2: *Representation of a synchronously-modelocked ring-cavity used with the stepping model*

Initially, the field $(\mathbf{V^{(0)}})$ experiences gain representing propagation through the gain medium. The resulting field is given by

$$V_{i,n}^{(1)} = V_{i,n}^{(0)} \exp\{(A_i - \Gamma)/2\} + S_{i,n} \qquad \text{Equation (3.2)}$$

where Γ is the intrinsic loss of the crystal and $\mathbf{S_{i,n}}$ represents the stochastic background noise due to spontaneous-emission (fluorescence) in the gain medium. The amplification coefficient $\mathbf{A_i}$ is found by solving the following first-order differential equation which is derived from a simple four-level rate equation approximation[27]

$$\frac{dA_i}{dt} = \left[\frac{\sigma_e}{E_p}\left\{1 - \exp\left(\frac{\sigma_a}{\sigma_e}(A_i - A_T)\right)\right\} I_p(t_i)\right] - \left[\frac{\sigma_e}{E_s}\{\exp(A_i) - 1\} \cdot I_s(t_i)\right] - \left[\frac{A_i}{T_{1a}}\right]$$

Equation (3.3)

(i) (ii) (iii)

The three terms in this equation are:

i) increase in gain due to the pump pulse

ii) depletion of the gain resulting from stimulated emission by the circulating laser field inside the cavity

iii) depletion of the gain due to spontaneous emission.

σ_e is the stimulated emission cross-section, σ_a is the absorption cross-section and T_{1a} is the upper state lifetime of the gain medium. E_p is the pump photon energy, E_s the signal photon energy, and A_T is the maximum amplification that would result if all the laser active centres were excited to the upper state.

$I_s(t_i)$ is the intensity of the signal laser field given by

$$I_s(t_i) = \left|V_{i,n}^{(0)}\right|^2 \qquad \text{Equation (3.4)}$$

$I_p(t_i)$ is the intensity of the pump laser field. This is assumed Gaussian throughout the model and is:

$$I_p(t_i) = \frac{P_{avg}}{1.065 f_{rep} . A_{beam} . \tau_{fwhm}} . \exp\left(-\left(\frac{1.665 t_i}{\tau_{fwhm}}\right)^2\right) \qquad \text{Equation (3.5)}$$

P_{avg} is the average pump power, f_{rep} the repetition frequency of the pump pulses and τ_{fwhm} is the full width at half maximum duration of the pump pulses. A_{beam} is the cross-sectional area of the pump beam inside the gain medium (assumed a constant value throughout the medium).

The noise term in equation (3.2) represents light of a stochastic nature resulting from spontaneous emission from the gain medium. This both initiates laser action and affects the stability of the mode-locked pulse train[24]. The noise term is identical to that used by Amman et al.[28] and includes a realistic dependence on the amplification factor $A_{i,n}$. This simulates Gaussian noise with a Lorentzian spectral profile[29].

$$S_{i,n} = S_{i-1,n} . e^{-\frac{\delta t}{t_{coh}}} + N\sqrt{A_{i,n}} . e^{i\phi_i} \qquad \text{Equation (3.6)}$$

N is the noise level, the coherence time (t_{coh}) is determined from the spectral linewidth and ϕ_i are random phases.

The loss function represents the effect of an output coupler.

$$V_{i,n}^{(1)} = \sqrt{1-T} . V_{i,n}^{(1)} \qquad \text{Equation (3.7)}$$

T is the intensity transmittance of the output coupler.

The bandwidth limitation is included by a simulation of a Fabry-Pérot etalon tuned to resonance with the circulating signal wavelength. If the transit time of the etalon, $\mathbf{t_e}$, is taken to be the same as the mesh spacing, $\delta\mathbf{t}$, a single pass through an etalon having plate reflectivity, **R**, performs the following transformation[30]:

$$V_{i,n}^{(2)} = (1-R)V_{i,n}^{(1)} + RV_{i-1,n}^{(2)} \qquad \text{Equation (3.8)}$$

This etalon has a group time delay, $\mathbf{t_f}$, governed by the plate reflectivities and the etalon transit time:

$$t_f = \frac{R.\delta t}{1-R} \qquad \text{Equation (3.9)}$$

The cavity mismatch operation simply involves shifting the slave laser field values on the mesh. i.e.

$$V_{i+m,n}^{(0)} = V_{i,n}^{(2)} \qquad \text{Equation (3.10)}$$

The cavity transit time mismatch introduced is thus $\mathbf{t_m}=\mathbf{m}.\delta\mathbf{t}$ but the group delay of the etalon must be considered for the total effective mismatch between the slave and pump cavities.

$$t_{m_{eff}} = m.\delta t + t_f \qquad \text{Equation (3.11)}$$

For positive values of **m** (ie. slave longer than pump cavity) the missing values on the leading edge of the mesh window can be set to 0. Negative mismatches are more problematic because no knowledge of the field values beyond the trailing edge of the window is known. It has been argued[31] that this can be successfully approximated by repeating the last calculated value of the field on the mesh and this was done throughout the implementation of this model.

The model was originally developed to describe dye lasers which have short upper state lifetimes ($\mathbf{T_{1a}}$ ~100 ps) compared with the cavity round-trip time ($\mathbf{T_{cavity}}$ ~10 ns) and so the amplification factor (**A**) was assumed to decay to zero between pump pulses. This assumption is not true for colour-centre lasers where the upper state lifetime can be as long as 1.6 μs (in the case of the $KCl:Tl^{(0)}$ laser). The initial amplification value $\mathbf{A_0}$ must then be set as:

$$A_{0,n} = A_{L,n-1}.e^{-\left(\frac{T_{cavity}-T_{window}}{T_{1a}}\right)}$$ Equation (3.12)

where $\mathbf{T_{cavity}}$ is the cavity round-trip time, and $\mathbf{A_{L,n-1}}$ refers to the last amplification value calculated for the previous round trip.

The synchronously-modelocked laser constructed in practice was of a standing-wave design, hence the circulating laser field experienced two passes through the gain medium and bandwidth limiting element. To fully simulate this, the model was adapted slightly to take these effects into account. This model flow diagram is illustrated in figure 3.3.

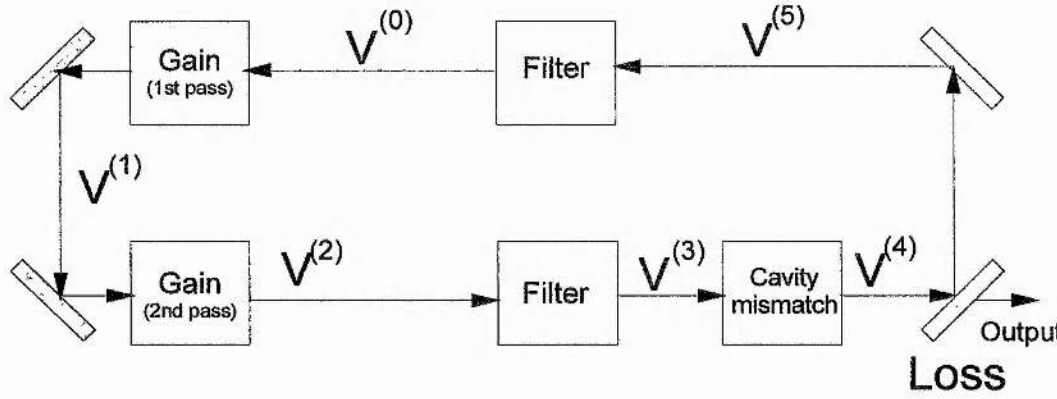

FIGURE 3.3: *Model of a linear cavity SPML laser*

The two spectral filtering operations are identical to equation (3.8) but the second pass through the gain is modelled by slightly modified forms of equations (3.2) and (3.3) which exclude the pumping pulse term:

$$V_{i,n}^{(2)} = V_{i,n}^{(1)} \exp\left\{\left(A_i^{(2)} - \Gamma\right)/2\right\} + S_{i,n}$$ Equation (3.13)

where the amplification term during the second pass is calculated by:

$$\frac{dA_i^{(2)}}{dt} = -\frac{\sigma_e}{E_s}\left\{\exp\left(A_i^{(2)}\right) - 1\right\} \cdot I_s(t_i) - \frac{A_i^{(2)}}{T_{1a}}$$ Equation (3.14)

The initial amplification $\mathbf{A_0^{(2)}}$ remaining in the laser medium before the second pass of the circulating pulse is found from:

$$A_0^{(2)} = A_L^{(1)}.e^{-\left(\frac{T_d}{T_{1a}}\right)}$$ Equation (3.15)

where $A_L^{(1)}$ refers to the last value of the gain calculated for the first pass within the narrow time window and T_d is the delay between the first and second passes through the gain medium.

The simulation involves applying reiteratively the appropriate operations for ring or linear cavities. The two differential equations (3.3 and 3.14) were solved using a fourth-order Runge-Kutta algorithm[32].

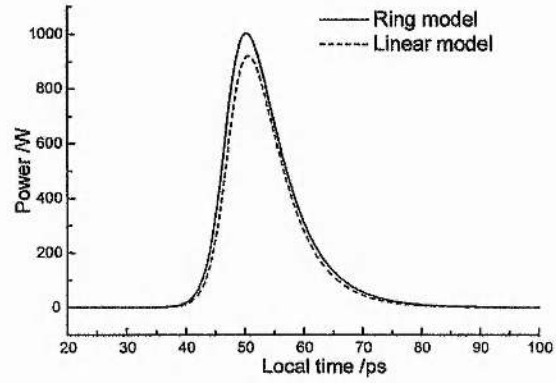

FIGURE 3.4: *Demonstration of the similarity between the pulses obtained from the linear and ring cavity models.*

The differences between the results obtained with the ring and linear cavity models were slight as illustrated in figure 3.4, which shows stable simulated SPML pulses for both models. Surprisingly, the peak power of the pulse obtained from the linear model which includes two passes through the gain medium is lower than that for the ring cavity. This is due to the high intrinsic loss of the NaCl:OH^- gain medium (~5%); the inverted gain remaining after the first pass through the gain medium being insufficient to negate the parasitic losses associated with a second pass. The ring cavity also produces slightly more asymmetric pulses to the linear case. Unless stated otherwise, all numerical results which follow were actually performed with the ring cavity model to minimise the computational time.

3.3.2 Implementation of the model

The ring-cavity model, as described, is based on that used to simulate a SPML KCl:Tl^0 laser by Kelly et al[21]. For the case of the NaCl:OH^- laser, the following appropriate parameter values were initially used: σ_e=8.5x10^{-17} cm^2, σ_a=9.2x10^{-17} cm^2, T_{1a}=150 ns, λ_p=1.064 μm, λ_s=1.5 μm, A_T=5[33]. The pump was set to τ_{fwhm}=90 ps, P_{avg}=3 W, A_{beam}=10^{-9} m^2, f_{rep}=82 MHz. For the spontaneously emitted background light the coherence time (inverse of the laser linewidth) was taken to be t_{coh}=31.7 fs.

The noise level depends on the upper state lifetime, the cavity geometry and how far above threshold the laser is operating, but the actual value used is not critical to results finally obtained. A value of $N=10^{-5}$ as used in reference 34 was used initially. For the bandwidth limiting element, the etalon reflectivities could be varied to give different group delay times according to equation 3.9. A value of 1 ps was chosen as a realistic value to represent the available bandwidth of a 6 mm thick single plate birefringent filter (BRF) in the NaCl:OH^- laser, as this is approximately the shortest pulse duration possible with such an arrangement using coupled-cavity modelocking. The output coupling was fixed at 30 %.

To demonstrate how the model reaches a steady-state solution, the noise term of equation 3.6 was replaced with a constant value (equal to N). An initial result obtained from the ring cavity model is in figure 3.5 which shows that the steady-state condition was reached after ~1000 round trips. For this particular case, the pump pulse was set to ~85 ps in duration (full-width at half-maximum). The etalon group delay time was 1 ps and the cavity mismatch was fixed at $t_m=0$ i.e. $t_{meff}=1$ ps

The short SPML pulse is found to occur after the peak of the much longer pumping pulse. The precise time of formation of the modelocked pulse depends on a subtle balance between the different cavity parameters, particularly the cavity mismatch and, interestingly, the level of the background spontaneously emitted light. The single-pass gain of equation 3.2 is quickly pumped well above threshold by the pump pulse (gain modulation). Once the SPML pulse forms, the gain is rapidly depleted until it is below the laser threshold level (dynamic gain saturation) and so the trailing edge of the synchronously-modelocked pulse is effectively 'trimmed'. Closer observation of figure 3.5 reveals that there is still sufficient pump pulse remaining after the main SPML pulse has passed to raise the gain above threshold again thus allowing the formation of a small 'satellite' pulse.

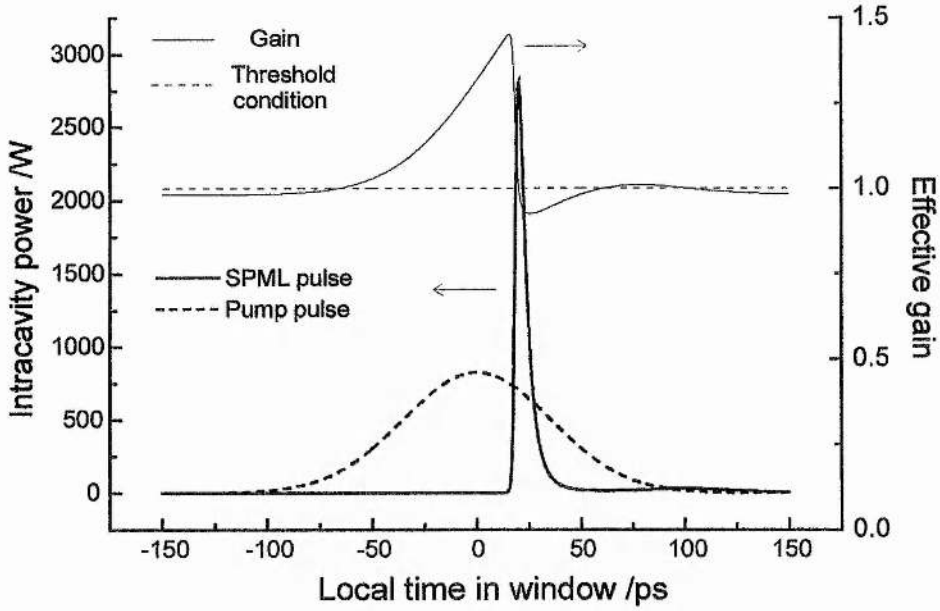

FIGURE 3.5: *Dynamics of a synchronously-modelocked laser*

From figure 3.5 it can be seen that the SPML pulse is not Gaussian in profile (which has often been assumed when taking pulse duration readings from intensity autocorrelations) but instead is highly asymmetric (leading edge half-width at half-maximum (hwhm)=2 ps, trailing edge hwhm=3.8 ps).

It is important to realise that the gain is able to be pumped well above threshold before the SPML pulse causes it to be rapidly depleted because of the positive mismatch present between the pump laser cavity and the 'slave' SPML laser (i.e. the slave laser is longer than the pump laser) but the repetition rate of the SPML slave laser must be the same as the repetition rate of the pump laser. This discrepancy is compensated for by the modelocking dynamics occurring inside the gain medium. The peak of the SPML pulse for the next round trip is effectively formed from the wings of the SPML pulse of the previous round trip.

The necessary positive mismatch for optimal modelocking was first proposed after numerical modelling[35]. Several other authors disagreed and early experimental evidence appeared to disprove it where it was concluded that the master and slave cavities were of identical optical length[36]. Later, with research into passive-modelocking of NaCl:OH^- lasers initiated with synchronous-pumping, it became obvious that the shortest SPML pulses were obtained at a different repetition rate to the passively modelocked pulses, thereby proving beyond doubt that a mismatch exists between the

pump and slave cavity lengths. This was observed as a low frequency modulation on the coupled-cavity-modelocked pulse sequence[37].

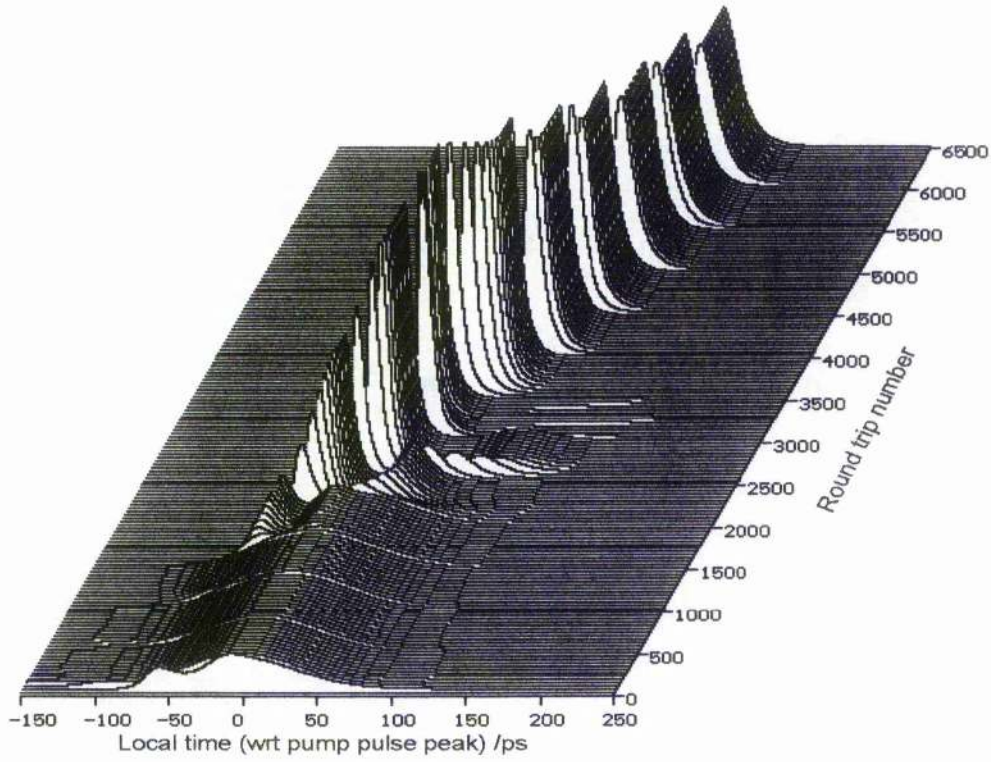

FIGURE 3.6: *Effect of increasing the cavity mismatch of a SPML laser. Pulse recorded every 40 round trips. Mismatch increased by 400 fs every 500 round trips*

An illustration into the importance of the mismatch between the master and slave lasers is given in figure 3.6. The model automatically increases the effective cavity mismatch by 400 fs (corresponding to increasing the length of the linear SPML cavity by 60 μm) every 500 round trips from t_{meff}=−0.8 ps to t_{meff}=+4 ps. It is immediately apparent that for negative (and zero) mismatches, the SPML pulse is of similar duration to the pump pulse. As the mismatch becomes more positive, a short SPML pulse is created but sufficient pump pulse remains after it has passed to allow the creation of a satellite pulse or pedestal. The pulse with the highest peak power is formed after 3000 round trips (t_{meff}=1.6 ps) and increasing the mismatch beyond this increases the pulse width.

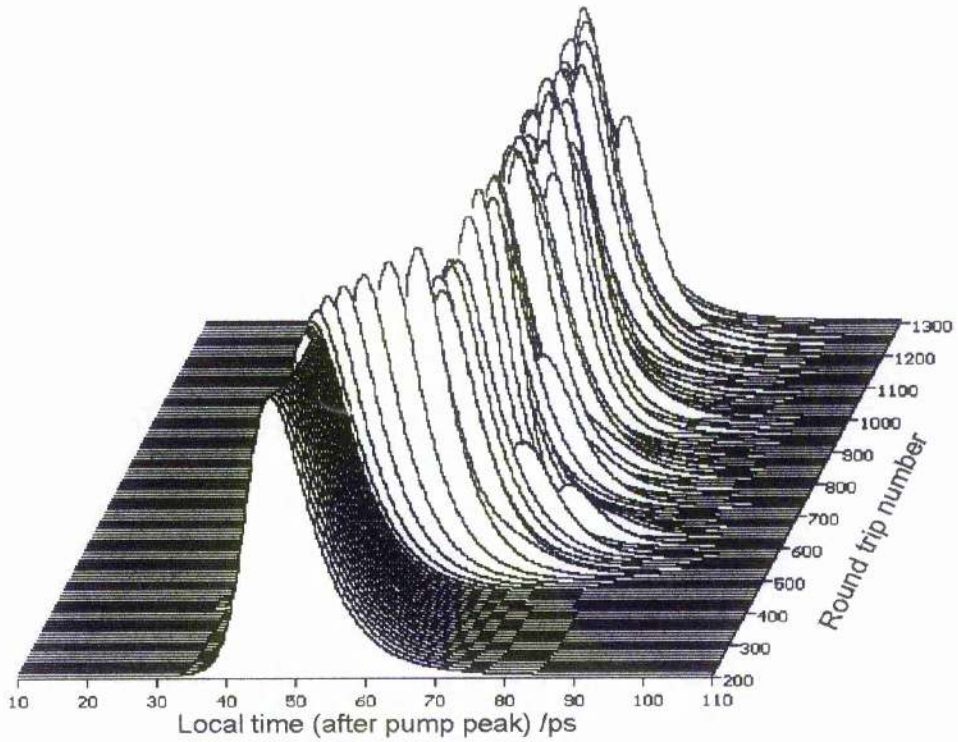

FIGURE 3.7: *Effect of stochastic background noise on SPML laser pulse stability. Noise turned on after 400 round trips.*

To demonstrate the significance of the stochastic background noise on pulse-pulse stability, figure 3.7 shows pulse evolution without noise (a fixed background value is used to initiate modelocking) but after 400 round trips the noise term in equation 3.6 is included in the model. After the 600^{th} round trip the new pseudo-steady-state is reached where the pulse jitters around a central position. This is summarised in figure 3.8 which illustrates the high frequency amplitude-noise associated with synchronously modelocked lasers. Note that the slight shift in position which occurs around the 500^{th} round trip is only due to the reduced overall background light level when the constant term is replaced with the noise term (equation 3.6).

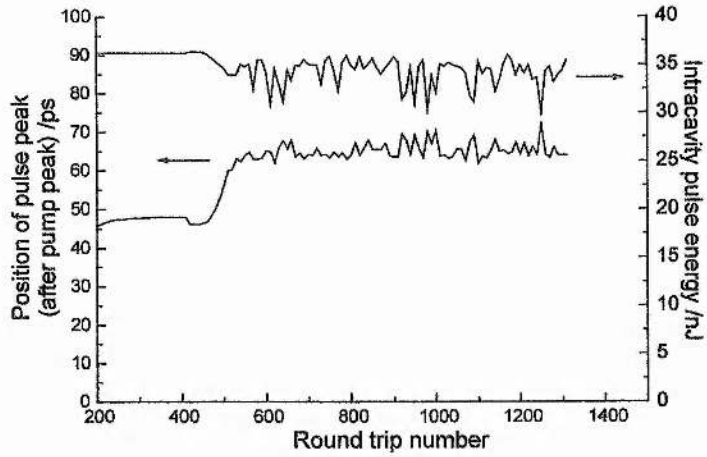

FIGURE 3.8: *Effect of stochastic background light on SPML pulse energy stability and pulse jitter. (data taken from figure 3.7)*

The stepping model has successfully identified the source of the high frequency noise associated with the synchronous-modelocking technique. It should have been an elementary step using this model to demonstrate that it is possible to eradicate entirely this instability simply by overcoming the noise term with a coherent signal derived from the circulating field. Unfortunately, this was not done until after coherent-photon-seeding had been discovered experimentally, and the numerical model then only served to confirm the explanation of why the technique actually works.

3.4 Passive Stabilisation Using Coherent-Photon-Seeding

Coherent-photon-seeding was first demonstrated by Beaud et al.[38] on a synchronously-modelocked IR26 dye laser possibly as an accidental observation when setting up a coupled-cavity modelocked laser. An external cavity of approximately the same length as the SPML laser was coupled to the main cavity via the output coupler. Attenuators placed inside the external cavity allowed the quantity of light reflected back into the main cavity to be varied. Feeding back even minute fractions ($\sim 10^{-10}$) of the circulating laser light into the main cavity dramatically improved the stability of the synchronously-modelocked pulse train. This was observed as 'cleaner' cusp free autocorrelation traces, reduced amplitude-noise on the average output power of the laser and a dramatic reduction of the duration-bandwidth product indicating more complete modelocking. In this early experiment it was not possible to determine the precise lengths of the main SPML laser cavity and the stabilising coupled-cavity, though it was

observed that stabilisation occurred over a wide range of auxiliary cavity lengths (in contrast to coupled-cavity modelocking which necessitates interferometric matching of the main and external laser cavities). It was suggested that feeding back a weak replica of the coherent circulating SPML pulse overpowered the background incoherent spontaneously emitted light and so must be fed back in advance of the main laser pulse by approximately twice the modelocked pulse length. The name 'coherent-photon-seeding' (CPS) was therefore adopted to describe this technique.

Soon after the first experimental observation of passive stabilisation of a synchronously-modelocked laser, the stepping model was applied to investigate the effect of feeding back a fraction of the main laser pulse on pulse stability[39]. This demonstrated that the seeding pulse must be somewhat in advance of the main cavity pulse for optimal effect though the parameters governing the optimum seeding position were uncertain.

One enormous advantage offered by CPS in synchronously-modelocked lasers is the ability to 'tune' the duration of the modelocked pulse whilst maintaining near-bandwidth limited operation, simply by increasing the length of the slave cavity. This was first realised by Hooker[40] who also suggested that the seeding pulse should be fed back into the main laser by approximately the pump pulse duration in front of the circulating pulse. Without stabilisation, modelocked performance quickly deteriorates when the cavity length is increased beyond the point which produces the shortest pulse.

Coherent-photon-seeding was subsequently applied to a number of laser systems including actively modelocked laser diodes[41], synchronously-pumped surface-emitting semiconductor lasers[42] and hybrid-modelocked dye lasers[43]. Möllmann and Gellermann first applied CPS to a synchronously-modelocked NaCl:OH^- colour-centre laser demonstrating a useful tool for generating picosecond pulses tunable in wavelength and duration covering the 1.5 μm telecommunications band[44]. An experimental and numerical investigation of this system follows.

3.5 Coherent-Photon-Seeding Applied To The Synchronously-Modelocked NaCl:OH- Colour-Centre Laser

The schematic in figure 3.9 is the experimental configuration adopted to assess coherent-photon-seeding with the NaCl:OH^- laser. No additional intracavity elements were required as leakage from a cavity HR mirror (R~99.8%) provided the required signal for CPS. The seeding cavity comprises mirrors M6 and M7 which are arranged to match the remaining main cavity mirrors M4 and M5. The use of the 1 m radius of curvature mirror in the external cavity ensures good overlap of the seeding mode with the main cavity mode inside the gain medium.

Without further attenuation, the seeding level provided by this arrangement was ~4.10^{-6} (as a fraction of the main intracavity power). Neutral density filters placed inside the external cavity could further reduce the seeding level.

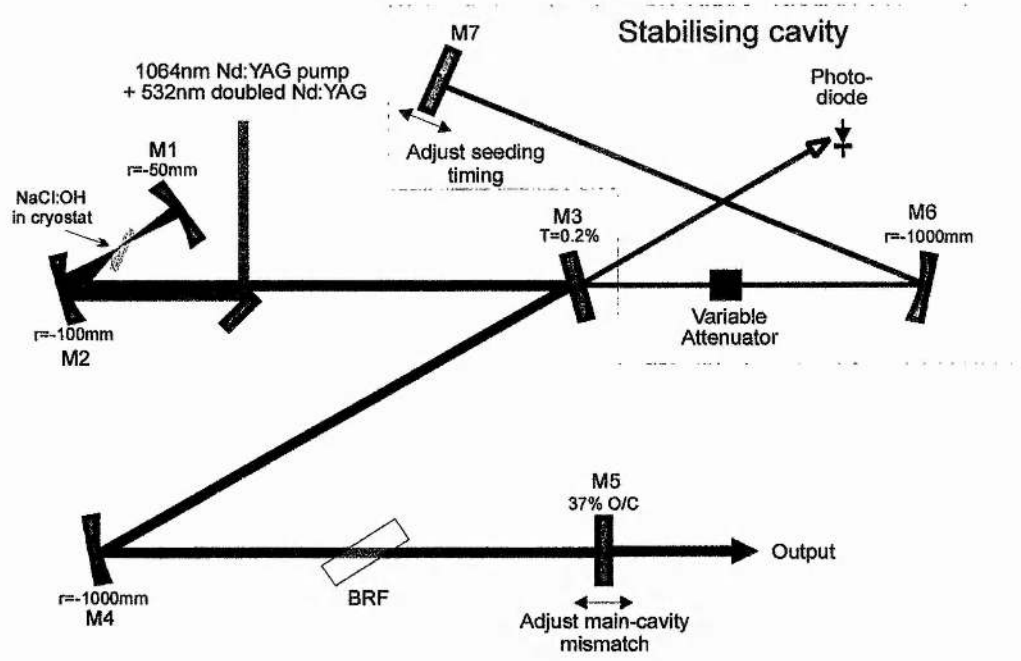

FIGURE 3.9: *Schematic of the NaCl laser showing the external cavity for providing passive stabilisation through coherent-photon-seeding.*

The scheme in figure 3.9 permitted the precise timing of the seeding pulse with respect to the main SPML laser pulse to be determined: mirrors M7-M6-M3 and M5-M4-M3 create a Michelson interferometer where M3 is the beam-splitter. At the position when the length of the stabilising cavity matches that of the remaining main

laser cavity (M3-M4-M5), the interference fringes observed by the photodiode from the second leakage beam are strongest.

For full characterisation of the modelocked performance, a Photochron II synchroscan streak-tube[45] was used as well as a second-harmonic co-linear autocorrelator for pulse duration measurement. A real-time scanning plane-parallel Fabry-Pèrot interferometer with variable plate separation was used to measure the linewidth of the modelocked laser. The drive signal to the streak camera was derived, via a tunnel photodiode, from the actively-modelocked Nd^{3+}:YAG pump laser to permit the movement of the SPML pulse relative to the pump pulse to be determined. An RF spectrum analyser with a 9.5 GHz InGaAs photodiode enabled the RF-amplitude-noise, corresponding to pulse energy noise, to be recorded.

Once the SPML laser was set up as in figure 3.9, and the external cavity aligned to feed back a signal into the main cavity, it was straightforward to gradually shorten the external cavity arm so the seeding pulse was timed to arrive in front of the main cavity pulse. The initial stabilising level was determined to be 4.10^{-6}. Coherent-photon-seeding was observed to have the most dramatic stabilising effect when the main cavity was positively detuned (lengthened) slightly from the position where the shortest pulse was generated.

3.5.1 General observations on applying coherent-photon-seeding

The key observations of passive stabilisation with coherent-photon-seeding are summarised in figures 3.10-13 which are measurements taken from the SPML NaCl:OH^- laser detuned by +40 μm from the optimum modelocking position.

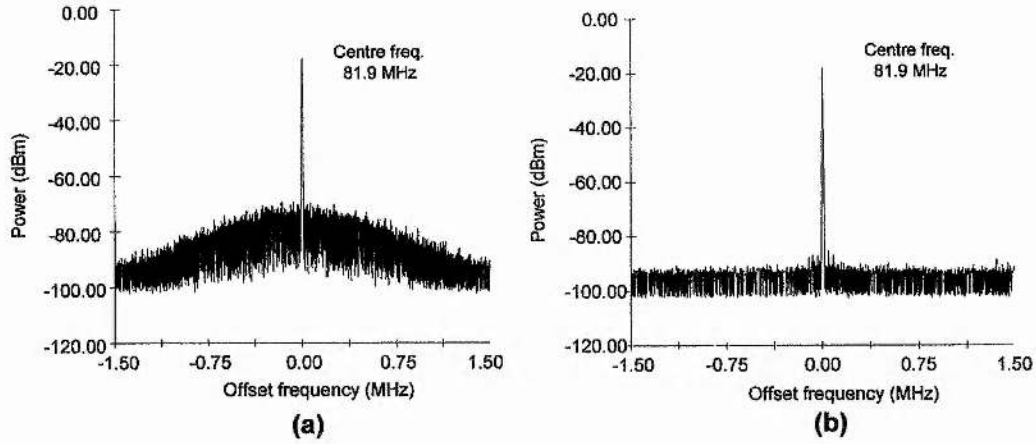

FIGURE 3.10: *Stabilising effect of coherent-photon-seeding on pulse energy:* **(a)** *RF power spectrum taken without CPS.* **(b)** *Spectrum with CPS level at* 4.10^{-6}

The dramatic reduction in pulse energy noise obtained by applying CPS is illustrated in figure 3.10. The RF-spectrum of the conventional free-running SPML laser exhibits a broad noise band when observed at a 3 MHz span around the fundamental cavity frequency (fig. 3.10(a)). This suggests high frequency pulse energy fluctuations. With the length of the external cavity of figure 3.9 set to induce the maximum effect on the synchronous-modelocking by CPS, the noise band is reduced by over 20 dBm indicating a significant improvement in pulse-pulse energy stability.

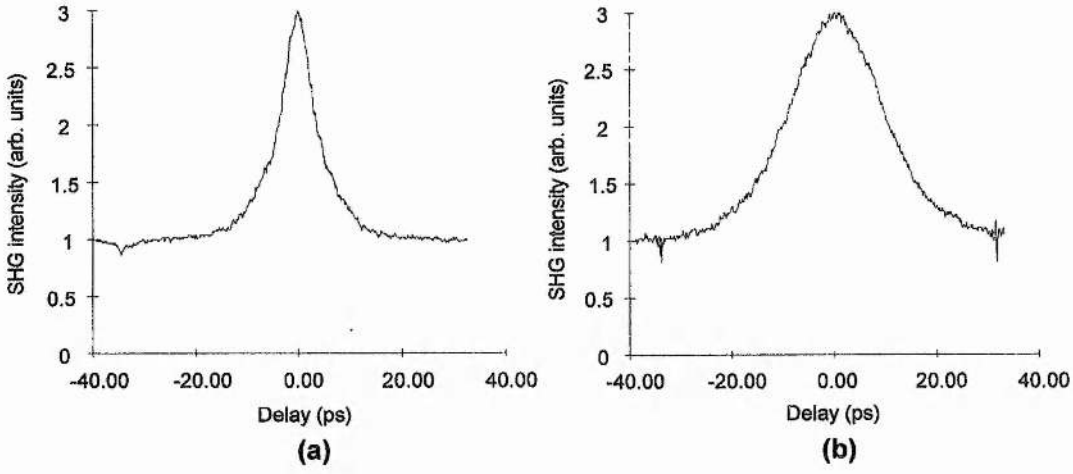

FIGURE 3.11: *Stabilising effect of coherent-photon-seeding observed in the autocorrelation trace:* **(a)** *Typical autocorrelation trace obtained from an unstabilised SPML laser exhibits broad wings.* **(b)** *Trace from stabilised laser (CPS level=4.10^{-6})*

Figure 3.11(a) illustrates the unusual 'cusp shaped' autocorrelation trace with broad wings associated with unstabilised SPML dye and colour-centre lasers. It was suggested that this resulted from fluctuations in the output of the modelocked pulse train on a pulse-pulse timescale[23]. With CPS, the autocorrelation in figure 3.11(b) suggests a much broader pulse (~20 ps cf. ~10 ps without seeding) but the trace no longer exhibits broad wings.

Probably the most dramatic improvement in stability is observed in the optical spectrum of the modelocked laser. An unstabilised slightly-detuned SPML laser generally suffers from incomplete modelocking. The noisy, broad spectrum of figure 3.12(a) suggests that a periodic noise burst would be a better description of a detuned SPML laser, but even when optimally aligned, the pulses obtained from the modelocked laser are not transform-limited. Coherent-photon-seeding causes the oscillating bandwidth to narrow appreciably (figure 3.12(b)) and eliminates the noise features of the unstabilised laser.

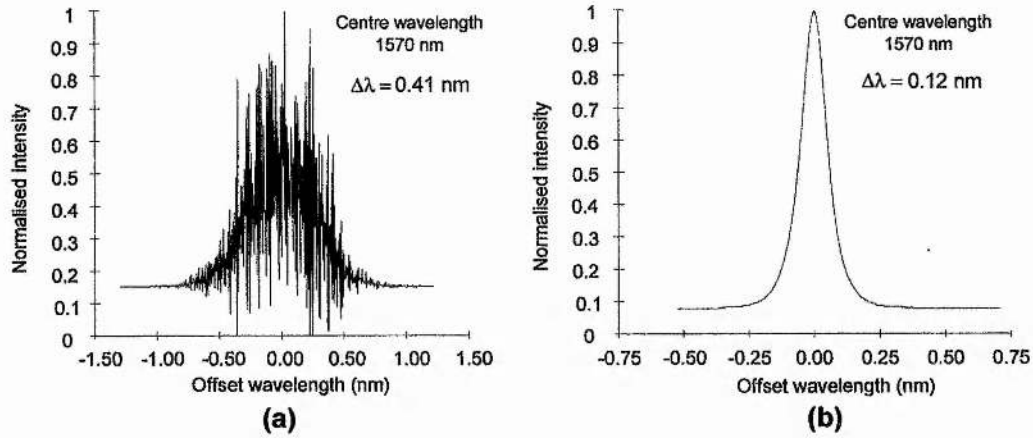

FIGURE 3.12: *Stabilising effect of coherent-photon-seeding observed in the optical spectrum:* **(a)** *Without stabilisation, the spectrum is broad ($\Delta\tau\Delta\nu \sim 0.9$) and noisy.* **(b)** *Trace from stabilised laser (CPS level=4.10^{-6}) is near transform-limited for highly asymmetric sech^2 pulses ($\Delta\tau\Delta\nu \sim 0.22$)*

Finally, the synchroscan-streak-camera records a trace comprising several thousand pulses integrated over one scan of the optical-analyser camera. In figure 3.13, the pulse duration recorded from the stabilised laser (fig. 3.13(b)) is unexpectedly shorter than the free-running unstabilised SPML laser (fig. 3.13(a)). This contradicts the autocorrelation trace measurements from figure 3.11. Also, for a SPML laser of optimum length, the pulse duration measured from the streak trace of the unstabilised laser is slightly shorter than the measurement obtained from the laser with CPS, confirming earlier reported observations[38]. The probable explanation is that when the SPML laser is detuned (as was the case with these measurements), very high frequency noise on the pulse train is of such a magnitude as to cause a 'blurring' of the pulse streak hence recording a longer pulse duration than for the stabilised case.

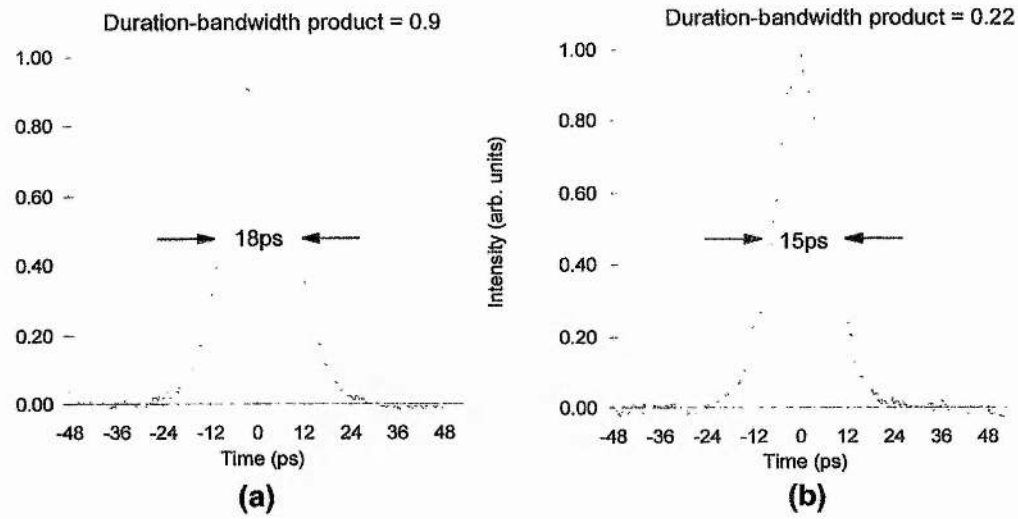

FIGURE 3.13: *Streak camera traces recorded from:* **(a)** *The unstabilised, detuned synchronously-modelocked NaCl:OH⁻ laser.* **(b)** *The same laser after applying seeding at a level of* 4.10^{-6}

3.5.2 Importance of the timing of the seeding pulse

When passive stabilisation of a synchronously-modelocked laser with coherent-photon-seeding was first observed, it was noted that an important requirement was that the seeding pulse be fed somewhat in advance of the main circulating SPML pulse within the cavity. However, the precise relationship on which this timing depended was uncertain. Early on, it was suggested that the seeding pulse should be advanced by twice its duration for optimum effect[46]. Later, with longer pulse SPML lasers, it was proposed that the duration of the pump pulse was the crucial factor in determining the optimum timing for the seeding pulse[40]. This could be explained by considering the timing period over which the destabilising, spontaneous background light is likely to undergo amplification within the gain medium. This depends on the duration of the pumping pulse, not on the duration of the SPML pulse. Hooker et al.[40] reported an investigation into the importance of the feedback pulse lead time by recording the improvement in duration-bandwidth product noted when seeding is operationally. An asymmetric response was reported where the duration-bandwidth product rapidly decreased to a minimum value as the pulse was advanced, then slowly increased again as the pulse timing was advanced beyond the optimum point. Unfortunately, the precise location of the optimum point was difficult to establish because the duration-bandwidth product 'saturated' to a minimum value.

An alternative method of deducing the feedback advance with the greatest effect is to measure the change in the formation of the SPML pulse relative to the pump pulse. This is observed as a jump in pulse position on the streak camera (triggered off the pump pulse) when CPS is applied. This was easy to measure in practice: a 50% duty cycle chopper was placed inside the auxiliary feedback cavity permitting both the unstabilised SPML pulse and the pulse stabilised by CPS to be observed simultaneously on the optical-analyser screen, as illustrated in figure 3.14.

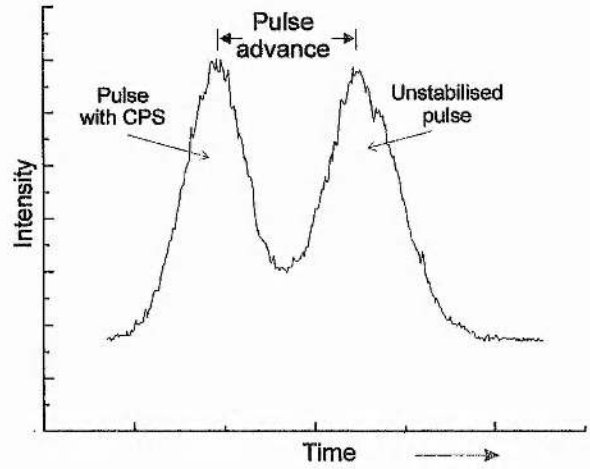

FIGURE 3.14: *Measurement of the SPML pulse advance on applying seeding. 50% chopper inserted in auxiliary cavity.*

The timing of the feedback pulse could be determined by first setting up the auxiliary cavity to form strong interference effects on the photodiode in figure 3.9, which corresponds to a precise overlap of the main SPML pulse and the seeding pulse. By measuring the translation of the feedback mirrors from the actuator scale, it was then straightforward to calculate the timing of the feedback pulse relative to the SPML pulse.

The leakage through the intracavity mirror providing the seeding (M3 in figure 3.9), was determined (by comparison with a known output coupler) to correspond to 0.2% of the circulating power. Thus the maximum seeding level was 4×10^{-6} of the intracavity power. To reduce the seeding level, neutral-density filters were inserted in the auxiliary cavity. Using a linear response photodiode, the exact attenuation level afforded by the filters (uncalibrated in the infrared) was ascertained.

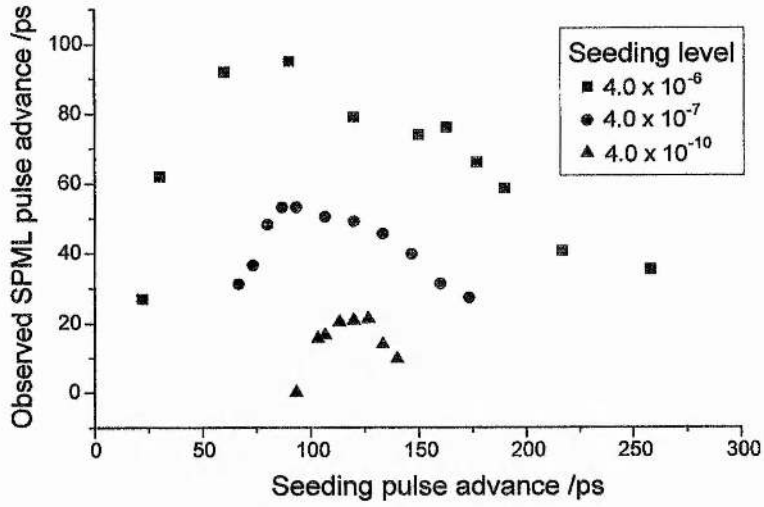

FIGURE 3.15: *Effect of varying the seeding pulse timing and seeding level on the time of formation of the SPML pulse.*

The effect of varying the advance of the CPS pulse for three different seeding levels is summarised by the graph in figure 3.15. The Nd^{3+}:YAG pump pulse duration was 90 ps, which accounts for the location of the peaks, corresponding to the seeding advance when CPS has the greatest effect on SPML dynamics. The peak appears to shift to favour a greater feedback pulse advance for lower seeding levels.

The stabilising effect could still be observed by the improvement in pulse energy noise (via the RF spectrum analyser trace) and the cleaner optical spectrum, for seeding advances outwith those plotted on figure 3.15, and for seeding levels as low as $4x10^{-12}$. However, at levels as low as this, no shift in pulse formation is discernible on the streak camera. Interestingly, for a typical intracavity power of 1.0 W, a feedback level of $4x10^{-12}$ implies feeding back 0.4 photons per round trip. This indicates the low level of stochastic background light which normally disrupts the modelocking process.

3.5.3 Main cavity length detuning

An important factor which affects the operation of all synchronously-modelocked lasers is the effective mismatch between the modelocked pump laser and the SPML slave laser. As demonstrated by numerical modelling (figure 3.6), a slight positive mismatch (i.e. the round trip time of the slave laser is longer than the round-trip time of

the pump laser) is necessary for short pulse generation. If the two cavities were of identical length, the SPML pulse would be similar in duration to the pump pulse.

Several researchers have investigated experimentally, the effect of detuning SPML dye lasers and some colour-centre lasers[47]. An asymmetric response was noted when lengthening the slave cavity, which followed the same features as figure 3.6 –that is- the broad pulse quickly breaks up into a short pulse with several satellite pulses, then the pulse gradually broadens as the cavity is detuned further.

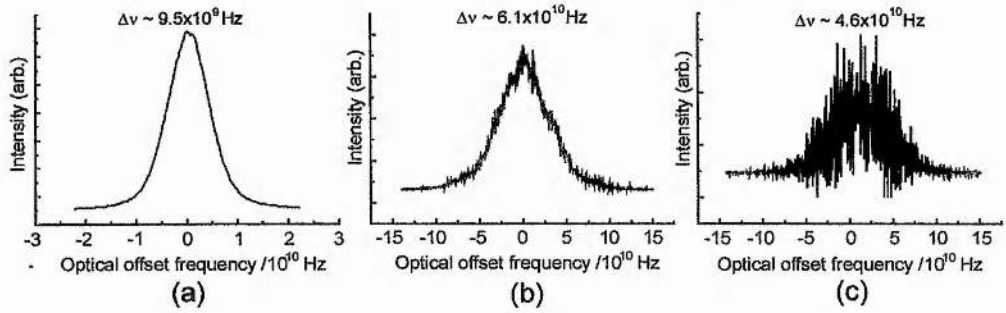

FIGURE 3.16: *Effect of detuning the SPML cavity length on the optical spectrum of an unstabilised laser:* **(a)** *No mismatch between pump and slave lasers results in a clean spectrum with broad, near transform-limited ($\Delta\nu\Delta\tau$~0.4) Gaussian pulses.* **(b)** *Round trip cavity lengthened by 60 μm creates short asymmetric pulses with excess bandwidth ($\Delta\nu\Delta\tau$~0.46)* **(c)** *Further lengthening (by 20 μm) creates broader pulses ($\Delta\nu\Delta\tau$~0.47) with noise evident on the optical spectrum.*

As noted by modelling, the stability of the pulse sequence from the SPML laser deteriorates as the slave cavity is increased in length[46]. This is evidenced in practice by an increase in the duration-bandwidth product of the SPML pulses. In figure 3.16, the optical spectrum of a free-running, unstabilised SPML laser is illustrated as the slave-cavity length is extended from the point where the slave and pump lasers are of equal length (when the pulse is broad ($\Delta\tau \sim 45$ ps) and near-transform limited). As the slave-cavity laser is lengthened, more stochastic background light must infiltrate into the circulating pulse per round trip for the slave- and pump-laser repetition rates to match with the result that the modelocked pulse sequence becomes noisier.

Detuning the SPML slave-laser offers the potential of 'tuning' the pulse duration, from the minimum obtainable (<10 ps), to a duration approaching that of the pump pulse. With the unstabilised laser, the incomplete modelocking typical of a detuned laser produces a pulse sequence suffering from excessive high frequency amplitude and phase-noise which prevents it from finding any practical application. However, once seeding is applied and the destabilising effect of the stochastic

background fluorescence is eliminated, a more useful system is created allowing the SPML pulse duration to be readily adjusted whilst maintaining near transform-limited operation as illustrated in figure 3.17. The low values obtained for the duration-bandwidth products in figure 3.17 (b) once seeding is applied provide further evidence of the highly asymmetric nature of the modelocked pulses, although this is not noticeable on the streak trace in figure 3.13. The pulse durations were taken from the streak camera so no assumption is made in advance of the pulse-shape.

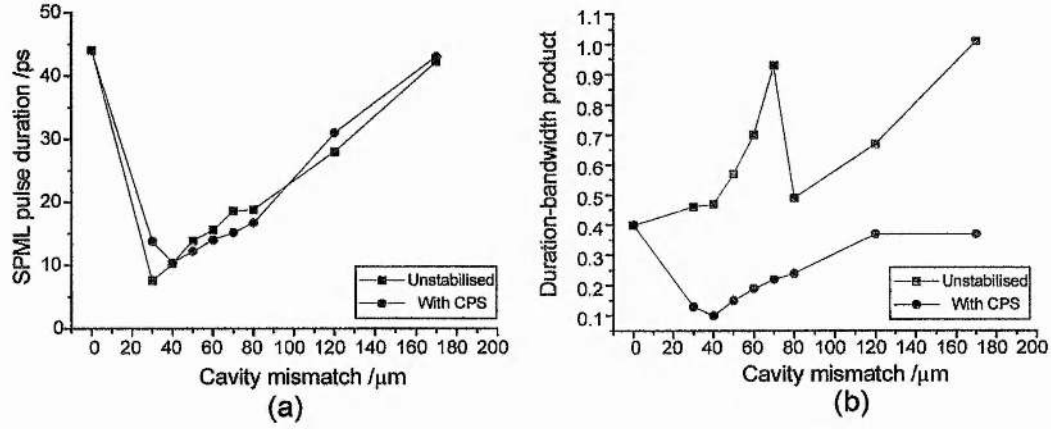

FIGURE 3.17: *Detuning the main cavity of a SPML NaCl colour-centre laser both without seeding and with CPS applied at a level of $4x10^{-6}$* **(a)** *Tuning of the pulse duration by increasing the length of the SPML laser* **(b)** *duration-bandwidth product as the SPML cavity is detuned.*

A second result of increasing the mismatch between the pump and slave lasers as suggested by numerical modelling, is to increase the advance in time of formation of the SPML pulse when CPS is applied to the laser. Figure 3.18 shows the measured jump observed on the streak camera, following the procedure outlined in section 3.5.2 with a seeding level of $4x10^{-6}$, as the main cavity is lengthened from a broad pulse. This suggests that at this seeding level, the CPS pulse fed-back into the laser is of substantially greater power than the background light level, as the effect on modelocking dynamics is so pronounced.

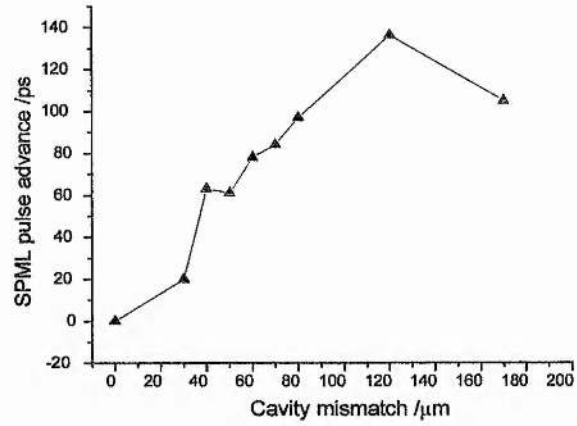

FIGURE 3.18: *Effect of increasing cavity mismatch on the observed SPML pulse advance on applying coherent-photon-seeding*

This ability to tune the modelocked pulse duration was exploited by Kennedy et al. in an experiment which measured the intensity dependence of the transparency current of InGaAsP amplifiers[48]. It was desired to keep the average power into the waveguide constant whilst varying the peak power, and detuning a passively stabilised NaCl:OH^- colour-centre laser permitted this.

3.5.4 High frequency pulse jitter reduction by coherent-photon-seeding.

Whereas the reduction in pulse energy noise and modelocked pulse quality on applying CPS to a synchronously modelocked laser is immediately apparent from the RF and optical spectrum analyser traces, it is suggested by numerical modelling (in figure 3.8) that the stochastic background light also contributes to severe pulse jitter (phase-noise) at high frequencies.

Characterisation of the phase-noise of a modelocked laser

In an ideal modelocked laser system, the output pulse sequence would consist of pulses of identical energy and shape. Additionally, the temporal separation of two consecutive pulses would be fixed at the laser repetition frequency. Unfortunately, real systems depart from this ideal in several respects.

For the particular case of an unstabilised synchronously-modelocked colour-centre laser, noise arises from both external environmental and electronic perturbations, as well as intrinsically from the SPML process. The severe high frequency pulse energy noise associated with SPML lasers, observed in the RF spectra, is primarily due to the

stochastic background noise. Measurements performed on SPML lasers to characterise the pulse timing jitter have previously concentrated on the lower frequency components resulting from noise transferred from the actively modelocked pump laser, which in turn is mainly caused by the noise of the acousto-optic modulator drive electronics. Any high frequency components are usually discarded in the measurement. To confirm the presence of the high frequency pulse jitter predicted by the 'stepping-model' in figures 3.7 & 3.8, a phase-noise measurement was carried out on the SPML NaCl:OH^- laser concentrating on the high frequency components.

A technique for the characterisation of the pulse jitter associated with a modelocked laser was described by von der Linde[49], based on an analysis of the RF power spectra of the modelocked pulse sequence. A brief description of this method follows but for greater detail refer to reference 49.

First, the pulse sequence obtained from a real laser may be described as:

$$F(t) = F_0(t) + F_0(t) \cdot A(t) + \frac{dF_0(t)}{dt} TJ(t) \qquad \text{Equation (3.16)}$$

$F_0(t)$ refers to an ideal, noise-free modelocked laser sequence:

$$F_0(t) = \sum_n f(t + nT) \qquad \text{Equation (3.17)}$$

where **f(t)** describes the temporal intensity profile of an individual pulse in the train, **T** is the pulse repetition time and **n** is an integer describing the infinite pulse sequence: $-\infty < n < +\infty$.

A(t) describes the random amplitude fluctuations of the pulse sequence

J(t) is a random function describing the relative deviation from the average pulse repetition time **T**.

The RF power spectrum of the modelocked pulse sequence is represented by the Fourier transform of the intensity autocorrelation function:

$$P_f(\omega) = \left(\frac{2\pi}{T}\right) \cdot \left|\tilde{f}(\omega)\right|^2 \cdot \sum_n \left[\delta(\omega_n) + P_A(\omega_n) + (2\pi)^2 n^2 P_J(\omega_n)\right] \qquad \text{Equation (3.18)}$$

The three terms in the infinite summation are:

$\delta(\omega_n)$: delta functions separated by the pulse repetition frequency, representing the n^{th} harmonic of the laser repetition rate for a noise-free ideal modelocked laser.

$P_A(\omega_n)$: function representing the spectral density of the amplitude-noise sidebands.

$P_J(\omega_n)$: function representing the spectral density of the phase-noise sidebands.

From equation 3.18, it is important to note that the amplitude-noise spectral density ($P_A(\omega)$) remains unchanged with harmonic number n whereas the phase-noise term is scaled by a factor n^2. This is illustrated (exaggerated) in figure 3.19.

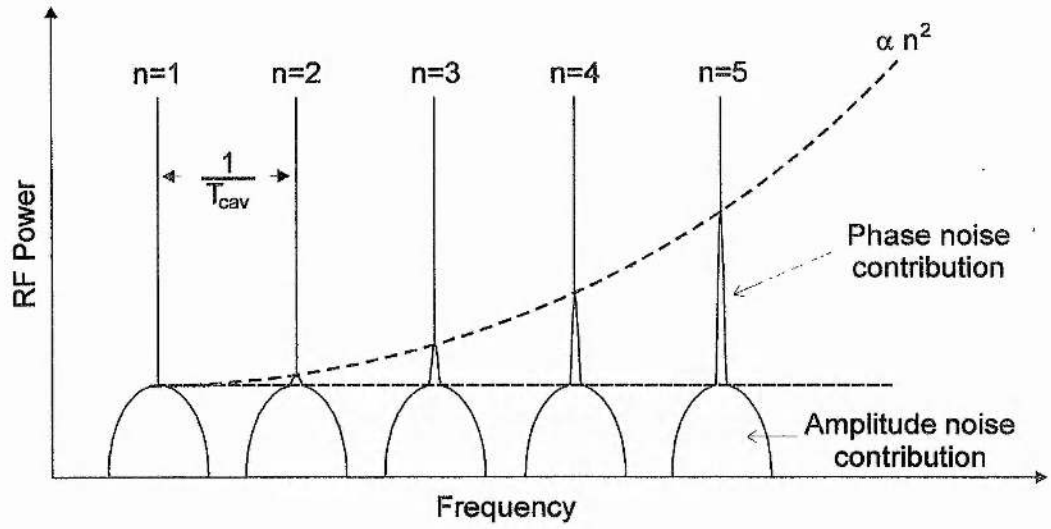

FIGURE 3.19: *Representation of the RF power spectrum of a noisy modelocked laser illustrating the different dependence of phase and amplitude-noise with harmonic number.*

From figure 3.19 it should be apparent that the different contributions of amplitude-noise and phase-noise of a noisy modelocked pulse sequence can be determined by measuring the noise sidebands for the fundamental laser repetition rate and a higher harmonic.

A phase-noise measurement normally involves the following steps:

1. A broadband (reverse-biased) photodiode, connected to an RF spectrum analyser is used to detect the power spectra of the modelocked pulse sequence.

2. The RF power spectra of the modelocked laser is recorded at the fundamental pulse repetition frequency for different frequency span and resolution bandwidth settings of the RF-spectrum analyser. This measurement is then repeated at a higher n^{th} harmonic of the pulse repetition frequency.

3. Using the $\mathbf{n^2}$ dependence of phase-noise (figure 3.19), the amplitude and phase-noise components are separated and the single-sideband phase-noise power spectrum ($\mathbf{L_J(f)}$) is plotted. This is the ratio of the power in the noise sideband within a 1Hz bandwidth to the power in the carrier (units of dBc/Hz) plotted on a log-log scale.

4. Within any particular frequency band, the rms timing jitter may be evaluated by integrating the single sideband noise spectrum over the interval of interest:

$$\sigma_J(f_1, f_2) = \frac{1}{2\pi f_0} \cdot \sqrt{2 \cdot \int_{f_1}^{f_2} 10^{\frac{L_J(f)}{10}} \cdot df} \qquad \text{Equation (3.19)}$$

In practice, steps 2-4 were performed automatically using an IBM-compatible PC with in-house developed software.

Phase-noise measurement of a SPML NaCl:OH^- laser

Previous phase-noise measurements performed on a SPML NaCl:OH^- laser have concentrated on the low frequency components, dominated by the noise components of the modelocked pump laser. Since the low-frequency amplitude-noise is low compared with the phase noise, it is elementary to isolate the phase noise component from a low harmonic of the pulse repetition frequency in step 3 above (usually the 10^{th} harmonic is used). For investigating the high frequency jitter (~1-10 MHz) expected as a result of a detuned, unstabilised SPML laser, it was necessary to resort to using a high harmonic number **n** since the amplitude-noise level is the dominant component in the noise sidebands. An InGaAs photodiode with a bandwidth of 9.5 GHz permitted the 56^{th} harmonic of the 82 MHz fundamental repetition rate to be measured.

The standard Spectra-Physics frequency synthesiser driving the AO-modulator of the pump laser, was replaced by a low-noise crystal oscillator. This helped to reduce the noise component of the final measurement that replicated the noise of the pump laser.

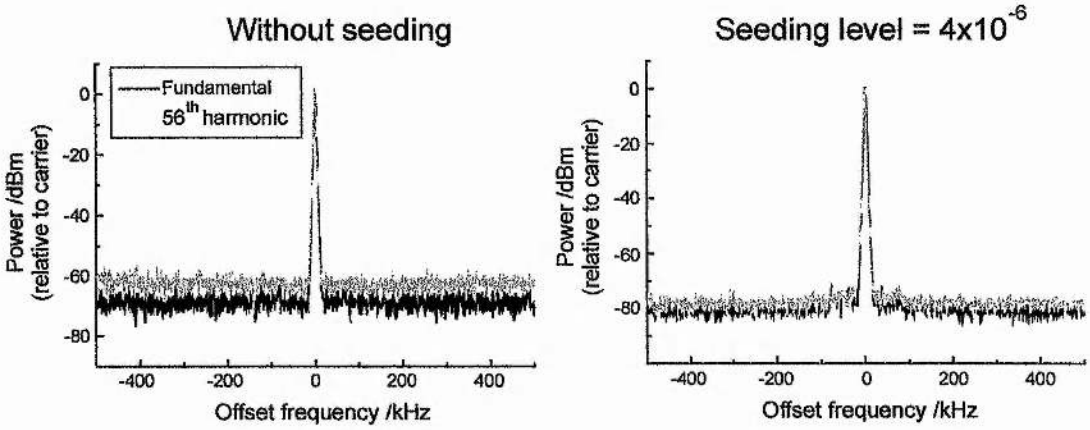

FIGURE 3.20: *RF spectra of the SPML NaCl:OH laser: 1 MHz span, resolution bandwidth=3 kHz at the fundamental and 56th harmonics of the pulse repetition frequency, showing the reduction of the phase-noise contribution on applying coherent-photon-seeding.*

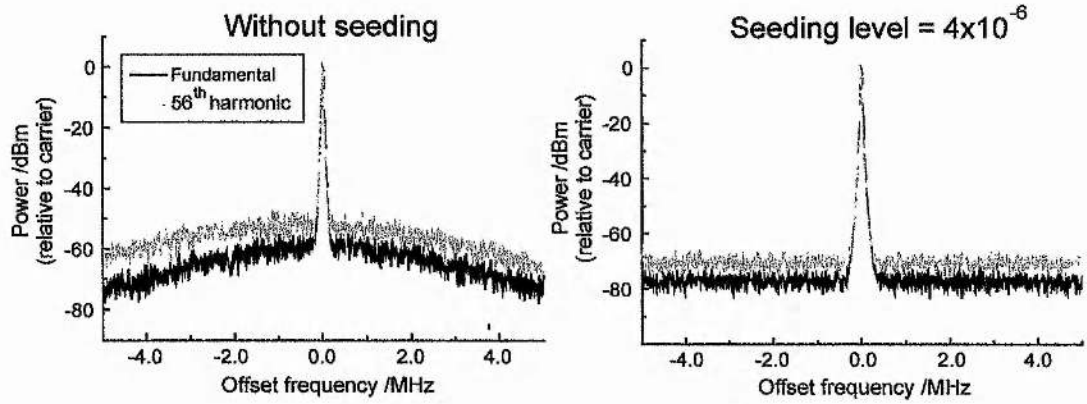

FIGURE 3.21: *RF spectra of the SPML NaCl:OH laser: 10 MHz span, resolution bandwidth=30 kHz at the fundamental and 56th harmonics of the pulse repetition frequency. CPS appears to have little effect on reducing the phase-noise*

Figures 3.20 and 3.21 are RF spectrum analyser traces at 1 MHz and 10 MHz spans respectively around the carrier frequency. Both the fundamental and 56th harmonics of the pulse repetition rate are plotted. For the 1 MHz span (figure 3.20), the 56th harmonic sideband power is ~10 dB higher than for the fundamental frequency before stabilisation, suggesting the presence of pulse jitter within this frequency band. On applying CPS, both the fundamental and 56th harmonics have sidebands of approximately equal power indicating that the high frequency phase-noise has been eliminated. In contrast, for the 10 MHz span (figure 3.21), even after applying seeding, there is still additional sideband noise in the 56th harmonic above the fundamental frequency. This appears to suggest an upper limit to the frequency of the pulse jitter

introduced in SPML lasers by the stochastic modelocking dynamics. Further evidence of this is obtained from the single-sideband phase-noise spectra for the laser both with and without CPS in figure 3.22 calculated following the outline in step 3 in section 3.5.4.1.

In figure 3.22, the phase noise is shown to be unchanged at frequencies less than 10 kHz on applying coherent-photon-seeding. However, above this frequency, an almost constant improvement of ~10 dB is suggested before falling off again at frequencies higher than 4 MHz. At this upper frequency level, the measurement is certainly limited by the noise floor dictated by the equipment.

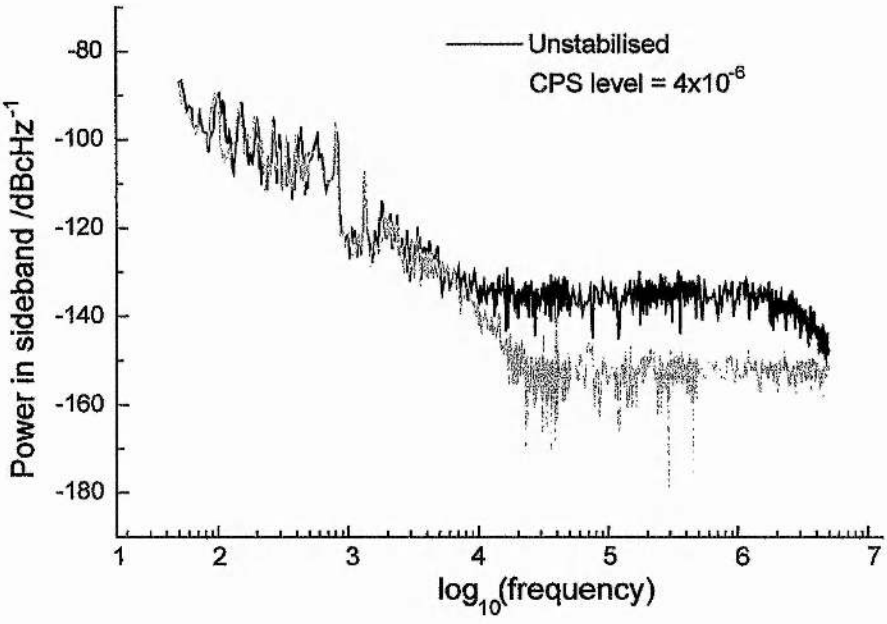

FIGURE 3.22: *Single-sideband phase-noise spectra obtained from a SPML NaCl:OH laser with and without seeding.*

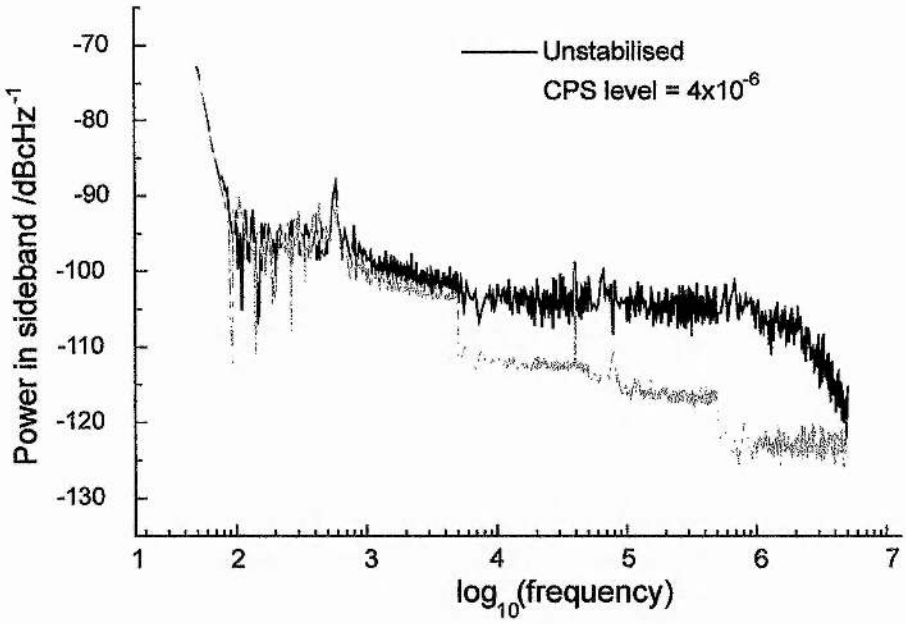

FIGURE 3.23: *Amplitude-noise spectra of the SPML NaCl:OH laser with and without seeding.*

The amplitude noise spectrum may also be deduced, once the phase noise component has been removed. This is plotted in figure 3.23 both for the free-running case and, for the laser once CPS has been applied. The sharp transitions in the spectrum for the seeded laser indicate the RF-analyser changing ranges during the measurement: the noise level of the stabilised laser is below the noise floor of the equipment at frequencies greater than 4 kHz. At frequencies greater than 2 MHz the amplitude-noise of the unstabilised laser drops off suggesting an upper limit to the frequency of the pulse instability.

The numerical values for the rms timing jitter corresponding to figure 3.22 are summarised in table 3.2. This clearly shows a notable reduction in pulse jitter for frequencies above 5 kHz. Note that the values corresponding to the stabilised laser represent an upper limit to the pulse jitter as they are limited by the noise floor of the apparatus.

It is important to remark that although a reduction in pulse jitter does appear possible by employing CPS, the overall phase-noise is dominated by pulse jitter at lower frequencies. The contribution by the stochastic modelocking dynamics is negligible in comparison, hence any experiment requiring a laser with low phase-noise would desire the low-frequency noise sources (electronic modulator signal and environmental perturbations) to be refined.

Frequency band	rms jitter level without seeding /fs	rms jitter level CPS level=4×10^{-6} /fs
50 Hz – 500 Hz	690	610
500 Hz – 5 kHz	400	350
5 kHz – 50 kHz	105	50
50 kHz – 500 kHz	320	36
500 kHz-5 MHz	600	110

TABLE 3.2: *rms timing jitter figures for the SPML laser both without and with CPS*

3.6 Numerical Modelling of Coherent-Photon-Seeding

3.6.1 Adapting the stepping-model to include CPS

It is straightforward to adapt the models of ring and linear synchronously-modelocked lasers in section 3.3 to include the effect of including coherent-photon-seeding, first described by New[46]. A small fraction of the circulating signal from the model is added back to the circulating signal, after including the mismatch between the main and seeding cavities. In the case of the linear cavity model (figure 3.3), the seeding signal was taken after the second pass of the gain element, to be fed back to the laser for the next round trip (corresponding more accurately to the actual laser in figure 3.9).

$$V_{i,n}^{(0)} = V_{i,n}^{(0)} + f \cdot V_{i+s,n-1}^{(2)} \qquad \text{Equation (3.20)}$$

The subscript **s** refers to the actual seeding pulse advance defined by the mismatch of the auxiliary cavity with respect to the main laser cavity ($t_{seeding\text{-}advance}=s.\delta t$). This is similar to the main cavity mismatch expression in equation 3.10, for negative cavity mismatches, requiring the last calculated field value to be duplicated to 'fill in' the missing values on the mesh.

The seeding level in the model is simulated by the factor **f** in equation 3.20. Note that this is the field amplitude seeding factor which needs to be squared to obtain the corresponding seeding intensity.

A simple simulation of a free-running SPML NaCl:OH^- laser which has seeding applied after 1000 cavity round trips, is presented in figure 3.24. Initially, a quasi-stable situation is obtained with the destabilising effect of the stochastic background radiation included. The SPML pulse is recorded every 10 cavity trips. After the 1000^{th} round trip, the simulation includes the stabilising CPS pulse modelled by equation 3.20. The intensity seeding level is $4x10^{-6}$ and the seeding pulse advance is 100 ps. The modelocked pulse is shown to 'advance' in time with respect to the pump pulse and become broader. The high frequency noise, characteristic of a free running SPML laser and visible as jitter and amplitude noise in the pulse sequence of figure 3.24 before the 1000^{th} round trip, is predicted to be eliminated completely on applying CPS.

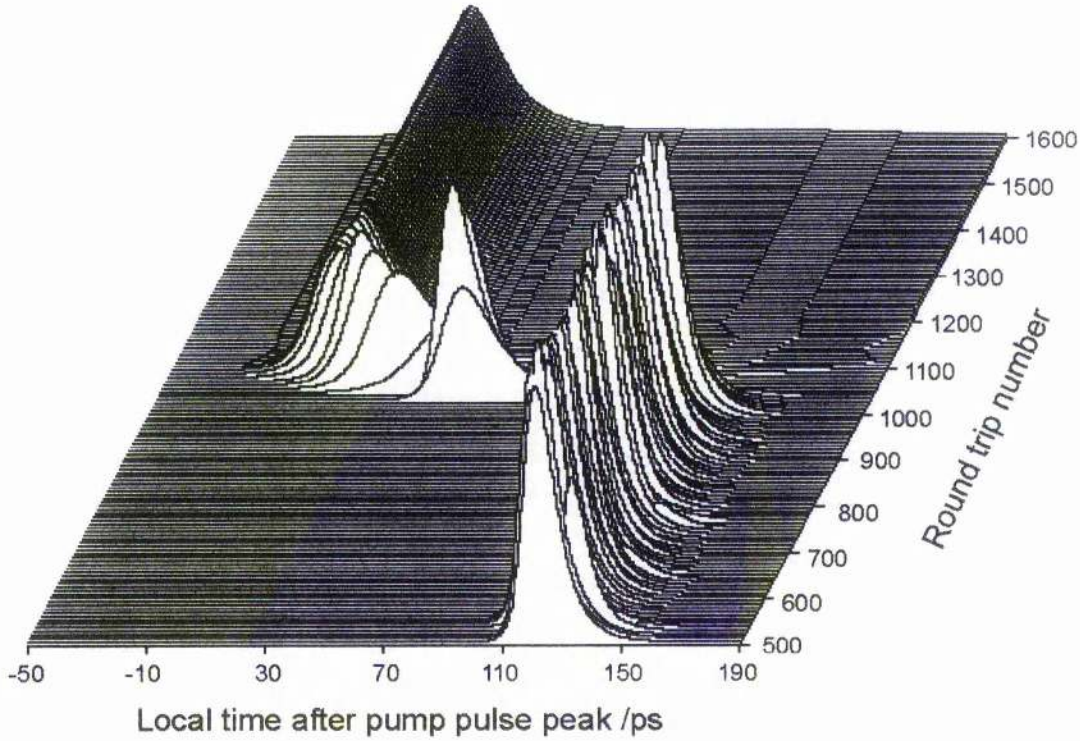

FIGURE 3.24: *Simulation of coherent-photon-seeding applied to a SPML laser. Seeding applied after 1000 round trips. Pulse recorded every 10 round trips.*

Figure 3.24 only records every 10^{th} output pulse from the modelled laser. To demonstrate the deleterious effect of the spontaneous background light on pulse-pulse stability, the pulse evolution over every round trip between trips 500 and 680 in figure 3.24 is plotted in figure 3.25. The pulse sequence is shown to be generally smooth with a disturbance occurring once every 15-20 round trips. This would give an

upper limit to the frequency of the amplitude and phase noise found experimentally to be ~4 MHz (figures 3.22 & 3.23).

In figure 3.26, the results of the model are reproduced on a pulse-pulse timescale for simulated cavity round-trips 1000 to 1180 in figure 3.24 (i.e. once CPS has been applied). The model suggests there is a delay of ~20 round trips before CPS starts to take effect. The stable steady state is reached after ~150 round trips.

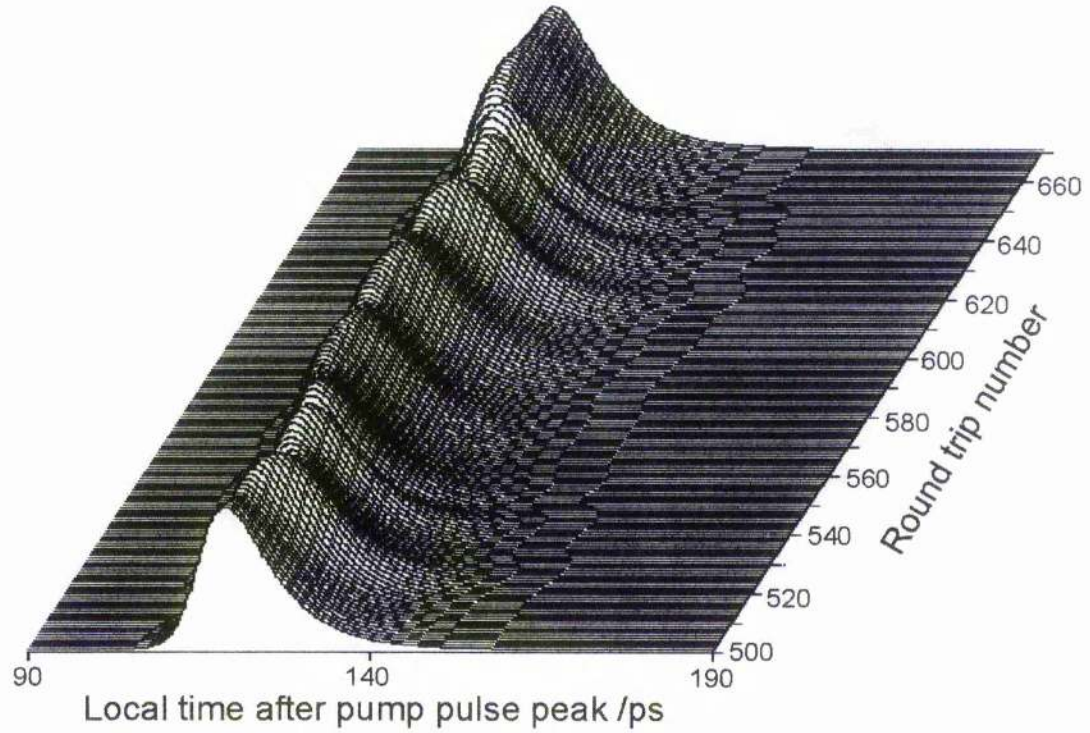

FIGURE 3.25: *Simulated SPML pulse sequence in the presence of stochastic background noise on a timescale corresponding to the laser repetition rate.*

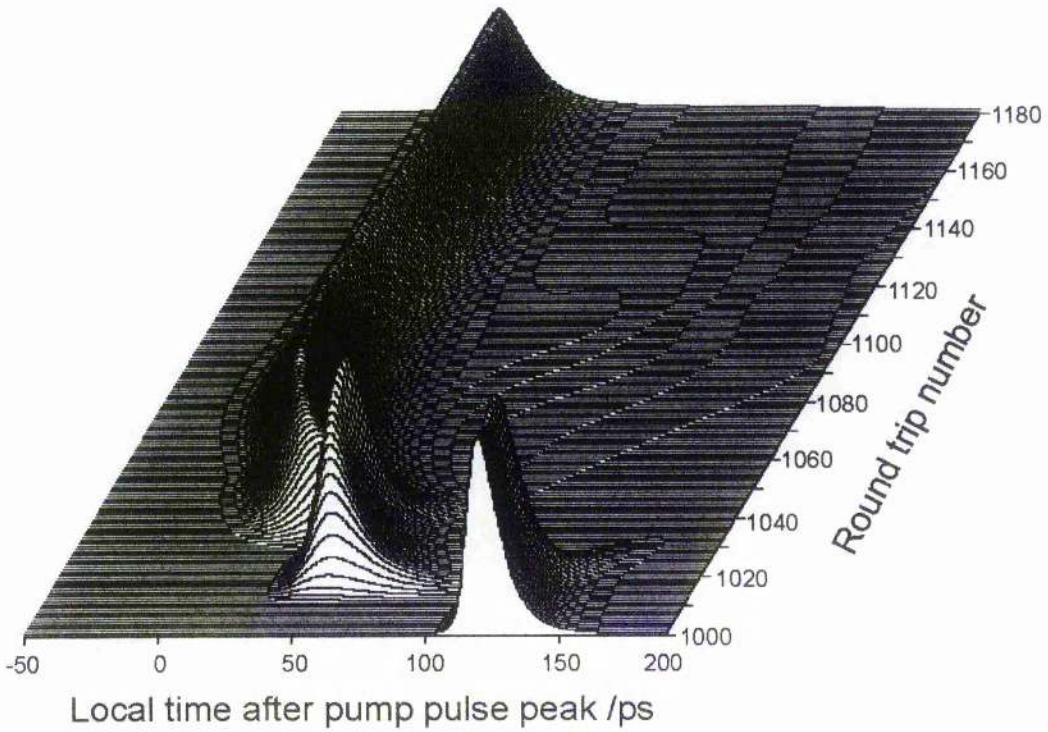

FIGURE 3.26: *SPML pulse evolution into a steady state on applying CPS recorded on a timescale corresponding to the laser repetition rate.*

Second-harmonic autocorrelations of the pulse sequences obtained from the numerically simulated SPML laser without and with coherent-photon-seeding are presented as figure 3.27. The pulses are highly asymmetric both with and without CPS, but the noisy pulse train of the unstabilised laser gives rise to a 'cusp-shaped' autocorrelation with broad wings, as predicted by Van Stryland[23]. (The trace for the unstabilised laser is not smooth due to the small number (300) of round trips used in the simulation. In an actual measurement, this 'lumpiness' is smoothed out over many autocorrelation scans.) The duration measured from the unstabilised autocorrelation trace suggests a pulse duration of ~16 ps (assuming a Gaussian pulse-shape), however the average pulse duration is actually greater than 17 ps. Conversely, once passive stabilisation with CPS is applied and assuming a Gaussian pulse-shape, the autocorrelation measurement suggests a somewhat longer pulse duration than was actually simulated (21.4 ps cf. 19.5 ps). These simulated results suggest that there is quite a wide margin of error in measuring the pulse duration of SPML lasers using a second-harmonic autocorrelation technique.

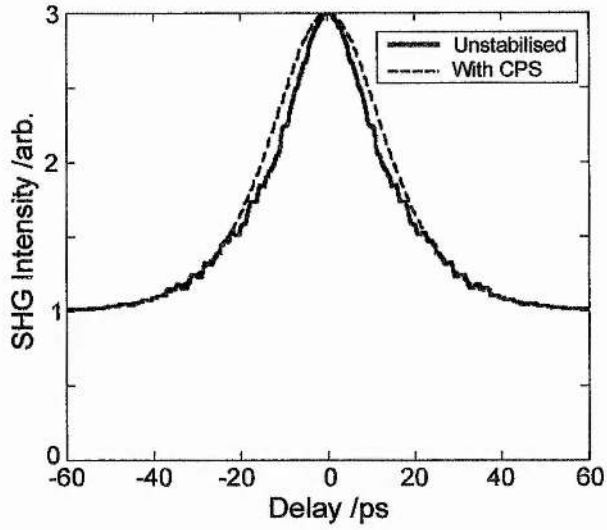

FIGURE 3.27: *Autocorrelation traces of the simulated 'noisy' SPML laser, and for the stabilised laser once seeding is applied.*

3.6.2 Modelling the effect of adjusting CPS timing on pulse stability

The stepping-model may be used to model the effect of varying the seeding level and seeding pulse timing for comparison with the experimental results presented in section 3.5.2. The model was modified to allow the seeding pulse timing to be automatically advanced by 15 ps every 1000 simulated cavity round trips and was repeated for different seeding levels. As for the practical assessment of the stabilising effect used in section 3.5.2, the timing of the stabilised main pulse with respect to the unseeded pulse was compared on applying CPS. The results of this simulation are summarised in figure 3.28, which plots the timing of the SPML pulse every 1000^{th} round trip (i.e. before the seeding pulse timing is adjusted).

A comparison of this simulation with the experimental results of figure 3.15 demonstrate similar trends. The simulated pump pulse duration at 90 ps FWHM, accurately represents the measured pump pulse duration in section 3.5.2. The seeding is shown to have greatest effect when the seeding pulse advance is approximately the pump pulse duration. As in practice, the model suggests that the optimum seeding pulse advance is increased for lower seeding levels although the reason for this is uncertain.

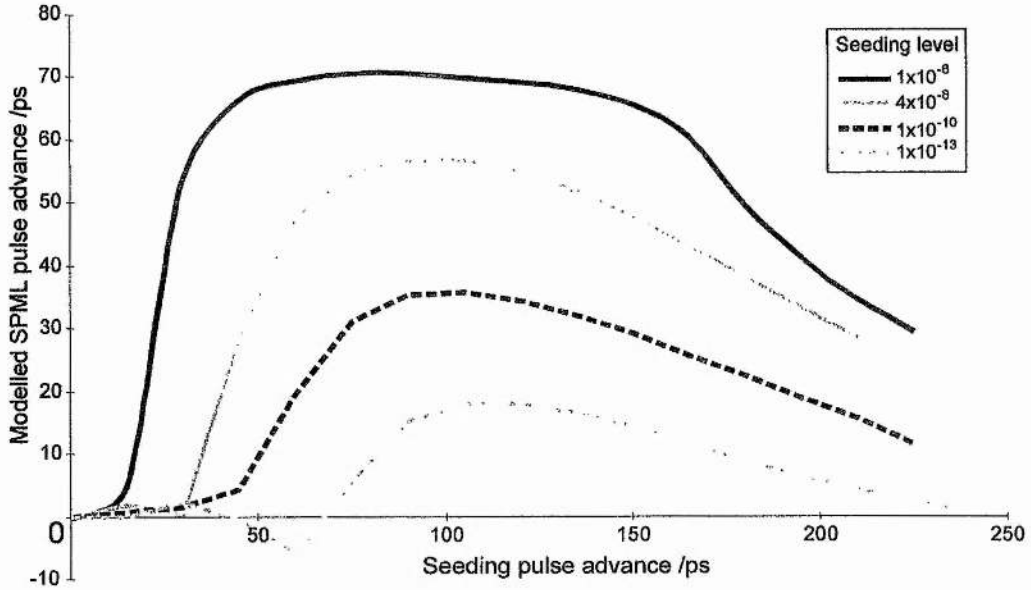

FIGURE 3.28: *Effect of varying the seeding pulse timing and seeding level on the time of formation of the simulated SPML pulse.*

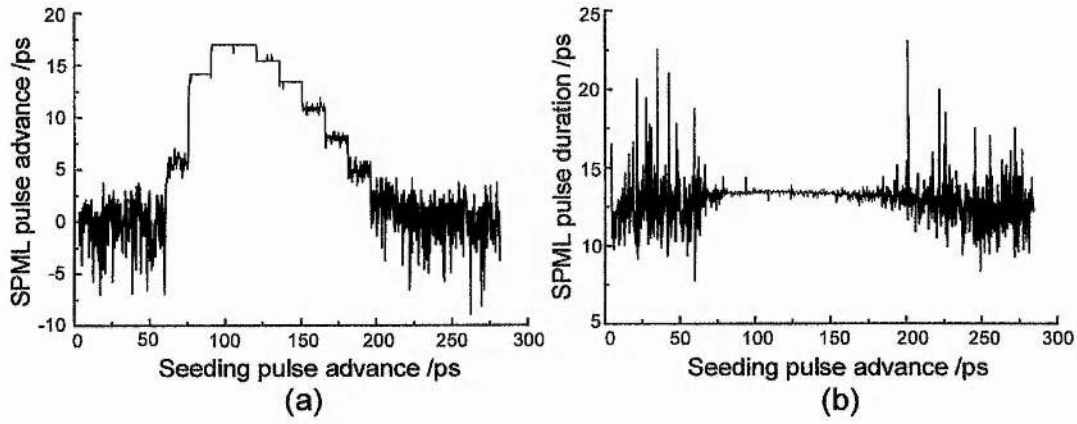

FIGURE 3.29: *Numerical simulation showing variation of the stabilising effect of CPS with timing of the seeding pulse for very low seeding levels. (Intensity seeding level ~10^{-13})*

In figure 3.29, the SPML pulse timing and duration for the lowest seeding level of figure 3.27 (10^{-13}) are plotted for every 10 round trips of the simulation. This clearly shows the simulated stabilising effect of CPS having greatest effect when the pulse advance is ~110 ps. The plot of pulse duration vs. seeding pulse advance (figure 3.29(b)) demonstrates that it is possible, with low seeding levels, to obtain stabilisation with a negligible increase in pulse duration. Note that in practice, the small SPML pulse advances modelled in figure 3.29(a) could not be measured on the streak camera (for inclusion in figure 3.15).

3.6.3 The stabilisation mechanism explained using the stepping-model.

The stepping-model may be used to elucidate the mechanism by which coherent-photon-seeding 'overpowers' the destabilising effect of the stochastic background fluorescence to enable stable modelocked pulses to be obtained. Figure 3.30(a) shows a typical SPML pulse obtained from the simulation without any seeding. A clearer picture of the modelocking mechanism is obtained by taking the log of the intracavity intensity (figure 3.30(b)). The random background fluorescence is now clearly visible on the pulse leading edge, sixteen orders of magnitude below the pulse peak power. Due to the positive mismatch which exists between the pump and slave lasers, the background light migrates into the leading edge of the pulse on successive cavity round trips, clearly visible in figure 3.30(b). The threshold condition of the SPML laser, which dictates the time of the laser pulse on successive cavity round trips, depends on the amplified stochastic background light which has migrated into the leading edge on previous round trips.

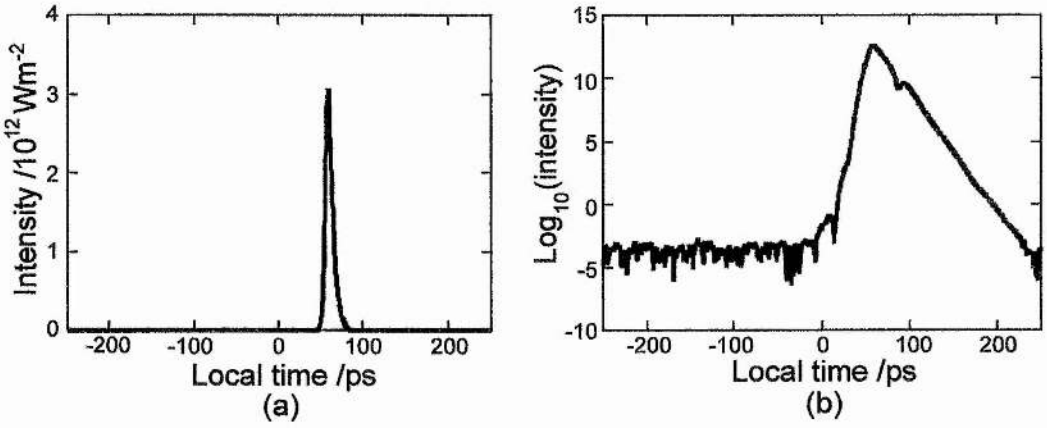

FIGURE 3.30: *Simulated SPML pulse without seeding*

When CPS is applied at the optimum timing with respect to the main cavity pulse, the situation presented in figure 3.31 results. Again, it is necessary to look at the log of the intensity (figure 3.31(b)) to understand the effect of CPS. The more intense CPS pulse overpowers the much weaker stochastic background light to migrate into the leading pulse edge for amplification.

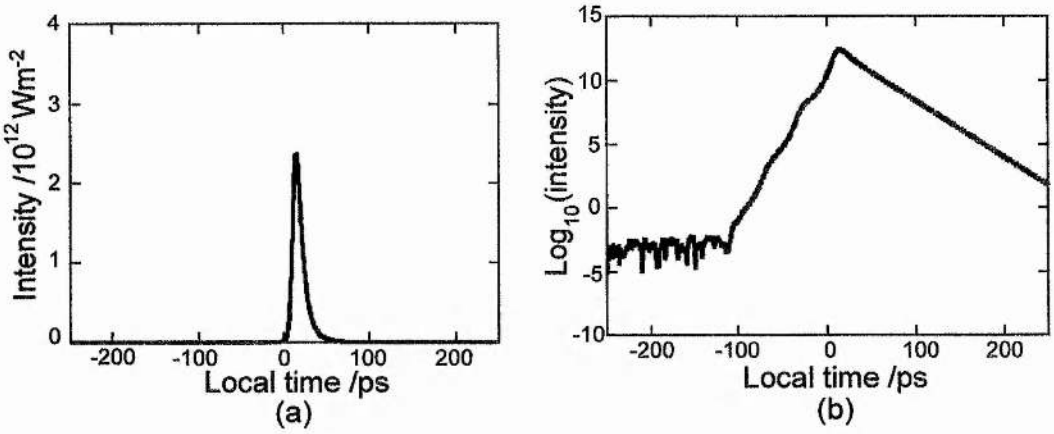

FIGURE 3.31: *Simulated SPML pulse with seeding applied at the optimum timing (~90 ps in front of the main pulse).*

The asymmetric response of the seeding-pulse timing measurements in figures 3.15 & 3.28 may be understood if the logarithm of the intensity is examined for the case of a SPML laser seeded far in advance of the optimum timing position (figure 3.32(b)). If the CPS is applied insufficiently in advance of the main pulse, only the leading edge of the pulse may contribute to the stabilisation. In addition, on subsequent round trips, when the seeding pulse of previous round trips is in-effect re-injected into the main cavity, the small advance results in insufficient intensity to overpower the background light on the main pulse leading edge.

For the case of CPS applied far in advance of the optimum timing position (shown in figure 3.32), the coherent seeding-pulse structure on the leading edge of the pulse builds up on consecutive round trips (after attenuation by the seeding level). This is evident on the logarithmic plot in figure 3.32(b) which shows two replicated pulses (due to the seeding cavity) on the leading edge of the main pulse. There is apparently a broader 'window' over which the seeding pulse overpowers the weak spontaneous background noise than with the case where the seeding advance is less than optimum. Also the seeding pulse is highly asymmetric (as is the main SPML pulse) therefore the long trailing edge permits a greater margin of error for seeding pulse timing than does the short leading edge.

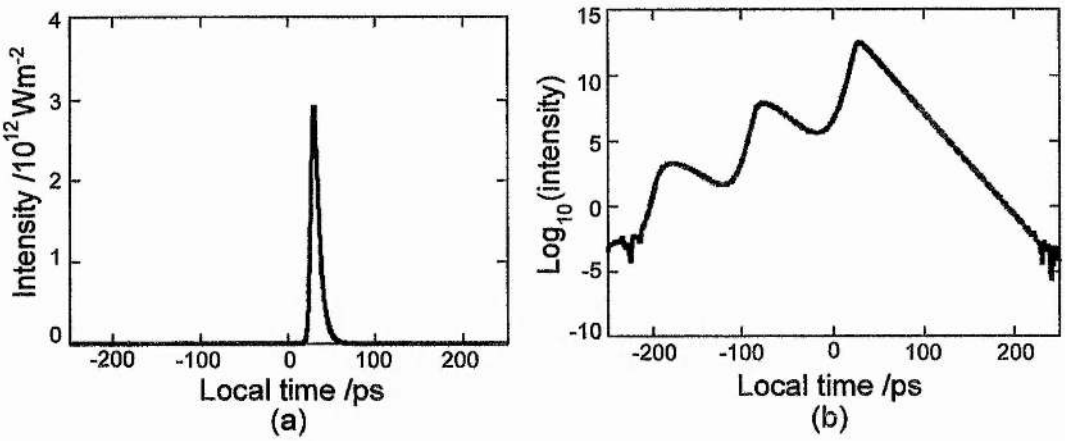

FIGURE 3.32: *Simulated SPML pulse with seeding applied far in advance of the optimum timing (200 ps in front of the main pulse).*

3.7 Concluding Remarks

In this chapter, a simple technique of passively stabilising a synchronously modelocked NaCl:OH$^-$ laser has been described. The fundamentals of actively modelocking a laser by gain modulation using a modelocked pumped source (synchronously-pumped modelocking (SPML)) were described with the assistance of a simple but versatile numerical model (the 'stepping model'). The model predicted that SPML lasers intrinsically suffer from severe instability on a pulse to pulse timescale due to the destabilising effect of the incoherent background light emitted between modelocked pulses (fluorescence). This instability was apparent in practice through numerous observations which included noisy RF and optical spectra, 'cusp shaped' autocorrelation traces and non-transform-limited pulses suggesting incomplete modelocking. As the mismatch between the SPML laser and the pump laser was increased, the destabilising effect was exacerbated.

The technique of coherent-photon-seeding (CPS) first applied to SPML dye lasers, was applied to the NaCl:OH$^-$ laser. This merely involves re-injecting a highly attenuated portion of the circulating laser field back into the laser cavity with the correct timing. A significant improvement in modelocked pulse quality and stability was immediately obtained. In addition, this technique permitted variable duration bandwidth-limited modelocked pulses to be readily generated from the SPML laser by detuning the main laser cavity with respect to the pump laser. This permitted the SPML

NaCl:OH^- laser to be used in an experiment which required the peak-power delivered into a semiconductor waveguide structure to be varied whilst maintaining constant average power[48].

Both the numerical model and the actual experimental setup were utilised to explore the effect of varying the seeding level and seeding timing. The optimum timing was found to correspond to re-injecting the seeding pulse by one pump pulse duration (FWHM) in front of the main SPML pulse.

The stepping-model predicted that the stochastic background light would contribute to the overall phase-noise (pulse jitter) of the modelocked pulse sequence at high frequencies. For the first time, this was demonstrated in practice by measuring the phase-noise of a synchronously-modelocked NaCl:OH^- laser before and after stabilisation with CPS using a high harmonic of the laser repetition frequency. A considerable reduction in high frequency pulse jitter figures was obtained on applying CPS.

Although SPML colour-centre lasers have been mostly replaced by all-solid-state systems which do not require cryogenic equipment, for applications which desire stable, low-noise, broadly-tunable, variable-duration pulses in the 10's of picoseconds regime at 1.55 μm, there is no suitable, high-power alternative to the synchronously-modelocked NaCl:OH^- laser, once stabilisation with coherent-photon-seeding has been applied.

This system should prove to be exceptionally versatile if a modelocked, diode-pumped Nd^{3+}:YAG laser was deployed as the pump source. Assuming pump pulses as short as 12 ps[50] could be obtained, transform-limited, tunable pulses with durations varying from 1 ps to ~10 ps should be obtainable from a simple SPML system with seeding applied.

References

1 A.V. Shestakov, N.I. Borodin, V.A. Zhinyuk, A.G. Ohrimtchyuk, and V.P. Gapontsev, in Post-Deadline paper in *Conference on Lasers and Electro-Optics* (Optical Society of America, Washington, D.C. 1991) paper CPDP11-1

2 K.R. German and C.R. Pollock, *Opt. Lett.* **12** , 474 (1986). See also ref. 17

3 L.F. Mollenauer and R.H. Stolen, *Opt. Lett.* **9** , 13 (1984)

4 A. Sennaroglu, C. R. Pollock, and H. Nathel, *Opt. Lett.* **19**, p390 (1994)

5 P. Beaud, J.Q. Bi, W. Hodel and H.P. Weber, *Opt. Commun.* **80** , 31 (1990)

6 C.R. Pollock, *J. Luminesc.* **35**, 65 (1986)

7 B. Fritz and E. Menke, *Solid St. Commun.* **3** , 61 (1965)

8 L.F. Mollenauer, R.H. Stolen and J.P. Gordon, *Phys. Rev. Lett.* **45**, 1095 (1980)

9 L.F. Mollenauer, *Opt. Lett.* **5** ,188 (1980)

L.F. Mollenauer, *Opt. Lett.* **6** ,342 (1981)

10 I. Schneider and C.R. Pollock, *J. Appl. Phys.* **54**, 6193 (1983)

11 J.F. Pinto, L.W. Stratton and C.R. Pollock, *Opt. Lett.* **10** , 384 (1985)

12 J.F. Pinto, E. Georgiou and C.R. Pollock, *Opt. Lett.* **11** , 519 (1986)

13 E. Georgiou, J.F. Pinto and C.R. Pollock, *Phys. Rev. B* **35** , 7636 (1987)

14 D. Wandt, W. Gellermann, F. Luty and H. Welling, *J. Appl. Phys.* **61** , 864 (1987)

15 R. Beigang, K. Klameth, B. Becker, Z. Yoon and H. Welling, *Opt. Commun.* **65** , 383 (1988)

16 K. Möllmann and W. Gellermann, *Opt. Lett.* **19** , 490 (1994)

17 J.F. Pinto, E. Georgiou and C.R. Pollock, *Opt. Lett.* **11** , 519 (1986)

18 B.H. Soffer and J. W. Linn, *J. Appl. Phys.* **39**, 5859 (1968)

19 T. Kurobori, A. Nebel, R. Beigang and H. Welling, *Opt. Commun.* **73** ,365 (1989)

20 K. Smith, J.M. Catherall and G.H.C. New, *Opt. Commun.* **58** ,118 (1986)

see also refs. 36

21 L.M. Davis, J.D. Harvey and J.M. Peart, *Opt. Commun.* **50** , 49 (1984)

Z.A. Yasa, *Appl. Phys. B* **30** , 135 (1983)

S. Kellys. *B* **47** , 349 (1988)

W. Forysiak and J.V. Moloney, *Phys. Rev. A* **45** , 8110 (1992)

See also refs. 35

22 N. Langford, K. Smith and W. Sibbett, *Opt. Commun.* **64**, 274 (1987)

also ref. 19

23 E.W. Van Stryland, *Opt. Commun.* **31**, 93 (1979)

24 J.M. Catherall and G.H.C. New, *IEEE J. Quantum Electron.* **QE22**, 1593 (1986)

25 D.J. Kuizenga and A.E. Siegmann, *IEEE J. Quantum Electron.* **QE6**., 694 (1970)

26 G.H.C. New, J.M. Catherall, *Opt. Commun.* **50**, 111 (1984)

27 J.M. Catherall, G.H.C. New and P.M. Radmore, *Opt. Lett.* 7 ,319 (1982)

28 H. Amman, W. Hodel and H.P. Weber, *Opt. Commun.* **95**, 345 (1993)

29 J.A. Fleck, Phys. *Rev. B* **1**, 84 (1970)

30 J.M. Catherall and G.H.C. New, *IEEE J. Quantum Electron.* **QE22**, 1593 (1986).

31 J.Q. Bi, W. Hodel and H.P. Weber, *Opt. Commun.* **81**, 408 (1991)

32 A Runge-Kutta Pascal routine supplied with the Borland Turbo-Pascal Mathbox library was used to perform the integration.

33 The value of AT was approximated considering the effective doping level of the laser material and the pumped volume. The actual value used is not important to the calculation and an alternative equation not dependent on this factor was derived in:

S. Kelly, G.H.C. New and D. Wood, *Appl. Phys. B* **47** , 349 (1988)

34 J.Q. Bi, W. Hodel and H.P. Weber, *Opt. Commun.* **81**, 408 (1991)

35 A. Scavennec, *Opt. Commun.* **17**, 14 (1976)

C.P. Auschnitt, R.K. Jain and J.P. Heritage, *IEEE J. Quantum Electron.* **QE15** , 912 (1979)

D.M. Kim, J. Kuhl, R. Lambrich and D. von der Linde, *Opt. Commun.* **27** ,123 (1978)

J. Herrmann and U. Motschmann, *Opt. Commun.* **40** ,379 (1982)

36 D.B. McDonald, D. Waldeck and G.R. Fleming, *Opt. Commun.* **34**, 127 (1980)

P.G. May, W. Sibbett, K. Smith, J.R. Taylor and J.P. Willson, *Opt. Commun.* **42**, 285 (1982)

37 G.T. Kennedy, R.S. Grant and W. Sibbett, *Opt. Lett.* **18**, 208 (1993)

38 P. Beaud, J.Q. Bi, W. Hodel and H.P. Weber, *Opt. Commun.* **80** , 31 (1990)

39 G.H.C. New, *Opt. Lett.* **15**, 1306 (1990)

J.Q. Bi, W. Hodel and H.P. Weber, *Opt. Commun.* **81**, 408 (1991)

40 C.J. Hooker, J.M.D. Lister and I.N. Ross, *Opt. Commun.* **80**, 375 (1991)

41 H. Kawaguchi and A.K. Sarwar, *Appl. Phys. Lett.* **62**, 2164 (1993)

P. Langlois, D. Gay, N. McCarthy and M. Piché, *Opt. Lett.* **23** , 114 (1998)

42 D. Sun and Y. Yamamoto, *Appl. Phys. Lett.* **60**, 1286 (1992)

43 J.Q. Bi, W. Hodel and H.P. Weber, *Opt. Commun.* **89**, 240 (1992)

44 K. Möllmann and W. Gellermann, *Opt. Lett.* **19** , 490 (1994)

45 W. Sibbett, J.R. Taylor and D. Welford, *IEEE J. Quantum Electron.* **QE17**, 500 (1981)

46 See refs. 38-39

47 See refs. 20-22 and 35-36

48 G.T. Kennedy, P.D. Roberts, W. Sibbett, D.A.O. Davies, M.A. Fisher and M.J. Adams, in Digest of *Conference on Lasers and Electro-Optics* (Optical Society of America, Washington, D.C. **1996**) paper

49 D. von der Linde, *Appl. Phys. B* **39** , 201 (1986)

50 G. T. Maker and A. I. Ferguson, *Opt. Lett.* **14**, p788 (1989)

4 The CW Cr^{4+}:YAG Laser

4.1 Introduction

The rapid development of the telecommunications industry has necessitated research into new approaches for distributing signals. One system adopted exploits the low-loss window of silica optical fibres around the 1.55 μm region[1]. It is essential to be able to fully characterise optical devices designed to operate at this wavelength during development hence it is desirable to have access to a tunable source of high peak-power ultrashort pulses. Earlier examples of such sources include the $KCl:Tl^0$ and $NaCl:OH^-$ colour-centre lasers which have the major disadvantage of requiring cryogenic cooling. One alternative all-solid-state laser material which has emerged recently is the Cr^{4+}:YAG crystal[2], which has a broad fluorescence spectrum spanning 1.3-1.6 μm, and a broad absorption band covering the 1.064 μm emission of the Nd^{3+}:YAG laser and the 980 nm emission of InGaAs laser diodes. This should permit a compact, low-cost laser source of ultrashort pulses centred at 1.55 μm to be constructed.

In this chapter, details of the Cr^{4+}:YAG laser are presented including its basic spectroscopy, cw operation and tuning range. Finally, the material's suitability as the basis for a femtosecond laser are discussed with possible approaches for the development of such a system considered.

4.2 Vibronic Gain Media

Tunable laser systems are important in many fields of scientific research. In the past, tunable lasers have been based on organic fluorescent dyes[3] dissolved in liquid solvents. These had numerous drawbacks: the dye had to be circulated necessitating a pump/dye-jet assembly adding to the laser noise and instability; the lifetime of the organic dye was limited and needed to be periodically replaced which was an unpleasant, messy operation; the actual tuning range available from each individual dye was limited, and certain dyes, particularly those operating in the infrared were highly toxic and possibly carcinogenic. For a short while, the near-infrared region

(800-1800 nm) was addressed by colour-centre crystals[4]. However these had their own problems associated with their use- namely the requirement of access to liquid nitrogen for cooling. During the 1980's, renewed interest was shown in doping transition metal elements into various insulating hosts permitting stable, room-temperature operation of tunable solid-state lasers to be demonstrated.

The development of the titanium sapphire gain medium[5] (Ti^{3+}:Al_2O_3) created almost the 'ideal' tunable laser material: high-optical quality, excellent thermal characteristics, an exceptionally broad tuning range (700-1100 nm) replacing several laser dyes and colour-centre crystals and an absence of excited-state absorption (ESA) and non-radiative transitions. The only apparent drawback of this material is its requirement for pumping in the blue-green spectral region necessitating expensive pump sources (e.g. argon-ion lasers or intracavity-doubled Nd^{3+} lasers). Perhaps as the development of reliable blue laser diodes proceeds, this should address this issue.

The broad bandwidth accessible by Ti:sapphire has permitted exceptionally short duration optical pulses to be generated (down to 6.5 fs[6]) from a simple laser system.

Perhaps spurred on by this 'wonder-material', several research groups demonstrated new transition-metal doped laser materials throughout the 1980's and 90's to address the drawback of the location of the absorption band in Ti:sapphire creating laser media which could be directly diode-pumped (e.g. Cr^{3+}:LiSAF). Also, research into gain media which would extend the spectral regions accessible by solid-state materials was carried out.

4.2.1 Gain Media with Vibronic and Electronic Transitions

Although the first transition-metal ion doped gain media were demonstrated in the 1960's[7], these had problems, principally the possession of excessive excited-state absorption, which prevented their general acceptance, and research into tunable solid-state lasers was succeeded by dye laser development. One exception was the ruby laser[8] which was based on a transition metal ion (chromium) doped into sapphire (Cr^{3+}:Al_2O_3) but this represents a non-tunable laser.

In contrast, solid-state gain media based on rare-earth metal ion doped insulating crystals were very successfully developed during the 1960's, in particular, the Nd^{3+}:YAG laser was demonstrated[9] which subsequently became the most successful

solid-state laser medium. Unfortunately, in general, solid-state lasers based on rare-earth metal ion doped media are non-tunable.

To understand the differences between the operational behaviour of transition-metal ion doped media with rare-earth ion doped crystals, it is instructive to examine the electronic structure of the active ion.

Elements in the lanthanum series (rare-earth metals) usually comprise a closed xenon shell with chemical reactions involving outer 6s and 5p (and 5d) electrons. Successive elements in the series involve filling the inner 4f shell with electrons hence the chemical properties of lanthanum elements are very similar. However, the 4f shell is the one involved in the optical excitation and emission of rare-earth ions, which is shielded from any external field perturbation by the 5p electrons. Hence a rare-earth ion behaves in similar optical terms whether in free-space or doped inside a crystalline host, with very narrow absorption and emission bands and hence no tunability. The crystalline Stark effects induced in the outer electrons of the ion caused by bonds with surrounding ions in the crystal matrix do not affect the inner, shielded 4f electrons to any degree hence the similarity in the emission and absorption properties rare-earth ions in different crystal hosts. This also goes some way to explain the rapid success of rare-earth ion doped laser systems in the early years of laser history: high quality crystal growth with rare-earth ion activated hosts which themselves contain rare-earth ions (e.g. Nd^{3+} in YAG) is straightforward, and the material will be a suitable laser medium provided the host has good physical properties and the activator ion has suitable laser characteristics (e.g. low ESA).

Conversely, the electronic structure of transition-metal ions comprises no shielding outer electron shell, that is, it is the outer electron itself which is involved in optical absorption, emission and chemical bonding. This implies that the behaviour of a transition metal ion when involved in bonding inside a crystal host matrix will differ considerably from the behaviour of an isolated ion, depending on the strength of the crystalline Stark effects induced by the crystal field. Hence there will be a variation in the wavelength region accessed by the active ion dependent on the host crystal into which it is doped, e.g. the Cr^{3+} ion in LiSAF and alexandrite has peak gain at 825 nm and 752 nm respectively.

The interaction between the host crystal field and the active ion outer electron,

also serves to broaden the transitions involved. This is due to coupling between the active ion electron and the vibrational modes in the host medium: the transitions can be described as vibronically broadened. This is in contrast to the case where the host is activated with a rare-earth metal ion: the outer electrons shield the electron involved in the optical transitions from the host crystal field and hence no appreciable coupling between the vibrational modes (phonons) in the crystal and the active electron occurs therefore the linewidth is narrow.

The vibronic broadening effect can be understood with consideration of the configurational co-ordinate diagram in figure 4.1. The configurational co-ordinate is the separation of the active ion from the first shell of neighbouring ions. The phonon energy states are represented by horizontal lines within the potential wells associated with the energy levels of the active ion. The probability of a photon being absorbed from the ground state to a specific phonon level in the excited state is governed by the overlap integral of the wave function of the lowest level in the ground state with the wave function of the target phonon level in the excited state (the Franck-Condon principle). The excited electron relaxes to the first level of the excited state (the relaxed excited state (RES)) by phonon emission into the crystal lattice. A broad photon energy emission range results from phonon broadening of the ground state, with the choice of final level in the ground state governed by an overlap integral. In the absence of vibronic broadening of the energy levels, as would be the case if the medium was cooled to ~0K, the absorption and emission features become very narrow, peaking at photon energies equal to the zero phonon energy. For an efficient 4-level laser system, the decay rate of the excited electron in the higher phonon energy level should be rapid (~ femtosecond timescale) compared to the lifetime of the RES (~ μs).

One interesting exception to the crystal field leading to a broadening of the absorption and emission bands of transition-metal ions doped in crystalline hosts was the first laser ever demonstrated- the ruby (Cr^{3+}:Al_2O_3) laser. In this special case, the crystal field is of such strength as to completely shift the vibronically broadened $^4T_2$ level (normally the excited state of Cr^{3+} lasers) to a level higher than the ^2E electronic state, whose levels depend mainly on a spin-orbit interaction between the electrons of the Cr^{3+} ion and are largely unaffected by direct phonon coupling. Hence, emission in ruby occurs between the ground state and the ^2E state resulting in limited tunability, but absorption can occur between the ground state and the usual $^4T_2$ state creating a broad

absorption band suitable for flashlamp pumping.

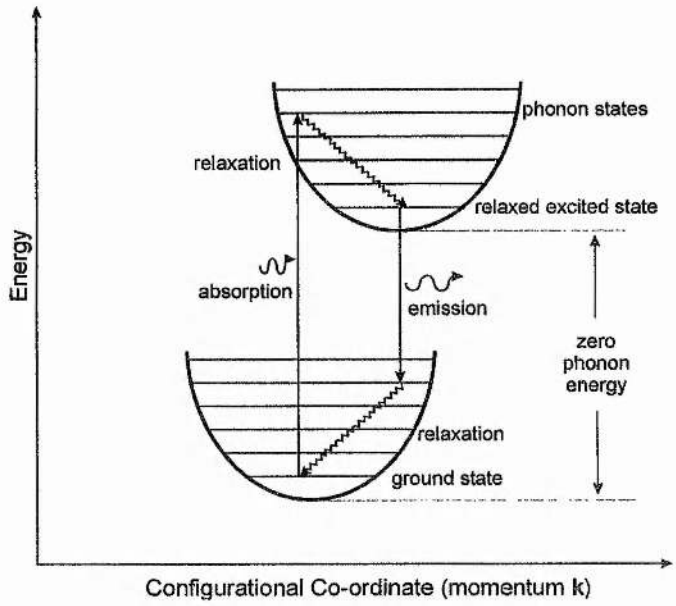

FIGURE 4.1: *Configurational co-ordinate diagram for a vibronically broadened gain medium.*

The transition-metal ion doped hosts thus described all exhibit homogeneously broadened transitions, i.e. all active ions experience the same crystal field within the host crystal matrix. It is possible to develop tunable solid-state lasers by doping active ions into amorphous host materials (i.e. glasses). In these cases, each active ion experiences a different field because there is no regular (crystalline) structure to glassy materials and hence the line broadening is termed 'inhomogeneous'. Tunable, inhomogeneously broadened gain media capable of supporting femtosecond pulses based on doping rare-earth metal ions into glassy hosts have been demonstrated[10].

In table 4.1, spectroscopic properties of some vibronically broadened gain media are compared.

An important feature of broadband tunable lasers is their ability to create pulses of short duration. The duration and bandwidth of a laser pulse form a conjugate pair hence the broader the gain bandwidth of the laser medium, the shorter the optical pulse duration it should be capable of supporting.

Gain medium	Absorption band (μm)	Fluorescence band (μm)	Gain cross-section (10^{-19} cm^2)	Upper-state lifetime (μs)
Ti^{3+}:sapphire ($Ti^{3+}:Al_2O_3$) [11]	0.45-0.6	0.66-1.18	3.8	3.2
Cr^{3+}:LiSAF ($Cr^{3+}:LiSrAlF_6$) [12]	0.4-0.75	0.76-0.92	0.48	67
Emerald ($Cr^{3+}:Be_3Al_2(SiO_3)_6$ [13]	0.39-0.7	0.7-0.86	0.31	60
Cr^{4+}:forsterite ($Cr^{4+}:Mg_2SiO_4$) [14]	0.85-1.2	1.167-1.345	1.1	15
Cr^{4+}:YAG ($Cr^{4+},X^{2+}:Y_3Al_5O_{12}$) [15]	0.88-1.1	1.25-1.6	0.75	3.3

TABLE 4.1: *Spectroscopic properties of some vibronically broadened gain media.*

4.3 The Cr^{4+} Ion in YAG

Prompted by the successful demonstration of tunable room-temperature alexandrite[16] and emerald[13] lasers, crystal growth researchers concentrated their efforts into finding new host materials for the chemically stable trivalent chromium ion to access new wavelength regions and for optimising efficiency. The olivine mineral 'forsterite'[17] (Mg_2SiO_4) was one such host investigated which was found to provide laser gain at a peak of 1.235 μm and a very broad absorption covering the visible and near infra red spectral regions when activated with chromium. Initially a green (532 nm) pump source was used to provide inversion since this falls within the usual absorption band of Cr^{3+} ions in the visible part of the spectrum. Later, independent spectroscopic studies by two groups[18,19] suggested that the laser action was actually due to Cr^{4+} ions substituting for silicon (Si^{4+}) in the tetrahedral sites in the crystal and that pumping the weaker absorption around 1 μm with the 1.064 μm emission from a Nd^{3+}:YAG laser was more appropriate.

The early development of Cr^{4+}:YAG was similarly confused by a

misunderstanding of what the laser active species was. In 1987 yttrium aluminium garnet (YAG) was doped with chromium which was subsequently oxidised to the tetravalent ion[20]. This treatment was thought to form impurity colour-centres within the YAG lattice which were found to possess a broad absorption band covering the 1.064 μm emission of an Nd^{3+}:YAG laser, and luminesced in the near-infrared region from 1.25-1.7 μm. Interestingly the material was only found to provide gain from 1.3-1.5 μm and laser action, when pumped with a Q-switched Nd^{3+}:YAG laser, was achieved within these limits only.

Later by spectroscopic investigation, it was realised that the activation of the YAG host was in fact provided by the Cr^{4+} ions themselves[21]. The material is interesting from a spectroscopic point of view for numerous reasons which will be discussed in section 4.4.

The first room temperature cw operation of a Cr^{4+}:YAG laser was described by Shestakov et al.[22] in 1991. Up to 1W output power was produced at the peak of the emission at ~1.42 μm. The laser could be tuned from 1.35-1.56 μm.

A second application of the Cr^{4+}:YAG laser which stems from the low saturation intensity of its absorption band, is as a passive Q-switch[23] in laser systems operating around 1 μm (e.g. Nd^{3+}:YAG).

4.4 Spectroscopy and Growth of Cr^{4+}:YAG

Yttrium aluminium garnet ($Y_3Al_5O_{12}$) is an overall cubic crystal system. However, the site symmetry of the active Cr^{4+} ions is less than cubic: we have the unusual case of creating anisotropic centres in an isotropic host material. YAG offers a large variety of site symmetries into which dopant ions may be assimilated: the Y^{3+} ions are dodecahedrally co-ordinated, 40% of the Al^{3+} ions are octahedrally co-ordinated and the remaining 60% are tetrahedrally co-ordinated[24]. To incorporate tetravalent ions (e.g. Cr^{4+}) into a trivalent site (Y^{3+} or Al^{3+}), a divalent charge compensating ion needs to be included for valence balancing. This could be Ca^{2+} or Mg^{2+} and complicates both the growth of Cr^{4+}:YAG crystals and the study of its dynamics since charge compensating ions are known to affect the optical spectra of materials into which they are doped[25].

Because of the predominance of the trivalent sites within the YAG matrix, it is

natural for trivalent chromium ions to be incorporated into YAG. Crystals of Cr^{4+}:YAG are usually prepared by the Czochralski technique: typically 0.2 mol % Cr and 0.1 mol % charge compensating Ca or Mg are added to the melt, and the crystal must be grown in an oxidising atmosphere to encourage formation of the Cr^{4+} ions.

Studies have shown that the majority of the dopant chromium is incorporated as Cr^{3+} in the octahedral Al^{3+} sites[24] however the optical spectra of $Cr^{4+}X^{2+}$:YAG is dominated by the Cr^{4+} ions in the tetrahedral sites as these sites lack inversion symmetry. Eilers et al.[24] showed from examination of the absorption spectra of a typical crystal grown along the [111] axis obtained from Union Carbide, that only 2% of the doped chromium is actually incorporated into the tetrahedral sites and contributes to laser action.

The actual sites of the active Cr^{4+} ions are elongated tetrahedrons (described by the local symmetry class D_{2d}) and exhibit orbital splitting of the excited states and changes from the ground state compared to an ideal tetrahedron with T_d symmetry. Figure 4.2 summarises the energy levels involved in laser action for the Cr^{4+} ions in distorted tetrahedral sites. Note that this differs from the original energy level diagram suggested by Shestakov[22] in that near-infrared pump absorption (at ~1 μm) involves excitation from the $^3B_1$ to the $^3A_2$ level as opposed to the earlier proposed $^3B_1$ to $^3E_1$ transition. This is a more recent energy level description given by Eilers et al.[24] and confirmed independently by Kück et al.[26] and is able to support the polarisation dependent observations discussed later.

Values pertinent to Cr^{4+}:YAG for use as a laser gain medium are given in table 4.2.

Several authors have reported measuring differing values for certain parameters relating to Cr^{4+}:YAG, in particular, the value given to the gain cross-section varies by an order of magnitude. Both Kück et al.[32] and Eilers et al.[31] have recently carried out a detailed investigation into the spectroscopy of Cr^{4+}:YAG and the value of $\sim 3.3 \times 10^{-19}$ cm^2 is probably the correct one. Note that it is also likely that the laser parameters may vary considerably from sample to sample: the unusual growth requirements for Cr^{4+}:YAG leads to a variation in the ratio of dopant chromium ions accepted as Cr^{4+} into the tetrahedral sites. Several other parasitic dopants are present including Cr^{3+}, probably Cr^{2+}, and non-laser active Cr^{4+} in octahedral sites. In addition

the concentration of the charge compensating ions adds an extra variable to the growth procedure. After growth in an oxidising atmosphere, it is usual to anneal the crystal in an oxidising atmosphere by heating it close to its melting point (at ~2000K), or by exposure to gamma rays, to further convert impurity Cr^{3+} ions into active Cr^{4+} ions[27]. Such harsh treatment is similar to the growth conditions for certain colour-centre crystals and doubtless contributes to a variation between laser crystals obtained from different boules.

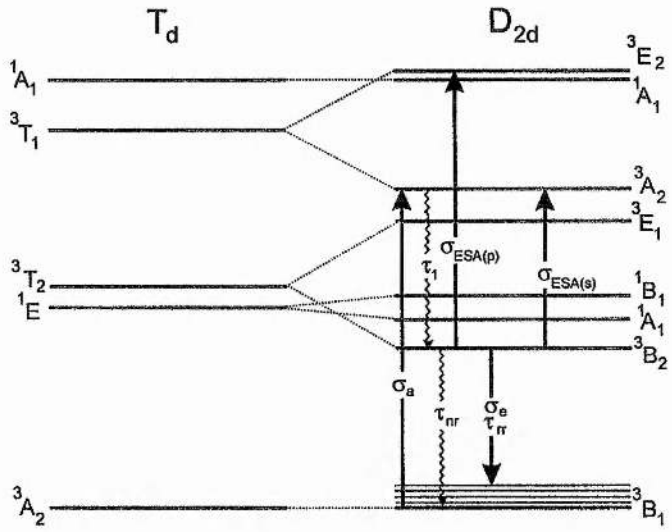

FIGURE 4.2: *Energy level diagram for Cr:YAG after Shestakov and Eilers. Values given in table 4.2.*

One unfortunate feature of Cr^{4+}:YAG is the temperature dependence of the upper-state lifetime. At 77K, the lifetime is an order of magnitude greater than at room temperature[28]. Also the non-radiative decay rate has a similar temperature dependence to the radiative rate leading to a much lower quantum efficiency at room temperature compared to other laser materials e.g. Ti:sapphire (η~0.8).

Property	Value
Refractive index (n)	1.81
Pump absorption cross-section (σ_a)	5^{29} , 1.3^{30} , 5.7^{31} x10^{-18}cm^2
Peak emission cross-section (σ_e)	8^{29} , 0.75^{30}, 0.95^{30} , $3.3^{31,32}$ x10^{-19}cm^2
Pump band	0.8-1.15 μm
Peak laser emission wavelength	1.45^{30} μm
Radiative lifetime (τ_{rr})	$4^{29,32}$ μs , $3.4^{30,31}$ μs @300K 48^{30} μs @77K, 62.4^{31} μs @0K
Non-radiative lifetime (τ_{nr})	60^{31} μs @0K
Pumping quantum efficiency (η)	$0.15^{31,32}$, 0.22^{33} @300K, 0.49^{31} @10K
Signal ESA cross-section ($\sigma_{ESA(s)}$)	4^{29} , 0.25^{30} x10^{-19}cm^2
Pump ESA cross-section ($\sigma_{ESA(p)}$)	5^{29} x10^{-19}cm^2

TABLE 4.2: *Laser parameters for Cr:YAG.*

Crystal growth researchers have attempted to grow other garnets[32,33] incorporating the Cr^{4+} ion with the main aim being to shift the peak emission wavelength from ~1.38 μm (in the case of Cr^{4+}:YAG) to coincide with the more useful telecommunications centre wavelength of 1.55 μm. This essentially requires a host with a larger lattice constant (and therefore a weaker crystal field) than YAG. Unfortunately, it has been observed that the radiative and non-radiative lifetimes both decrease as the peak emission wavelength is increased. Figure 4.3 illustrates the temperature dependence of the upper-state-lifetime for the Cr^{4+} ion in YAG and some other garnets. This is in stark contrast to the temperature dependence of the Cr^{3+} ion in most colquiriites which shows no variation in lifetime in the temperature range 0-300 K. The upper-state-lifetime as a function of the peak emission wavelength for different garnet hosts is shown in figure 4.4.

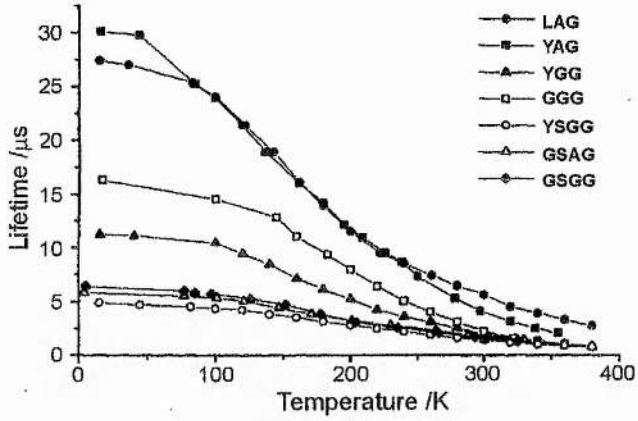

FIGURE 4.3: *Temperature dependence of the total effective upper-state-lifetime for different garnet hosts for the Cr^{4+} ion. (After Kück Ref. 32)*

In addition to a decrease in the upper-state-lifetime, garnets with larger lattice constants for peak emission at longer wavelengths have even lower quantum efficiencies than Cr^{4+}:YAG (i.e. the ratio of the radiative decay rate to the total decay rate decreases). It is therefore unlikely that any of the other garnets listed in figure 4.3 could be developed as useful laser gain media.

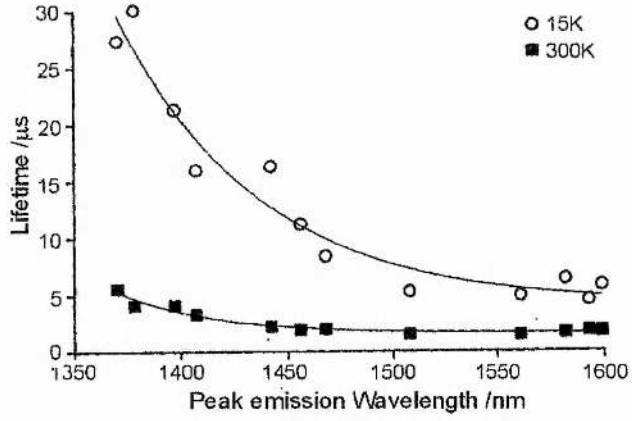

FIGURE 4.4: *Decrease of upper-state-lifetime for different garnet hosts with increasing peak gain wavelength. (After Kück Ref. 32)*

4.4.1 Absorption and Fluorescence Spectra

Several Cr^{4+}:YAG laser crystal samples were obtained from Union Carbide[34], IRE-POLUS[35], and the university of Hamburg[36] of differing quality and doping. All were co-doped with calcium for charge compensation except the most recent obtained from Union Carbide which used magnesium. A study of this material by M. Kokta

suggested that magnesium co-doping was the most suitable approach for growing laser quality crystals[37] (but calcium co-doping is better suited to Q-switch growth). The essential features of the absorption and fluorescence spectra of all these samples were, surprisingly, identical and an example absorption spectrum measured on a 20 mm long Cr^{4+}:YAG crystal supplied by Union Carbide and co-doped with calcium is shown in figure 4.5.

The absorption measurement was carried out using an incandescent white light source (a 250 W tungsten filament 'heat-lamp' with emission peaking in the infra-red), a scanning monochromator (Applied Photophysics Ltd.) and a large area germanium photodiode attached to a lock-in-amplifier (LIA). A chopper placed directly in front of the monochromator served to modulate the signal to be extracted by the LIA. A Schott RG650 filter placed between the monochromator and the photodiode cut off the higher diffracted orders of visible light from the monochromator. Polarising cubes placed before and after the Cr^{4+}:YAG crystal ensured the absorption of the appropriate active centres (i.e. p-polarised with respect to the Brewster angle) was measured. An IBM PC compatible computer running in-house developed software controlled the scanning of the monochromator and took readings from the LIA to perform the measurement. Two scans were taken over the desired wavelength region both with and without the absorbing sample, and the computer calculated the effective absorption from each point recorded. No separate calibration of the spectral response of the germanium photodiode needed to be carried out as this was accounted for in the subtraction measurement of the two scans taken by the computer. The peak absorption is at ~1.03 μm, however there is still significant absorption at 1.064 μm (85% of peak) permitting efficient pumping with a Nd^{3+}:YAG laser, and the high absorption on the short wavelength side of the peak (82% of peak at 980 nm) allows direct-diode-pumping with InGaAs laser diodes[38]. Note that there is still high absorption at ~850 nm (40% of peak) which might permit direct-diode-pumping with high power AlGaAs diodes[39].

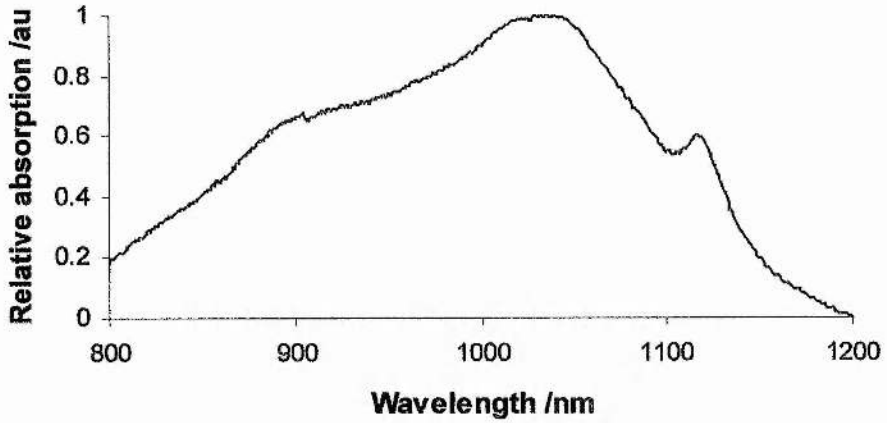

FIGURE 4.5: *Absorption spectrum of Cr:YAG*

The fluorescence spectrum in figure 4.6 was taken with a similar arrangement to the absorption measurement but with the Cr^{4+}:YAG crystal pumped with a chopped 1.064 μm signal. Only one scan of the monochromator was required and the resulting spectrum needed to be calibrated against the manufacturers published spectral response curve for the photodiode using a spreadsheet package. The peak of the fluorescence emission occurs around 1.35 μm whereas the peak gain is closer to 1.45 μm.

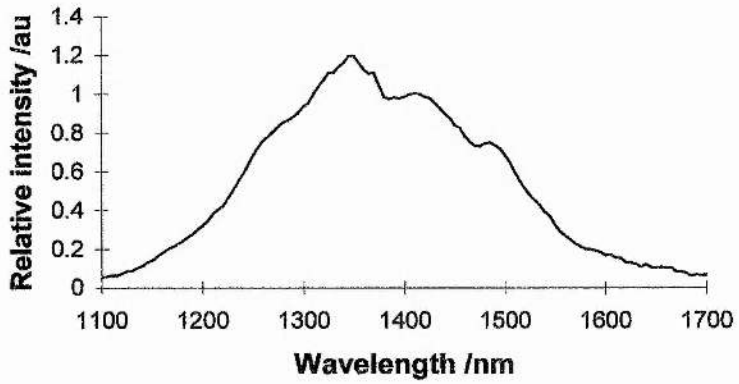

FIGURE 4.6: *Fluorescence spectrum of Cr:YAG pumped with an Nd:YAG laser*

4.4.2 Polarisation-dependent Emission and Absorption

One unusual feature of Cr^{4+}:YAG is the positioning of its active Cr^{4+} ions in anisotropic sites (stretched tetrahedrons) within an isotropic lattice. This results in a variation of the absorption and emission features depending on the polarisation being observed. Eilers et al.[40] reported a dependence on the pump polarisation of the absorption saturation of a Cr^{4+}:YAG sample for use as a possible Q-switch for 1μm lasers. Depending on whether the crystal was grown along the [111] or [001] axes, either 6 or 4 cycles (peaks and troughs) in the transmission of 1.064 μm pump light were observed respectively as the polarisation of the pump light was rotated. The transmission peaks observed with the crystal grown along the [001] axis were due to maximum saturation by pump light polarised parallel to one of the transition moments [010] or [100] (i.e. one third of the optically active centres sampled). With the [111] crystal, it was not possible to polarise light along one of the transition moments and a minimum of two thirds of the active centres could only be sampled at a time (i.e. maximum transmission occurs when sampling a projection of the [100], [010] or [001] transition moments along the [111] axis hence the 6 cycles observed as the pump polarisation was rotated by 360^0). These results implied that the most efficient Q-switch should be grown along the [100] axis and oriented with either the [100] or [010] planes parallel to the polarisation of the Q-switching laser for maximum saturation effect.

When operated as a laser gain medium, this polarisation dependence has a second important effect. Kück et al.[41] reported the effect of rotating the polarisation of pump light from a long-pulse flashlamp pumped Nd^{3+}:YAG laser on the polarisation and output power of a Cr^{4+}:YAG laser based on a plane-plane gain medium grown along the [111] axis. Their results are summarised in figure 4.7 which is a plot of output power versus pump polarisation. The output reaches a maximum when the pump beam is polarised parallel to a crystallographic [100] axis and is a minimum when polarised parallel to [110] axis. The polarisation of the laser output flips when the pump polarisation rotates through the [110] direction. The reason for this dependence stems from the lack of symmetry of the site of the active Cr^{4+} ion (a stretched tetrahedron) similar to the absorption saturation dependence. The distortion axis of this site coincides with a crystallographic axis therefore there are three classes of sites oriented along the crystallographic axes ([100], [010] and [001]). Polarised pump light selectively excites these centres hence different centres are excited as the polarisation is rotated. When the

pump radiation is polarised along a [110] direction, two classes of centres are excited and hence only half the pump power is effectively pumping each individual class therefore the output power is reduced. This is described in greater detail in references 31,42.

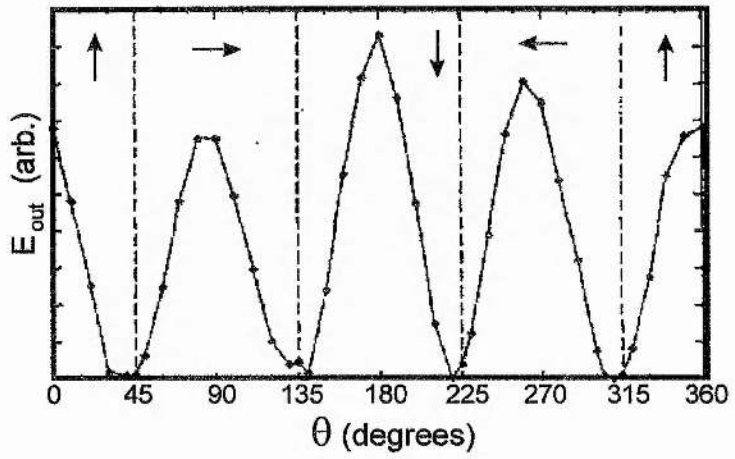

FIGURE 4.7: *Dependence of the laser emission on the angle between the pump polarisation and the [100] direction. The arrows indicate the polarisation of the Cr:YAG laser emission. (after Kück et al.[41])*

4.5 Construction and Operation of a CW Cr^{4+}:YAG Laser

The essential requirement for a cw laser based on a low-gain laser material such as Cr^{4+}:YAG is a good overlap of tightly focussed laser and pump beams inside the gain element. Although it is possible to achieve a tight intracavity focus using a two-mirror resonator consisting of two concave mirrors operated at the edge of its stability condition, such a resonator will be difficult to align and will be very sensitive to misalignment. An alternative is to use three- or four-mirror resonators which allow a tightly focused resonator mode when operated at the centre of a large stability region. Since it is usual to Brewster-angle the ends of the laser rod to minimise Fresnel losses, it is necessary to compensate for the astigmatism introduced by the rod in the cavity by suitably angling the folding mirror(s). This is illustrated in figure 4.8 which is a schematic of the standard 4-mirror cavity used to assess the Cr^{4+}:YAG material. Each of the curved mirrors 'folds' the resonant beam through an angle of 2θ which ensures the sagittal and tangential stability regions coincide for all separations of the curved mirrors. The precise angle, θ, was determined using a resonator modelling package

based on ABCD matrix multiplication, however for the usual case of a symmetric 4-mirror resonator, the following equation also balances the astigmatic effects of a curved folding mirror and a Brewster-angled gain element[43]:

$$R.Sin(\theta).Tan(\theta) = \frac{(n^2-1).(n^2+1)^{\frac{1}{2}}.l}{n^4} \qquad \text{Equation (4.1)}$$

where **n** is the refractive index of the laser rod of length **l**. **R** is the radius of curvature of both identical folding mirrors, each folded through a half angle θ.

The design of an astigmatically compensated laser cavity will be discussed in greater detail in chapter 5 with emphasis on fulfilling the conditions required for reliable self-modelocking.

The Cr^{4+}:YAG rod was wrapped in thin indium foil and very tightly clamped in a brass or copper water cooled mount cooled to ~15° C. The rod was excited by pump light focussed by a 10 cm lens through a dichroic curved folding mirror, which permitted excellent laser-pump mode matching throughout the length of the crystal.

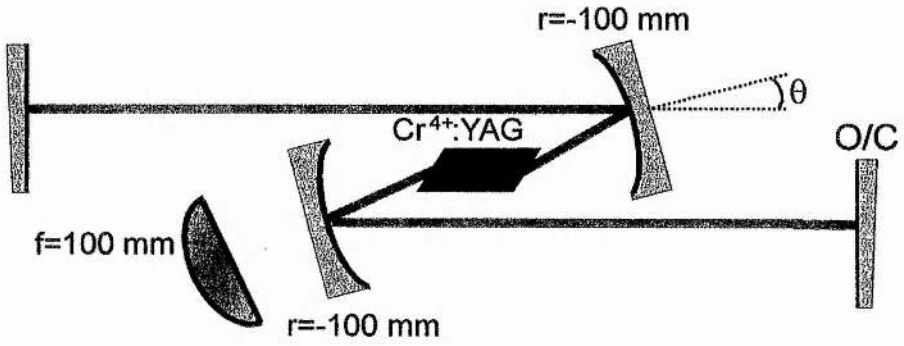

FIGURE 4.8: *Schematic of a 4-mirror, astigmatically compensated laser cavity.*

4.5.1 Assessment of the Cr^{4+}:YAG Gain Medium

The first Cr^{4+}:YAG crystal utilised in a laser cavity was a 13 mm rod co-doped with Ca^{2+} for charge compensation, with an unbleached pump absorption coefficient of 1.01 cm^{-1}. Using the relation[15]:

$$N_0 = -\frac{1}{l.\sigma_a}.\ln(T_0) \qquad \text{Equation (4.2)}$$

it is possible to determine the concentration of active Cr^{4+} ions in the crystal. With the values pertinent to this crystal, (length l=1.3 cm, small-signal transmission[44] T_0=0.28 and using a pump absorption cross section[29] σ_a=5 x 10^{-18}), this suggests a Cr^{4+} concentration of just N_0=1.96x10^{17} cm^{-3}. This is two orders of magnitude less than the typical concentration of Ti^{3+} ions in a Ti:sapphire rod (~2x10^{19} cm^{-3}) and demonstrates the unusually high absorption cross section of active ions positioned in a site without inversion symmetry. Unfortunately, the low concentration of Cr^{4+} ions in the laser active material leads to significant bleaching by the high intensity of the pump beam.

The setup in figure 4.8 permitted the pump transmission to be determined both with and without stimulated emission depleting the excited state by unblocking and blocking the resonator respectively. Figure 4.9 is a graph of pump absorption in the gain element for increasing incident pump powers both for the isolated crystal (cavity blocked) and for the crystal inside a resonator. Below the threshold of the laser cavity, blocking the laser has no effect on pump absorption, as expected. However, once the laser begins to oscillate (at ~5 W incident pump), there is an appreciable difference between the two cases: for increasing pump powers, the pump absorption for the isolated rod bleaches due to a reduction in the number of Cr^{4+} ions remaining in the ground state; for the rod inside a resonator, stimulated emission provides an additional mechanism (as well as spontaneous decay) for increasing the number of Cr^{4+} ions capable of capturing pump photons. This results in the fraction of incident pump power absorbed in the crystal reaching a plateau once laser oscillation is established and contradicts the statement by Sennaroglu et al.[30] that 'decreasing [pump] absorption with increasing [incident] pump power leads to [laser] output power saturation': laser oscillation effectively 'clamps' the pump absorption to a constant value. Nevertheless it is important to note that in the case of this crystal with such a low active ion concentration, only ~50% of the incident pump power is absorbed by the gain element in the laser even though the small signal absorption is somewhat higher (at 72%).

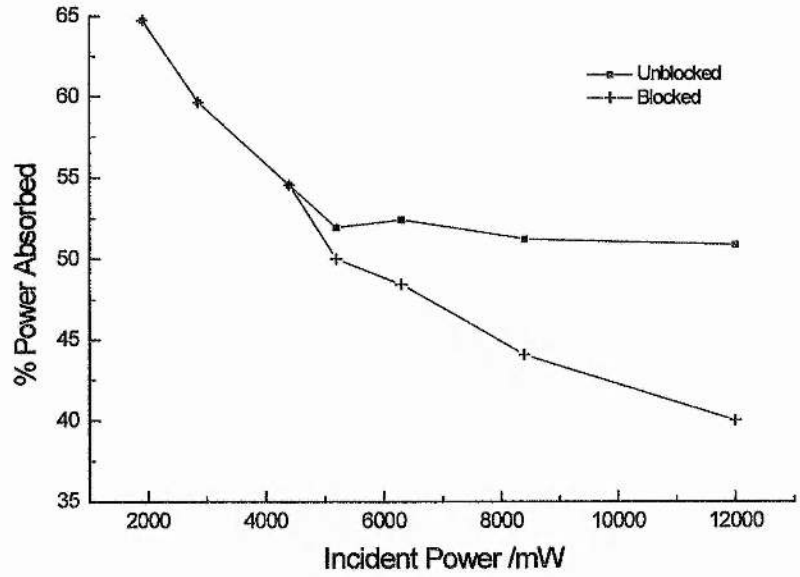

FIGURE 4.9: *Plot of pump absorption (at 1.064 μm) vs. incident pump power for a Cr,Ca:YAG rod inside a laser resonator both blocked and unblocked.*

The mirrors used in the cavity were high-reflecting (HR>99.8%) 1.4-1.5 μm (LaserOptik GmbH), centred at 1.45 μm. A 1% output coupler (O/C) was used as one end mirror. The operating wavelength without any tuning element was 1.44 μm. Using a 6.6 mm quartz birefringent crystal plate (BRF) at Brewster's angle, the limited tuning range shown in figure 4.10 was accessible. The narrow tuning range is an indication of the exceptionally low gain provided by this crystal.

Other laser crystals obtained from Moscow (IRE-Polus) and Union Carbide demonstrated considerably broader tuning range and higher gain enabling output powers of up to 1 W to be obtained at the gain peak wavelength 1.44 μm. However for operation beyond 1.5 μm (necessary for ultrashort pulse generation, discussed later), the gain was noted to drop off considerably quickly. Whereas ~200 mW could be extracted at 1.48 μm, only 30 mW was obtained from a 20 mm calcium co-doped Union Carbide Cr^{4+}:YAG rod at 1.52 μm. Figure 4.11 illustrates the power transfer characteristics of this laser using long wavelength mirrors (transmission curves of these mirrors given later in figure 4.18).

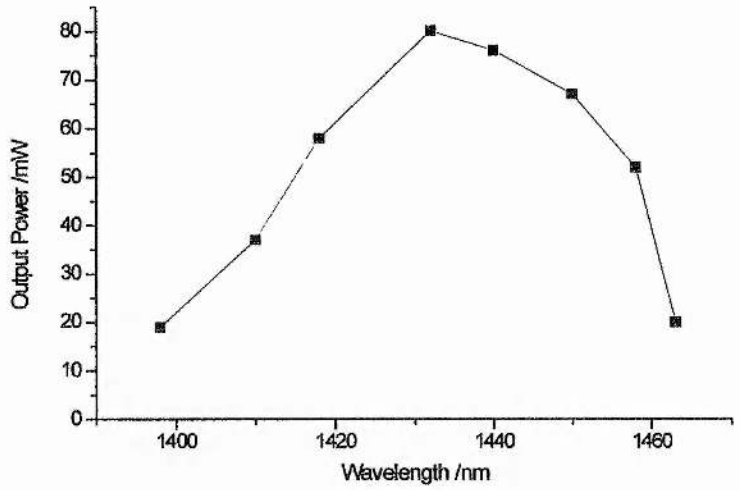

FIGURE 4.10: *Tuning range of Cr^{4+}:YAG laser based on 13 mm Hamburg crystal*

The measurements for figure 4.11 were taken quasi-cw; i.e. with a 20:1 optical chopper placed within the pump beam. This prevented heating of the Cr^{4+}:YAG rod hence the long term thermal degradation experienced with this material (discussed in section 4.5.2.1) did not occur. Without this precaution, the cw output powers of this laser system were considerably less than suggested by figure 4.11 and operation with an output coupler was limited to a few minutes.

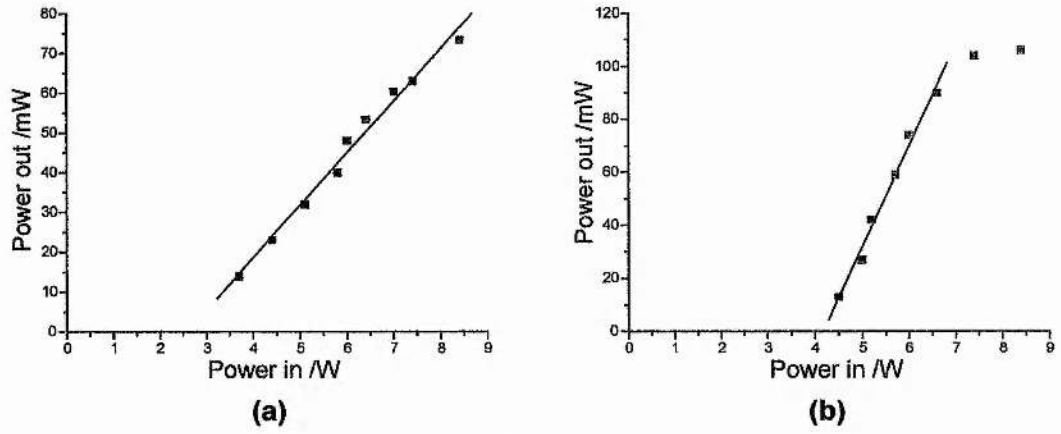

FIGURE 4.11: *Power transfer characteristics of a 4-mirror laser based on a 20mm Cr,Ca:YAG crystal obtained from Union Carbide fitted with long wavelength mirrors.* **(a)** *output coupling through an HR mirror (λ=1.508μm)* **(b)** *fitted with 0.5% output coupler (λ=1.525μm)*

From figure 4.11 the slope efficiency with the HR mirrors was 1.3% (considering just the output from one HR end-mirror) or 7.8% assuming equal power leakage from each HR reflection. The threshold for this laser was 2.6W (without any additional intracavity elements). Fitting the 0.5% output coupler increased the

threshold to 4.2W and the useful slope efficiency to 3.6%. Note that the free running wavelength also increased from 1.508μm to 1.525μm. The output power was shown to degrade for high pump powers for the laser fitted with the output coupler (figure 4.11(b)).

A 23 mm x 5 mm rod of Cr^{4+},Mg^{2+}:YAG with a small-signal pump absorption coefficient of 2.2 cm^{-1} supplied by Union Carbide, was found to possess considerable gain at wavelengths out to 1.58 μm. The mirror set covering the wavelength range 1.52-1.62 μm (LaserOptik GmbH) centred at 1.58 μm (R>99.95%) was obtained to exploit this range. The full tuning range of this rod at 5.5 W pump using the two mirror sets spans 200 nm and is presented as figure 4.12. Tuning was accomplished using a 3-plate BRF obtained from a Spectra-Physics Ti:sapphire laser. Without any tuning element, the free running output power was 200 mW at 1.526 μm using mirror set 2, and 210 mW at 1.449 μm (through a 1% output coupler centred at 1.45 μm) using mirror set 1.

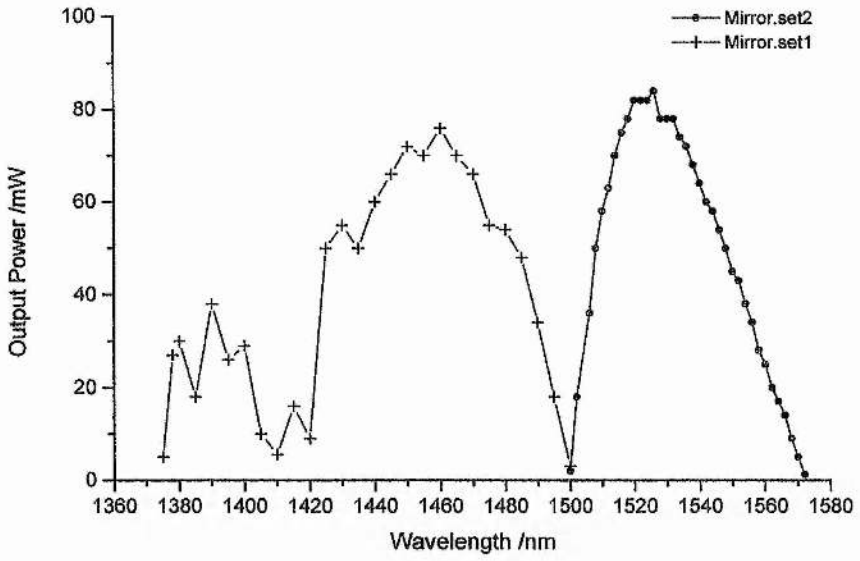

FIGURE 4.12: *Tuning range of Union-Carbide Cr,Mg:YAG rod with two mirror sets. (mirror set 1: HR 1400-1500 O/C=1%; mirror set 2: HR 1520-1620 O/C=0.5%)*

One striking feature of the graph in figure 4.12 is the smooth nature of the tuning using the second mirror set at wavelengths >1.5 μm which contrasts with the discontinuous tuning below 1.5 μm. In particular, for wavelengths between 1.4-1.43 μm the output power decreases considerably. This results from discrete

resonances in the water present in the laser crystal, tuning plates and the atmosphere. Gilmore et al.[45] used a multi-axial mode Cr^{4+}:YAG laser in a technique called Intracavity Laser Spectroscopy (ILS) to detect absorption features due to atmospheric water vapour for wavelengths from 1.4-1.5 μm by purging the laser cavity with dry nitrogen. Several strong, discrete absorption features were measured at wavelengths below 1.48 μm (figure 4.13). These resonances have important consequences when attempting to produce ultrashort pulses from a laser, as discussed later.

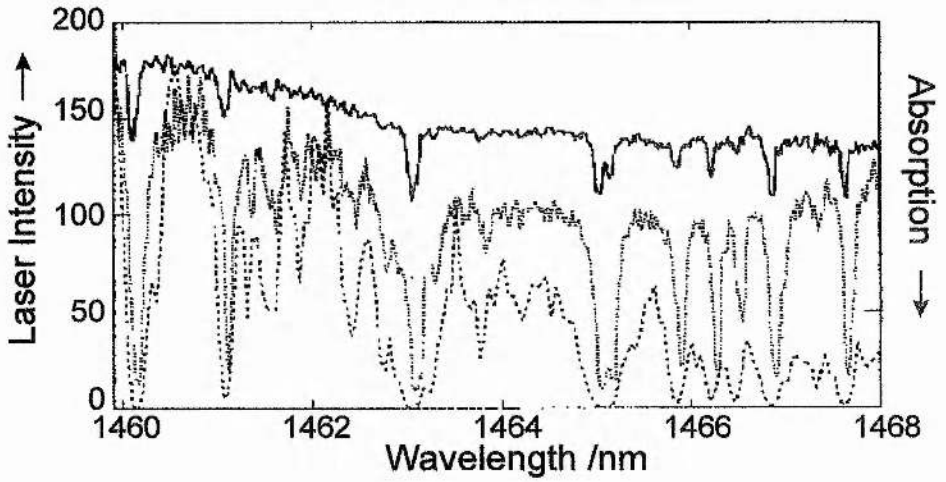

FIGURE 4.13: *ILS spectra of water vapour: (i) dashed line- dry N_2 purging for 20 mins. (ii) dotted line- dry N_2 purging for 45 mins, and (iii) solid line- dry N_2 purging for 19 hrs. (After Gilmore et al.[45])*

The full tuning range of Cr^{4+}:YAG at wavelengths >1.5 μm shown in figure 4.14, was accessible by replacing the output coupler with a high-reflecting end-mirror from mirror set 2. The highly asymmetric tuning curve results from a balance of the high gain of Cr^{4+}:YAG at short wavelengths and the unusually long centre HR wavelength of the mirror set (figure 4.18).

A simple design technique for determining the output power from a longitudinally pumped Ti:Sapphire laser was developed by Alfrey[46], which permitted various cavity parameters to be optimised (e.g. active medium length, pump absorption coefficient and output coupling) for maximum efficiency. This was adapted to simulate a Cr^{4+}:YAG laser by use of the appropriate material parameters from table 4.2, and including a term for the pumping quantum efficiency (assumed unity in Alfrey's original model.)

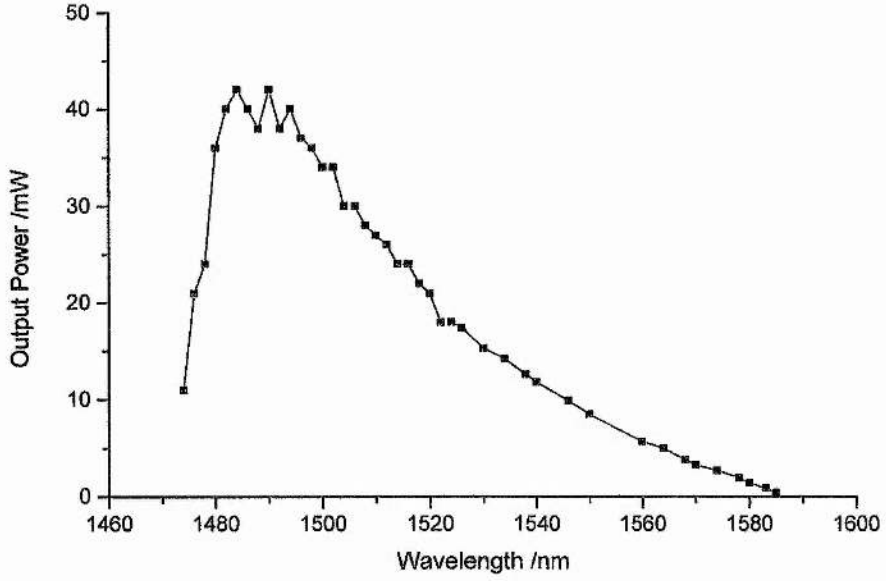

FIGURE 4.14 *Tuning range of Cr,Mg:YAG laser in a resonator with all HR mirrors from mirror set 2.*

The model considers the relationship between the absorbed pump power and the circulating laser field:

$$P_p = \frac{(T+\Lambda)h\nu_p\pi^2}{8\eta_p\sigma\tau\alpha_p\int_0^L \frac{e^{-\alpha_p z}}{w_c^2(z)w_p^2(z)}Q(z)dz} \qquad \text{Equation (4.3)}$$

$\mathbf{P_p}$ is the absorbed pump power; **T** and Λ are the useful (output-coupled) and parasitic cavity-losses respectively; $\mathbf{h\nu_p}$ is the pump photon energy; σ and τ are the material gain cross-section and upper-state lifetime respectively; α_p is the pump absorption coefficient. **L** is the crystal length; **z** is the axial distance from the crystal face. $\mathbf{w_p(z)}$ and $\mathbf{w_c(z)}$ describe the diverging pump and cavity mode beams respectively:

$$w_p^2(z) = w_{p0}^2\left\{1+\frac{(z-z_p)^2\lambda_p^2}{\pi^2 w_{p0}^4 n_p^2}\right\}, \quad w_c^2(z) = w_{c0}^2\left\{1+\frac{(z-z_c)^2\lambda_c^2}{\pi^2 w_{c0}^4 n_c^2}\right\}, \qquad \text{Equation (4.4)}$$

$\mathbf{z_p}$ and $\mathbf{z_c}$ define the location of the pump and cavity beam waists inside the crystal respectively (both set to zero (pumped end of rod) for this simulation). **Q(z)** is defined by integrating the pump and laser fields over the radial co-ordinate **r** and accounts for the effect of gain saturation by the circulating laser field.

$$Q(z) = 2\pi \int_0^{\infty} \frac{e^{-Ar^2} r dr}{1 + Be^{-Dr^2}}$$ Equation (4.5)

where

$$A = \frac{2\left(w_p^2 + w_c^2\right)}{w_p^2 w_c^2}, \quad B = \frac{4}{\pi w_c^2} \frac{P_c}{I_s} \quad \text{and} \quad D = \frac{2}{w_c^2},$$ Equation (4.6)

P_c is the intracavity power and I_s is the saturation intensity, dependent on the parameters of the gain medium:

$$I_s = \frac{h\upsilon_c}{\sigma\tau}$$ Equation (4.7)

where $h\nu_c$ refers to the circulating laser photon energy. The pumping quantum efficiency, η_p in equation 4.3, is set to 20% to simulate the poor efficiency of Cr^{4+}:YAG. An output coupling of 2% and a round trip parasitic loss of 1.5% were used in the simulation as estimated from the Laseroptik mirror reflectivity curves supplied with the mirrors for the 1% output coupler and high-reflectors operating at 1520 nm (figure 4.18). The pump absorption coefficient was simulated at a fixed 2.0 cm^{-1}.

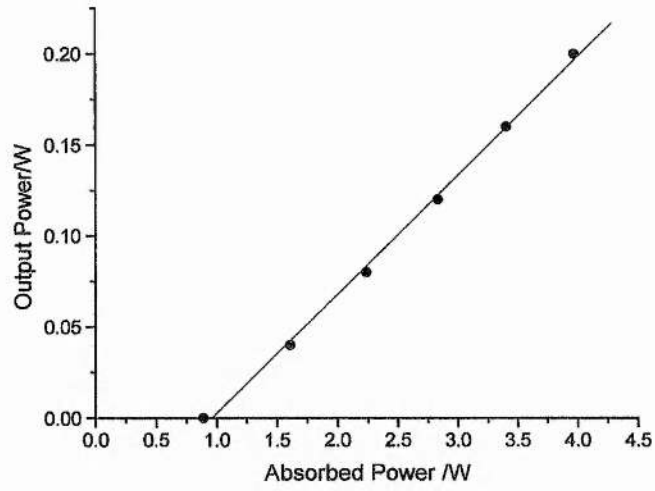

FIGURE 4.15: *Simulation of the power transfer characteristics of a Cr:YAG laser (model developed by Alfrey[46])*

The results of the simulation are summarised in figure 4.15 with a best straight line fit. Despite the poor quantum efficiency of this material, a low cw-threshold of ~700 mW is predicted with a slope efficiency of 6.5%.

The actual power transfer characteristics of the Cr^{4+}:YAG laser for different output coupling arrangements using mirror set 1 (centred at 1.45 μm) are presented in figure 4.16. Due to the limited range of output couplers available, it was necessary to 'double-up' the output coupling in two cases by placing output couplers in each of the long arms in the cavity in figure 4.8. Output powers of up to 370 mW were achieved for 6 W incident pump with slope efficiencies as high as 17 % with 4 % total output coupling. In figure 4.17 the power transfer characteristics with mirror set 2 are summarised. Note that at the free-running wavelength of the laser with these output couplers (1.526 μm for 0.5% O/C and 1.54 μm for the 1% O/C), the actual output coupling is somewhat higher than their rated value: the 0.5% output coupler is closer to 1% while the 1% is nearer 2%, as measured from the manufacturer's measured transmission curves for the mirrors in figure 4.18. The slope efficiency at the longer wavelength region is nearly 8 %.

These results are somewhat different to the theoretically predicted power transfer characteristics in figure 4.15: the slope efficiency is approximately as expected (~7% with 2% output coupling), however the threshold is considerably higher (by more than a factor of two). By adjusting the model parameters for the useful and parasitic losses and the pumping quantum efficiency it is still not possible to model the results observed in practice. Possibly, the crystal used has somewhat different gain cross-section and upper-state lifetime values from the ones reported[31] and used for the model, however, it is also possible that this high threshold is a result of the pump absorption saturation prior to oscillation: below threshold, the pump absorption coefficient 'bleaches' due to increasing pump intensities; once oscillation is established, this saturation reaches a constant level, as was demonstrated in figure 4.10. The model developed by Alfrey does not take into account any variation in pump absorption with intensity and hence a slightly more sophisticated model is essential to accurately simulate a Cr^{4+}:YAG laser.

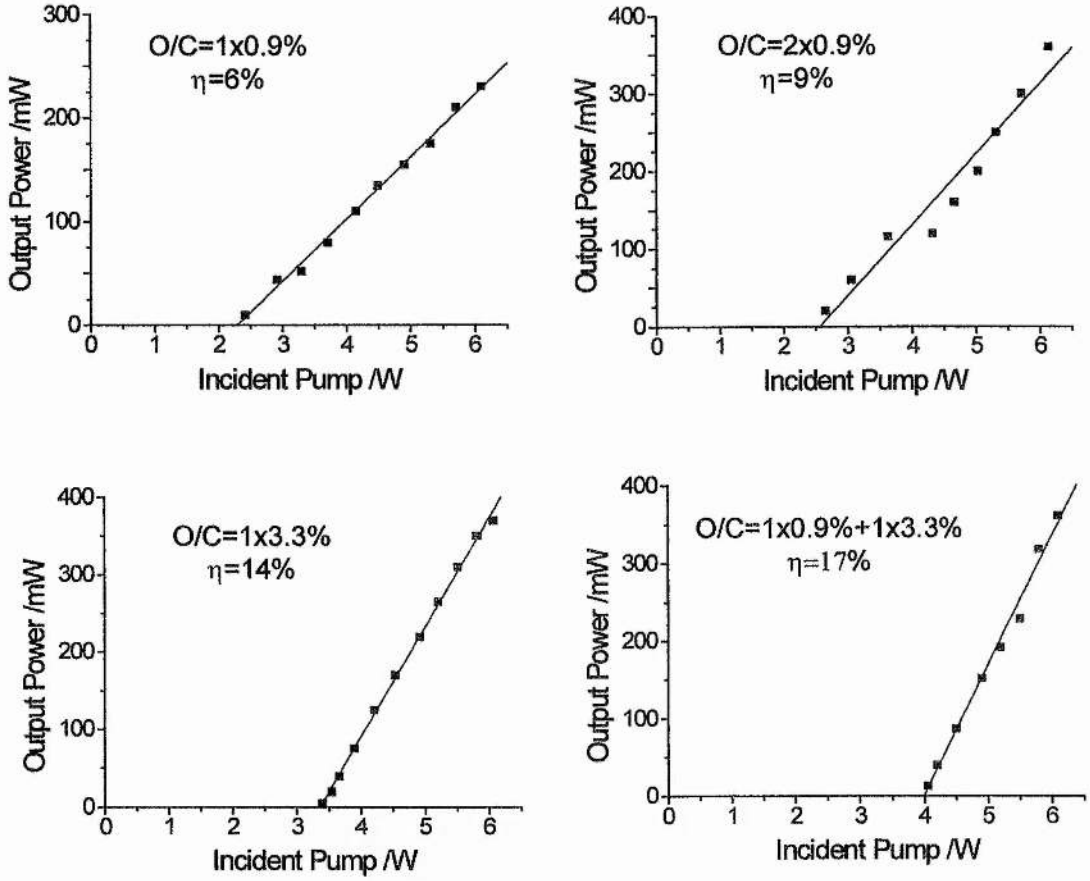

FIGURE 4.16: *Total power out vs. incident pump power for different output coupling arrangements (mirror set 1).*

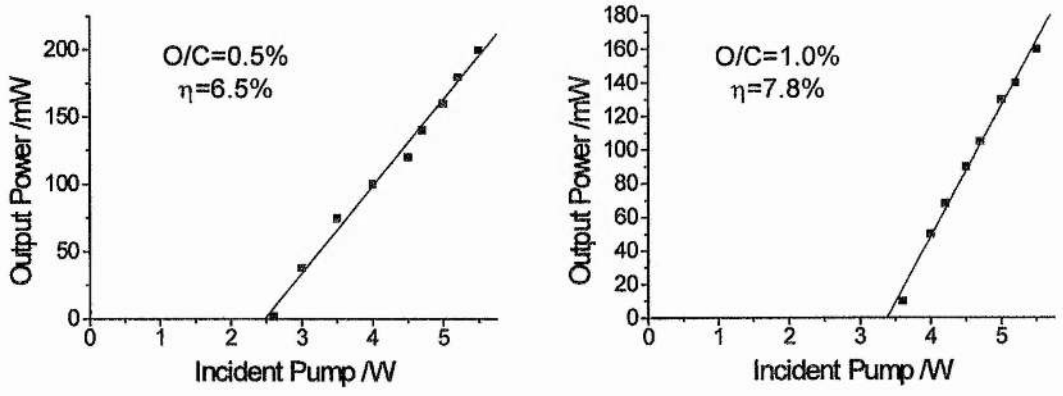

FIGURE 4.17: *Output power vs. incident pump power for Cr,Mg:YAG laser. (mirror set 2)*

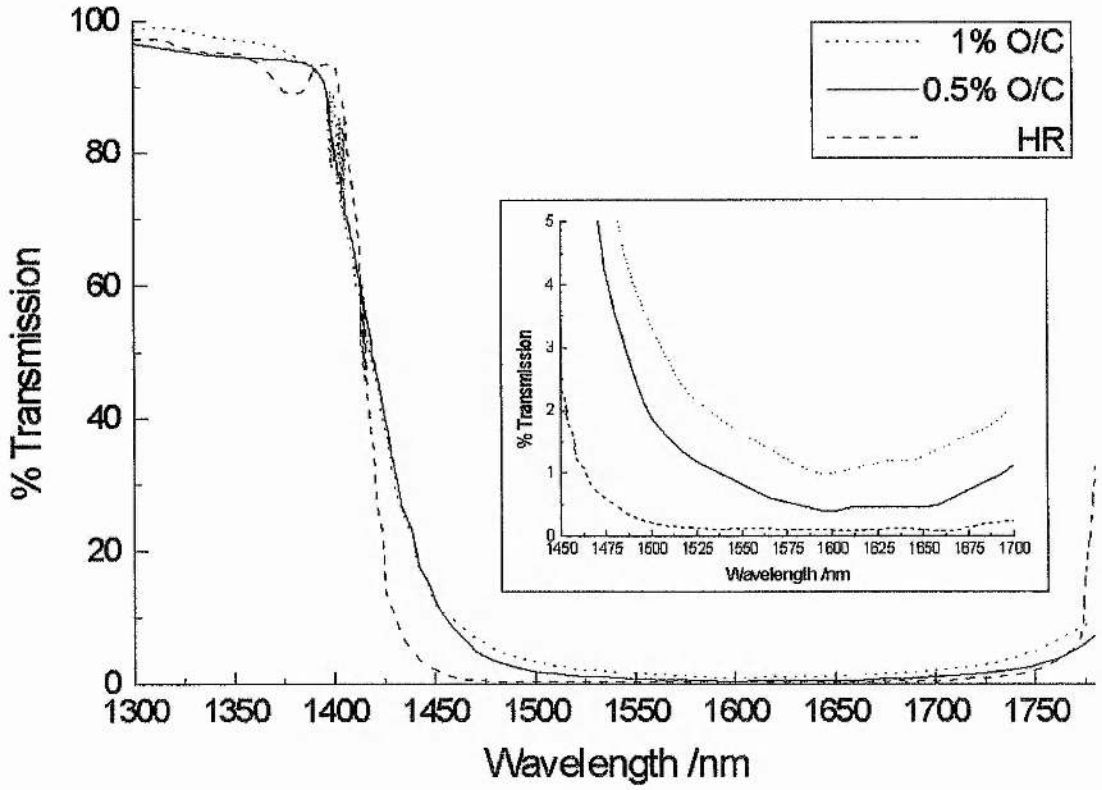

FIGURE 4.18: *Transmission curves for mirror set 2 (long wavelength set) supplied by manufacturers (LaserOptik GmbH). Inset: Detail of transmission near 1.5 μm.*

Using the technique described in ref. 12, it is possible to estimate the intrinsic slope efficiency of the laser η_0, and the total intracavity parasitic losses from the equation:

$$\eta_s = \eta_0 \frac{T}{T+L} \qquad \text{Equation (4.8)}$$

using the measured slope efficiencies η_s, for each output coupling **T**. **L** is the residual parasitic loss in the cavity. By plotting the inverse output coupling against the inverse slope efficiency, a straight line results from equation 4.8 with y-intercept $\mathbf{c}= \eta_0^{-1}$ and gradient $\mathbf{m}=\mathbf{L}/\eta_0$. From figure 4.19, the intrinsic slope efficiency is estimated to be 28 %. This is considerably less than the efficiency predicted by the quantum defect alone (66 %) due to the presence of excited-state-absorption. The total parasitic round-trip cavity losses (including 5 HR-mirror reflections and two passes through the 23mm crystal) are estimated to be as high as 3.5%.

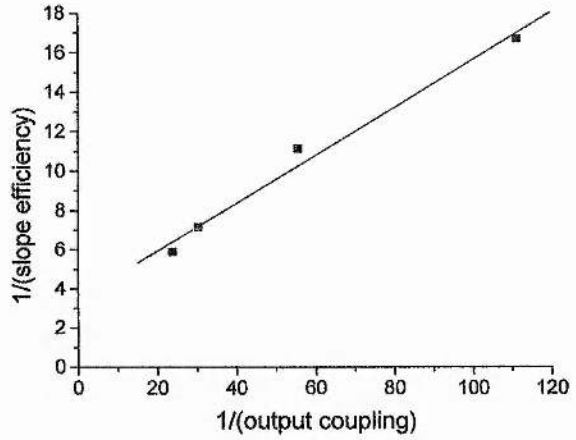

FIGURE 4.19: *Plot of inverse output coupling vs. inverse slope efficiency (data from figure 4.16) to determine intracavity loss and intrinsic slope efficiency.*

4.5.2 Thermal Effects

Property	Value
Melting point	1970° C
Rupture stress	1.3-2.6x10^3 kg.cm^{-2}
Thermal conductivity	0.13 W.cm^{-1}.K^{-1} (at 300K)
Specific heat capacity	0.59 J/gK (at 300K)
Thermal expansion coefficient	7.7-8.2x10^{-6} K^{-1} (0-250°C)
Refractive index (**n**)	1.81 (at 1.5 μm)
Nonlinear refractive index ($\mathbf{n_2}$)[47]	1.9x10^{-15} cm^2W^{-1}
$\frac{dn}{dT}$	7.3x10^{-6} K^{-1}

TABLE 4.3: *Important physical and optical properties of the YAG host crystal*[48].

Yttrium aluminium garnet (YAG) is an excellent host material for laser active ions (as demonstrated by the success of Nd^{3+}:YAG). Some relevant physical and optical properties are presented in table 4.3. Important characteristics are its high thermal conductivity and physical toughness. Unfortunately, the refractive index of the material

has a large temperature dependence (i.e. large **dn/dT**) and it possess a high thermal expansion coefficient resulting in strong thermal lensing under high pump power excitation. Using the method suggested by Innocenzi[49] for estimating the thermal lensing induced in a rod, described in section 2.4.2.1, with parameters pertinent to the Cr^{4+}:YAG laser (partially saturated differential absorption coefficient α~1.8 cm^{-1}; crystal length **l**=23 mm; diffraction-limited pump beam of incident power $\mathbf{P_{ph}}$=6.0 W, focussed in the end of the rod to a waist of size $\mathbf{w_0}$=40 μm), the total effective thermal lens of the rod is $\mathbf{f_{eff}}$=2.6 mm. Note that a normal diverging Gaussian beam was modelled here unlike the non-diffraction-limited beam modelled in section 2.4.2.1. This is a substantially stronger lens than that normally encountered with a Nd^{3+}:YAG laser and results from the tight focussing of the pump beam: focal length is proportional to the square of the pump radius. The lens is likely to be slightly weaker than this as no variation in the differential absorption coefficient through the crystal is taken into account. As discussed in section 4.5.1, pump absorption saturation plays an important role in the operation of this laser and it is likely that at the pump focus, the absorption coefficient is less than the 1.8 cm^{-1} estimated here.

This strong thermal lens is not as problematic in a Cr^{4+}:YAG laser as in a Nd^{3+}:YAG laser: for good pump-laser mode overlap, the location of the strongest thermal lens should coincide with the intracavity beam waist, where the lens will have least effect. In figure 4.20, the effect of varying the focussing condition of the pump inside the rod is modelled. Non astigmatic pump beams were assumed and no variation in absorption saturation due to tight focussing was taken into account. For the case with the foci located on the pumped end of the rod, a highly localised thermal lens at the laser beam waist results in minimal detrimental effect on laser cavity stability. In contrast, if the pump is focussed to match a beam in the centre of the crystal, the thermal lens is equally distributed throughout half the laser rod. Finally, if the pump is focussed on to the far side of the laser rod, a completely non-localised thermal lens results, although the overall effective focal length is considerably weaker.

Considering that in a normal symmetric 4-mirror Z-cavity layout based around a Brewster-angled gain medium the intracavity laser mode suffers from a 'distributed' focus inside the rod due to astigmatic effects, the deleterious effect of a distributed thermal lens will be exacerbated thus severely affecting laser cavity stability. The ideal situation is to locate the tangential and sagittal intracavity laser modes simultaneously

on the pumped end of the rod to match a focussed pump beam. How this can be achieved will be discussed in chapter 5.

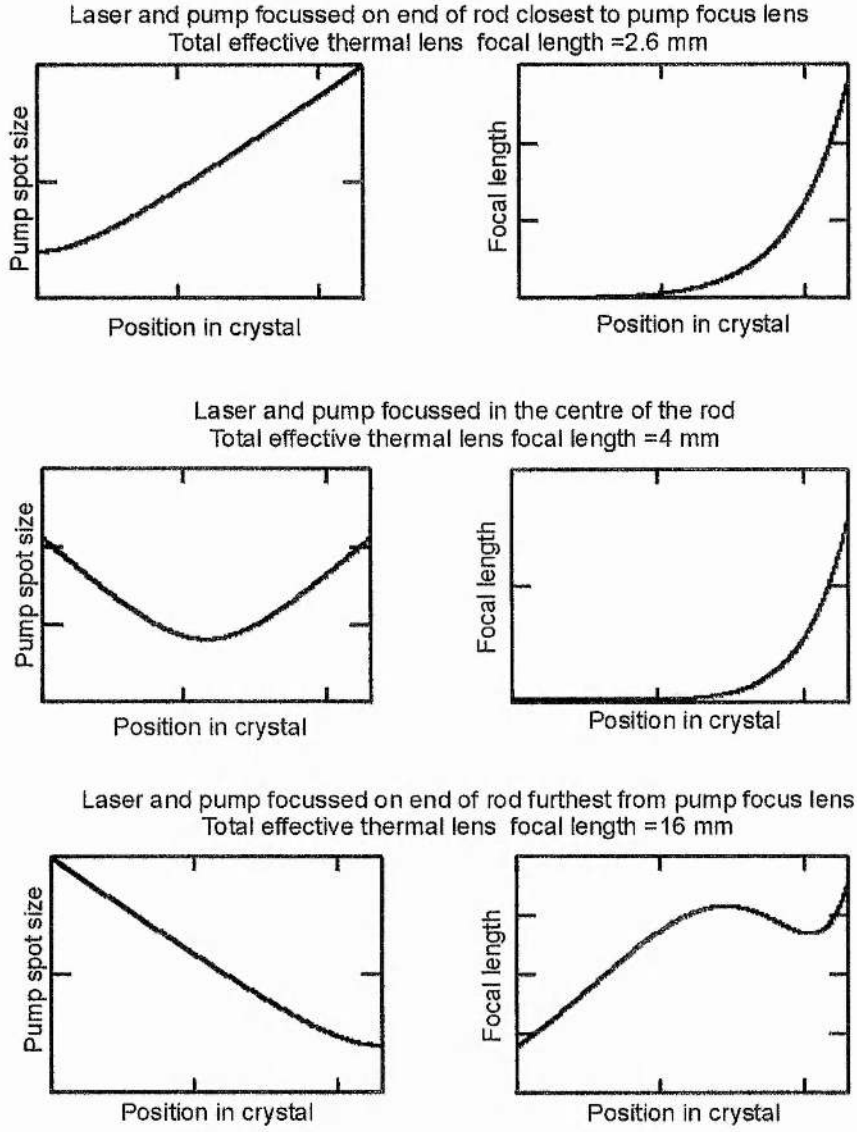

FIGURE 4.20: *Location of the thermal lens inside a Cr:YAG rod for three different cases of pump and laser mode focussing.*

A simple model of the distributed thermal lens can be developed based on the thermal lens equation of Innocenzi[49] in a round-trip resonator simulation using ABCD matrices: the distributed thermal lens matrix is constructed by 'slicing up' the laser rod and calculating the lens strength in each slice for the diverging pump beam of decreasing power. The final matrix is a product of all these slices with the thickness of each slice and is included as an element in the round trip matrix of the laser resonator. Using this simple technique, it is straightforward to predict the effect of strong thermal

lensing on laser cavity stability. Based on a standard symmetric 4-mirror Z-cavity with a Brewster-angled gain medium, the simulation was performed for different incident pump powers, summarised in figure 4.21. Contour plots of the changing spot size (calculated at the pumped end of the laser crystal) are shown in figure 4.21 as the folding mirror separation and the position of the laser rod between the folding mirrors are varied. The stability zone for the sagittal plane is shown as a greyscale plot behind a transparent black-line plot for the corresponding tangential plane in each contour plot. The laser cavity is only stable in areas where the both the sagittal and tangential regions coincide. For zero incident pump power (figure 4.21(a)), there is no distributed lens present and hence moving the laser rod between the two folding mirrors has no effect on the stability of the laser resonator; only varying the mirror separation changes the laser cavity stability. The sagittal and tangential stability zones are completely overlapped as these parameters are varied as the angle of the folding mirrors has been set to entirely compensate for the astigmatism introduced by the Brewster-angled gain element. As the pump power is increased to 1W, the deleterious effect of a distributed thermal lens becomes apparent (figure 4.21(b)). The position of the laser rod between the folding mirrors now has an obvious effect on the overall cavity stability as it is now a lens of considerable strength. The tangential and sagittal stability zones now overlap for only approximately half of the total area; it is impossible to completely compensate for the astigmatism of a Brewster-angled rod containing a distributed lens for all folding mirror separations. Increasing the incident pump power to 5W considerably compromises the range of parameters over which the resonator is stable: the sagittal and tangential planes overlap over a very small region.

Inevitably it follows that aligning a laser such as this to operate cw under high pump powers is difficult as the range of cavity parameters over which the resonator is stable is small. Often it is necessary to use a chopped pump beam for alignment. One simple approach to reducing the destabilising effect of the distributed thermal lens is to use a plane-plane gain element with anti-reflection coatings and operating the folding mirrors at near normal incidence. This prevents any differentiation of the sagittal and tangential planes inside the resonator and hence much larger stability zones result –that is- the sagittal and tangential zones are always overlapped.

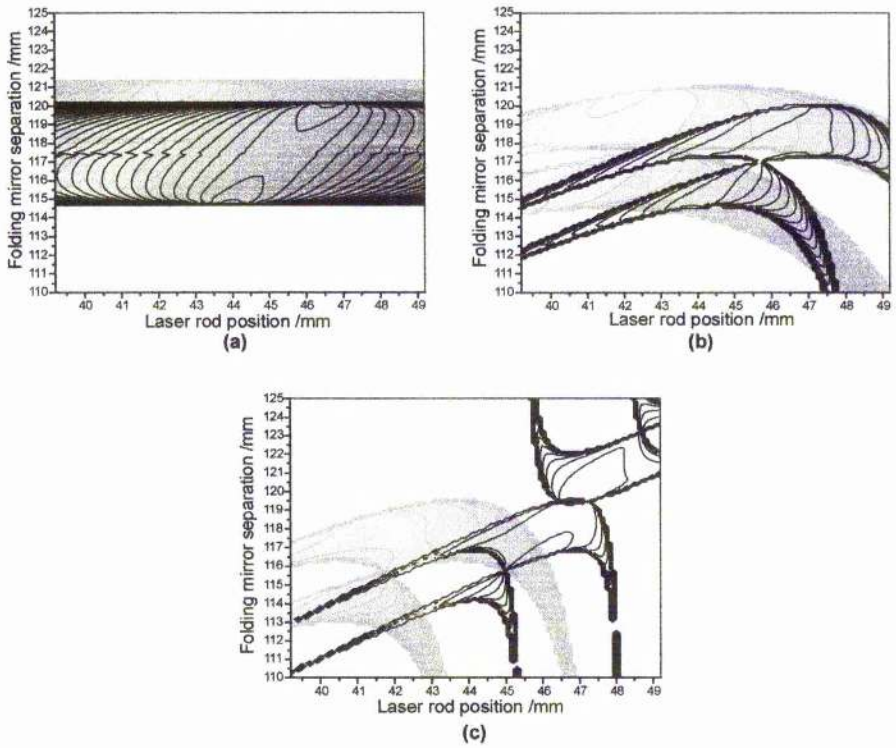

FIGURE 4.21: *Contour plots of the tangential (black outline) and sagittal (variable greyscale) stability regions for a symmetric 4-mirror Z-cavity based on a Brewster-angled gain element as the folding mirror separation and gain element position are varied for increasing thermal lens strength.*
(a): $P_{incident}=0W$, **(b):** $P_{incident}=1W$, **(c):** $P_{incident}=5W$

A simple demonstration of how the destabilising effect of the thermal lens is minimised by placing the cavity focus on the pumped end of a plane-plane rod is given in figures 4.22-4.23. In figure 4.22(a), both the cavity and pump foci are made to coincide on the end of the rod (z=0) for zero incident pump power. Applying 1W incident pump (figure 4.22(b)) has no noticeable effect on the beam inside the laser rod (and hence on overall cavity stability). Conversely, if the cavity focus is positioned on the far side of the rod (z=23mm) from the pumped facet (figure 4.23(a)), applying just 1W incident pump power has a dramatic effect on the beam inside the rod (and hence on the beam throughout the laser resonator). No resonator would normally be operated at this extreme but it does illustrate the importance of carefully matching the location of the intracavity foci with the strongest point of the distributed thermal lens, and suggests that pumping a laser rod from both ends which suffered from strong thermal lensing would be difficult.

For a Brewster-angled rod inside a symmetric resonator, it is impossible to place both the sagittal and tangential foci simultaneously on the pumped end of the rod hence

the distributed lens will always have a considerable destabilising effect on such a resonator. In chapter 5 alternative resonator designs are developed which do allow both foci to coincide on the pumped end of a Brewster-Brewster laser rod and the improvement in immunity to strong thermal lensing will be modelled.

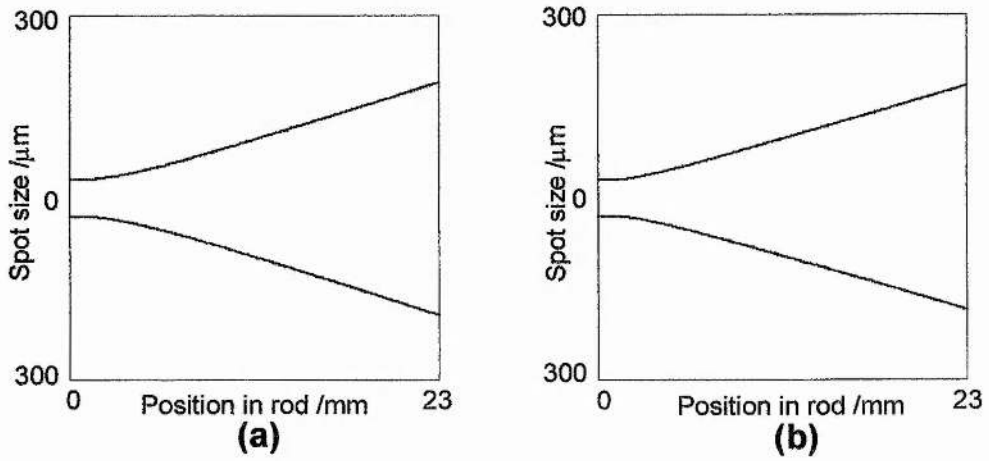

FIGURE 4.22: *Effect of a distributed thermal lens on the beam inside the 'lensed' plane-plane laser rod with the intracavity focus placed to coincide with the pump focus on the pumped side of the rod at z=0* **(a)** *zero pump power.* **(b)** *pumped with 1W incident.*

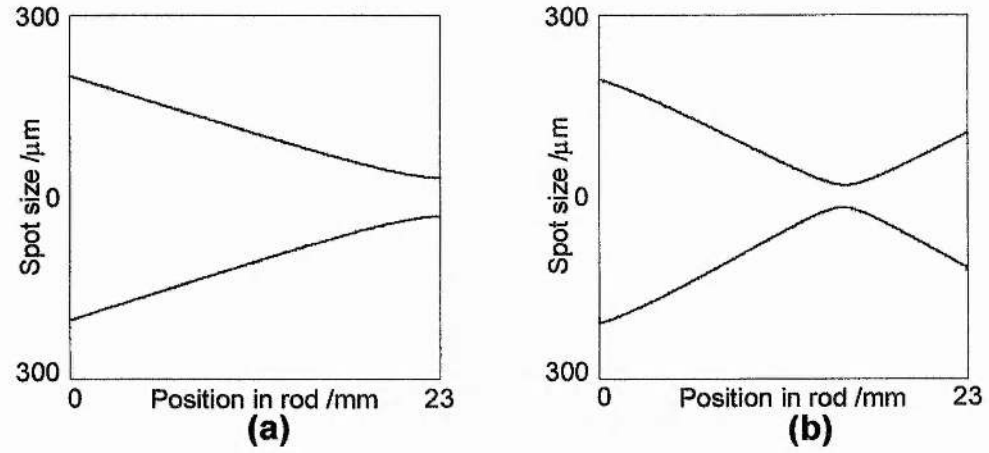

FIGURE 4.23: *Effect of a distributed thermal lens on the beam inside the 'lensed' plane-plane laser rod with the intracavity focus placed on the 'unpumped' end of the rod. Pump focus is still placed at z=0.* **(a)** *zero pump power.* **(b)** *pumped with 1W incident.*

A dramatic practical demonstration of the deleterious effect of the thermal lens on laser cavity stability can be clearly shown by observing how the Cr^{4+}:YAG laser output power fluctuates during a chopped pump pulse (figure 4.24). A chopper wheel with a

10 % duty cycle was placed in the pump path of a Cr^{4+}:YAG laser optimised for cw operation at high pump powers. The actual laser cavity studied was a symmetric ring laser which was optically equivalent to a symmetric 4-mirror Z-cavity. A large area germanium photodiode had sufficient bandwidth to permit fast fluctuations in output power to be resolved.

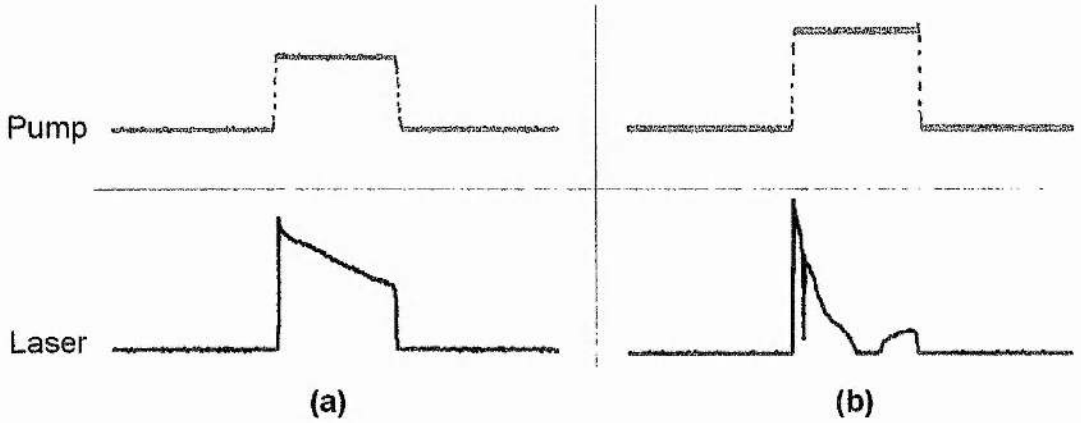

FIGURE 4.24: *Effect of a changing thermal lens with a chopped (10% duty cycle) pump beam.* **(a):** *Low threshold laser (all HR mirrors) pumped with a low pump power (1.5 W).* **(b):** *Laser fitted with 0.5 % output coupler with high incident pump power (6.0 W). Note: vertical axes not to scale. See text for details.*

Using a cavity consisting of all high-reflecting mirrors permitted cw oscillation to be attained for low incident pump powers (figure 4.24 (a)). For just 1.5 W peak pump power, forming a thermal lens which stabilises at ~10 mm, the laser output power slowly decreases during the pump pulse due to heating of the Cr^{4+}:YAG rod. Installing a 0.5 % output coupler to the laser cavity and pumping at high peak powers (6.0 W) resulted in the laser output trace shown in figure 4.24 (b). The laser oscillates on and off during the rising edge of the pump pulse. Laser output then rapidly decreases due to heating of the laser rod and thermal lens strength increases to a point where the cavity is no longer stable and laser output ceases. However, a short while further into the pump pulse, the stronger thermal lens permits a second resonant stability condition to be accessed causing the laser to start emitting once again. Careful observation of the trace in figure 4.24 (b) shows a slight increase in output power during the remaining pump pulse suggesting that oscillation would continue on removal of the chopper (i.e. under cw excitation).

From the results shown in figure 4.24 it should be clear how important the role of the thermal lens is for optimum operation of a Cr^{4+}:YAG laser. A Cr^{4+}:YAG laser could operate satisfactorily under quasi-cw (chopped) excitation, however the presence of a

strong thermal lens during cw-pumping will compromise cavity stability to the point where resonance can no longer be achieved. During the initial stages of laser cavity design, it is imperative that a thermal lens is included in any modelling to ensure the final laser operates with maximum performance under cw-pumping. Often a strong thermal lens necessitates a larger mirror folding angle to compensate for the astigmatic Brewster-cut gain element.

Output power deterioration during CW-pumping

Even after compensating for thermal lensing, Cr^{4+}:YAG suffers from an unfortunate drawback under cw excitation: the output power slowly deteriorates over time. Figure 4.25 comprises three traces of output power vs. time each of ~5 mins duration taken over a 2½ hour interval. For clarity, the plot is broken into five sections (A-E):

A: Pump unblocked at 0 seconds: after a stable thermal lens is reached permitting laser oscillation, the initial laser output of 47 mW rapidly decreases to 44 mW then more slowly decreases to 42 mW after 400 secs.

B: 1 hour later, laser output has dropped to 37 mW. There is no appreciable change over a 9 minute interval.

C: 1½ hours later, laser output power is just 32 mW.

D: Laser rod is transversally translated to access a cooler unpumped region of the crystal. Output power increases from 32 mW to 48 mW then rapidly decreases to ~44 mW.

E: During the next five minutes the output power once again drops to ~40 mW and the cycle continues.

Note that these measurements were taken from a laser fitted with all HR-mirrors pumped cw at 6.0 W. For high output coupling (~1%) the situation is considerably worse since the laser is operating closer to threshold, and laser oscillation might even cease after a few hours. Simply translating the crystal permits operation once again however the output power will deteriorate over a period of a few hours.

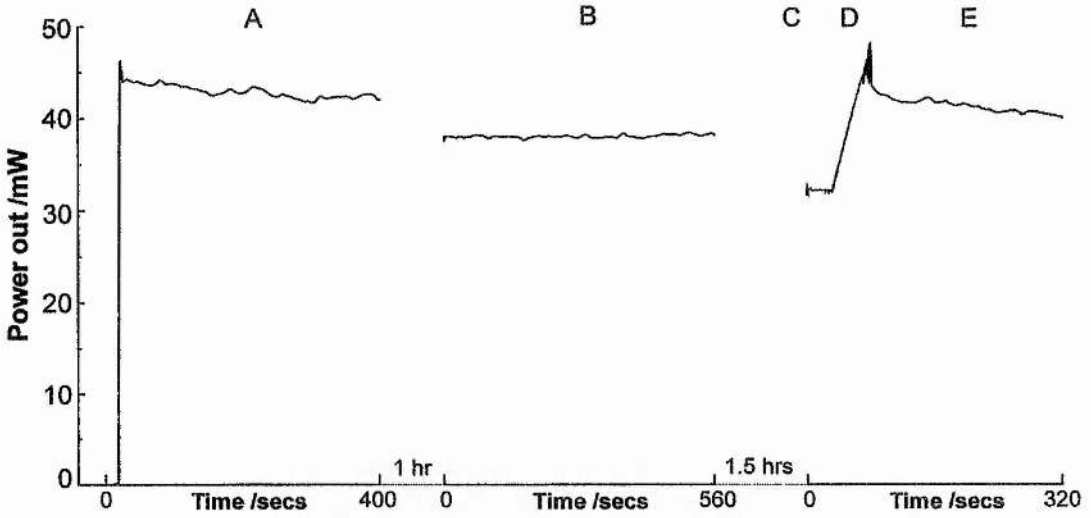

FIGURE 4.25: *Decrease in Cr:YAG output power during cw operation at high (6.0 W) incident pump powers. See text for details.*

The precise reason why the output power should deteriorate in such a way over such long time intervals is unclear. The problem only arises under high pump power excitation. Photorefractive damage has been suggested as a possible cause: most thermal effects occur over a much shorter time interval[50].

4.6 Requirements for a Self-Modelocked Cr^{4+}:YAG Laser

Cr^{4+}:YAG exhibits broadband tunability from ~1.38-1.58 μm and so it was expected that it would be a suitable gain medium for a self-modelocked laser producing tunable femtosecond pulses throughout this wavelength region. Although the quantum efficiency of Cr^{4+}:YAG is somewhat less than other materials which have been successfully incorporated into self-modelocked laser systems (e.g. Ti:sapphire, Nd:YAG and Cr^{3+}:LiSAF), the crystal quality is sufficient to permit high intracavity powers to be maintained with low output coupling providing high useful output powers of up to 1.2 W at the gain peak at ~1.45 μm. In addition, the YAG host material has a high nonlinear refractive index (n_2=1.9x10^{-15} cm^2W^{-1}) implying that a strong nonlinear lens could be formed inside the gain medium itself for successful self-modelocking.

First attempts to establish femtosecond operation were unsuccessful. Even the incorporation of a regenerative modelocking initiation scheme failed to create pulses shorter than ~20 ps. Other research groups reported similar observations. Conlon et al.[51] postulated that the discrete atmospheric water resonances known to exist below 1.5 μm

(as demonstrated by Gilmore et al.[45] reproduced in figure 4.13) created sharp dispersion features which severely limit the bandwidth available to support modelocked pulses. Evidence for this was the possibility of only passively modelocking the laser to generate pulses as short as ~3 ps at discrete wavelengths as the laser was tuned from 1.4-1.5 μm. To confirm that dispersion was discontinuous, a technique similar to that described by Knox[52] was carried out by Conlon et al.[53] Originally, this technique involved tuning a passively modelocked laser and recording variations in the pulse repetition rate which corresponded to changes in the overall effective optical length of the laser cavity. Hence it was possible to determine the overall dispersion in the cavity from the expression for the cavity round trip time **T**:

$$T = \frac{2}{c}(L-1) + \frac{2l}{v_g} \qquad \text{Equation (4.9)}$$

L is the total cavity length and ***l*** is the total length inside all dispersive elements inside the cavity; $\mathbf{v_g}$ is the group velocity.

Because it was not possible to successfully passively modelock the Cr^{4+}:YAG laser, a slightly modified technique was employed by Conlon et al. A synchronously-pumped modelocked Cr^{4+}:YAG laser was set up (similar to the $NaCl:OH^-$ laser in chapter 3) and the slave cavity length detuning which was necessary to maintain the shortest SPML modelocked pulse was recorded as the slave Cr^{4+}:YAG laser was tuned. Two mirror sets were used: one covering up to 1.5 μm, the other centred for ~1.54 μm. In figure 4.26(a), the necessary detuning is plotted as a function of wavelength. From this it is straightforward to determine the wavelength dependence of the group velocity. Using the expression[53]:

$$\frac{dL}{d\lambda} = -cl\frac{d}{d\lambda}\left(\frac{1}{v_g}\right) = -clD \qquad \text{Equation (4.10)}$$

it is straightforward to determine the wavelength dependence of the dispersion parameter, **D** (show in figure 4.26(b)), from differentiation of the data in figure 4.26(a).

From figure 4.26(b), it can be observed that there are small discontinuities in the cavity dispersion throughout the 1.4-1.5 μm region which are impossible to compensate for using conventional techniques. However it is important to note that beyond 1.5 μm the dispersion is smooth allowing straightforward GVD compensation using a simple prism pair or chirped mirrors.

After substitution of the short wavelength mirror set, optimised for maximum output power from the laser, with a longer wavelength set (mirror set 2 in figure 4.26) to allow operation at wavelengths longer than 1.5 μm, Conlon et al. reported femtosecond pulsed operation with a suitably aligned cavity via self-modelocking.

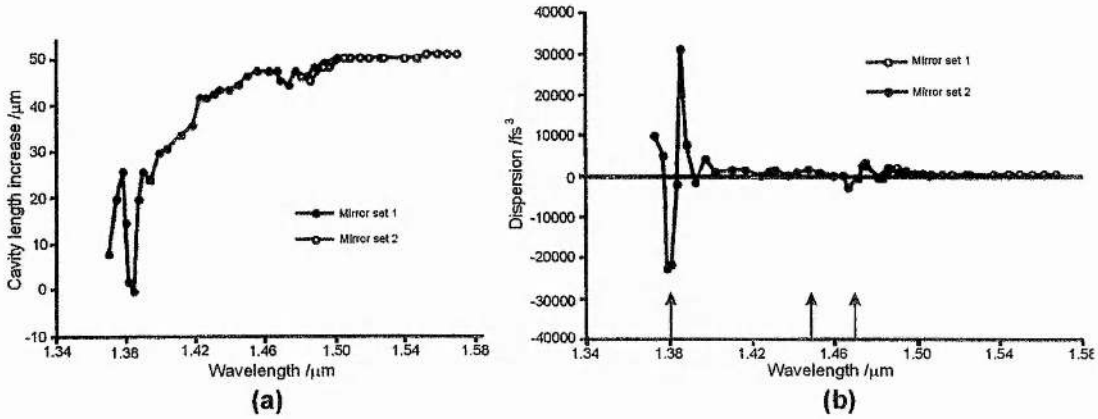

FIGURE 4.26: *Measurement of intracavity dispersion between 1.34-1.58 μm using a Cr:YAG laser (after Conlon et al.[53]).* **(a):** *Required cavity length detuning of a synchronously modelocked Cr:YAG laser to maintain the shortest pulse duration as the laser is tuned.* **(b):** *Intracavity dispersion vs. wavelength calculated from (a). The arrows indicate strong water absorption lines.*

For the first Cr^{4+}:YAG laser studied, a conventional astigmatically compensated 4-mirror Z-cavity laser (discussed in chapter 5) was employed with intracavity negative group velocity dispersion provided by a fused silica prism pair. The original Cr^{4+}:YAG mirror set was highly reflecting from 1.35-1.5 μm but the operating wavelength was shifted to 1.48 μm using a colour-centre laser high reflector (optimised for operation at 1.58 μm) as an output coupling plane end-mirror. This provided 0.3% output coupling at 1.48 μm. A Brewster-angled fused silica acousto-optic modulator was incorporated into the cavity to assist in initiating passive-modelocking via the Kerr-lens effect inside the gain medium (self-modelocking). Initially this was driven actively using a frequency synthesiser, but later a regenerative initiation scheme was deployed which derived the modulator drive frequency from the longitudinal mode-beating signal of the laser cavity itself[54].

Self-modelocked operation was observed after careful adjustment of the cavity mirrors, in the form of a rapid spiking of the second harmonic signal from the autocorrelator indicating that modelocked operation was occurring for exceptionally short durations. The spiking frequency and duration were insufficient to permit an

autocorrelation trace to be constructed by the autocorrelator. Dispersing dry nitrogen gas around the folding section of the laser cavity increased the frequency of the spiking, further reinforcing the suggestion that atmospheric water was terminating modelocked operation. In an attempt to overcome this effect, a Perspex box was placed around the entire laser cavity and filled with dry nitrogen. Modelocking could then be routinely obtained after careful adjustment of the folding mirrors permitting a partial trace to be recorded, however it was still exceptionally unstable.

A new mirror set was obtained for operation centred at ~1.58 μm covering the region 1.51-1.6 μm to force the laser to operate outside the peak gain region of the Cr^{4+}:YAG gain medium thus avoiding all atmospheric water absorption effects. This now permitted stable self-modelocking to be routinely established. Unfortunately it was soon apparent that the gain of all of the early Cr^{4+}:YAG samples was exceptionally low when operated beyond 1.5 μm and the useful output power available from the early 4-mirror Z-cavity design self-modelocked lasers was disappointing. A new approach for operating this laser self-modelocked was necessary to maximise the useful output power which is the subject of the next chapter.

4.7 Concluding Remarks

In this chapter, some of the characteristics of the Cr^{4+}:YAG gain medium have been outlined in the context of a material for the construction of a tunable laser covering the 1.55 μm spectral region. The fundamental features which make vibronically broadened gain media attractive as tunable solid-state lasers were described and the basic spectroscopy of the Cr^{4+} ion in the YAG host matrix was also presented.

Unusual features of Cr^{4+}:YAG were discussed. Crystals of Cr^{4+}:YAG require charge-compensating dopant ions and an oxidising atmosphere during growth using the Czochralski method. Post growth annealing at high temperatures in an oxidising atmosphere is often necessary. The Cr^{4+} ions are incorporated into anisotropic sites inside an isotropic crystal creating an exceptional highly active optical centre with unusual polarisation dependent properties. Absorption saturation plays an important part in the operation of the Cr^{4+}:YAG laser and a measurement was performed showing the effect of stimulated emission inside a laser resonator on the saturation of the crystal pump absorption.

Some of the basic operating characteristics of a cw pumped Cr^{4+}:YAG laser were detailed with difficulties unique to the Cr^{4+}:YAG system highlighted: all earlier crystal samples had exceptionally low gain at wavelengths >1.5 μm preventing efficient operation in the interesting 1.55 μm communications region. One later rod obtained from Union Carbide possessed high gain extending to the 1.58 μm region, however, surprisingly a second rod of different dimensions cut from the same boule showed the same low gain at long wavelengths as the earlier rods. The reason for this is unclear but excited state absorption due to a contaminant is a possibility. Historically, all early Cr^{4+}:YAG lasers reported[22,29] showed no appreciable gain at longer then 1.5 μm which may be an indication that improved crystal growth enables higher gain at longer wavelengths.

Due to the low pumping quantum efficiency (~15%) of Cr^{4+}:YAG, it is necessary to use high incident pump powers to access useful output powers. This leads to a strong thermal lens inside the laser crystal which must be taken into account when designing laser resonators. A simple model of a distributed thermal lens was developed to demonstrate the important destabilising effect of high pump powers on a laser resonator.

Despite drawbacks of low efficiency and inconsistent crystal gain performance, Cr^{4+}:YAG is the most promising solid-state material for operation in the 1.5 μm region: it can be conveniently pumped at 1.064 μm with a diode-pumped Nd:YAG laser; direct diode pumping with InGaAs diodes at 970 nm is also possible[38] and the host material is physically tough and possesses excellent thermal conductivity. Although other garnet host materials have been used for Cr^{4+} in an attempt to shift the peak of the gain band to longer wavelengths, their efficiencies have been considerably lower than Cr^{4+}:YAG.

At the conclusion of this chapter, the potential of this gain medium for ultrashort pulse generation has been considered using passive modelocking and the difficulties associated with the discrete absorption features of atmospheric water have been highlighted. In the chapter following, laser cavity design is discussed with the aim of building an efficient self-modelocked laser system based on a gain medium with low gain (such as Cr^{4+}:YAG operated beyond 1.5 μm). Results from several self-modelocked Cr^{4+}:YAG laser configurations will be described.

References

1 D.M. Spirit and M.J. O'Mahony in *'High Capacity Optical Transmission Explained'* (John Wiley and Sons-BT Series Chichester 1995)

2 A.P. Shkadarevich, *OSA Proceedings on tunable solid state lasers* (Optical Society of America, Washington D.C. 1989) **Vol 5**, p 60

3 F.P. Schafer, F.P.W. Schmidth and J. Volze, *Appl. Phys. Lett.* **9**, 306 (1966)

4 W. Gellermann, *J. Phys. Chem. Solids* **52**, 249 (1991)

5 Naturally occurring corundum contaminated with Ti^{3+} was examined spectroscopically in the 1960's (D.S. McClure *J. Chem. Phys.* **36**, 2757 (1962)) however the first laser based on this material was reported at the IQEC in 1982 by Moulton, details are given in: P.F. Moulton, *J. Opt. Soc. Am. B* **3**, 125 (1986)

6 I.D. Jung, F.X. Kärtner, N. Matuschek, D.H. Sutter, F. Morier-Genoud, Z. Shi, V. Scheuer, M. Tisch, T. Tschudi and U. Keller, *Appl. Phys. B* **65**, 137 (1997)

7 L.F. Johnson, R.E. Dietz and H.J. Guggenheim, *Phys. Rev. Lett.* **11**, 318 (1963)

8 T.H. Maiman, *Nature* **187**, 493 (1960)

9 J.E. Geusic, H.M. Marcos and L.G. Van Uitert, *Appl. Phys. Lett.* **4**, 182 (1964)

10 J. Aus der Au, F.H. Loesel, F. Morier-Genoud, M. Moser and U. Keller, *Opt. Lett.* **23**, 271 (1998)

11 P.F. Moulton, *J. Opt. Soc. Am. B* **3**, 125 (1986)

12 S.A. Payne, L.L. Chase, L.K. Smith, W.L. Kway, and H.W. Newkirk, *J. Appl. Phys.* **66**, 1051 (1989)

13 S.T. Lai, *J. Opt. Soc. Am. B* **4**, 1286 (1987)

14 V. Petricevic, S.K. Gayen, and R.R. Alfano, *Opt. Lett.* **14**, 612 (1989)

15 A. Sennaroglu, C.R. Pollock, and H. Nathel, *J. Opt. Soc. Am. B* **12**, 930 (1995)

16 S.T. Lai, and M.L. Shand, *J. Appl. Phys.* **54**, 5642 (1983)

17 V. Petricevic, S.K. Gayen, and R.R. Alfano, *Appl. Phys. Lett.* **52**, 1040 (1988)

18 V. Petricevic, S.K. Gayen, and R.R. Alfano, *Appl. Phys. Lett.* **53**, 2590 (1988)

19 H.R. Verdun, L.M. Thomas, D.M. Andrauskas, T. McCollum, and A. Pinto, *Appl. Phys. Lett.* **53**, 2593 (1988)

20 N.B. Angert, N.I. Borodin, V.M. Garmash, V.A. Zhitnyuk, A.G. Okhrimchuk, O.G. Siyuchenko, and A.V. Shestakov, *Sov. J. Quantum Electron.* **18**, 73 (1988)

V.M. Garmash, V.A. Zhitnyuk, A.G. Okhrimchuk and A.V. Shestakov, *Inorganic Materials* **26**, 1448 (1990)

21 N.I. Borodin, V.A. Zhitnyuk, A.G. Okhrimchuk, A.V. Shestakov, Bull. Acad. Sci. USSR Phys. Ser. (publ. USA) **54**, 54 (1990)

22 A.V. Shestakov, N.I. Borodin, V.A. Zhinyuk, A.G. Ohrimtchyuk, and V.P. Gapontsev, in Post-Deadline paper in *Conference on Lasers and Electro-Optics* (Optical Society of America, Washington, D.C. 1991) paper CPDP11-1

23 Y. Shimony, Y. Kalisky and B.H.T. Chai, *Opt. Mater.* **4**, 547 (1995)

24 H. Eilers, U. Hömmerich, S.M. Jacobsen, W.M. Yen, K.R. Hoffman and W. Jia, *Phys. Rev. B* **49**, 15505 (1994)

25 A. Brenier, A. Suchoki, C. Pedrini, G. Boulon and C. Madej, *Phys. Rev. B* **46**, 3219 (1992)

26 S. Kück, K. Petermann, U. Pohlmann and G. Huber, *Phys. Rev. B* **51**, 17323 (1995)

27 A. Ikesue, K. Yoshida and K. Kamata, *J. Am. Ceramic soc.* **79**, 507 (1996)

28 S. Kück, K. Petermann and G. Huber, *OSA proc. On advanced solid state lasers* (Optical Society of America, Washington D.C. 1991) vol. **10**, p92

29 A.V. Shestakov, N.I. Borodin, V.A. Zhinyuk, A.G. Ohrimtchyuk, and V.P. Gapontsev, in Post-Deadline paper in *Conference on Lasers and Electro-Optics* (Optical Society of America, Washington, D.C. 1991) paper CPDP11-1

30 A. Sennaroglu, C.R. Pollock, and H. Nathel, *J. Opt. Soc. Am. B* **12**, 930 (1995)

31 H. Eilers, U. Hömmerich, S.M. Jacobsen, W.M. Yen, K.R. Hoffman and W. Jia, *Phys. Rev. B* **49**, 15505 (1994)

32 S. Kück, K. Petermann, U. Pohlmann and G. Huber, *Phys. Rev. B* **51**, 17323 (1995)

33 S. Kück, K. Petermann, U. Pohlmann and G. Huber, *J. Lumin.* **68**, 1 (1996)

34 Union Carbide Corporation, 750 South 32nd St., Washougal, WA 98671

35 IRE POLUS Co. Vvedenskogo Sq. 1, Fryazino, Moscow, Russia. UK agents: Elliot Scientific Ltd., St. Albans, Herts.

36 Institut für Angewandte Physik, Universität Hamburg, D-2000 Hamburg, Germany.

37 Y. Kalisky, R.. Mencorge, Y. Guyot and M. Kokta in *Advanced Solid State Lasers* (1998) Vol. **19** of OSA Technical Series (Optical Society of America, Washington D.C. 1998) p175

38 I. Sorokina, S. Naumov, E. Sorokin and E. Wintner, in Digest on Conference on Lasers and Electro-Optics/Europe, Glasgow (Optical Society of America, Washington D.C. 1998) paper CTuK7

39 Y.P. Tong, X. Long, P.M.W. French, J.R. Taylor and A.V. Shestakov, Digest of Conference on Lasers and Electro-Optics (Optical Society of America, Washington D.C. 1995) paper CTuI55

40 H. Eilers, K.R. Hoffman, W.M. Dennis, S.M. Jacobsen and W.M. Yen, *Appl. Phys. Lett.* **61**, 2958 (1992)

41 S. Kück, J. Koetke, K. Petermann and G. Huber, in Digest of *Advanced Solid-State Lasers* (Optical Society of America, Washington D.C. 1993) paper LDSaP77

42 S. Kück, K. Petermann, U. Pohlmann, G. Huber and T. Schönherr , *J. Lumin.* **60 & 61**, 192 (1994)

43 H. Kogelnik, *IEEE J. Quantum Electron.* **QE-8**, 373 (1972)

44 The small signal differential absorption coefficient (1.0 cm-1 for this crystal) was performed in the lab using the highly attenuated output of an arc-lamp pumped Nd:YAG laser tightly focussed inside the Cr^{4+}:YAG rod using a 10 cm lens. Due to absorption saturation, the pump transmission increases for large incident pump powers.

45 D.A. Gilmore, P. Vujkovic and G.H. Atkinson, *Opt. Commun.* **103**, 370 (1993)

46 A. J. Alfrey, *IEEE J. Quantum Electron.* **25**, 760 (1989)

47 Nonlinear refractive index from: Cr4+:YAG data sheet, IRE-POLUS (Elliot Scientific)

48 Source of all other data: www.laseroptics.com/tbl_i.htm (web page of VLOC)

49 M. E. Innocenzi, H. T. Yura, C. L. Fincher, R. A. Fields, *Appl. Phys. Lett.* **56**, p1831 (1990)

50 Private communication with M. Piché, Univ Laval.,Dept. Phys.,CTR OPT, Equip. Laser & Opt. Guidee, St. Foy,PQ G1K 7P4,Canada

51 P.J. Conlon, Y.P. Tong, P.M.W. French, J.R. Taylor and A.V. Shestakov, *Electron. Lett.* **30**, 709 (1994)

52 W.H. Knox, *Opt. Lett.* **17**, 514 (1992)

53 P.J. Conlon, Y.P. Tong, P.M.W. French, J.R. Taylor and A.V. Shestakov, *Opt. Lett.* **19**, 1468 (1994)

54G.R. Huggett, *Appl. Phys. Lett.* **13**, 186 (1968)

5 Construction of an Efficient, Femtosecond Cr^{4+}:YAG Laser

5.1 Introduction

The demonstration that femtosecond pulses could be produced directly from a cw-Ti:sapphire laser via self-modelocking (SML) without requiring any extra modelocking devices[1] proved to be a key advantage of solid-state vibronic lasers over earlier tunable dye and colour-centre lasers. With the demonstration of the cw Cr^{4+}:YAG laser[2], a practical room-temperature replacement for the femtosecond coupled-cavity modelocked (CCM) NaCl:OH^- and KCl:Tl^0 colour-centre lasers (CCL) operating at the telecommunications window near 1.5μm was promised by application of the self-modelocking technique. Interestingly, self-modelocking had been demonstrated with the NaCl:OH^- CCL laser[3] eliminating the need for an interferometrically matched (and electronically stabilised) external cavity in the CCM scheme, but the requirement for a second intracavity nonlinear element of SF59 glass added to the complexity of the cavity. Also, the output power was rather low for a laser of this type: the high intracavity fields necessary for SML required low output coupling and since the parasitic losses of a CCL are high, overall efficiency was poor.

The first demonstration of femtosecond pulse generation from a self-modelocked Cr^{4+}:YAG laser was by Sennaroglu et al. in 1994[4] where near bandwidth limited 120fs pulses were obtained at 360mW output power for 8W absorbed pump power. Interestingly, it was observed that on modelocking, the emission wavelength of the laser shifted from 1.45μm to 1.52μm. The wavelength range over which modelocking could be sustained was limited to just 1.51-1.53μm and no modelocking was observed closer to the peak of the gain near 1.45μm. Despite the high output power, this laser was very difficult to align for stable self-modelocked operation[5], even with regenerative initiation. Other researchers, including those at St. Andrews, were unable to repeat these results, mainly because the Cr^{4+}:YAG crystals appeared to possess such low gain beyond 1.5μm. P.J. Conlon et al.[6] demonstrated sub-100fs pulse generation from a

Cr^{4+}:YAG laser, but, for 10W of incident pump power, only 70mW average output power was obtained from a 0.5% output coupler implying a lower gain of this crystal compared to that used by Sennaroglu.

Difficulties associated with aligning Cr^{4+}:YAG lasers based on standard 4-mirror geometries for self-modelocking led many researchers to abandon this passive modelocking technique, but used semiconductor saturable absorber structures instead to initiate and sustain femtosecond operation in a dispersion compensated laser cavity. The use of semiconductors to achieve modelocking is not a recent idea (indeed the first femtosecond, passively-modelocked, direct-diode pumped solid-state-laser laser used this technique[7]), however, recently there has been a renaissance in using semiconductor absorbers, particularly when grown on reflecting structures (e.g. Bragg stacks or silver) to create a semiconductor saturable-absorber mirror (SESAM) or saturable Bragg-reflector (SBR). This is due mainly to the added reliability of a SESAM (or SBR) based femtosecond system over self-modelocked systems, but the construction of more efficient, highly compact systems has been made possible using SESAMs[8].

Reliable femtosecond operation using saturable absorber mirrors has been demonstrated by Collings et al.[9] The laser cavity used was a conventional Z-cavity with a concave mirror in one cavity arm focusing tightly onto an SBR end-mirror. Whilst modelocking was self-starting, the performance of the SBR system was poor (110fs @ 70mW output) compared to the SML laser (85fs @ 150mW output), mainly due to the added parasitic losses and limited reflectivity of the SBR. Other groups have also reported the use of semiconductor structures[10,11], surprisingly however, whilst the average powers of these systems appear higher than described by Collings, the repetition rates of these later lasers is much higher such that the peak powers are approximately equal. The peak power may be limited by the damage threshold of the structures.

More recently, several researchers have resorted to building self-modelocked Cr^{4+}:YAG lasers based on unconventional laser cavity geometries which are easy to align for stable SML, in particular, using three-mirror lasers in a similar scheme to the design proposed by Ramaswamy-Paye et al.[12] This was first reported by St. Andrews researchers[13] using a standard Brewster-Brewster cut laser rod inside a 3-mirror astigmatically compensated cavity as originally described for use with dye lasers[14]. Other researchers reported lasers based on Brewster-plane Cr^{4+}:YAG rods which used a

high-reflecting coating on a plane rod surface as one cavity end-mirror[15]. These cavity designs have the potential for compactness and efficiency. In addition, with proper optimisation, the pump power requirements of a SML laser can be considerably reduced using a 3-mirror scheme.

In this chapter the chronological details are given for the construction and operation of an efficient SML Cr^{4+}:YAG laser. It begins with details of standard SML laser cavities and a simple model is introduced to simulate the Kerr-lens effect in a resonator. Early results are presented using the standard self-modelocked laser approach with 4-mirror Z-cavities. An alternative 3-mirror laser cavity scheme originally applied to Ti:sapphire lasers is introduced and simple modelling shows that this scheme is probably more appropriate for certain instances of SML than 4-mirror resonators. An adaptation of this laser resonator is described for use with the available Cr^{4+}:YAG rods and early mainframe pumped and all-solid-state results are presented. Further modelling of this resonator indicates how it may be further optimised and, after obtaining better Cr^{4+}:YAG crystals, femtosecond lasers are constructed which are efficient, highly compact and have low pump power requirements. Further unconventional laser resonators are then described and analysed which are intended to reduce the physical size of laser resonators in general.

5.2 Construction of a Self-modelocked Cr^{4+}:YAG Laser Based on a 4-mirror Z-cavity Geometry

Self-modelocking was first demonstrated in a Ti:sapphire laser based around a standard 4-mirror, astigmatically compensated Z-cavity arrangement using a Brewster-angled gain element[1]. The cavity was aligned close to the limits of its narrow stability range mainly due to the requirement that the repetition rate of the laser was ~80MHz. The laser was set up as a coupled-cavity modelocked system but non-transform-limited picosecond pulse generation was observed even with the control cavity blocked. The addition of group-velocity-dispersion compensation using a pair of prisms permitted femtosecond pulse production without any modelocking element. Since this first demonstration, with very few exceptions (until recently), all self-modelocked laser systems copied this basic design scheme; the modelocking worked successfully with this geometry and since the pump sources were usually large mainframe lasers there

was little advantage in making a laser more compact. Self-modelocked lasers based on several solid-state gain media were constructed using this successful design, hence the early SML Cr^{4+}:YAG lasers were also built using a near-symmetric, astigmatically compensated Z-cavity. Figure 5.1 illustrates this standard design showing an acousto-optic (AO) modulator in front of one end-mirror to assist in initiating SML. The total cavity length of the constructed laser was ~1.8m giving a pulse repetition rate of 82 MHz to permit active initiation with an AO-modulator having resonances located near 41 MHz.

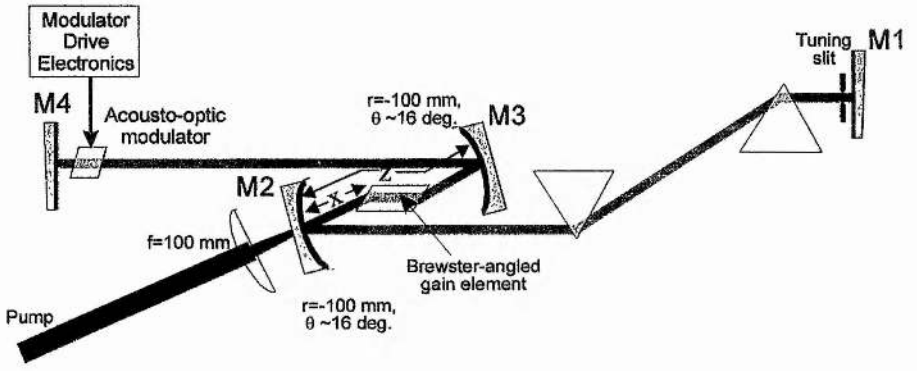

FIGURE 5.1: *Standard near-symmetric Z-cavity arrangement first used to achieve femtosecond operation with Cr:YAG. Included are dispersion compensating prisms and an AO-modulator to initiate SML.*

Normally, the two arms of the Z-cavity are of similar length, but it was found that owing to the limited aperture of the AO-modulator (~2mm), the laser suffered excessive intracavity loss. To overcome this, an asymmetric Z-cavity design was employed with the AO-modulator placed inside the short cavity arm (30cm long). Dispersion compensation was provided by a pair of low-loss fused silica (infrasil) prisms placed 40cm apart in the long cavity arm. This excessively large prism separation was chosen to match the cavity scheme described by Sennaroglu[4] who found that an enormous excess of negative GVD (~-2400 fs^2 total) was necessary for stable SML.

The folding mirrors (each angled by ~16^0) were aligned so the cavity operated in the low-misalignment-sensitivity (LMS) region giving a focus on the end-mirror of the short arm, hence the small aperture of the modulator was no longer problematic. The pump source was a Spectra-Physics SP3800 arclamp pumped Nd:YAG laser operating with the optics from a SP3000 system to increase amplitude stability (see section 2.2).

Successful, stable self-modelocked operation was first accomplished using a 20mm Cr^{4+},Ca^{2+}:YAG rod obtained from Union Carbide with colour-centre laser HR-

mirrors (HR 1.41-1.6μm) used for output coupling from both ends of the laser cavity (~0.1-0.3% transmission) all other mirrors were from set 1 (HR 1.38-1.5μm). Regenerative initiation was employed via an infrasil fused silica Brewster-angled AO-modulator. A maximum available 8W incident pump power was applied. After careful adjustment of the positioning of the cavity folding mirrors and the X and Y tilt of the plane end-mirrors, femtosecond production was observed in very short bursts. Since the free-running operational wavelength of the laser was quite short (1.48μm) due to the use of mirror set 1, it was presumed (after the observations of Conlon et al.[16]) that atmospheric water was rapidly terminating femtosecond operation. This was apparently confirmed by the increase in femtosecond 'spiking' frequency observed by spraying dry nitrogen gas around the gain medium inside the laser cavity. Subsequently, a perspex box was constructed to fully enclose the entire cavity to permit purging of the laser with dry white-spot nitrogen gas. Relatively stable modelocked operation could be accessed permitting an autocorrelation trace and spectrum to be taken (figure 5.2).

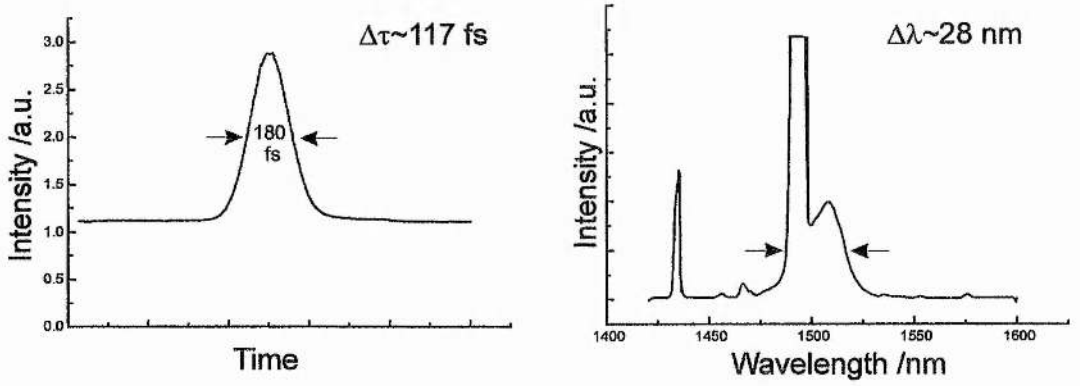

FIGURE 5.2: *Intensity autocorrelation and spectrum of pulses obtained from the 4-mirror self-modelocked Cr:YAG laser.*

A significant fraction of the overall laser power remained in cw components at ~1.43μm and much stronger at ~1.49μm. Although it was possible to reduce the cw features by careful laser adjustment and tuning with the slit in the dispersed cavity arm, modelocking was unstable and continuous re-adjustment of the laser cavity was found necessary. The relatively poor time-bandwidth product of ~0.4 derived from the results in figure 5.2 probably results from misreading the spectral width due to the distorting effect of the strong cw spike at 1.49μm. Despite the high pump power, the output power of this laser was very low at only ~7 mW.

Following on from this observation, a second mirror set was obtained having reflectivity at longer wavelengths (mirror set 2 curves given in figure 4.18 in chapter 4). It was hoped that use of this mirror set with very poor reflectivity below 1.5μm would force the laser to operate at a wavelength at which modelocking would not be perturbed by any water absorption features. Unfortunately the gain of this particular laser crystal was very poor beyond 1.5μm and hence the laser could only operate with all HR coated mirrors (i.e. no output coupler). To compound the low gain problem, the short wave cut-off of the second mirror set occurred at a longer wavelength than originally specified; as shown in figure 4.18, the mirrors were only truly high-reflecting at wavelengths greater than 1525 nm and the 0.5% output coupler only operated satisfactorily in the range 1560-1660 nm, well beyond the long wavelength gain cut-off for Cr^{4+}:YAG. Regeneratively initiated self-modelocking could be achieved with this mirror set without resorting to nitrogen purging but due to the restriction imposed on the use of an HR mirror for output coupling, the output power was again exceptionally low (10mW from each HR reflection implying 60mW total). No further work was carried out on SML Cr^{4+}:YAG lasers based on 4-mirror semi-symmetric Z-cavities.

5.3 Development of an Efficient 3-mirror Cr^{4+}:YAG Laser

5.3.1 Designing a Self-modelocked Laser Resonator

Although when self-modelocking was first discovered the exact mechanism responsible which favoured modelocked operation over cw-operation was uncertain, it was quite soon realised that intensity dependent lensing inside the gain medium played a crucial role. Two similar mechanisms were proposed to explain the source of the self-amplitude-modulation (SAM) within a SML laser:

i) **Hard-aperture modelocking**; this relies on a physical constriction to the intracavity laser beam somewhere in the cavity[17]. With suitable cavity alignment, the stronger Kerr-lensing in the gain medium resulting from higher intracavity peak powers, causes the intracavity beam to 'contract' at the point of the constriction and hence less intracavity loss results.

ii) **Soft-aperture modelocking**; this is similar to hard-aperture modelocking except the stronger Kerr-lensing due to higher intracavity peak powers reshapes

the intracavity beam inside the laser crystal itself to increase the extraction efficiency of the pumped (inverted) gain region. (i.e. a better pump-mode laser-mode overlap results.)[18]

Both these individual techniques have their advantages: usually soft-aperture modelocking is the active mechanism in SML lasers which are pumped by other lasers giving well defined TEM_{00} beams. Hard-aperture modelocking is useful for lasers which are directly diode pumped (e.g. Cr^{3+}:LiSAF) as these pump beams are often so poor that soft-aperturing cannot discriminate between modelocked and cw operation. Unfortunately, it is much harder to align a SML laser to operate with a hard-aperture effect alone.

Several design schemes have been developed to assist in the construction of self-modelocked lasers. Recently, Ritsitaki et al.[19] have developed a comprehensive (but complicated) model for soft-aperture modelocking, which includes the effects of gain-guiding and gain saturation. A very simple design technique was reported for hard-aperture modelocked laser cavities by Cerullo et al.[20] It is intrinsically much simpler to model a hard-aperture based system as the self-amplitude effect results from a one dimensional change at an intracavity slit. Soft-aperturing results from a three dimensional change and is computationally intensive, plus there is the added variability of the pump profile. Since the Cerullo approach is straightforward to use and the results simple to interpret, this was the design technique employed throughout this work and is introduced in the next section.

Overview of the Cerullo Design Technique for Self-modelocked Laser Cavities

Since self-modelocking relies on a subtle change in the lensing effect of an intracavity element induced by a variation in the intracavity field, the precise construction and alignment of the laser is crucial to maximise the resulting self-amplitude modulation. The Cerullo model[20] (and other derivatives of this original scheme) defines a 'Kerr-lens sensitivity parameter' (KLS) given by the expression:

$$\delta = \frac{1}{w}\frac{dw}{dP}\Big|_{P=0} \qquad \text{Equation (5.1)}$$

i.e. the normalised rate of change of spot size with power calculated for zero intracavity power. Originally this expression was calculated for the beam at the end-mirrors (where

a slit could be placed). For a laser cavity with astigmatic elements (e.g. with a Brewster angled rod), the KLS is different in the sagittal and tangential planes. The original Cerullo model did not take into account the coupling between the sagittal and tangential planes within the Kerr-medium and it was a later derivative of this model by Magni et al.[21] which sliced the Kerr-medium and evaluated the lensing effect within each slice that was used throughout most of the later cavity modelling because it more accurately simulates the effect of astigmatic elements.

All the models assume the aberrationless theory of self focussing holds i.e. that a Gaussian profile is maintained by the beam as it propagates through the nonlinear medium.

The Cerullo model was developed from a technique for modelling the nonlinear Kerr-medium inside a self-modelocked laser cavity given a certain intracavity power[22]. The nonlinearity was 'lumped' at the centre of the Kerr-medium and was found to have a positive lensing effect and a 'shortening' effect on a nonlinear medium having a positive nonlinear refractive index. This simple technique permitted the spot size anywhere inside the laser cavity to be evaluated for a given intracavity power, hence the KLS could be evaluated from this for zero intracavity power. Since there is no actual nonlinear lensing effect for zero intracavity power, a much simpler model was developed by Cerullo[20] which simply considered the ABCD matrices[23] of the cavity elements either side of the nonlinearity at the centre of the Kerr-medium. The KLS could be evaluated as the relative positions of each of the cavity elements was changed and hence the cavity alignment giving the greatest propensity to achieve self-modelocking (i.e. with the most negative KLS) was deduced. Because most early SML lasers were based on astigmatically compensated Z-cavities with Brewster-cut gain media, Cerullo and co-workers concentrated on discovering the optimum alignment of such a cavity. Thus a comparison of semi-asymmetric Z-cavities (i.e. with equal folding mirror radii and angles but unequal arm lengths) with a symmetric cavity was made for optimum hard-aperture modelocking alignment.

Although there are several elements of a 4-mirror cavity which can be varied, the two most important are the folding mirror separation and the relative position of the nonlinear element within the folding section (labelled **z** and **x** respectively in figure 5.1). Thus a 3D plot can be constructed for the KLS parameter as these two parameters are varied. Cerullo showed that the optimum arrangement for such a Z-

cavity to be hard-aperture modelocked was with both arms of equal length and the mirror separation set so the laser operated in the centre of the stability region. This is illustrated in the contour plot in figure 5.3 which is the KLS calculated in the tangential plane at the end-mirror M4 in figure 5.1. The darkest regions indicate the alignment (of **x** and **z**) which results in the greatest contraction of the laser beam in front of mirror M4 and hence the greatest loss modulation from a slightly closed slit clipping the beam in the tangential plane.

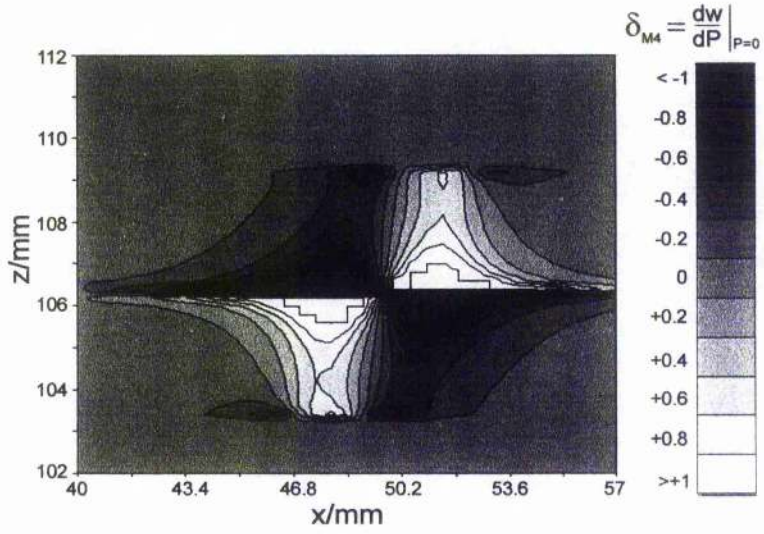

FIGURE 5.3: *Plot of the Kerr-lens sensitivity parameter (KLS) calculated at an end-mirror for a symmetric 4-mirror Z-cavity*

Although from figure 5.3 it might appear trivial to simply build a symmetric Z-cavity laser having a slit in one arm and setting the mirror separations as indicated in the contour diagram, the reality is often more complicated. For lasers operating at low intracavity powers (with low pump power requirements), the actual amplitude modulation induced by a contracting effect of the beam at a hard aperture is often insufficient to favour self-modelocked operation over cw. Also, for lasers suffering from strong thermal lensing (such as Cr^{4+}:YAG under high pump power excitation) the plot in figure 5.3 would be considerably distorted possibly to the point where hard-aperture modelocking is no longer possible.

Compact, 3-Mirror Ti:sapphire Laser Proposal

An analysis of alternative laser resonators for suitability to SML operation using the Cerullo scheme was first performed by Bouma et al.[24] Simple three-mirror

Ti:sapphire lasers were analysed based on plane-plane and Brewster-plane rods with one plane face HR-coated as a cavity end mirror. Such a cavity is illustrated in figure 5.4 with its optical equivalent for modelling purposes using a nonlinear matrix ($\mathbf{M_K}$) to simulate the effect of the Kerr lensing. Although specifically developed to optimise hard-aperture modelocked lasers, Bouma was able to apply the nonlinear matrix model of Cerullo to the soft aperture modelocked system in figure 5.4(a) by examining the spot size at the pumped end of the plane-plane coated laser rod ($\mathbf{w_0}$) for different intracavity powers.

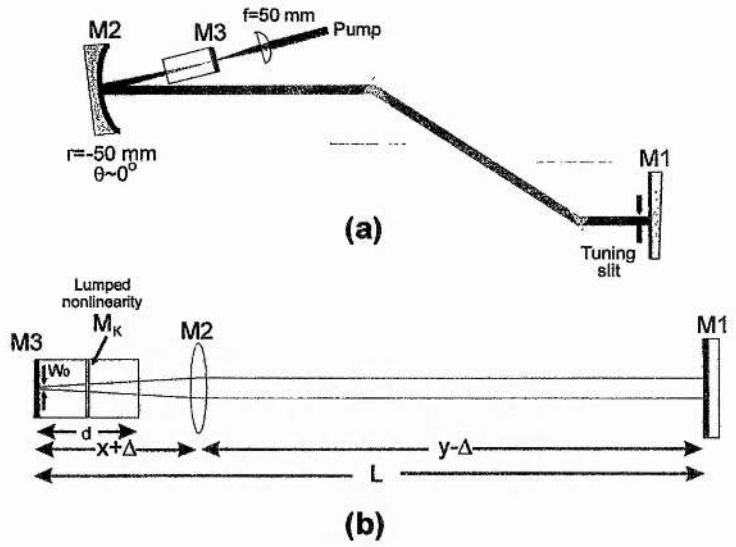

FIGURE 5.4: (a) *3-mirror laser cavity analysed by Bouma et al.*[24] **(b)** *Simplified optical equivalent illustrating the parameters used in the model.*

The nonlinear matrix model considers the nonlinear medium as:

$$M_{rod} = \begin{pmatrix} 1 & d/2 \\ 0 & 1 \end{pmatrix} \cdot M_K \cdot \begin{pmatrix} 1 & d/2 \\ 0 & 1 \end{pmatrix} \qquad \text{Equation (5.2)}$$

where d is the length of the nonlinear medium and the 'lumped' nonlinearity is the matrix:

$$M_K = \frac{1}{\sqrt{1-\gamma}} \cdot \begin{pmatrix} 1-\gamma/2 & -d\cdot\gamma/4 \\ -\gamma/d & 1-\gamma/2 \end{pmatrix} \qquad \text{Equation (5.3)}$$

and γ is:

$$\gamma = \left[1 + \frac{1}{4} \cdot \left(\frac{2\pi w_c^{\,2}}{\lambda d} - \frac{\lambda d}{2\pi w_0^{\,2}}\right)^2\right]^{-1} \cdot \frac{P}{P_c} \qquad \text{Equation (5.4)}$$

$\mathbf{w_c}$ is the cavity spot size at the centre of the nonlinear medium and $\mathbf{w_0}$ is the radius of the corresponding beam waist (at mirror M3 in this case). **P** is the instantaneous intracavity power and $\mathbf{P_c}$ is the critical power for self trapping of the beam:

$$P_c = \frac{c\varepsilon_0\lambda^2}{2\pi n_2}. \qquad \text{Equation (5.5)}$$

For the purposes of the model, the total cavity length, L, was maintained at 20cm; simply the position (Δ) of the mirror M2 relative to the end-mirror M3 was varied and the spot size at the end-mirror, M3, calculated.

Figure 5.5 illustrates how the beam waist at the pumped end of a plane-plane rod can change, with suitable cavity alignment, with the presence of Kerr-lensing inside the gain medium. In figure 5.5(a), the spot size is plotted as the folding mirror is translated for three different intracavity powers: **P=0** is equivalent to the spot size predicted by normal ABCD matrix analysis of this laser resonator; **P=0.1P$_c$** is the realistic case of a SML laser with an instantaneous intracavity power of one tenth that for critical self-focussing (trapping). **P=0.5P$_c$** is a much higher intracavity power than would normally be achieved inside such a laser.

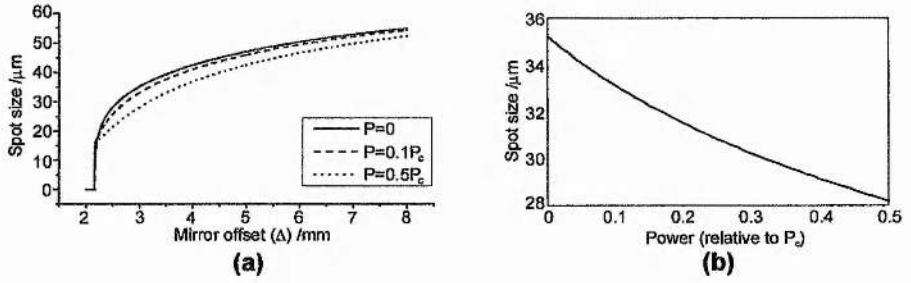

FIGURE 5.5: *Effect of nonlinear lensing on the spot size at the pumped end of the plane-plane rod.* **(a):** *Effect of translating the cavity mirror for different intracavity powers.* **(b):** *Beam waist vs. intracavity power for a fixed cavity alignment (Δ=3mm)*

Although this is only modelling a one-dimensional variation due to Kerr-lensing and does not consider the full three-dimensional overlap of the pump and cavity modes to be a full soft-aperture analysis, the general trend for the beam waist to contract at the pumped end of the rod is sufficient to imply that soft-aperture modelocking will be

successful: because the pump light is of a shorter wavelength than the resonant laser light, the pump beam would be expected to be located completely inside the intracavity mode, hence for stronger lensing (due to higher powers in figure 5.5(b)), the intracavity mode will extract the inverted gain region better and hence experience greater gain. From figure 5.5(a), it is expected that modelocking would occur on translating the curved cavity mirror (M2) towards the gain element close to the edge of the cavity stability limit.

For low values of $\mathbf{P/P_c}$, it is possible to determine the value of the Kerr-lens sensitivity parameter from this model by calculating the normalised change in spot size with respect to the intracavity power. This is plotted in figure 5.6, which again shows that the optimum position for modelocking (i.e. negative KLS) is approached by translating the cavity mirror towards the gain element (Δ~2.4mm). Note, however, that extremely close to the this stability edge, the KLS becomes positive and large implying that the spot size will expand for stronger lensing, and so modelocking will not be possible in this extreme case.

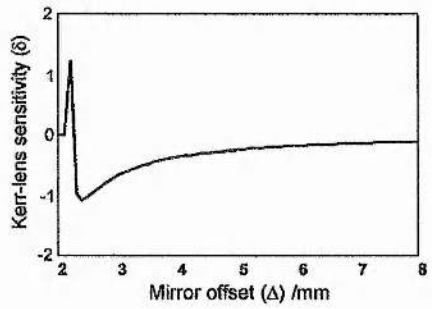

FIGURE 5.6: *Kerr-lens sensitivity parameter calculated at the pumped end of the gain element as the folding mirror (M2 in figure 5.4) is translated.*

5.3.2 Femtosecond 3-Mirror Cr^{4+}:YAG Laser

Ramaswamay-Paye et al.[12] and Bouma et al.[24] were interested in constructing 3-mirror femtosecond lasers as they have the potential to be extremely compact, especially if a plane-Brewster cut gain medium and prismatic output coupler replace the dispersion compensating prism pair. However, from the perspective of optimising the efficiency of a self-modelocked laser based on a gain element with very low round trip gain, such as this Cr^{4+},Ca^{2+}:YAG crystal operated beyond 1.5μm, the 3-mirror approach has two advantages:

i) Two mirror reflections have been eliminated per round trip: considering the mirror transmission curves for mirror set 2 (shown in figure 4.18), 2 HR-mirror reflections for a laser operating at 1.5μm amounts to ~0.5% transmission which would appear to be a significant amount for this low-gain laser medium.

ii) A 3-mirror resonator permits a very tight, localised focus to be placed on the end of an 'off-the-shelf' Brewster-Brewster cut laser rod without resorting to using special optical coatings. This aspect of the 3-mirror design will be discussed in greater detail in section 5.3.3.

From the aspect of exploiting the former advantage, a 3-mirror laser design was developed with minimum parasitic intracavity losses. Since no specially coated Cr^{4+}:YAG crystals were available, an adaptation on Ramaswamy-Paye's design was employed which could be constructed with the available Brewster-Brewster cut rods. This early design, illustrated in figure 5.7, uses a curved 'retroflecting' end-mirror and one curved mirror operated off-axis to compensate for the astigmatism of the Brewster cut rod. This cavity, pumped through the folding mirror, is identical to that proposed by reference 14 for use as an astigmatically compensated dye laser resonator, and later employed with colour-centre lasers (as in chapter 3). The radius of curvature of this retroflecting mirror is irrelevant to the operation of the laser; it merely 're-images' the beam back upon itself inside the rod.

A relatively compact system was possible by the use of a silica prism modulator which (in conjunction with an infrasil cavity prism) provided negative group-velocity dispersion, and permitted regenerative initiation to be employed without incurring additional parasitic loss from an acousto-optic modulator. The prism modulator (from a Spectra-Physics argon-ion mainframe laser[25]) was originally designed to operate at a frequency of ~40MHz, however, strong acoustic resonances were found near 96MHz allowing a compact laser with a repetition rate of 192MHz and a total cavity length of ~78cm to be built.

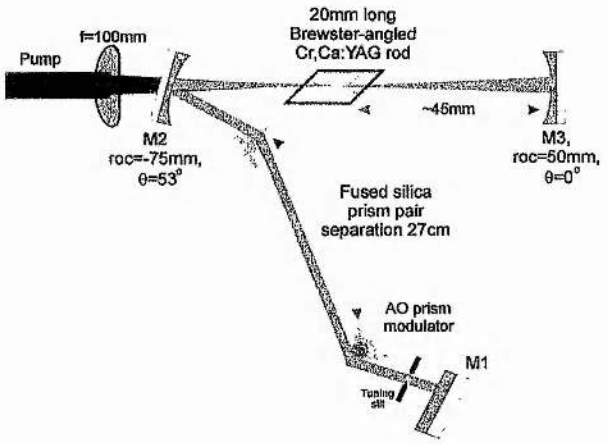

FIGURE 5.7: *Schematic of the 3-mirror system employed for a compact, self-modelocked Cr:YAG laser.*

One unfortunate consequence of pumping through the folding mirror, as in figure 5.7, is that for an optimally aligned pump beam, the residual unabsorbed pump light is reflected exactly back on itself by mirror M3 through the Cr^{4+}:YAG rod into the pump laser. Even though this represents a minute fraction of the output power of the SP3800 laser, it is sufficient to result in chaotic Q-switching of the pump laser which would prevent stable SML operation of the Cr^{4+}:YAG laser. To prevent these back reflections, it was necessary to place an optical isolator in the pump path which had a high insertion loss of 20%. The isolator comprised one Glan-Taylor polariser oriented to pass the horizontally polarised pump light, and an AR-coated Faraday rotator which rotated the plane of polarisation of light by 45^0. An AR-coated half-wave plate was then necessary to re-orientate the polarisation of the pump light to the horizontal plane. The optical isolation obviously significantly increases the cost of the modelocked system and reduces the maximum power available to pump the Cr^{4+}:YAG laser.

To optimise the mode-matching of the pump mode with the resonant laser mode inside the gain medium, a simple adjustable telescope was included in the pump path (shown in figure 5.8) which expanded the pump beam by approximately four times. Unlike most telescope schemes, which only permit the optimisation of the pump beam divergence by adjusting the lens separation, the second lens of this telescope was mounted on a rotary base allowing the astigmatism of the pump focus inside the laser crystal to be controlled. A tighter pump focus is gained by decreasing the telescope lens separation and increasing the pump focus lens to crystal distance. A less divergent beam in the tangential plane results (and a more divergent beam in the

sagittal plane) if the second telescope lens is rotated; hence the final tangential focus will be in front of the sagittal focus. Because the effective length of a Brewster cut rod in the tangential plane is $1/n^2$ x length in the sagittal plane, the tangential cavity focus moves faster than the sagittal focus when the laser crystal is translated so optimised mode-matching is possible with this telescope.

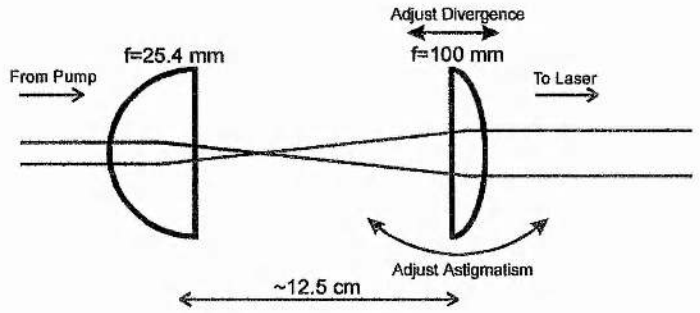

FIGURE 5.8: *Telescope scheme adopted to optimise pump-mode matching inside the gain medium.*

The cw oscillation threshold for this complete laser (including dispersion compensating prisms/modelocker) was 1.8W incident pump power. With the maximum available 5.2W incident on the Cr^{4+}:YAG rod, 20 mW cw (not chopped) output power was available from the HR coated end-mirror when the laser was tuned to 1.51 μm.

The prism modulator was driven actively with 1.5W RF power at 96MHz from a frequency synthesiser and the cavity length carefully adjusted until the beating signal, detected with a broadband germanium photodiode and observed on an RF spectrum analyser, was maximised. This corresponded to a partially actively modelocked laser system and a broad noise burst of ~20ps duration could be observed on an autocorrelator. With careful adjustment of the retroflecting end-mirror position while keeping the total cavity length constant, stable self-modelocked operation was attainable producing pulses of ~140 fs duration (figure 5.9) with a duration-bandwidth product of 0.39. The output power through each HR reflection was 13 mW (total output ~50 mW) at a centre wavelength of 1508 nm when modelocked, rising to 17 mW at 1510 nm when SML operation ceased and the laser operated cw. Note that unlike the earlier unstable result obtained with a conventional Z-cavity arrangement, there was no cw spike on the modelocked spectrum indicating that SML was complete. Once initiated, self-modelocked operation would only continue for up to ~30 seconds with the active initiation turned off and hence the acousto-optic

modulator was powered permanently. Although SML was stable with this arrangement, temperature induced drifts in the laser cavity length periodically caused the actively-modelocked initiated self-modelocking to 'drop-out' hence the cavity length had to be continually re-adjusted. To overcome this problem, a regenerative initiation scheme was later adapted to operate at the high cavity frequency of 192 MHz.

One drawback of this laser system under high pump excitation was that the output power fade associated with Cr^{4+}:YAG (discussed in chapter 4) crippled modelocked operation after ~10 minutes continuous pumping. However, this usually merely required periodic translation of the Cr^{4+}:YAG rod along the x or y axes to enable SML once more.

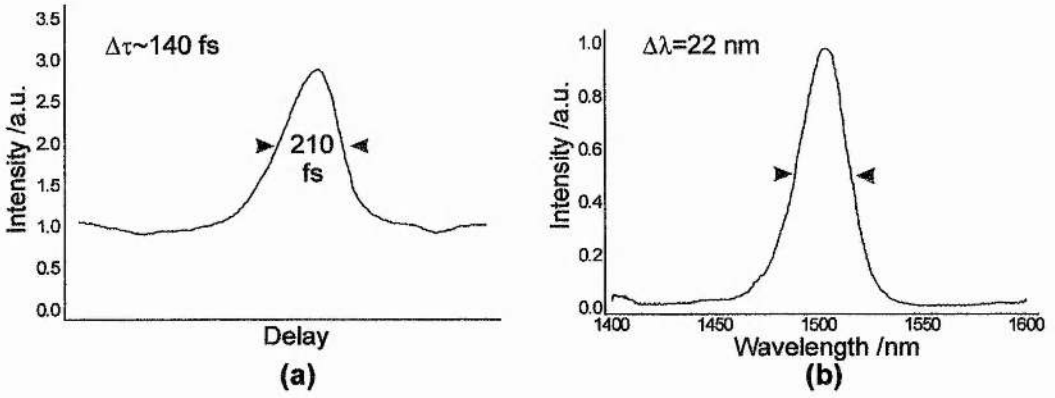

FIGURE 5.9: (a) *Intensity autocorrelation and* **(b)** *corresponding spectrum of typical 140 fs pulses obtained from the mainframe Nd:YAG pumped, actively initiated 3-mirror Cr:YAG laser.*

All-solid-state, Self-modelocked 3-mirror Cr,Ca:YAG Laser

The development of the laser-diode-pumped Nd:YAG laser described in chapter 2 opened up the possibility of a tunable, high power all-solid-state femtosecond laser operating at the telecommunications window at 1.55μm. An additional advantage of this holosteric alternative is its greater stability (both in amplitude and beam pointing) compared to its arclamp pumped predecessor (see chapter 2).

With the Nd:YAG mini-laser operating with 8W output power, only 5.5W maximum incident power was available after the isolator, half-wave plate, telescope and pump steering mirrors.

With regenerative initiation, modelocking was straightforward to accomplish after

adjustment of the folding mirror and curved retroflecting end-mirror positions. The lowest pump power requirement to enable SML was 4.5W incident. For 4.7W pump, 22mW modelocked output power was available from each HR mirror reflection (~85mW total). 180 fs bandwidth limited ($\Delta\nu\Delta\tau$=0.32) pulses were measured.

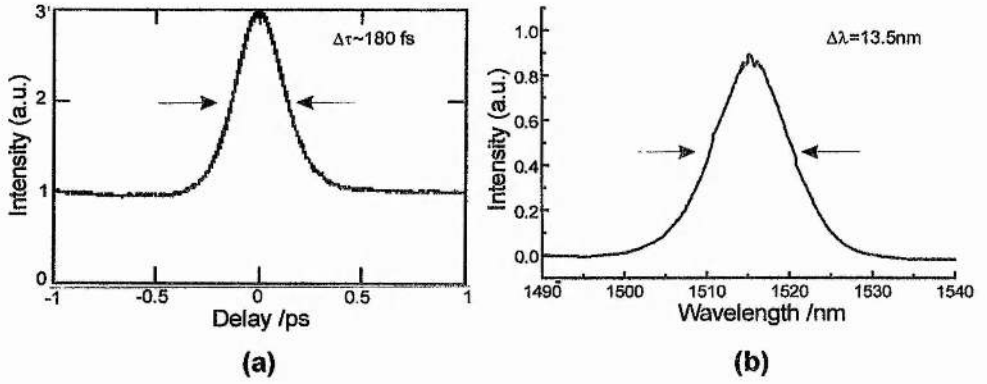

FIGURE 5.10: *Characterisation of pulses from the all-solid-state, 3-mirror self-modelocked Cr:YAG laser* **(a):** *intensity autocorrelation of typical 180 fs pulses* **(b):** *corresponding spectrum.*

5.3.3 Analysis of Laser Resonators for Self-modelocking

It is instructive to analyse the 3-mirror resonator design introduced in section 5.3.2, with regard to self-modelocked operation, to permit further optimisation of the resonator. The choice of pump beam direction, i.e. through the angled folding mirror, was initially chosen as it was the most straightforward scheme to assemble in practice; the initial alignment procedure is identical to that employed with standard 4-mirror resonator schemes, whereas pumping through the curved end-mirror is difficult as optimising this mirror for feedback causes significant pump beam steering thus masking the feedback amplitude variation. However, analysis of this resonator design will indicate that pumping through the curved end-mirror is the most optimal.

The 'Magni' Model

Magni et al.[21] developed an adaptation of Cerullo's[20] earlier model to more completely determine the effect of a Kerr-lens in a resonator with astigmatism. This involved slicing up the nonlinear medium into infinitesimal thin 'elliptic' Kerr-lenses of dioptric powers ϕ_x & ϕ_y in the tangential and sagittal planes respectively, calculating the effect of this slice on the spot size at the end of the cavity, then integrating over the whole length of the gain medium.

The model considers the propagation of astigmatic Gaussian beams in a Kerr medium governed by the paraxial wave equation with the aberrationless approximation[26]. An expression is thus derived for the dioptric power in an infinitesimal slice, $\mathbf{d}\zeta$, in each plane:

$$\phi_x = p\left(\frac{\lambda}{n.\pi}\right)^2 \cdot \left(\frac{\omega_x}{\omega_y}\right)^{\frac{1}{2}} \cdot \frac{1}{\omega_x^{\,2}} \cdot d\zeta \qquad \text{Equation (5.6)}$$

The subscripts (**x** and **y**) refer to the corresponding value in the tangential and sagittal planes respectively. **n** is the linear refractive index. As before, **p** is the ratio of intracavity power with the power for critical self focussing. $\omega = w^2$ where **w** is the spot size. From this definition, the Kerr-lens sensitivity (KLS) parameter is defined as:

$$\delta = \left(\frac{1}{2\omega}\frac{d\omega}{dp}\right)_{p=0} \qquad \text{Equation (5.7)}$$

The effect of the thin lens on the spot size at end-mirror M1 is thus:

$$d\delta_{1x} = \left(\frac{1}{2\omega_{1x}}\frac{d\omega_{1x}}{d\phi_x}\right)_{\phi_x=0} \cdot \left(\frac{d\phi_x}{dp}\right)_{p=0} \qquad \text{Equation (5.8)}$$

Considering the general cavity scheme in figure 5.11; the single pass matrix from end-mirror M1 to end-mirror M2 is denoted in the tangential plane without the thin lens by elements $\mathbf{M_x}$, and with the thin lens by $\mathbf{M_x(\phi_x)}$. Elements $\mathbf{M_{ix}}$ (i=1,2) denote the single pass matrix from the thin lens (at ζ) to end mirror Mi.

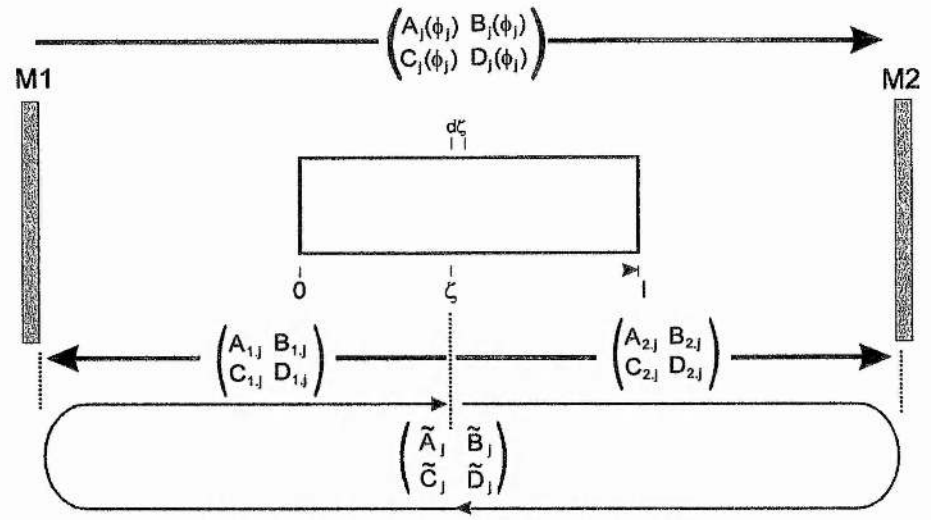

FIGURE 5.11: *Matrix system used by the 'Magni' model.*

The spot size on mirror M1 is given by the expression[27]:

$$\omega_{1x}^{\ 2} = -\left(\frac{\lambda}{\pi}\right)^2 \frac{B_x(\phi_x)D_x(\phi_x)}{A_x(\phi_x)C_x(\phi_x)} \qquad \text{Equation (5.9)}$$

From figure 5.11, the one way matrix from M1 to M2 including the thin lens may be expressed as:

$$\begin{bmatrix} A_x(\phi_x) & B_x(\phi_x) \\ C_x(\phi_x) & D_x(\phi_x) \end{bmatrix} = \begin{bmatrix} A_{2.x} & B_{2.x} \\ C_{2.x} & D_{2.x} \end{bmatrix} \cdot \begin{bmatrix} 1 & 0 \\ 0 & n^{-1} \end{bmatrix} \cdot \begin{bmatrix} 1 & 0 \\ -\phi_x & 1 \end{bmatrix} \cdot \begin{bmatrix} 1 & 0 \\ 0 & n \end{bmatrix} \cdot \begin{bmatrix} D_{1.x} & B_{1.x} \\ C_{1.x} & A_{1.x} \end{bmatrix} \qquad \text{Equation (5.10)}$$

where n is the linear refractive index of the nonlinear medium. Differentiating this expression with respect to ϕ and equation (5.6) with respect to **p** and substituting into equation 5.8 with ϕ=0 and **p**=0 gives (after extensive algebraic re-arrangement):

$$d\delta_{1x} = -\frac{1}{n}\left(\frac{1-S_y^{\ 2}}{1-S_x^{\ 2}}\right)^{\frac{1}{4}} \cdot \left|\frac{\tilde{B}_x}{\tilde{B}_y}\right|^{\frac{1}{2}} \cdot \frac{B_{2.x}D_{2.x}S_x + B_{1.x}D_{1.x}}{\tilde{B}_x^{\ 2}} \cdot d\zeta \qquad \text{Equation (5.11)}$$

S_j refers to the stability condition given by the expressions:

$$S_j = \frac{\tilde{A}_j + \tilde{D}_j}{2} = A_jD_j + B_jC_j \text{ where the cavity is stable if } -1 \le S_j \le 1 \qquad \text{Equation (5.12)}$$

The matrix elements $\tilde{M}$, refer to the element from the round trip matrix starting and finishing at point ζ in figure 5.11. Integrating the expression in equation 5.11 from

ζ=0 to ζ=l (i.e. along the whole length of the nonlinear medium) yields the KLS in the tangential plane at the end-mirror M1. It is straightforward to calculate this for the sagittal plane by swapping the x and y subscripts, and for mirror M2 by swapping subscripts 1 and 2. In practice the integration was performed using the trapezium rule.

By varying different cavity parameters (principally the folding mirror separation and the position of the nonlinear medium between the folding section) and re-integrating equation 5.11 above for each position, it is possible to locate the optimum cavity alignment which maximises the Kerr-lens sensitivity at the end-mirror.

Since we are mainly interested in self-modelocked lasers using a soft-aperture, a slightly adapted form of the model was employed to calculate the spot size change (KLS) on the end of the crystal. If $\mathbf{A_{XTLi,j}}$ and $\mathbf{B_{XTLi,j}}$ are elements for plane j (j=x,y) from the one way matrix for propagating from the end-mirror Mi to the closest crystal facet, the spot size at this crystal facet may be found from the transformation applied to the Gaussian beam parameter:

$$\omega_{XTLi,j} = \omega_{i,j}\left[A_{XTLi,j}^{\ 2} + \left(\frac{\lambda.B_{XTLi,j}}{\pi.\omega_{i,j}}\right)^2\right] \qquad \text{Equation (5.13)}$$

where ω=$\mathbf{w}^2$ as defined earlier. Magni then derives an expression for the KLS at this plane in the cavity using the chain rule and algebraic manipulation:

$$\delta_{XTLi,j} = \frac{A_{XTLi,j}^{\ 2} - \left(\lambda.B_{XTLi,j}/\pi.\omega_{XTLi,j}\right)^2}{A_{XTLi,j}^{\ 2} + \left(\lambda.B_{XTLi,j}/\pi.\omega_{XTLi,j}\right)^2}\cdot\delta_{i,j} \qquad \text{Equation (5.14)}$$

It is anticipated that any tendency for the spot size to shrink at the focus of the intracavity (and pump) beams should permit SML. Although equation 5.14 allows the KLS to be determined at the crystal face, it should not be used for calculating the KLS *inside* the rod itself.

Simple matrix algebra shows that the beam waist in the crystal is the Fourier plane of an image at a cavity end-mirror (i.e. $\mathbf{A_{i,j}}$=0, where A is the element of the one way matrix from the end-mirror to the beam waist). Therefore, the beam waist has the greatest tendency to shrink in size (most negative KLS) when the KLS calculated at an end-mirror is most *positive* (i.e. when hard-aperture modelocking is impossible). Optimising a cavity for maximum propensity to self-modelock via soft-aperture modelocking therefore requires finding the alignment which gives the largest positive Kerr-lens sensitivity at a cavity end-mirror.

General 3-mirror Resonator Characteristics

All 3 and 4-mirror laser designs have two distinct stable operating regions as the mirror separation is varied. For 4-mirror resonators with an asymmetric design, one of these regions (for largest mirror separation) corresponds to the cavity beam focusing onto the end-mirror in the short arm (low-misalignment sensitivity region (LMS)), but when operated in the inner stability region the beam is collimated in the short arm (high-misalignment sensitivity region (HMS)). In the case of symmetric 4-mirror resonators, the inner edge of the LMS region is the outer edge of the HMS region hence the laser is operating on the stability edge when aligned in the centre of the total stable operating range of the laser cavity. This explains the Cerullo contour plot for a symmetric 4-mirror Z-cavity in figure 5.3: the Kerr-lens sensitivity is maximised near the centre of the stability region as this is also a stability edge.

This is clarified by consulting the plots of the resonator stability parameter calculated with equation (5.12) in figure 5.13. The stability plots have the form of a parabola but the laser cavity is stable only in the range –1 to 1 (the region within the dotted lines). In figure 5.13(a) corresponding to a symmetric 4-mirror design (both arms=80cm long), the minimum point of the stability parabola is –1, hence this appears to be a single large stability zone but the centre of the zone is actually the stability edge. The parabola shifts downwards slightly for an asymmetric resonator (arm1=60cm, arm2=120cm) hence the stability zone separates. However, unless the cavity is very highly asymmetric, the two stability zones are close together and may be accessed within the operating range of a standard translation mount.

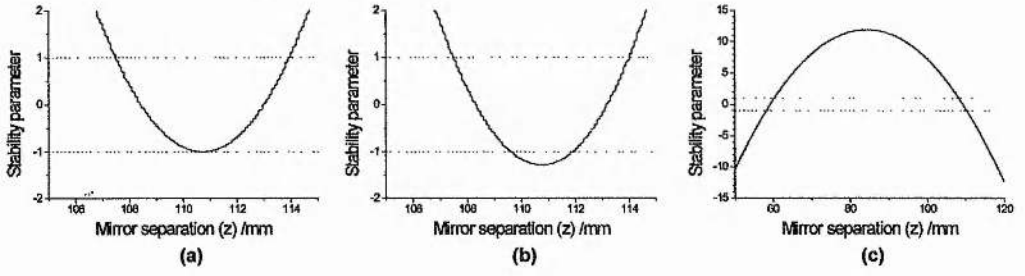

FIGURE 5.13: *Stability plots for* **(a)**: *symmetric 4-mirror cavities;* **(b)**: *asymmetric 4-mirror cavities;* **(c)**: *3-mirror cavities*

The situation for a 3-mirror resonator (figure 5.13(c)) is somewhat different: the inverted parabola has two regions which are well separated from each other and correspond to two entirely different laser alignment arrangements. The key stability

criterion for a 3-mirror resonator is that the radius of curvature (ROC) of the retroflecting end-mirror must match the ROC of the wavefront of the resonant beam. Hence for a focused Gaussian beam, there are two possible positions which satisfy this condition: one either side of the Rayleigh range (where the wavefront ROC is maximum). A simple equation for the two possible distances of the retroflecting end-mirror from the cavity beam waist may be developed from the well known expression for the radius of curvature of a Gaussian beam[28]:

$$R(z) = z + \frac{z_R^{\,2}}{z} \quad \text{where } \mathbf{z_R} \text{ is the Rayleigh range: } z_R = \frac{\pi . w_0^{\,2}}{\lambda} \qquad \text{Equation (5.15)}$$

w_0 is the size of the beam waist. Solving this for z gives the mirror to beam waist distance:

$$z = \frac{R}{2} - \frac{1}{2}\sqrt{R^2 - 4z_R^{\,2}} \qquad \text{Equation (5.16(a))}$$

$$z = \frac{R}{2} + \frac{1}{2}\sqrt{R^2 - 4z_R^{\,2}} \qquad \text{Equation (5.16(b))}$$

For small w_0 (relative to the curvature of the retroflecting mirror) equation (5.16(b)) can be simplified to $z=R$.

The 3-mirror cavity proposition by Ramaswamy-Paye is simply a particular case of resonator operating in the stability zone governed by equation (5.16(a)) for which the end-mirror ROC is infinite. The other stability condition is thus only satisfied at infinity (and therefore is not accessible). It might be expected that for the condition that the mirror ROC was equal to half the Rayleigh range in equation (5.15), there should be only one stability region; and that there would be no stability condition for mirrors of shorter ROC than this. However, because the mirror is in a resonator, in practice as the ROC is reduced to approach the Rayleigh range, the beam waist w_0 shrinks hence the condition for a single stability zone is unrealisable: the earlier statement that the ROC of the retroflecting end-mirror is immaterial to the operation of the laser no longer holds true. Equations 5.16(a) and (b) are only of use for ROC considerably greater than the Rayleigh range. In practice this is not a problem since for tightly focused beams, the Rayleigh range is of the order of 2 mm –considerably shorter than the available concave mirrors.

An important point to bear in mind with equations (5.16) is that astigmatism is not taken into account: because the effective length of a Brewster-cut laser crystal is different in the tangential and sagittal planes, the locations of the two waists inside such a crystal which satisfy equations 5.16 will be different, i.e. there will be a distributed focus *inside* a Brewster-angled laser crystal. The exception to this is when one focus is placed on the rod end adjacent to the retroflecting end-mirror: the effective length of the crystal in this plane is zero hence the focus for the orthogonal plane will also occur on the rod end. Thus a 3-mirror cavity has the capability of creating a strong, very highly localised focus on the end of the rod adjacent to the retroflecting end-mirror. This helps to ensure a low cw-threshold and therefore high efficiency operation but also, more importantly, creates a strong nonlinear-lens and maximises the propensity for self-modelocking, as disclosed in the next section.

Optimisation of the Intensity-induced Nonlinear-lensing

The dioptric power of the intensity induced Kerr-lens in a thin slice Δz of dielectric material at position z is given by the expression[29]:

$$P_K(z) = \frac{8 n_2 n_0 P_0}{\pi \cdot a \cdot w_S^2(z) \cdot w_T^2(z)} \cdot \Delta z \qquad \text{Equation (5.17)}$$

n_0 and n_2 are the linear and nonlinear components of the refractive index; P_0 is the instantaneous power. A correction factor, a, is required ($3 < a < 7$) because the above equation assumes that the Gaussian beam induces a quadratic refractive index variation. The laser spot size at position z in the sagittal and tangential planes are given by w_S and w_T respectively.

First, consider the case of a symmetric 4-mirror Z-cavity laser built around a Brewster-angled Cr^{4+}:YAG laser crystal. With the rod placed equidistant from the two identical folding mirrors of equal angle, the beam profile illustrated in figure 5.14(a) results: each half of the cavity possesses equal astigmatism hence a tight cavity focus can be produced exactly in the *centre* of the Brewster-cut rod[30]. Slicing up the rod and using equation (5.17) to calculate the effective focusing power in each slice for an intracavity power of 1kW creates the plot shown in figure 5.16(b) of inverse focal length vs. rod location. A localised Kerr-lens is formed at the rod centre, but note that this lens is *symmetric*. Although the overall lens strength may be strong (and may be increased by reducing the mirror radii of curvature or increasing the arm lengths), there will be no net effect on the intracavity laser beam. At the exact point of the beam waist

a strong lens has no focusing effect on the intracavity beam, whilst the effects due to lenses of equal strength either side of this cavity focus will cancel. Therefore it will be impossible to self-modelock a laser operating in this arrangement as there is no source of self-amplitude modulation. This is confirmed with reference to the Cerullo plot for a symmetric 4-mirror cavity in figure 5.3: the focus is in the centre of the crystal when the four distinct zones meet and along a vertical line here where the mirror separation is varied but the crystal is maintained central between the two mirrors. The KLS has a very small value (~0) along this line.

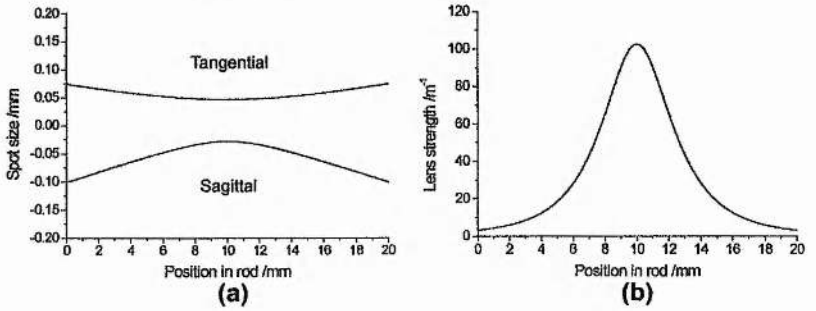

FIGURE 5.14: *Symmetric 4-mirror resonator with nonlinear element exactly central between the two folding mirrors.* **(a):** *Beam profile in 20mm Cr:YAG rod and* **(b):** *resulting Kerr-induced distributed lens for an intracavity power =1kW*

Further Cerullo-style analyses of this cavity (by taking a horizontal slice through figure 5.3, corresponding to varying the laser rod position for a fixed mirror separation) reveal that the maximum value for the KLS occurs when the tangential focus is located close to the end of the laser rod. A Brewster-angled rod has different lengths in the sagittal ($\mathbf{d_{eff.sag}=d/n_0}$) and tangential ($\mathbf{d_{eff.tan}=d/n_0^3}$) planes hence translating the rod off-centre causes the tangential beam waist to move faster than the sagittal waist. Obviously, this effect is worst for materials with higher refractive indices such as YAG than lower index materials (e.g. LiSAF).

Figure 5.15(a) illustrates the intracavity beam inside the rod with the tangential focus positioned at the rod facet. Note that the sagittal focus remains inside the rod and therefore the overall distributed lens (figure 5.15(b)), although asymmetric, is considerably weaker and less localised than was the case with the two foci coincident in the rod centre.

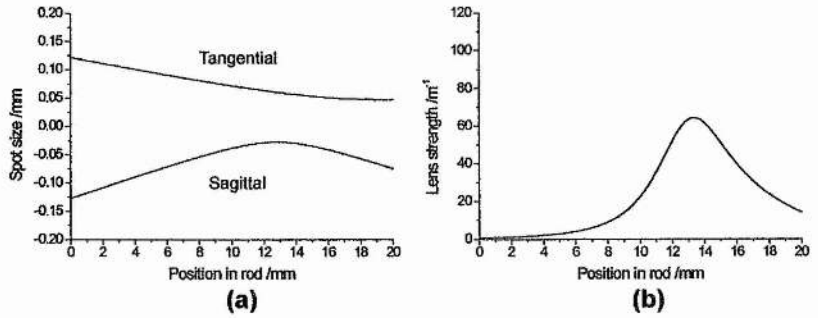

FIGURE 5.15: *Symmetric 4-mirror resonator with nonlinear element positioned to give a focus at the end of the rod.* **(a):** *Beam profile in 20mm Cr:YAG rod and* **(b):** *resulting Kerr-induced distributed lens for an intracavity power =1kW*

The 3-mirror cavity may be considered as an extremely asymmetric 4-mirror cavity with all the astigmatic elements on one side of the cavity. Alternatively it may be thought of as a totally symmetric cavity folded back on itself at the end of the rod adjacent to the retroflecting end-mirror. This is easier to visualise for the Ramaswamy-Paye type cavity discussed earlier. Either way, the only condition for which the tangential and sagittal waists coincide is when the focus is located at the rod end, illustrated in figure 5.16(a). An exceptionally asymmetric nonlinear distributed lens results (figure 5.16(b)) which has a peak strength approximately equal to the lens for the 4-mirror resonator. In the modelling of this cavity, the 3-mirror cavity was basically just the 4-mirror cavity with one arm removed and a curved end-mirror placed at a distance equal to its ROC from the Brewster surface to complete the resonator. Thus the cavity beam is focused approximately equal to the full 4-mirror cavity but the resonator is almost half the physical size. Note that although the peak lensing strength has not been reduced from the case in figure 5.14(b), the overall nonlinear lens strength of the rod will be halved since half of the original lens is absent.

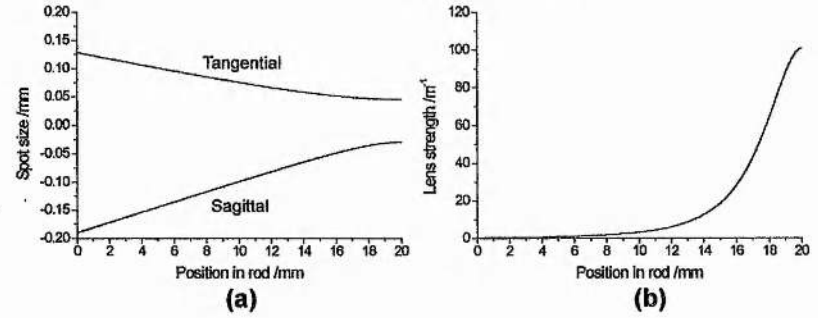

FIGURE 5.16: *3-mirror resonator with nonlinear element positioned at a distance equal to the mirror ROC from the curved retroflecting end-mirror giving a tight localised focus on the end of the rod.* **(a):** *Beam profile in 20mm Cr:YAG rod and* **(b):** *resulting Kerr-induced distributed lens for an intracavity power =1kW*

The final configuration to consider is the case when the tangential focus is placed

on the opposite end of the rod to the retroflecting end-mirror. This is the most likely scenario for the case occurring in practice for the 3-mirror Cr^{4+}:YAG laser presented in section 5.3.2. The resulting beam profile in figure 5.17(a) is an extremely distributed focus with the sagittal beam waist close to the opposite end of the rod. Inevitably, an extremely weak, highly distributed Kerr-lens is created (figure 5.17(b)) implying that this arrangement is less suited to self-modelocking than the original 4-mirror design. This may explain why the modelocking threshold of the laser in section 5.3.2 was so high (4.5W) compared to its cw-oscillation threshold (1.8W).

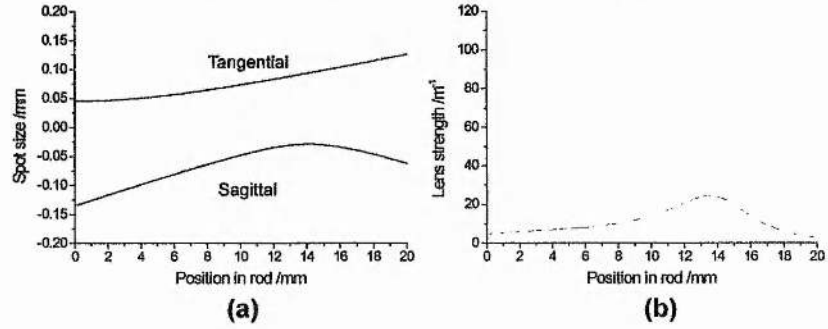

FIGURE 5.17: *3-mirror resonator with tangential focus located at the rod end adjacent to the folding mirror giving a distributed focus.* **(a):** *Beam profile in 20mm Cr:YAG rod and* **(b):** *resulting Kerr-induced distributed lens for an intracavity power =1kW*

Optimisation of Laser Efficiency and Threshold Reduction

For optimising the efficiency of a laser resonator (maximising the useful output power), a good pump-laser mode overlap is required and parasitic losses should be minimal. Because a diffraction-limited pump source was used for the Cr^{4+}:YAG laser, a good overlap was ensured, and minimising the number of cavity components with a 3-mirror design reduced the parasitic losses. The output power of a laser for a given pump power is then determined by how high above cw-threshold the laser is operating and hence the cw-threshold must be minimised.

It is generally accepted that for a low cw-threshold, a tight focus at, or close to, the pumped end of the laser gain medium is desirable. Indeed, recent work involving Cr^{3+}:LiSAF has shown that tight focusing in a low loss Brewster-cut laser crystal with a high pump absorption coefficient placed inside a 3-mirror resonator as described here, permits cw-oscillation thresholds as low as 7mW pump[31]. The situation with Cr^{4+}:YAG is somewhat different, principally due to the low pump absorption coefficient of available laser grade crystals.

In table 5.1 a comparison is made between the simulated cw-oscillation thresholds for the laser schemes with intracavity beams modelled in

figures 5.14(a)-5.17(a) inside a 20mm long rod of Cr^{4+}:YAG. The model for the power transfer characteristics described by Alfrey[32] and detailed in section 4.5.1 was used with zero intracavity power to simulate the threshold condition. A perfect pump-laser mode overlap was modelled by scaling the intracavity beam profiles, calculated for the figures 5.14-5.17, with the square root of the ratio of the pump/laser wavelengths. The results are shown normalised with respect to the case for the symmetric laser with a tight focus at the rod centre. This was to remove the cavity loss and pumping quantum efficiency dependencies i.e. the overall loss is considered equal in all cases. Two pump absorption coefficients were modelled. The figure of 2 cm^{-1} was the value of the crystal used in experiments, however, the potential benefits to be gained by using higher doped crystals are apparent from the figures for 4 cm^{-1} pump absorption.

Cavity Description	α /cm^{-1}	Normalised cw-threshold
Symmetric 4-mirror laser with crystal in centre (fig. 5.14)	2	1
Symmetric 4-mirror laser with 1 focus on rod end (fig. 5.15)	2	0.68
3-mirror laser with both foci on retroflecting mirror end (fig. 5.16)	2	0.6
3-mirror laser with one focus on opposite end (fig. 5.17)	2	0.59
Symmetric 4-mirror laser with crystal in centre (fig. 5.14)	4	1.6
Symmetric 4-mirror laser with 1 focus on rod end (fig. 5.15)	4	0.85
3-mirror laser with both foci on retroflecting mirror end (fig. 5.16)	4	0.43
3-mirror laser with one focus on opposite end (fig. 5.17)	4	0.65

TABLE 5.1: *Comparison of simulated cw-oscillation thresholds for different laser resonator arrangements.*

As expected, translating the rod to place the tangential focus on the rod end in a symmetric cavity allows a threshold reduction but surprisingly, although the threshold for both 3-mirror resonators is less than the 4-mirror cavity, the 3-mirror laser pumped through the angled folding mirror, allowing only the tangential focus to be placed on this rod end, has slightly lower cw-threshold than obtained with the tight localised focus at the opposite end of the rod. For the higher absorbing case, the lowest threshold is, as originally expected, for the 3-mirror resonator with the tight localised focus on the retroflecting mirror end of the laser rod; this threshold is in fact a quarter of that for the symmetric laser with the focus at the rod centre, and half that for the symmetric laser with the tangential focus at the rod end using gain media with 4 cm^{-1} pump absorption coefficient. This clearly demonstrates the benefits of a 3-mirror resonator in lasers

based around high pump absorbing media, however, its superiority for low absorbing Cr^{4+}:YAG is minimal.

Thermal Lensing in 3-mirror Resonators

It is useful to simulate the effect of a distributed thermal lens on any new cavity design to predict its suitability to operation with high incident pump powers using the adapted Innocenzi[33] model developed in chapter 4. In comparison with the symmetric 4-mirror results from section 4.5.2, the 3-mirror cavity with the Brewster-angled gain medium is no worse for pump powers up to 5W (figure 5.18): although the sagittal and tangential zones are differentiated for 5W pump (figure 5.18(b)) the total overlap region is comparable with that for the 4-mirror resonator(figure 4.21(c)). Therefore operation at pump powers up to 5W should be feasible with this cavity design. Note that throughout this modelling, the pump beam was always focused on the pumped end of the rod.

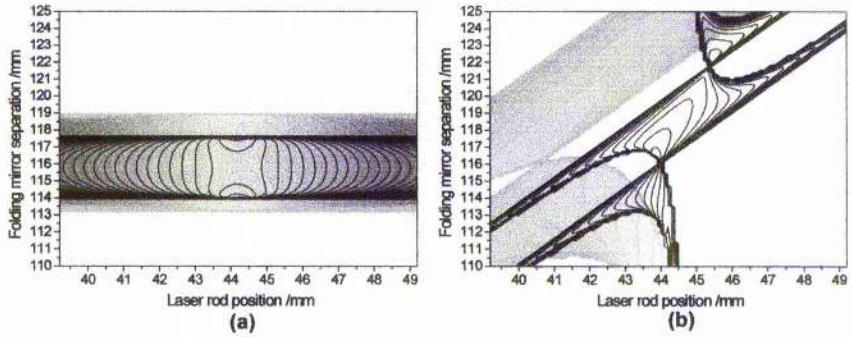

FIGURE 5.18: *Contour plots of the tangential (black outline) and sagittal (variable greyscale) stability regions for a 3-mirror cavity based on a Brewster-angled gain element pumped from the retroflecting mirror end, as the folding mirror separation and gain element position are varied for increasing thermal lens strength.* **(a):** *P=0 W has no lensing* **(b):** *P=5 W causes considerable separation of the stability zones*

For higher pump powers (up to 10W), it would appear from the contour plots in figure 5.19 that the 3-mirror design is superior to the usual 4-mirror symmetric resonator based around a Brewster-angled gain medium. The overlap region for the 3-mirror laser in figure 5.19(b) is considerably greater than the overlapped area in figure 5.19(a) corresponding to the alignment for operation of a 4-mirror resonator.

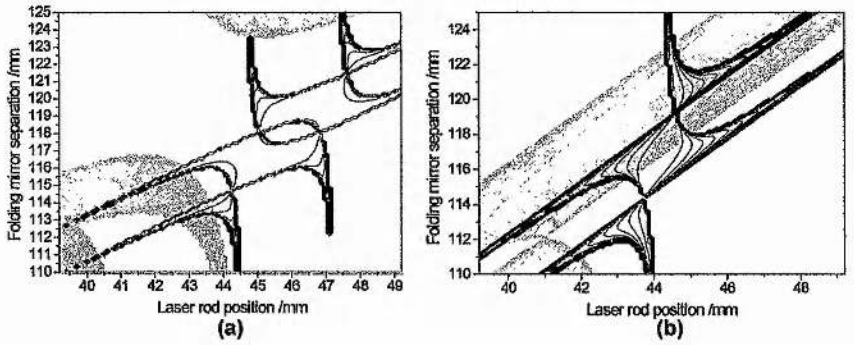

FIGURE 5.19: *Comparison of the thermal lens effect on cavity stability with P=10 W incident.* **(a):** *symmetric 4-mirror cavity.* **(b):** *3-mirror laser pumped through retroflecting mirror.*

In the following section, the Magni model is implemented to simulate the operation of 3-mirror resonators for self-modelocked operation, but it is important to note that no thermal lensing is taken into account throughout this modelling. It can be deduced from the plots in figures 4.21, 5.18 & 5.19 that the distributed thermal lens has a dramatic effect on overall resonator stability for high pump powers and hence on the laser alignment suitable for SML. An adaptation of the Magni model which includes this lensing effect would be a useful development for laser systems such as Cr^{4+}:YAG.

Implementation of the Magni Model for 3-mirror Resonators

Optimisation for soft-aperture based SML

We can calculate the Kerr-lens sensitivity at the pumped end of the rod using the Magni model described, for both the tangential and sagittal planes, provided that both beam waists remain fixed at the rod end. This is straightforward to achieve as according to equation 5.16(b), the retroflecting end-mirror should be fixed at a distance equal to its radius of curvature from the Brewster cut rod. The 3-mirror cavity can then be considered as a special case of the laser cavities studied by Bouma which had the end-mirror physically placed on the end of the laser rod.

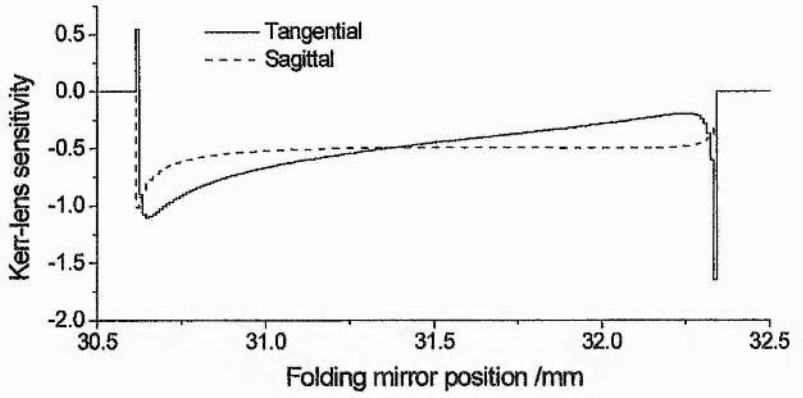

FIGURE 5.20: *Plot of the Kerr-lens sensitivity parameter for the sagittal and tangential planes calculated using equation 5.14 for the end of the Brewster-angled rod nearest the retroflecting end-mirror.*

The plot in figure 5.20 is the KLS calculated for both the tangential and sagittal planes at the rod facet, as the folding mirror is translated, with the retroflecting curved end-mirror fixed at a distance equal to its ROC from the Brewster rod. This arrangement has the fortunate consequence that the KLS is always negative in both planes throughout the adjustment, however, the greatest effect is accessed by translating the folding mirror towards the laser rod near the edge of the cavity stability (~30.7 mm away). Therefore it is anticipated that this laser would be more straightforward to self-modelock via a soft-aperture effect if optimised to create a tight focus at the rod end and by pumping through the retroflecting end-mirror.

Optimisation for hard-aperture based SML

A drawback of the semi-monolithic SML 3-mirror lasers (i.e. those with one end of the gain medium HR coated to form a cavity end-mirror) and the 'retroflecting' style cavity aligned as in the last section, is the inability to utilise a hard-aperture (i.e. a slit) to accomplish self-modelocking i.e. the soft-aperture effect *must* be relied upon to provide the necessary self-amplitude-modulation. This stems from the fact these cavities are acting optically as perfectly symmetric 4-mirror resonators with the laser rod positioned such that the spot in the arm on the end-mirror *always* expands for stronger lensing. The retroflecting 3-mirror design introduced in this chapter allows this perfect symmetry to be broken if the retroflecting end-mirror is not placed at a distance given by either equation 5.16(a) or (b) so the focus lies distributed inside the laser crystal i.e. no longer optimised for the strongest asymmetric nonlinear lensing. Because dispersion compensating prisms are often positioned in the arm of the SML laser, a slit placed here in the tangential plane would limit the oscillating bandwidth by clipping the spatially dispersed beam probably preventing SML operation. Unfortunately, modelling predicts that the KLS in the sagittal plane at the end-mirror for cavities with astigmatic elements is substantially smaller than the tangential, hence SML is unlikely. However,

this 3-mirror cavity may allow hard-aperture modelocking by clipping the non-dispersed beam in the tangential plane in front of the retroflecting end-mirror.

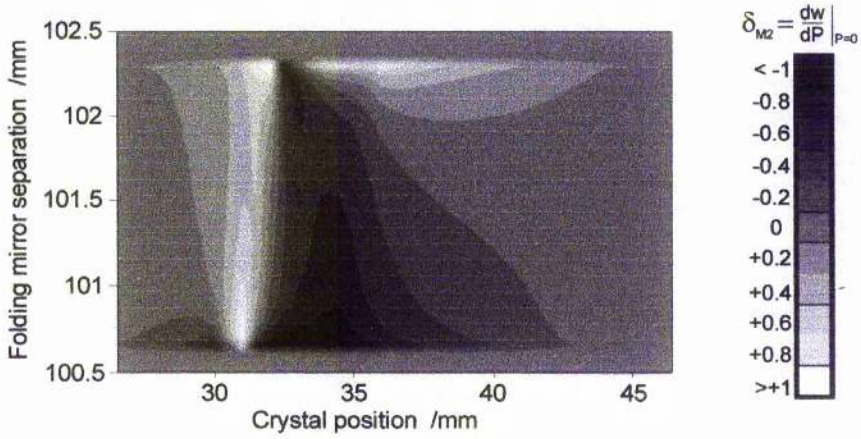

FIGURE 5.21: *Plot of the Kerr-lens sensitivity calculated at the curved retroflecting end-mirror as the folding mirror separation and rod position are varied.*

Figure 5.21 is a contour plot, similar to that usually calculated for 4-mirror resonators with the curved mirror separation and rod position both varied, but the KLS was calculated in front of the curved end-mirror. The darkest regions indicate a tendency for the spot to contract at this mirror for stronger Kerr-lensing and hard-aperture-based modelocking should be attainable for a laser aligned to operate in these zones. This would be of benefit for self-modelocking a laser pumped by a laser with poor beam quality e.g. a diode laser but is inappropriate for the Nd:YAG pumped Cr^{4+}:YAG laser described in this chapter and so was not implemented.

In practice, this approach to hard-aperture self-modelocking will be difficult since the pump beam would be focused through the mirror with an aperture placed in front and may be clipped.

Optimisation of Intracavity Dispersion

The effect of dispersion is treated briefly here for reasons which will become apparent. The main approaches to intracavity dispersion compensation have been discussed in chapter 1 section 1.4.3, where an expression for the relationship between the output pulse duration, pulse energy, effective spot size, and dispersion, was developed from the soliton model[34]:

$$\tau_{p0} = \lambda \cdot w_{eff}^2 \cdot \frac{|\beta_2|}{E \cdot n_{2I}}. \qquad \text{Equation (5.18)}$$

Important points note about this equation are the linear dependence on dispersion,

square dependence on spot size and inverse dependence on pulse energy. This last point has important consequences when reducing the intracavity power of a laser for modelocking near a low cw-threshold for low pump power requirements: dispersion therefore becomes increasingly dominant as the intracavity power is reduced and/or pulse repetition rate is increased. This may be partially counterbalanced by a reduction in the effective beam waist.

With regard to a Cr^{4+}:YAG laser, dispersion compensation is limited in the available degree of optimisation. At 1.5 microns, many materials possess anomalous (i.e. negative) group-velocity-dispersion (GVD); indeed even the YAG host material itself has only a small amount of positive GVD requiring compensation (+16.4 fs^2/mm). Surprisingly then, reported SML Cr^{4+}:YAG lasers possess a huge amount of excess negative GVD, for example the laser reported by Sennaroglu et al. possessed over -2500 fs^2 excess GVD intracavity. This excess compensation is intended to balance the self-phase modulation induced in the gain medium. An unfortunate consequence of requiring this degree of geometric dispersion compensation is the massive excess (~15,000 fs^3) of third-order dispersion which always remains in lasers of this type. The approach to third and second-order dispersion optimisation prescribed by Lemoff et al. is not applicable to a low-gain laser operating at 1.5 μm: exotic prism materials are required (eg. ZnSe) which possess too much intrinsic loss to be viable for inclusion in a Cr^{4+}:YAG laser.

An expression for the residual contribution to GVD in a Cr^{4+}:YAG laser cavity from section 1.4.3 using values pertinent to a Cr^{4+}:YAG laser with a fused silica prism pair is:

$$\beta''(\lambda_0) = 16.4 \times d_{YAG} - 161 - 6.61 \times d_{prism} \qquad \text{Equation (5.19)}$$

Other drawbacks of the Cr^{4+}:YAG system which hinder dispersion compensation include the large physical length of the gain medium due to the low pump absorption such that gain media are usually more than two centimetres long.

5.3.4 Construction of an Efficient, 3-Mirror Femtosecond Cr^{4+},Mg^{2+}:YAG Laser

From the modelling presented in section 5.3.3, it is apparent that pumping the 3-mirror resonator through the angled folding mirror is not the most efficient way to operate this cavity design: optimising the laser for cw operation leads to a highly distributed focus and results in a weak non-localised nonlinear lens as was illustrated in figure 5.17. A much more effective way to utilise this design would involve pumping through the retroflecting end-mirror: a laser then optimised for cw operation would

have a very tight localised intracavity focus on the pumped end of the rod creating a strong asymmetric nonlinear lens as in figure 5.16.

For the reasons given above, the layout illustrated in figure 5.22 was adopted for self-modelocking: all the cavity elements were as for the earlier 3-mirror design (figure 5.7) with the exception of the laser gain element (a more efficient 23mm long Cr^{4+}:YAG rod co-doped with magnesium was used as characterised in section 4.5.1) and the retroflecting end-mirror. A 75mm ROC end-mirror was used as this had greater transmission at the 1.064μm pump wavelength than the 50mm mirror originally used, although as discussed earlier, this change has no effect on overall laser cavity behaviour.

As with the earlier cavity design, regenerative modelocking was employed via a prism style modulator to initiate femtosecond operation. The modulator was operated at frequencies near 97 MHz permitting a pulse repetition rate of ~194 MHz from a laser of total length ~80cm. The direct laser-diode pumped Nd:YAG laser described in chapter 2 was employed as the pump source. One additional advantage of pumping the 3-mirror cavity through the curved end-mirror is the elimination of all reflections of the pump light into the pump laser. In this respect, the extended retroflecting 3-mirror design is superior to the semi-monolithic design which pumps through a plane HR facet end-mirror as some back reflections will result from this scheme unless the laser rod is misaligned. Thus the lossy and expensive optical isolator and half wave-plate are no longer required thus permitting more efficient use of the available pump light.

The construction of the laser scheme in figure 5.22 probably deserves a remark. As already stated, the retroflecting 3-mirror design was originally pumped through the folding mirror for ease of alignment: it was basically a simpler cavity than the 4-mirror design it replaced. However, pumping through the curved end-mirror is more difficult to set up: it is essential to ensure the pump beam goes through the centre of both the pump focus lens and the retroflecting mirror and at normal incidence before proceeding to construct the rest of the cavity. This is accomplished by observing the transmitted and reflected beams from both elements ensuring they remain along the original pump axis. The laser crystal is then placed at the ROC from the curved end-mirror. And the rest of the cavity constructed. Feedback from the curved end-mirror should then be straightforward to achieve (observed on a germanium photodiode immediately next to the folding mirror *not* at the end of the arm) with minimum pump beam disruption.

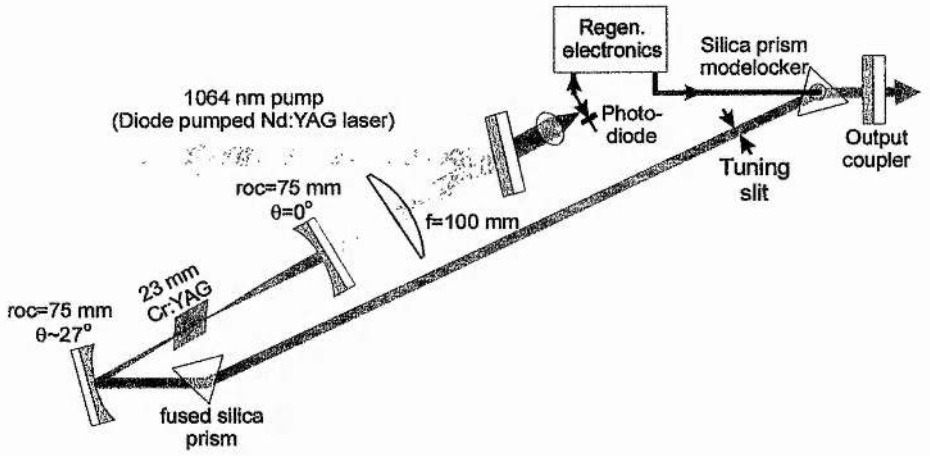

FIGURE 5.22: *Schematic of the optimised 3-mirror laser resonator pumping through the curved retroflecting end-mirror.*

The laser cavity was first aligned for a minimum cw threshold helping to ensure the intracavity focus was at the end of the rod. As the pump power was increased, minor adjustments were made to the folding mirror position from the optimum low threshold alignment to ensure stable cw operation. The higher gain of this Cr^{4+}:YAG rod permitted a 0.5% output coupler to be placed at the end of the arm. An initial prism separation of 36 cm (net cavity GVD = -2160 fs^2)was adopted for dispersion compensation.

This laser cavity was exceptionally easy to self-modelock: once regenerative initiation was applied with the maximum available pump power, femtosecond modelocked operation was observed with no cavity adjustments whatsoever Adjustment of the tuning slit and cavity alignment permitted stable femtosecond pulse generation centred at the important 1.55 μm telecommunications wavelength: 150 mW output power was produced through the 0.5% output coupler (nominal at 1550 nm, see figure 4.18) for just 4.5 W incident pump power. The 140 fs pulses were not bandwidth-limited assuming a $sech^2$ pulse shape ($\Delta\tau\Delta\nu$~0.37). Femtosecond operation was stable and would continue without regenerative initiation once modelocked until perturbed by draughts/vibrations etc.

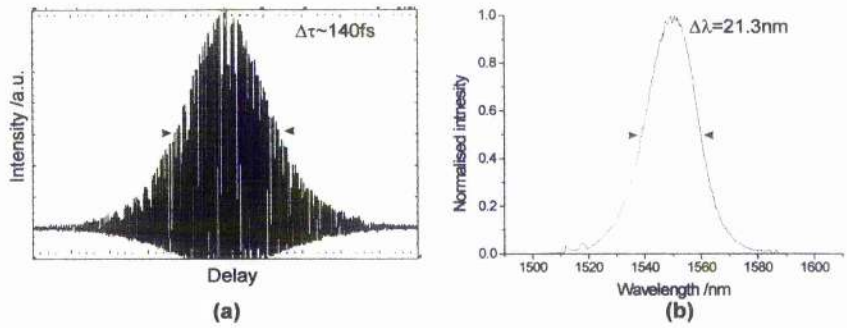

FIGURE 5.23: *Characterisation of 140fs pulses at the 1550nm telecommunications wavelength.* **(a):** *Interferometric autocorrelation,* **(b):** *corresponding spectrum*

With 4.73 W incident pump power, careful laser alignment permitted a self-start self-modelocking regime to be accessed at an average output power of 230 mW from the 0.5% nominal output coupler. Self-starting dispensed with the regenerative initiation altogether: the cavity could be blocked and femtosecond operation would immediately ensue once unblocked without any active perturbation to the resonator. 110 fs pulses were obtained which were near bandwidth limited at a centre wavelength of 1.53 μm (figure 5.24). A self-start self-modelocked Cr^{4+}:YAG laser was previously reported[35] which was based on a symmetric 4-mirror design, but there was a large cw component which, for an unexplained reason, had to be present for self-starting operation. The corresponding spectrum for the 3-mirror self-starting laser in figure 5.24(b) also shows a cw component near 1.492 μm but this constitutes less than 6% of the total laser output power.

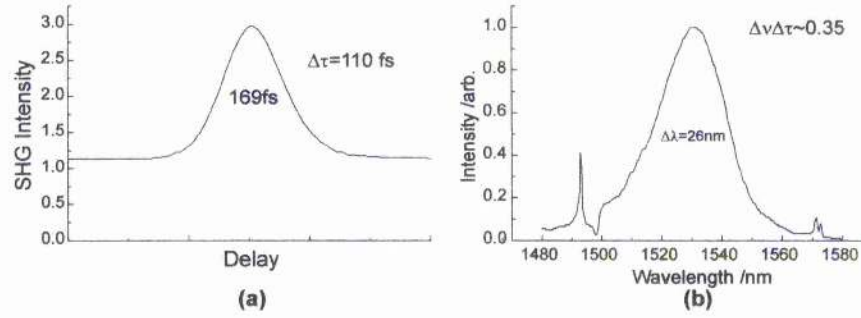

FIGURE 5.24: *Characterisation of pulses obtained from the 3-mirror Cr^{4+}:YAG laser aligned in a self-start, self-modelocked regime.* ***(a):*** *Intensity autocorrelation,* ***(b):*** *corresponding spectrum*

Low-threshold Optimisation

Replacement of the 0.5% output coupler with a HR plane mirror created a laser with all HR-mirrors as was used with the original 3-mirror schemes in section 5.3.2. After cavity optimisation, the cw threshold of this laser was 620 mW including all the cavity elements: significantly lower than the figure for the earlier laser though this

reduction is mainly due to the improved quality of the laser crystal. Significantly, however, is that with regenerative initiation, stable self-modelocked operation could be sustained for incident pump powers as low as 1.02 W. Although the pulses were long at 620 fs (figure 5.25) principally due to non optimised second and third-order dispersion, the low intracavity peak power of these pulses (~15kW) and the close proximity of the modelocking threshold to the cw threshold, demonstrate the high susceptibility of this laser to self-modelocking.

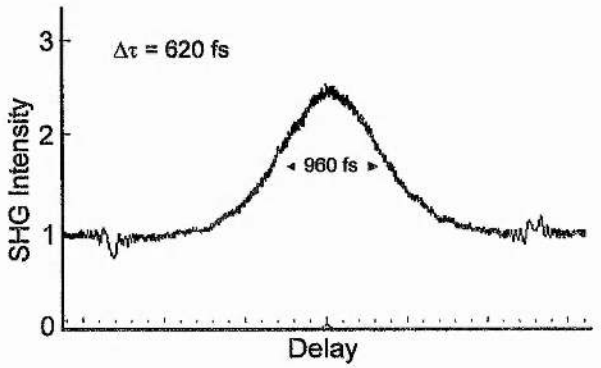

FIGURE 5.25: *Intensity autocorrelation of 600 fs pulses obtained near 1.5 μm for 1 W incident pump power*

5.3.5 Ultra-compact All-solid-state 3-mirror Femtosecond Cr^{4+}:YAG Lasers

The same silica-prism modelocker as was used for the 194 MHz cavity in the preceding section was found to possess a weak resonance at 160 MHz. After adjustment of the RF regenerative initiation circuitry, an ultra-compact femtosecond laser with a pulse repetition rate of 320 MHz and a total cavity length of just 47 cm was built.

Two alignments of the laser were constructed. For high power operation, a 75 mm ROC folding mirror was used with a 1% nominal output coupler. A HR end-mirror was deployed for low threshold operation and the folding mirror ROC reduced to 50 mm to decrease the spot size inside the crystal (area reduced from ~7000 μm^2 to ~3000 μm^2) ensuring a strong nonlinear lens was maintained. A shorter prism separation of 18 cm (total GVD= -970fs^2)was used.

When aligned for high power operation, the laser generated pulses as short as 120 fs (figure 5.26) with a maximum average output power of 300 mW at a pump power of 5.2W. The higher output coupling (1% nominal at 1.6μm) of 1.3% at 1.55 μm pushed the free running wavelength of the laser out to ~1.54 μm without tuning

elements. Modelocked operation was exceptionally stable and this laser was characterised for low-noise operation as presented in the next section.

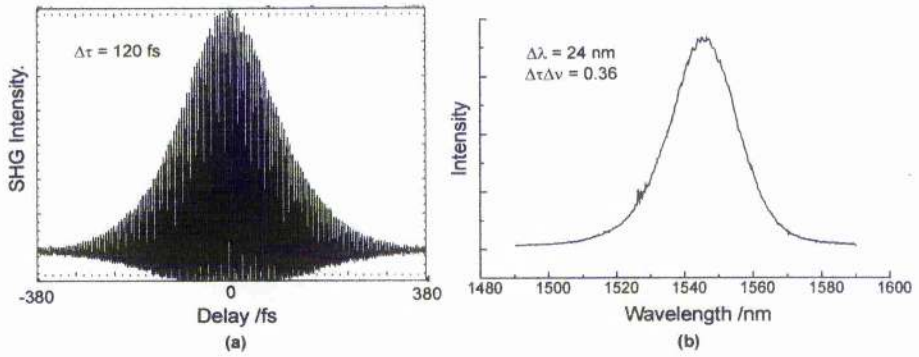

FIGURE 5.26: *Typical pulse characterisation for high power operation at 320 MHz repetition rate.* **(a):** *Interferometric autocorrelation,* **(b):** *corresponding spectrum*

The low threshold alignment required a 50 mm folding mirror from the colour-centre laser set which pushed the free-running wavelength down to ~1.5 μm, thus the two remaining HR mirrors provided considerable output coupling (~0.2%). The lowest pump power requirement for which femtosecond operation could be initiated and sustained by the regenerative modelocker was 1.5 W incident. Bandwidth-limited 160 fs pulses were obtained (figure 5.27). The measured average output power of 15 mW from the arm implied a total output of 30 mW through each end-mirror, thus further optimisation of this laser may be possible producing greater useful output power.

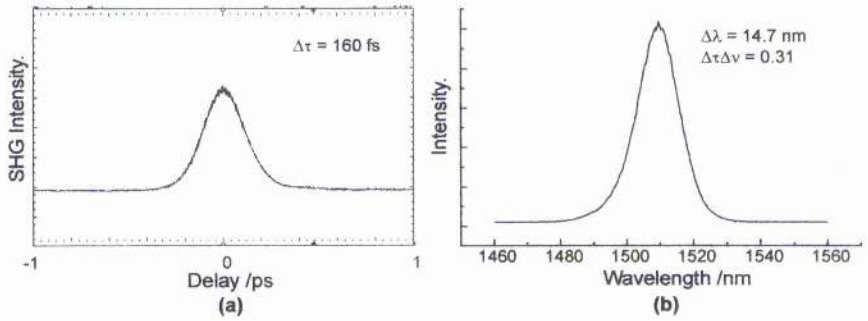

FIGURE 5.27: *Pulse characterisation of the low-threshold 320 MHz Cr^{4+}:YAG laser.* **(a):** *Intensity autocorrelation,* **(b):** *corresponding spectrum*

By eliminating the dependence on regenerative initiation and using a pair of standard infrasil (fused silica) prisms separated by just 9.5cm (net cavity GVD=-410 fs^2), an ultracompact laser was realised having a pulse repetition rate of 402 MHz and a total cavity length of 37 cm. The nominal 0.5% output coupler was used and a 75 mm ROC folding mirror.

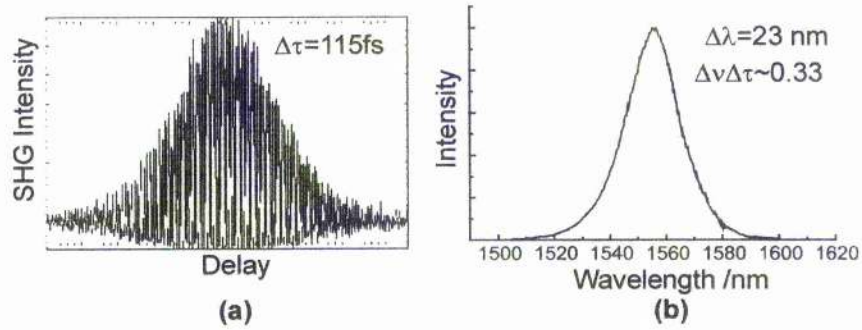

FIGURE 5.28: *Pulse characterisation of the ultra-high repetition rate 402 MHz Cr^{4+}:YAG laser.* **(a):** *Interferometric autocorrelation,* **(b):** *corresponding spectrum*

Femtosecond operation was initiated by tapping the back of the cavity output coupler or curved retroflecting end-mirror. Near-bandwidth-limited pulses of 115 fs were obtained centred naturally at the long wavelength of 1.55 μm (figure 5.28). The high reflectivity of the 0.5% output coupler at this wavelength explains the low output power (105 mW) for the pump power of 4.4 W. A more efficient arrangement of this laser might require the use of a 50 mm ROC folding mirror thus permitting greater output coupling to be used whilst maintaining a strong nonlinear lens inside the rod.

5.4 Noise Characterisation of the All-solid-state, Compact 3-mirror Cr^{4+}:YAG Laser

The all-solid-state systems described in the previous section were significantly stable once optimised for self-modelocked operation. The greatest contributory factor to this stability is the solid-state pump source. As discussed in chapter 2, both the beam pointing behaviour and the amplitude stability are significantly improved over the arc-lamp pumped mainframe lasers previously used as pump sources for femtosecond Cr^{4+}:YAG lasers.

Interestingly, at an early stage in the construction of the laser, it became apparent that one unlikely source of instability which caused cessation of modelocking (and prevented its re-initiation) on a periodic timescale, was the water cooler used to directly cool the Nd:YAG rod of the all-solid-state pump laser. This had a large temperature hysteresis over approximately 10 minutes causing the output power to fluctuate by ~500 mW. This variation could not be satisfactorily offset by adjusting the variable attenuator, possibly as the beam quality varied with the changing rod temperature. This instability was overcome by employing a closed-loop thermo-electric cooled Nd:YAG mount with mains water heating.

A summary characterisation of the 320 MHz compact laser was carried out to

determine the remaining instability of the all-solid-state femtosecond source. The regenerative initiation scheme was disconnected for all these measurements once SML was established to minimise possible external sources of perturbation.

In figure 5.29, the pulse train, detected using a 500MHz bandwidth germanium photodiode and fast oscilloscope, is displayed for two time intervals. Figure 5.29(a) is a snapshot over a 200 ns interval allowing the individual pulses to be resolved: no instability is observable at the top of the trace. A scan over a 2 second period (figure 5.29(b)) blurs the individual pulses into a solid black line at the top of the trace indicating constant pulse peak power. The sensitivity of this measurement is basically insufficient to resolve any amplitude noise on the pulse train.

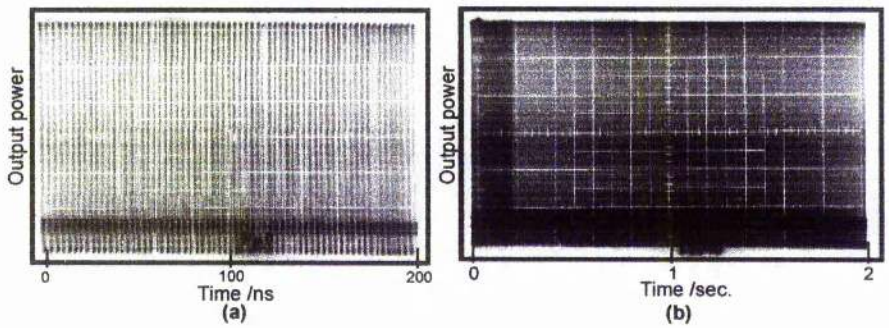

FIGURE 5.29: *Amplitude noise on the modelocked pulse train from the 320 MHz laser.* **(a):** *Sampled over a 200 ns interval.* **(b):** *Sampled over a 2 second scan.*

A much more sensitive appraisal of modelocked stability can be gained by observing the amplitude noise on the second harmonic generated signal using a non-linear crystal. In practice, the measurement in figure 5.30 was recorded from the autocorrelator with the variable delay arm blocked. Less than 3% rms noise was recorded over a two second interval indicating both excellent amplitude and pulse duration stability. This measurement is also very susceptible to modelocked pulse train instabilities caused by poor laser cavity alignment.

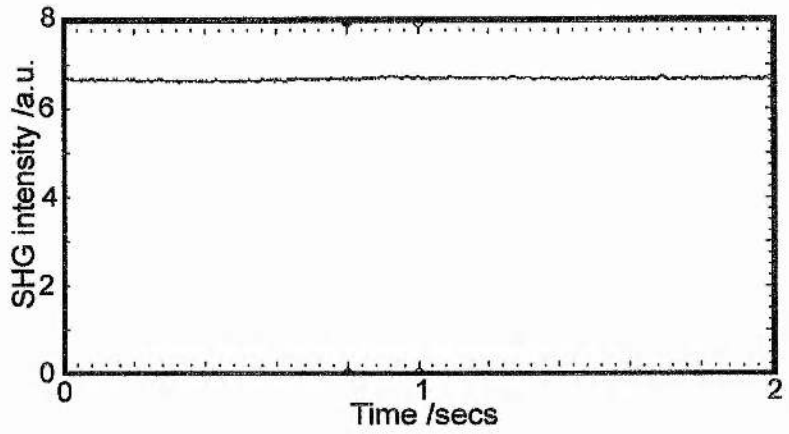

FIGURE 5.30: *Noise on the second-harmonic generated signal from the modelocked 320 MHz laser.*

As discussed in chapter 3, modelocked lasers suffer from variations in the repetition rate of the output pulses (pulse jitter) induced from numerous sources (environmental, pump source or noise sources intrinsic to the laser scheme itself etc.)[36]. This phase noise may be important in some measurements which depend on the periodic pulse occurrence. As explained in chapter 3, the phase noise causes a change in RF sideband noise level which increases with the square of the harmonic of the pulse repetition rate, hence the difference in noise components between two harmonics is due to phase noise. In figure 5.31, the fundamental and tenth harmonics of the 320 MHz laser are reproduced within frequency spans of (a) 100kHz and (b) 10kHz. There is a slight increase in the background noise level of the tenth harmonic within the 100 kHz scan however there appears to be significantly higher noise within the 10 kHz region using the higher resolving power.

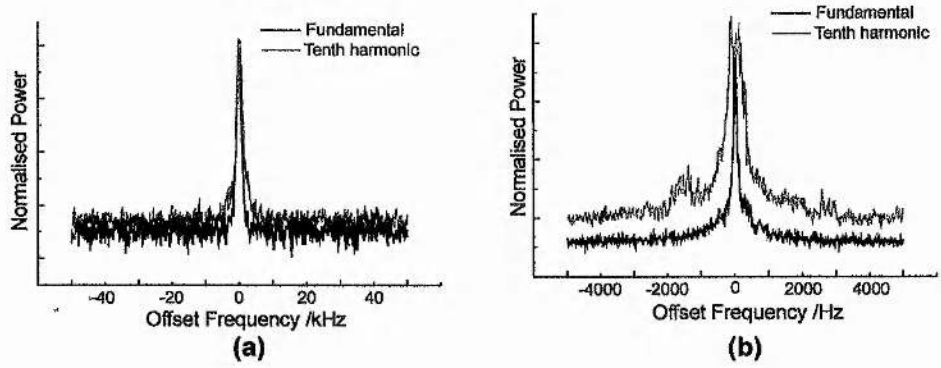

FIGURE 5.31: *RF spectra taken around the central cavity carrier signal of 320 MHz and its tenth harmonic for phase noise determination.* **(a):** *100 kHz scan, resolution bandwidth=300 Hz.* **(b):** *10 kHz scan, resolution bandwidth=30 Hz.*

An automated calculation of the single-sideband phase noise spectrum was carried out indicating significant pulse jitter remains below 1 kHz (figure 5.32).

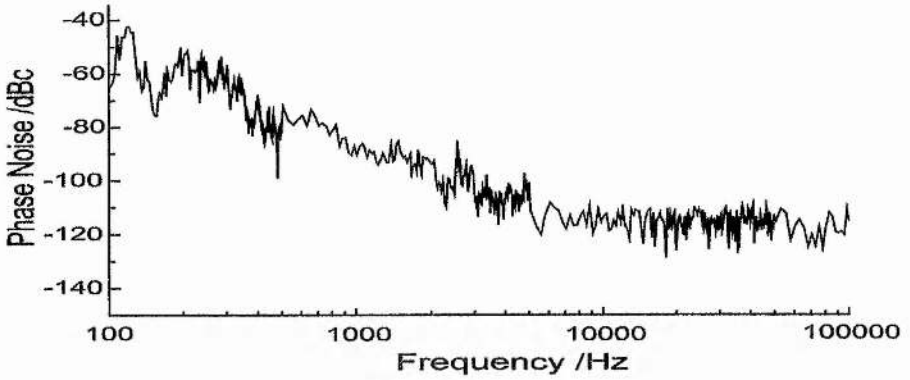

FIGURE 5.32: *Single sideband phase-noise spectrum of the free-running, self-modelocked 320 MHz laser with regenerative initiation disconnected.*

The rms timing jitter figures reproduced in table 5.2 are, surprisingly, extremely high for a laser of this type, though the reason for these poor figures is uncertain: although the Cr^{4+}:YAG rod itself is held in a water cooled mount, the mount was of sufficient mass to permit the circulating pump to be turned off and a phase noise measurement repeated on the laser with no cooling had similar figures to those reproduced here. A more plausible source of this instability is the pump source: while these measurements were carried out, the pump laser was observed to intermittently Q-switch, for unknown reasons and attempts to re-align the pump failed to eliminate the problem. Much later it was realised that accumulated dust in the laser, in particular on the intracavity lens and the output coupler, reduced power output and could cause pump instabilities. Further engineering of the pump laser should completely eliminate this noise source by eliminating necessary periodic removal of the box cover to re-align the laser.

Frequency band	50 Hz – 500 Hz	500 Hz – 5 kHz	5 kHz – 50 kHz
rms jitter figure	33 ps	2 ps	290 fs

TABLE 5.2: *rms timing jitter figures for the SML 3-mirror laser.*

5.5 Highly Asymmetric 4-mirror Resonator Designs

5.5.1 Tight Localised Focusing in a Z-cavity

The original benefit gained from adopting a 3-mirror resonator was the reduced parasitic losses from eliminating two lossy HR reflections per round trip. This was of importance for the laser based around the earlier Cr^{4+},Ca^{2+}:YAG rods which had very low gain beyond 1.5 μm, but was of less importance with the arrival of better gain

media such as the 23 mm Cr^{4+},Mg^{2+}:YAG used in the later laser schemes. The potential remaining benefit of the 3-mirror laser was the ability to create strong, localised, asymmetric intensity-induced nonlinear lensing -ideal for self-modelocked lasers- in an 'off-the-shelf' Brewster-Brewster cut gain medium. The principal reason for this capability is the effective separation of all astigmatic-elements onto one side of the laser cavity; the curved retroflecting end-mirror is used at normal incidence and therefore introduces zero astigmatism permitting the simultaneous positioning of sagittal and tangential foci on an angled dielectric interface. This ability is therefore not limited to a 3-mirror resonator: provided that a folding mirror is used close to normal incidence, the astigmatism introduced (scaled with **cos(θ)** where θ is the mirror half angle) is negligible, hence a 4-mirror resonator design could be used with one folding mirror angled as for a 3-mirror resonator (this is a larger angle than is used in a symmetric Z-cavity), and the other (through which the pump is focused) operated at near normal incidence (figure 5.33). The arm length of one of the arms (usually from the mirror used at normal incidence) is normally much shorter than the second arm, which could include dispersion compensation. Thus a non spatially-dispersed output beam is accessible from the arm without the prisms. It would be usual to align this cavity design to operate in the low-misalignment sensitivity (LMS) region, i.e. the beam would be focused on the end-mirror of the short arm.

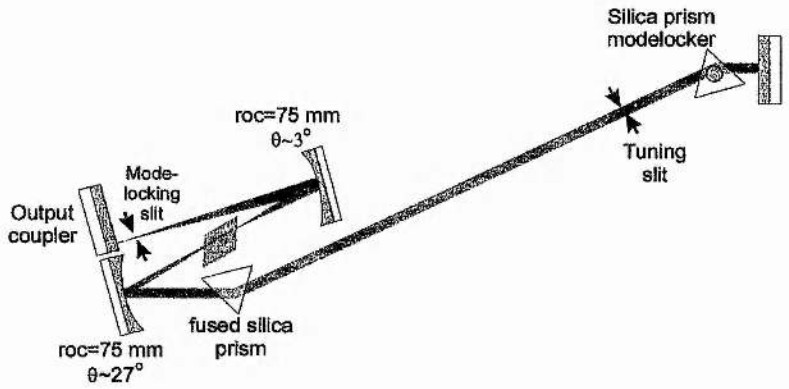

FIGURE 5.33: *Schematic of the highly asymmetric 4-mirror cavity design for achieving a tight focus on the end of a Brewster-cut rod in a Z-cavity layout.*

A potential benefit of this alternative design is to provide a straightforward means for achieving hard-aperture induced self-modelocking: a slit may be placed in the non-dispersed arm clipping the beam in the tangential plane. Using the Magni model, the contour plot in figure 5.34 was produced for the Kerr-lens sensitivity at this end-mirror, demonstrating that hard-aperture modelocking should be possible with this layout by aligning the laser to operate in the dark regions: i.e. translating the angled folding mirror towards the laser rod. No attempt was made to hard-aperture modelock this laser in

practice, although a novel soft-aperture SML version was successfully demonstrated as described in the next section.

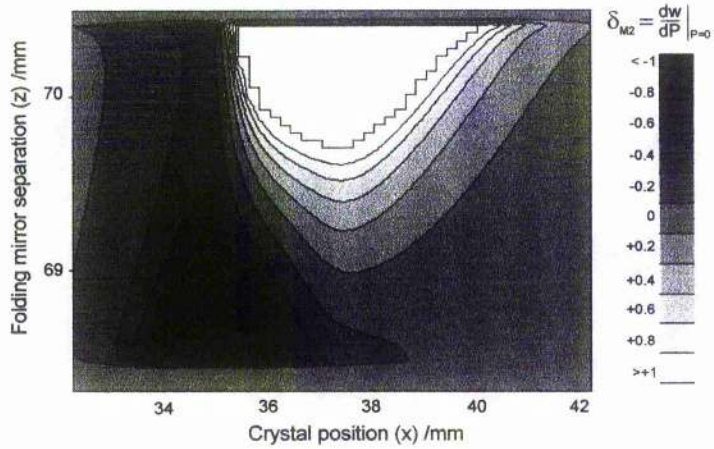

FIGURE 5.34: *Contour plot of the KLS calculated in the tangential plane at the end-mirror of the short arm (normal incidence) of a highly asymmetric 4-mirror laser design aligned in the LMS region.*

This cavity design has been successfully employed in Cr:LiSAF lasers modelocked using a semiconductor saturable absorber element (e.g. A-FPSA) by reducing the length of the short arm to give a tight focus on the saturable element[8].

5.5.2 Compact Approach to Dispersion Compensation in 4-mirror Resonators

One drawback to relying on prisms as the dispersion controlling elements in a femtosecond laser resonator, is the large prism separation which is often necessary, thus restricting the minimum size of the overall laser system. Although prisms made from more dispersive material may permit a more compact geometry, the resulting third order dispersion can be undesirable and restrict the shortest pulse duration.

Recently Aoshima et al.[37] described a novel SML Cr:LiSAF laser arrangement based on a standard symmetric 4-mirror Z-cavity geometry but placed a GVD compensating prism in each arm thus splitting the prism separation through the folding section. The optimum prism separation was first found experimentally in a standard Z-cavity arrangement with both prisms in one arm, then a more compact version was built with the prisms in each arm but maintaining the same total prism apex separation. Since the intracavity beam forms a focus within the folding section, Aoshima argued that the angularly dispersed rays 'flipped over' and hence both prisms must face the same way to allow re-collimation of the angularly dispersed spectral components.

There are several elements of this proposed explanation of the dispersion control through the folding section which require clarification as discussed later. However, the laser operated satisfactorily self-modelocked although the pulse durations obtained were substantially longer than were produced with the same prism separation in the same arm of a Z-cavity, suggesting that the proposed treatment of the dispersion was over simplistic.

Although this size reducing approach for SML lasers is not entirely appropriate to Cr^{4+}:YAG systems, as there is only a small amount of positive dispersion which requires compensation anyway, it does provide a good platform on which to assess the characteristics of the scheme: if it works with Cr^{4+}:YAG, it would probably work with any laser!

A modified version of the Aoshima approach was adopted, by employing the prisms in each arm of the highly asymmetric 4-mirror design proposed in section 5.5.1. This was aligned in the low-misalignment sensitivity region hence focusing through one of the prisms. The layout is illustrated in figure 5.35. The laser was designed to operate at a pulse repetition rate of ~320 MHz permitting regenerative initiation to be employed via the fused silica modelocker. The total footprint of the laser was just 25x20 cm including the pump steering mirror and pump focus lens. The total prism apex separation through the folding section was ~33 cm. A nominal 0.5 % output coupler was used.

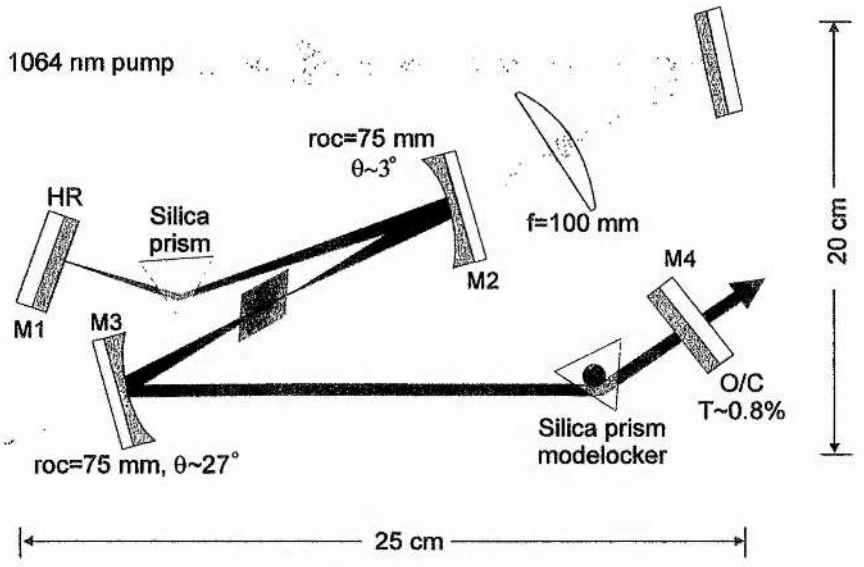

FIGURE 5.35: *Schematic of the ultra-compact highly-asymmetric 4-mirror laser with prisms in each arm.*

Self-modelocked operation was very straight forward to achieve once the regenerative initiation was applied. Significantly longer pulses were obtained from this laser than was previously described from the 320 MHz 3-mirror laser, however,

modelocked stability was not compromised. The minimum duration measured was 330 fs whilst the laser typically gave near-bandwidth limited pulses of approximately half a picosecond (figure 5.36). The average output power was 220 mW for 5.8 W incident pump power.

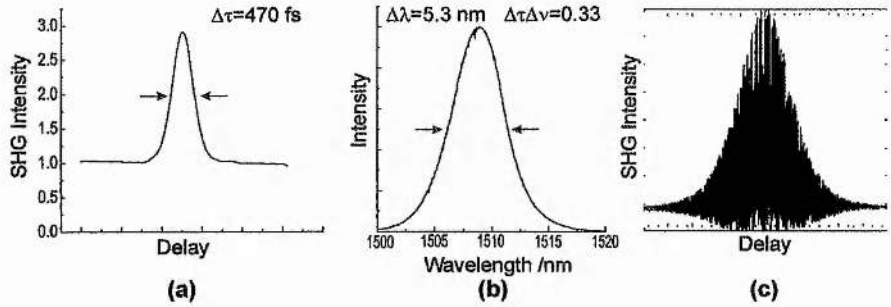

FIGURE 5.36: *Typical results obtained from the Cr:YAG laser in figure 5.35.* **(a):** *Intensity autocorrelation.* **(b):** *Corresponding spectrum.* **(c):** *Interferometric autocorrelation.*

With the intention of increasing the self-phase modulation in the gain medium to increase the bandwidth of the modelocked pulses[38], the angled 75 mm folding mirror was substituted with one of 50 mm radius of curvature. This reduced the cross sectional area of the intracavity beam focus from 12,300 μm^2 to 5060 μm^2. Surprisingly, the pulse durations obtained with this arrangement were somewhat longer than with a 75 mm mirror: typically the pulses were of 730 fs duration with a time-bandwidth product of 0.36 though the output power remained high (200 mW).

For certain applications, it may be desirable to generate pulses of high peak-power with durations of approximately 1 ps, and so it is worthwhile understanding the mechanism which leads to the generation of these stable, high quality longer pulses. The most likely rationale is the vast excess of negative GVD present in the cavity: considering Aoshima's simple explanation to be true, due to the physical prism separation alone the net excess cavity GVD is -1960 fs^2 compared to the –970 fs^2 with the 3-mirror cavity of identical repetition rate.

5.5.3 Ray-Pulse Matrix Analysis of the Compact Resonator

Kostenbauder[39] has developed a versatile technique for modelling systems of dispersive elements. This involves an extended ray matrix formulation which includes a temporal component. The general scheme of the technique is summarised by equation 5.20. For a full justification of this procedure refer to reference 39. The system is based around 4x4 matrix operators to represent an optical system. The matrix transforms an input vector comprising spatial information (x_{in} the axis offset and θ_{in} the slope of the input ray) as do standard ray matrices, and temporal information

($\mathbf{t_{in}}$ reference input time and $\mathbf{f_{in}}$ frequency) into an equivalent output vector as described by equation (5.20). The matrix operator contains the standard ABCD matrix elements of an optical element plus additional elements, which have a time dependence, derived as indicated in equation (5.20).

$$\begin{bmatrix} x_{out} \\ \theta_{out} \\ t_{out} \\ f_{out} \end{bmatrix} = \begin{bmatrix} A & B & 0 & \frac{\partial x_{out}}{\partial f_{in}} \\ C & D & 0 & \frac{\partial \theta_{out}}{\partial f_{in}} \\ \frac{\partial t_{out}}{\partial x_{in}} & \frac{\partial t_{out}}{\partial \theta_{in}} & 1 & \frac{\partial t_{out}}{\partial f_{in}} \\ 0 & 0 & 0 & 1 \end{bmatrix} \times \begin{bmatrix} x_{in} \\ \theta_{in} \\ t_{in} \\ f_{in} \end{bmatrix} \qquad \text{Equation (5.20)}$$

Elements can be cascaded as with standard ray matrices simply by multiplying constituent elements together. Thus, for an imaginary pulse of given initial carrier frequency, launch angle and position at time $\mathbf{t_{in}}$=0, the delay of an optical system may be determined by examining $\mathbf{t_{out}}$. By repeating this for different frequencies, the dispersion of the system can be evaluated.

The general form of the ray-pulse transfer matrix is given by:

$$T = \begin{bmatrix} A & B & 0 & E \\ C & D & 0 & F \\ G & H & 1 & I \\ 0 & 0 & 0 & 1 \end{bmatrix} \qquad \text{Equation (5.21)}$$

For a stable optical resonator, equation 5.20 could be used to determine both the net cavity dispersion and the relative positions of rays of different wavelength. If the ray-pulse transfer matrix, **T**, is computed from a complete round trip of all the cavity elements, and the resonator stability condition (equation 5.12) is satisfied, equation 5.20 becomes an equality in the spatial domain as each ray of certain frequency, $\mathbf{f_{in}}$, must be self reproducing. Hence from equation (5.20), and using the notation of equation 5.21, expressions for the axial positions and slopes of different rays of differing input frequency may be determined:

$$x_{in} = \Delta f_{in} \cdot \frac{E.(1-D) + B.F}{(D-1).(A-1) - B.C} \qquad \text{Equation (5.22)}$$

$$\theta_{in} = \Delta f_{in} \cdot \frac{F.(1-A) + C.E}{(D-1).(A-1) - B.C} \qquad \text{Equation (5.23)}$$

From these expressions, and equation 5.20, the relative delay of a 'pulse' of frequency $\Delta\mathbf{f_{in}}$ from a reference 'pulse' over one cavity round trip may be determined:

$$\Delta t = G.x_{in} + H.\theta_{in} + I.\Delta f_{in} \qquad \text{Equation (5.24)}$$

From several such pulses of differing $\Delta \mathbf{f_{in}}$, an equation for the group-velocity dispersion can be constructed:

$$D = \frac{\tau_1 - 8.\tau_2 + 8.\tau_4 - \tau_5}{24.\pi.\Delta f} \qquad \text{Equation (5.25)}$$

where τ_1, τ_2 and τ_4 , τ_5 are the relative delays of 4 pulses of relative frequency $-2\Delta\mathbf{f}$, $-\Delta\mathbf{f}$, $\Delta\mathbf{f}$, $2\Delta\mathbf{f}$, from a reference pulse with an arbitrarily set τ_3=**0** for $\Delta \mathbf{f_{in3}}$=**0**.

For a given stable cavity alignment, it is straightforward to determine the round trip matrix at different points around the cavity, and using equations 5.22 & 23, the relative positions of rays of different wavelength may be deduced. It is instructive to start with a much simpler laser cavity than the actual Cr^{4+}:YAG design used. The simple layout illustrated in figure 5.37(a) is similar to the original Aoshima design in that the arm lengths and the position of the prisms in each arm are identical (**d**=5cm), however, for simplicity no gain element is included, hence the folding mirrors are operated at normal incidence and are represented in the figure by lenses. Silica prisms were used in this simulation with both folding mirrors having 10 cm ROC. Degrees of asymmetry may be added to the cavity in figure 5.37(a) incrementally to observe the effects on the intracavity dispersed rays. The intracavity beam for a cavity such as shown in figure 5.37(a) is sketched over the optical elements, but the refractive effects of the prisms were neglected for this.

In figure 5.37(b), three rays are traced along a path (imported from Mathcad™) calculated using equation 5.22. The green ray is an arbitrary ray of carrier frequency $\mathbf{f_0}$; the red and blue rays are at offset frequencies $\Delta\mathbf{f}$ above and below this arbitrary frequency. Hence the dispersive mechanism of the resonator can be deduced. Note that the behaviour of the rays is not to be confused with the beam shape within the cavity. A feeling of the relationship between the rays to the beam may be contrived by arbitrarily placing the reference ray at the $1/e^2$ point of the cavity beam, and plotting the calculated rays around this reference.

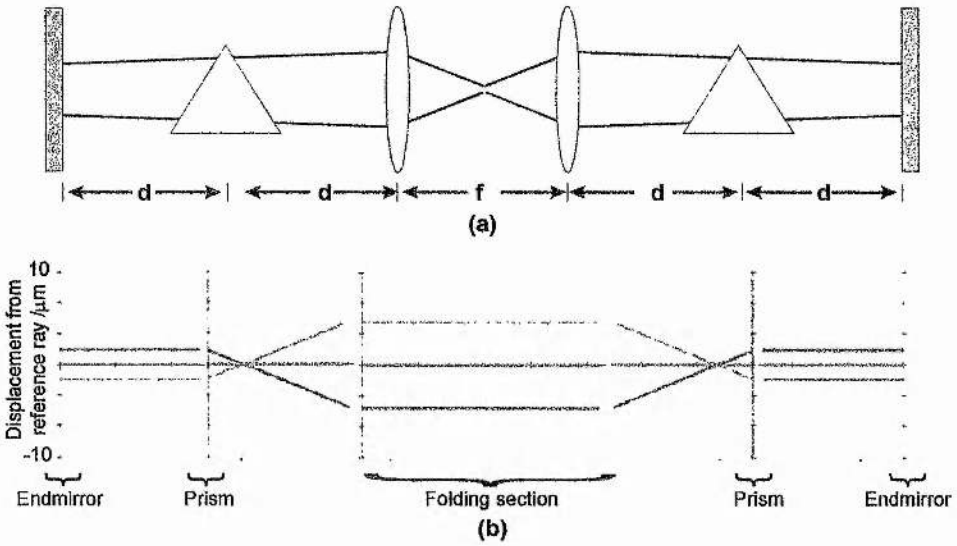

FIGURE 5.37: *Simple optical system to simulate the Aoshima laser cavity*[37]. **(a):** *Resonator schematic with simulated beam sketch.* **(b)** *Positions of rays of frequency +Δf (blue) and -Δf (red) relative to an arbitrary ray on-axis (green). Horizontal scale: 1 graduation=20mm*

Interestingly, in figure 5.37(b), the rays are parallel everywhere in this resonator except in the spaces between the folding mirrors and the prisms. This implies that the space in the folding section can be considered 'dead space' i.e. it contributes nothing to the net dispersion of the optical system and may be varied without affecting overall cavity GVD. This is confirmed by the simulation using equation 5.25: the net dispersion for the cavity remains –346 fs^2 throughout the cavity alignment adjustment covering the entire stable operating range of folding mirror separations. Similarly, the rays at each end-mirror are parallel and so the lengths of the arms beyond the prism may be varied with no net GVD change. Thus an asymmetric laser cavity may operate with the same GVD as this symmetric layout providing the prisms remain the same distance from the folding section.

The crucial parameter for controlling the GVD in a cavity of this type is the location of the prisms relative to the folding section: a highly angularly dispersed beam results from the effect of the prisms, hence the GVD can be easily changed by translating the prisms along the arms. The folding mirrors appear to perform an unexpected task of converting a highly angularly dispersed beam into a spatially dispersed beam. This is explained by the change in the effective focusing effect of the mirror experienced by rays of differing wavelength due to their different displacement from the optical axis. The rays are 'focused' to a point just in front of the prism ~38mm from the folding mirror. The GVD of this system can also be varied by changing the radius of curvature of the folding mirrors.

A plane-plane rod added to the scheme in figure 5.37(a) has no effect on the

behaviour of the rays though the dispersion of the cavity changes, of course, due to the added material.

A Brewster-angled rod can be added to the system with a very minor change in dispersion from the plane-rod case, but this type of rod does have an effect on the ray paths: the rays between the folding section become angularly dispersed.

A clear understanding of why the prisms must be orientated in identical ways is clearly seen from examining figure 5.37: the rays cross in each of the arms creating a second 'virtual' prism at this crossing point. Thus this cavity may be considered a symmetric Z-cavity with a pair of oppositely oriented prisms in each cavity arm. It was therefore incorrect of Aoshima's original approach to position the prisms such that their separation through the folding section was equal to their optimum separation in one cavity arm: further analysis is necessary to determine this optimum prism location.

Modelling the Cr^{4+}:YAG Highly Asymmetric Cavity.

The Cr^{4+}:YAG laser presented as figure 5.35 is interesting to study as it has almost every degree of asymmetry possible: the arm lengths differ, the relative prism positions from the folding mirrors are different, and the unusual technique of operating one mirror at near normal incidence and compensating for the Brewster angled rod with one large folding mirror angle. In addition, the asymmetric cavity is aligned in the low-misalignment sensitivity region causing the beam to be focused tightly through one prism whilst remain almost collimated during propagation in the other prism.

Using the technique discussed, the paths for two rays relative to a third reference ray were calculated throughout the cavity and are illustrated in figure 5.38. Each simulated ray is spaced +/-10nm relative to the reference ray wavelength. To clarify the dispersed nature of the cavity beam, these rays are plotted over the intracavity beam profile in figure 5.39.

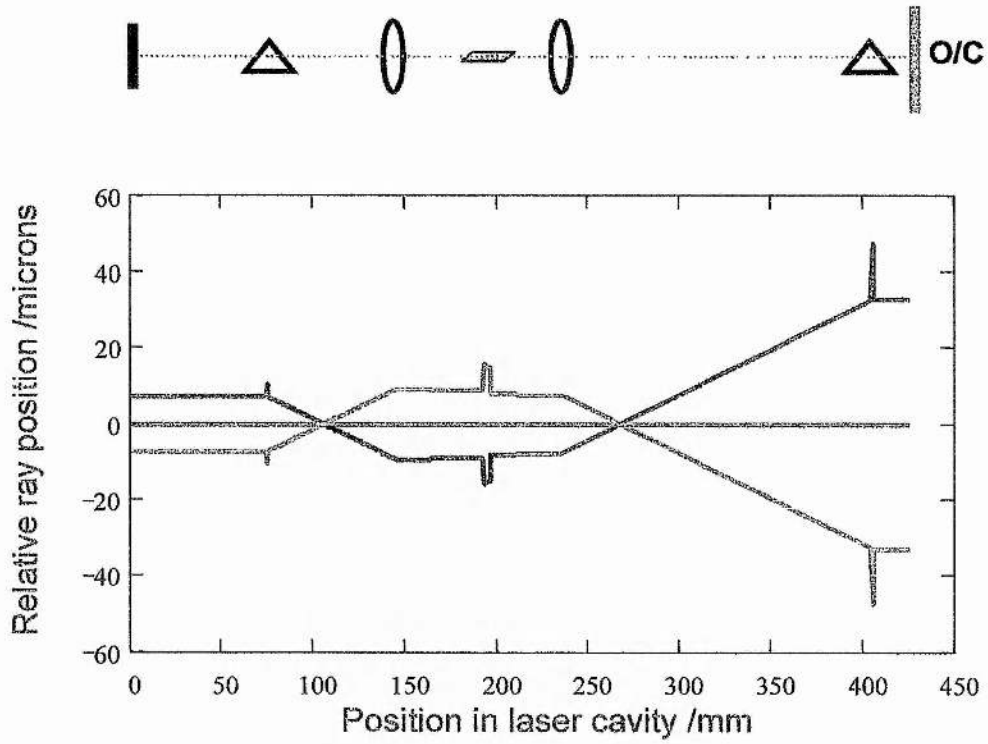

FIGURE 5.38: *Relative paths traced by three rays propagating round the highly-asymmetric cavity with a prism in each arm (green ray chosen arbitrarily to be a reference axis) The relative locations of the laser elements are shown above for clarity.*

Only a slight variation of the net cavity GVD was observed on re-aligning the model to simulate the laser aligned in the HMS region. The change in net GVD attainable by translating the folding mirrors is negligible, however, there may be some effect due to a variation of the angle of incidence of the beams on the prisms attained by moving the folding mirrors. This was not checked by the model.

The calculated value for net GVD (~-935 fs^2) is close to the original value for the 320 MHz 3-mirror laser (-970 fs^2).

Note that in this asymmetric resonator, the rays cross in each cavity arm thus a spatially dispersed beam is output from both cavity end-mirrors. If one of the prisms is re-located to coincide with the point where the rays cross, a non-spatially dispersed beam results. This coincidentally happens when the 75mm angled folding mirror is replaced with the 50mm one.

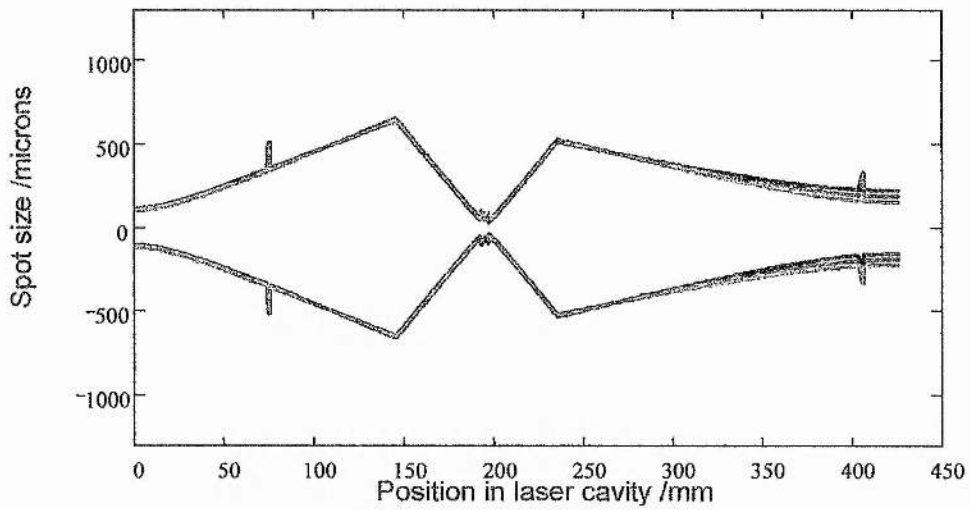

FIGURE 5.39: *Tangential beam inside the asymmetric resonator with the $1/e^2$ point taken to be the reference ray (at 1.51μm) and rays plotted which were 10nm longer and shorter in wavelength.*

5.6 Novel 4-mirror Cavity Design for Low cw-threshold or High Pump Powers.

To conclude this chapter, which has investigated a range of novel laser resonator designs for optimum self-modelocked operation, a new 4-mirror laser resonator design is proposed which permits an exceptionally tight focus on the end of a standard Brewster-cut laser rod.

As discussed earlier in this chapter, for optimum propensity to SML a highly nonlinear Kerr-lens is desired which requires a highly localised focus on the end of the Kerr-medium. Although a 3-mirror resonator permits this with a standard 'off the shelf' Brewster-cut rod, the focus in the tangential plane is still inflated in size compared to the sagittal. This is exacerbated as the refractive index increases, and for materials with very large refractive indices (e.g. ZnSe n=2.54) the beam waist size in the tangential plane is over double that in the sagittal plane; even in YAG (n=1.81) the beam waist is inflated by ~50% in the tangential plane. A spot is inflated by a factor equal to the material's refractive index on passing from free-space (n=1) into a Brewster angled dielectric medium. But, note there is no simple relationship between the size of the spot in the sagittal plane and the spot size in the tangential plane of an intracavity beam: it depends on the resonator configuration.

The rather unusual resonator design in figure 5.40 permits beam waists of equal size in both the tangential and sagittal planes inside a standard Brewster-cut gain medium regardless of the index of refraction of the material. The resonator is basically

the 3-mirror design introduced earlier with a second curved mirror at the end of the long arm operated at a large angle tightly focusing the beam onto an end mirror.

This resonator is designed to operate at 194 MHz repetition rate possibly permitting regenerative initiation with the prism modelocker.

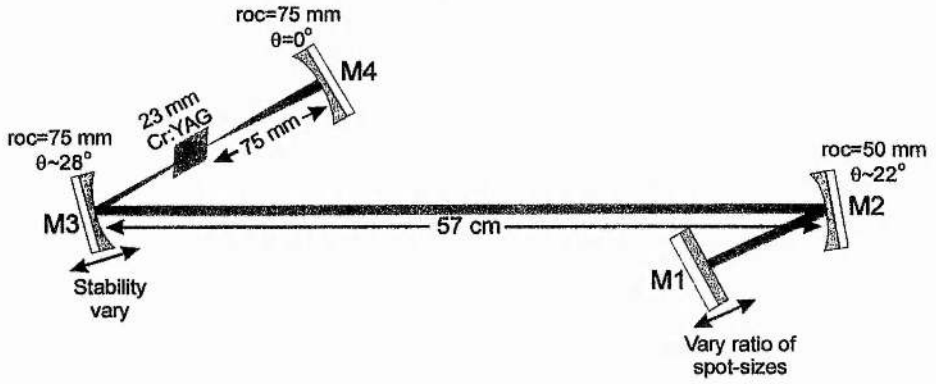

FIGURE 5.40: *Schematic of the novel 4-mirror resonator designed to maintain the same size of beam waist in the sagittal and tangential planes inside the laser rod.*

The beam waists inside the laser rod are controlled by translating the end-mirror M1. This is illustrated in figure 5.41(a). The sizes of the sagittal and tangential foci match where the stability curves cross. This cavity is aligned so the spot sizes match when operated at the centre of the cavity stability zone (figure 4.41(b)) defined by translating the cavity folding mirror M3. The angle of mirror M2 determines the position within the stability zones that the beam waist sizes match. Minor adjustments to the end-mirror separation permit the spot sizes to match away from the centre of overall cavity stability; possibly important if this cavity design is to be used for self-modelocking.

The sagittal and tangential beam profiles are clearly shown to match inside the laser rod in figure 5.41(c), but the overall beam inside the resonator shows considerable astigmatism (figure 5.41(d)) resulting in an asymmetric output beam. With further optimisation of the arm length and the folding angles and radii of curvature of mirrors M2 & M3, it is possible to produce a symmetric output beam from mirror M1 whilst maintaining equal spot sizes within the laser rod however this requires unusual mirror ROC and is not possible at a cavity repetition rate of 194 MHz.

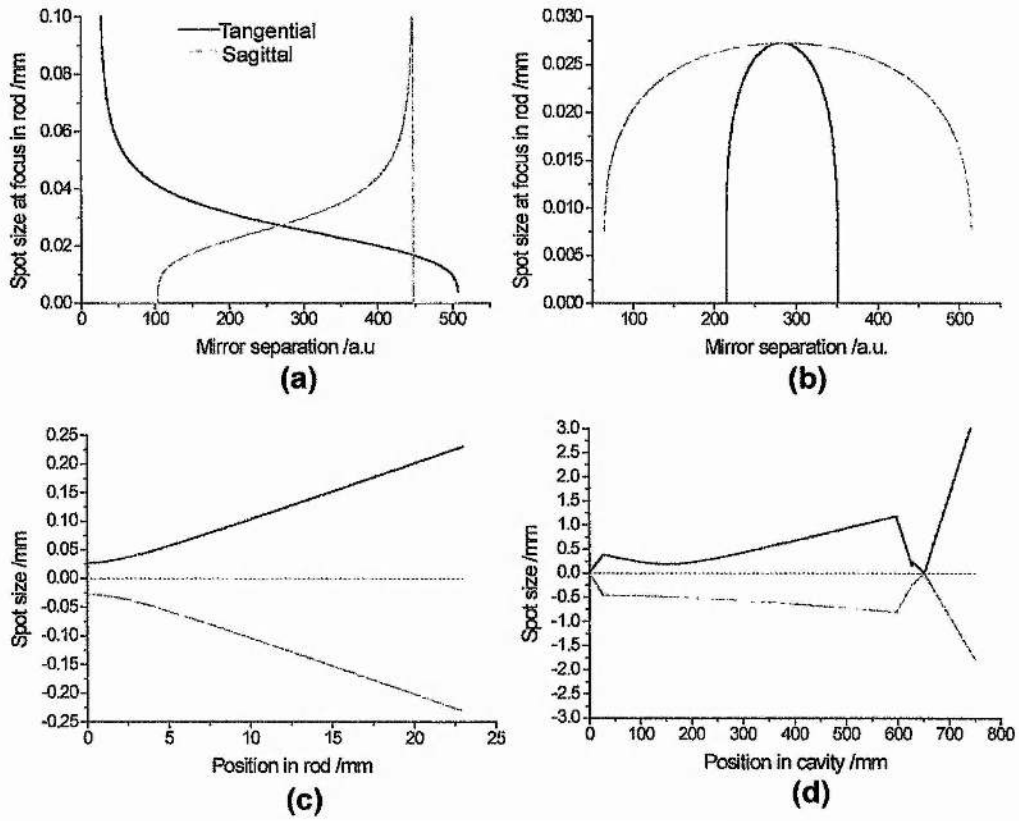

FIGURE 5.41: *Characteristics of the cavity in figure 5.40:* **(a):** *Control of the crystal beam waist sizes by translating end-mirror M1. (b): Cavity aligned to match spot sizes in the centre of the alignment for resonator stability. (c): Sagittal and tangential beam profiles inside the laser crystal. (d): Beam profile inside the whole resonator.*

Further modelling of the modelocking propensity using, for example, the Magni model described earlier, and the optimum positioning of prisms for dispersion compensation should be evaluated before developing this cavity further. This resonator design would be of greatest benefit for lasers based on materials having large refractive indices and high pump absorption coefficients, and hence Cr^{4+}:YAG is not really a suitable material to assess this resonator at this stage in the material's development; if/when higher doped Cr^{4+}:YAG crystals can be grown, this may be an alternative resonator design for low-threshold self-modelocking..

4-Mirror Resonator Under Intense Pumping.

One feature of this novel 4-mirror resonator which utilises a Brewster-angled rod, is its apparent immunity to a distributed thermal lens. Using the model described in chapter 4 for a distributed thermal lens[33], the stability contour plots shown in figure 5.42 were obtained for different incident pump powers. The important feature to note in these plots is the intersection between a mirror separation of 121 mm and a rod position

of 50 mm. For all pump powers up to 10 W, this point corresponds to an overlap of both the tangential and sagittal stability zones. Moreover, this crystal position (50 mm) corresponds to positioning both the sagittal and tangential spots on the end of the laser rod. Thus it is envisaged that this resonator will be more suited than the 3-mirror scheme for lasers undergoing high pump power excitation of Brewster-cut rods suffering from severe thermal lensing.

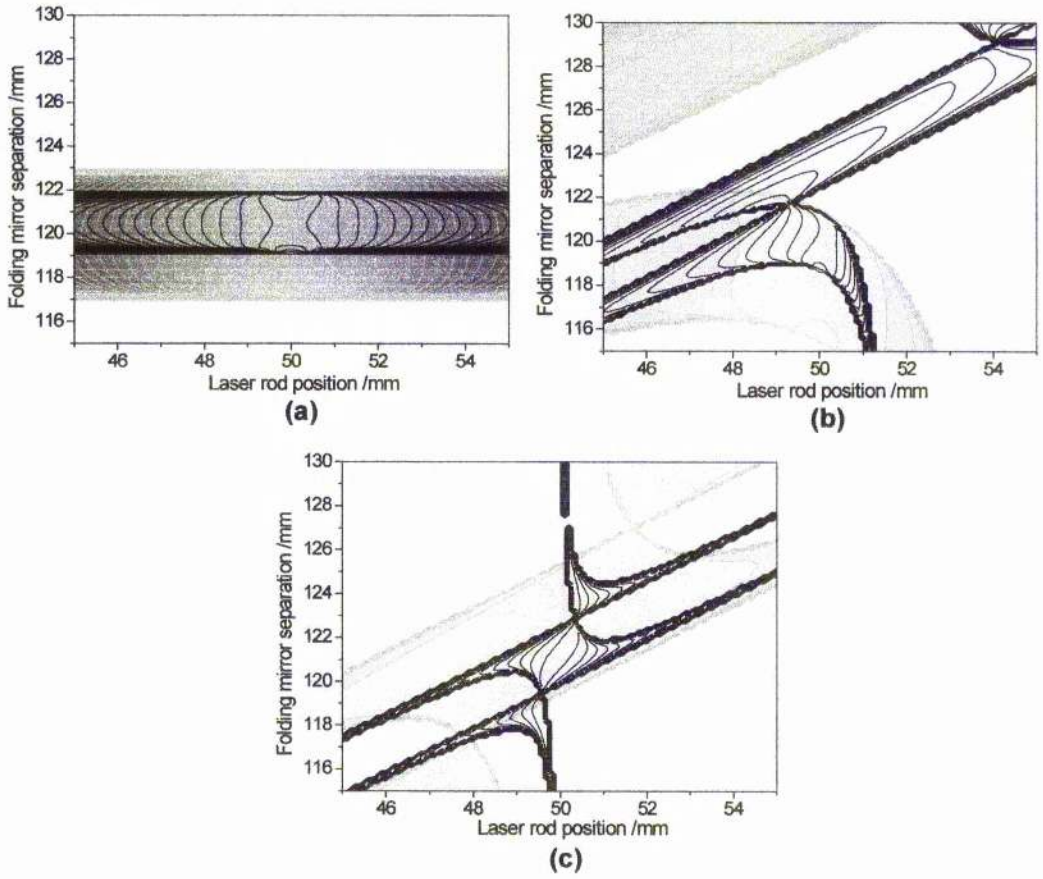

FIGURE 5.42: *Contour stability plots of the novel 4-mirror resonator for different pump powers.* **(a):** *P=0W.* **(b):** *P=2W.* **(c):** *P=10W*

5.7 Concluding Remarks

This chapter gives a comprehensive evaluation of self-modelocking obtained with a range of laser cavity designs. It began with a presentation of a Cr^{4+}:YAG laser based on a conventional astigmatically compensated 4-mirror resonator geometry aligned for femtosecond pulse generation via self-modelocking (Kerr-lens modelocking). Though femtosecond operation was observed, results were disappointing, for the simple reason that modelocking was only possible at long wavelengths to avoid atmospheric water absorption/dispersion effects. This in turn caused difficulties as the gain of the available

laser rods in this wavelength region was very low, and the reflectivities of the high-reflecting cavity mirrors was poor.

Principally to overcome the low-gain/high-intracavity-loss problem, an adapted form of a 3-mirror resonator, first described by Ramaswamy-Paye, was developed, which could be based on a Brewster-cut laser rod without requiring any special optical coatings. A compact, all-solid-state laser was developed using this scheme.

Cavity analyses were then presented including a nonlinear-lens localisation study, self-focusing induced amplitude modulation analysis and cw-operation optimisation, which concluded that this first use of the three-mirror cavity was not optimum; in essence the laser was pumped from the incorrect side.

Using this modified three-mirror scheme built around a new Cr^{4+}:YAG rod with greater gain, a significant improvement in output power and modelocking threshold was reported. In addition, very compact resonators with pulse repetition rates as high as 402 MHz were constructed.

With a 194MHz regeneratively-initiated system, pulse durations down to 110 fs at an average output power of 230 mW were generated. A self-starting regime could be accessed after suitable cavity alignment. SML could be initiated for pump powers down to 1.0W in an all HR-mirror cavity, though the pulse durations were long (620 fs).

A more compact regeneratively-initiated system with a repetition rate of 320 MHz achieved average output powers of up to 300 mW; the highest reported at the time from an all-solid-state Cr^{4+}:YAG laser.

A study of the noise characteristics of this latter system showed negligible amplitude noise on the fundamental signal and extremely low noise on the second harmonic signal taken over a two second interval (<3% rms). A phase noise measurement performed on this laser unexpectedly showed serious pulse jitter at low frequencies, though it was later realised that the pump source was unstable and intermittently Q-switched during the measurement. It is to be expected that these measurements would be comparable to an all-solid-state laser pumped modelocked Ti:sapphire laser if repeated on this Cr^{4+}:YAG laser, after re-alignment of the pump source.

A novel, highly asymmetric resonator design was then introduced, which retained the key benefit of the three-mirror laser; namely, the ability to form a tight localised resonant beam focus on one end of a standard Brewster-Brewster cut rod. Numerical modelling of this resonator suggested that it should be possible to self-modelock this design via a hard-aperture, though this was never assessed in practice. This resonator design was then used to assess the 'prism in each arm' laser design first demonstrated

by Aoshima et al.[37] with a Cr^{3+}:LiSAF laser to reduce the overall footprint of the laser. This laser was easy to modelock via SML and the average output power was high (200 mW) though the pulse durations were unexpectedly long (~470 fs).

The dispersive behaviour of this unconventional use of a prism pair separated by the laser folding section was difficult to conceive and numerical simulation of the resonator was carried out using 4x4 ray-pulse matrices. This gave a value for the net cavity group-velocity dispersion and the relative paths taken by rays of short and long wavelengths. This modelling tool should prove to be useful in determining the dispersive nature of other novel cavity configurations in the future.

Finally, with the object of promoting future interest in using unconventional laser arrangements for generating femtosecond pulses, a novel extension to the three-mirror cavity was proposed which not only permitted localisation of both the sagittal and tangential waists on the end of a standard Brewster-cut rod, but enabled the relative sizes of the orthogonal waists to be varied until they matched; normally only possible by use of anti-reflection coatings on plane-plane rods. This is of most importance for materials with high refractive indices which create large foci in the tangential plane in 3-mirror cavities (e.g. doped chalcogenide lasers in which interest is currently being shown as possible laser sources in the mid-infrared[40]). Thus cavity configurations may be preselected to suit particular performance requirements.

Interest was originally shown in Cr^{4+}:YAG as a possible room-temperature, all-solid-state replacement for the inconvenient colour-centre lasers operating near 1.55 μm. In this regard, the performance of lasers described in this chapter is partially successful. The Cr^{4+}:YAG laser cannot compete with colour-centre lasers, especially the NaCl:OH^- laser, with regard to overall tunability since its modelocked range is a limited 1.5-1.57 μm. The self-modelocked Cr^{4+}:YAG laser is a superior replacement for the femtosecond coupled-cavity modelocked KCl:Tl^0 and NaCl:OH^- colour-centre lasers within this wavelength range, provided that a good Cr^{4+}:YAG rod is available.

Cr^{4+}:YAG lasers are not as versatile as the colour-centre lasers with regard to the range of modelocked pulse durations, since colour-centre lasers may be successfully synchronously modelocked to produce stable pulses of ~10 ps. But, a Cr^{4+}:YAG laser was demonstrated in section 5.5.2 which produced high average modelocked pulses with durations ~0.5-1ps. This pulse duration regime is important for some applications that require high peak-power pulses of narrow bandwidth, or if the many nonlinear effects induced by femtosecond pulses are undesirable.

Therefore, Cr^{4+}:YAG lasers may offer a convenient alternative to colour-centre lasers in many applications, but it is not necessarily an all-out replacement for these systems.

References

1 D.E. Spence, P.N. Kean, and W. Sibbett. *Opt. Lett.* **16** , 42 (1991)

2 A.V. Shestakov, N.I. Borodin, V.A. Zhinyuk, A.G. Ohrimtchyuk, and V.P. Gapontsev, in Post-Deadline paper in *Conference on Lasers and Electro-Optics* (Optical Society of America, Washington, D.C. 1991) paper CPDP11-1

3 G.T. Kennedy, R.S. Grant and W. Sibbett, *Opt. Lett.* **18**, 1736 (1993)

4 A. Sennaroglu, C. R. Pollock, and H. Nathel, *Opt. Lett.* **19**, p390 (1994)

5 Private communication with C.R. Pollock, Cornell University, Ithaca, New York. USA

6 P.J. Conlon, Y.P. Tong, P.M.W. French, J.R. Taylor and A.V. Shestakov, *Electron. Lett.* **30**, 709 (1994)

7 R. Mellish, P.M.W. French, J.R. Taylor, P.J. Delfyett, and L. T. Florez, *Electron. Lett.* **30**, 223 (1994)

8 J.M. Hopkins, G.J. Valentine, W. Sibbett, J. Aus der Au, F. Morier-Genoud, U. Keller, A. Valster, *Opt. Comm.* **154**, 54 (1998)

9 B.C. Collings, J.B. Stark, S. Tsuda, W.H. Knox, J.E. Cunningham, W.Y. Jan, R. Pathak and K. Bergman, *Opt. Lett.* **21**, 1171

10 S. Spalter, M. Bohm, M. Burk, B. Mikulla, R. Fluck, I.D. Jung, G. Zhang, U. Keller, A. Sizmann and G. Leuchs, *Appl. Phys. B* **65**, 335 (1997)

11 M.J. Hayduk, S.T. Johns, M.F. Krol, C.R. Pollock, and R.P. Leavit, *Opt. Commun.* **137**, 55 (1997)

12 M. Ramaswamy-Paye and J.G. Fujimoto, *Opt. Lett.* **19**, 1756 (1994)

13 G.J. Valentine, G.T. Kennedy, and W. Sibbett, in Digest of *1996 Conference on Lasers and Electro-Optics Europe*, (IEEE Catalog 96TH8161), Paper CFF6

14 H.W. Kogelnik, E.P. Ippen, A. Dienes and C.V. Shank, *IEEE J. Quantum Electron.* **QE-8**, 373 (1972)

15 R. Mellish, S.V. Chernikov, P.M.W. French and J.R. Taylor, *Electron. Lett.* **34**, 552 (1998)

16 P.J. Conlon, Y.P. Tong, P.M.W. French, J.R. Taylor and A.V. Shestakov, *Opt. Lett.* **19**, 1468 (1994)

17 L. Spinelli, B. Couillaud, N. Goldblat, and D.K. Negus, in *Technical Digest of*

Conference on Lasers and Electro-Optics (Optical Society of America, Washington D.C. 1991) paper CPDP7

18 J. Herrmann, *J. Opt. Soc. Am. B*, **11** , 498, (1994)

19 A. Ritsataki, G.H.C. New, R. Mellish, S.C.W. Hyde, P.M.W. French, and J.R. Taylor, *IEEE J. Sel. Topics in Quantum Electron.* **4**, 185 (1998)

20 V. Magni, G. Cerullo, and S. De Silvestri, *Opt. Commun.* **101**, 365 (1993)

21 V. Magni, G. Cerullo, S. De Silvestri, and A. Monguzzi, *J. Opt. Soc. Am. B* **12**, 476 (1995)

22 V. Magni, G. Cerullo and S. De Silvestri, *Opt. Comm.* **96**, 348 (1993)

23 H. Kogelnik and T. Li, *Appl. Opt.* **5**, 1550 (1966)

24 B.E. Bouma, and J.G. Fujimoto, *Opt. Lett.* **19** , 1756, (1994)

25 A standard Spectra-Physics prism modulator (model no. 342) was used constructed from fused silica and design for use at ~80 MHz in K=krypton ion and argon ion lasers.

26 C.R. Giuliano, J.H. Marburger and A. Yariv, *Appl. Phys. Lett.* **21**, 58 (1972)

27 P. Baues, *Opto-electronics* **1**, 37 (1969)

28 A.E. Siegman in *Lasers*, (University Science Books, Mill Valley, California) 1986

29 M. Piché, *Opt. Comm.* **86**, 156 (1991)

30 Note that any 4-mirror Z-cavity laser creates a tight focus in the *middle* of the rod providing the angle of both folding mirrors is identical, not necessarily a symmetric cavity..

31 G. J. Valentine, J.-M. Hopkins, P. Loza-Alvarez, G.T. Kennedy, W. Sibbett, D. Burns, and A. Valster, *Opt. Lett.*, **22** , 1639, (1997)

32 A. J. Alfrey, *IEEE J. Quantum Electron.* **25**, 760 (1989)

33 M. E. Innocenzi, H. T. Yura, C. L. Fincher, R. A. Fields, *Appl. Phys. Lett.* **56**, p1831 (1990)

34 G.P. Agrawal in *Nonlinear Fiber Optics* (Academic Press, London 1995)

35 Y.P. Tong, J.M. Sutherland, P.M.W. French, J.R. Taylor, A.V. Shestakov and B.H.T. Chai, *Opt. Lett.* **21**, 644 (1996)

36 D. von der Linde, *Appl. Phys. B* **39** , 201 (1986)

37 S. Aoshima, H. Itoh and Y. Tsuchiya, *IEEE J. Sel. Topics Quantum Electron.* **3,** 95 (1997)

38 D. Kopf, K.J. Weingarten, L.R. Brovelli, M. Kamp, and U. Keller, in *Technical Digest of Conference on Lasers and Electro-Optics* (Optical Society of America, Washington D.C. 1995) paper CWM2

39 A.G. Kostenbauder, *IEEE J. Quantum Electron.* **26,** 1148 (1990)

40 R.H. Page, K.I. Schaffers, L.D DeLoach, G.D. Wilke, F.D. Patel, J.B. Tassano Jr., S.A. Payne, W.F. Krupke, K-T. Chen, and A. Burger, *IEEE J. Quantum Electron.* **QE-33,** 609 (1997)

6 Major Conclusions

The subject matter of this thesis has concerned the development and characterisation of all-solid-state, tunable modelocked laser sources at 1.5 μm. Several different laser systems have been entwined within this research and consequently different modelocking techniques utilised. Part of this development involved the design, construction and assessment of a 'mini' laser-diode pumped Nd:YAG laser for use as a pump source. The main emphasis of this work involved the development of a room-temperature femtosecond Cr^{4+}:YAG laser but the synchronously-pumped NaCl:OH^- colour-centre laser was also studied because this laser accesses a broader spectral range than the self-modelocked Cr^{4+}:YAG system and has pulse durations that extend to the picosecond domain.

The development of the all-solid-state pump source based on Nd^{3+}:$Y_3Al_5O_{12}$ (Nd:YAG) was described in chapter 2. This was designed to replace the ageing, inefficient arc-lamp pumped Nd:YAG lasers previously used to pump the colour-centre and Cr^{4+}:YAG lasers and so this chapter began with an examination of some of the features of the Spectra-Physics SP3800 mainframe Nd:YAG laser with emphasis on its poor amplitude noise performance and beam pointing instability.

Some of the basic design considerations for a longitudinally-pumped Nd:YAG laser were presented with particular regard to the poor beam quality of the pump source (fibre-coupled laser diodes) and strong thermal lensing in the Nd:YAG crystal. A linearly polarised laser was essential for pumping Cr^{4+}:YAG and so a Brewster-angled fused-silica plate was incorporated into the final resonator design. An adaptation of the 3-mirror laser cavity design developed previously by Yelland[1] for intracavity doubling, was employed for cw operation at the fundamental wavelength. This was a 'gain at the end' design and comprised two plane end-mirrors with an intracavity biconvex lens. After optimisation, this laser design produced up to 8.5W cw linearly polarised output at 1.064μm in a TEM_{00} beam, ideal for pumping the self-modelocked Cr^{4+}:YAG laser. A repeat of the characterisation experiments performed on the SP3800 laser on this holosteric alternative demonstrated its superiority in noise performance and beam stability.

As a possible pump source for the synchronously-pumped modelocked (SPML) colour-centre lasers, the all-solid-state laser was required to be actively modelocked. Design adaptations to the compact cw laser design were described to permit the laser cavity to be extended to match the pulse repetition rate of the mainframe laser. Initially,

the pulse durations of the 82MHz actively-modelocked laser were unexpectedly long, but it was later realised that etalon effects in the plane-parallel gain rod were hindering the modelocking process. By rotating the gain element off-axis slightly, a low power, sub-100 ps modelocked Nd^{3+}:YVO_4 laser was constructed and characterised. This produced pulsewidths down to 75 ps at average output powers of 3.5W.

A more compact actively-modelocked Nd:YAG laser was also constructed which had a pulse repetition rate of 194 MHz and relied on a high frequency resonance (97 MHz) found on an argon-ion prism modelocker. Pulse durations as short as 34 ps at average output powers of 6.0 W were routinely obtained. This pulse duration was somewhat shorter than expected and was attributed to enhanced spatial-hole-burning as a result of placing the gain medium at the end of the cavity.

An instability in the modelocking became apparent due to temperature induced changes in the laser cavity length. The mainframe modelocked laser did not suffer from this instability due to it being constructed from an invar alloy. An active stabilisation method for actively-modelocked mini-lasers was proposed and assessed on the SP3800. This consisted of adjusting the RF drive frequency to the acousto-optic modulator to track changes in the modelocked performance via the second-harmonic signal generated extracavity. Encouraging results suggested that this should successfully track the temperature-induced changes of a mini-laser, however, it would probably be more appropriate to actively stabilise the modelocked laser length using a piezo-mounted mirror.

The all-solid-state cw laser was later used to successfully pump the Cr^{4+}:YAG laser. The cw-actively modelocked designs have not yet been used successfully in practice to pump colour-centre lasers, but in principle, the 82 MHz scheme described should give SPML colour-centre performance similar to that obtained with the mainframe laser it was designed to replace.

A future improvement of the modelocked Nd:YAG laser would be to use a wedged plane-plane rod with one end-mirror coated on the rod itself: this would further enhance spatial hole burning and should permit actively modelocked pulses down to 10 ps to be obtained.

In chapter 3, the NaCl:OH^- synchronously-pumped modelocked colour-centre laser was studied. Whilst there is nothing new or unusual about this laser, it remains a versatile source of tunable, relatively high power picosecond pulses tunable in the 1.45-1.8 μm range. This chapter concentrated on a drawback associated with all synchronously-modelocked lasers; namely the incomplete modelocking, high frequency amplitude noise and instability on a pulse-pulse timescale caused by the spontaneously emitted background light. A simple passive stabilisation technique, called coherent-

photon-seeding (CPS) and first applied to dye lasers, was employed to greatly enhance modelocked performance of this laser. This simply involved adding an empty auxiliary laser cavity to the main laser to feed-back a highly attenuated replica of the main cavity pulse slightly ahead of the main circulating pulse itself. Key observations on applying CPS were described. An added versatility of SPML with CPS was then realised, viz., the ability to change the modelocked pulse duration simply by varying the modelocked laser cavity length.

The stepping model, described by New[2], was adapted to simulate the SPML NaCl:OH^- laser. The destabilising effect of the stochastic background noise was demonstrated and hence the mechanism by which the coherent-photon-seeding stabilised modelocked performance was illustrated: the coherent light fed-back into the SPML laser slightly ahead of the main modelocked pulse greatly exceeded the stochastic background light level and hence its chaotic effect was overpowered.

An additional destabilising effect of the spontaneously emitted background light level was suggested by modelling: a contribution to pulse jitter on almost a pulse-pulse timescale. This had never been observed previously in practice but was detected using a broadband (9.5GHz) InGaAs photodiode and observing high harmonics of the pulse repetition frequency. A notable improvement in this high frequency pulse jitter was demonstrated on applying the coherent photon seeding technique.

It is anticipated that the greatest benefit of applying CPS to a SPML NaCl:OH^- laser would be if a modelocked laser diode-pumped Nd:YAG laser was used as the pump source giving 10 ps pump pulses. Bandwidth limited SPML pulses tunable in duration from 1-10 ps should then be realisable.

Chapter 4 began with an outline of the Cr^{4+}:YAG gain material from a spectroscopic point of view, and highlighted some of its quirks which make it such a pleasure to use, such as its requirement for a linearly polarised pump source and the long term decay of its gain under intense cw pumping. The effect of pump absorption saturation during Cr^{4+}:YAG laser operation was discussed, which makes this material useful as a Q-switch for Nd:YAG lasers, but is another hindrance when used as a laser gain medium. The inexplicable variation in laser crystal quality was described: considerably different power transfer characteristics for two laser rods operating at long wavelengths were presented. All the laser rods obtained apart from one appeared to have very limited gain at wavelengths >1.5μm. One 23 mm long magnesium co-doped rod was found to possess much greater gain extending to 1.58 μm thereby permitting useful output powers to be obtained in this spectral region.

The thermal characteristics of the Cr^{4+}:YAG medium under intense optical excitation were modelled. The strong distributed thermal lens was shown to result in

further separation of the sagittal and tangential stability zones of a compensated laser cavity based around a Brewster-angled gain medium.

Finally, the chapter discussed some considerations for using the material as a modelocked source of femtosecond pulses, in particular, the effect of discrete atmospheric water absorption transitions below 1.5μm of restricting the bandwidth available to modelocked laser pulses was described.

This thesis concluded in chapter 5 with a detailed description of the optimisation of a resonator design for obtaining self-modelocked (SML) operation from low-gain laser media such as Cr^{4+}:YAG. Inspired by B.E. Bouma's results with a SML semi-monolithic 3-mirror Ti:sapphire laser[3], an alternative, 3-mirror design was proposed which could be used with standard Brewster-angled gain media without necessitating special coatings. Initial results with this laser scheme were an improvement over the performance achieved with the same laser crystal with standard 4-mirror laser designs: up to 22 mW 180 fs pulses were obtained from a high-reflecting end-mirror for 4.7 W incident pump power.

Modelling of this 3-mirror laser scheme with regard to maximising the propensity for self-modelocking suggested that improved performance would be obtained by pumping the laser crystal through the curved end-mirror (the folding mirror used at normal incidence). This arrangement, accompanied with the better laser crystal, permitted self-modelocking at high output powers and low pump power requirements. A self-starting self-modelocked laser was demonstrated producing pulses of 110 fs duration with a pulse repetition rate of 194 MHz and 230 mW average output power for incident pump powers of 4.7 W. After optimising for low power operation, self-modelocking was demonstrated for incident pump powers down to 1.02 W, although the pulse durations, at 620 fs, were long. With optimisation of the intracavity second and third order dispersion, the pulse durations might be improved.

More compact SML lasers operating at 320 and 402 MHz were also constructed. The highest average output powers yet reported from an all-solid-state SML Cr^{4+}:YAG laser were obtained from the 320 MHz cavity (120 fs at 300 mW).

A novel, compact 4-mirror cavity design based on the Cr^{3+}:LiSAF laser designed by Aoshima[4] was constructed. This was a highly asymmetric 4-mirror laser design that had a prism in each laser cavity arm. Long duration pulses were obtained (470 fs) but at high average powers (220 mW). To gain insight into the dispersive mechanism inside this resonator, the ray-pulse matrix method was employed in a resonator configuration permitting ray paths of different wavelengths to be plotted through the laser cavity. This model should enable laser cavity optimisation such that shorter duration pulses may be obtained from this resonator design in the future.

Finally a new proposal for an alternative self-modelocked laser design was made which is optimised for Brewster-angled gain media having large linear refractive indices and pump absorption coefficients by allowing exceptionally tight focussing on the end of the rod. Thermal lens modelling of this design suggests it is less prone to stability zone disturbance than other designs based around Brewster cut gain elements.

In the longer term, Cr^{4+}:YAG lasers should find applications in research laboratories both as high power cw sources tunable from ~1.37-1.58 μm and as high average power femtosecond modelocked sources tunable from 1.5-1.58 μm. This laser is especially convenient with the demonstration that it can be pumped successfully with highly efficient, compact solid-state fibre-lasers[5]. With the recent demonstration that it can be direct laser diode-pumped, a lower cost Cr^{4+}:YAG laser source may be developed. The main drawback of Cr^{4+}:YAG appears to be the inconsistent quality of the laser crystals, though the development of the magnesium co-doped variety may help to eliminate this disadvantage such that Cr^{4+}:YAG is the preferred option as a modelocked source near 1.55 microns.

It is instructive to examine other available modelocked sources near 1.55 μm as alternatives to Cr^{4+}:YAG. Colour-centre systems are inconvenient due to their cryogenic requirements. Optical parametric-oscillators (OPO) may be a viable alternative in the laboratory, especially if an all-solid-state variety could be developed pumped by a direct diode-pumped Cr^{3+}:LiSAF laser. The wavelength range over which modelocked pules may be tuned is not restricted by the gain bandwidth of a laser material, indeed femtosecond pulses may be tuned through the water absorption regions below 1.5 μm without problems[6]. But OPOs remain an inelegant solution as a source at 1.55 μm because a high-power, femtosecond modelocked laser source is required to pump the OPO initially.

Probably the most cost-effective alternative to Cr^{4+}:YAG is the erbium fibre laser. Passively modelocked erbium-fibre ring lasers have generated pulses as short as 80fs[7], however the average power was low (~10's mW). Higher power Er/Yb fibre systems[8] have produced ~200fs pulses at average powers up to 1.7W and repetition rates of 18 MHz indicating exceptionally high peak powers. The main drawback of these lasers is their extremely limited tunability: operation is limited to 1.55 μm. Overall, the lowest cost, most convenient tunable source of femtosecond pulses near 1.5 μm is currently the modelocked Cr^{4+}:YAG laser.

References

1 C. Yelland, Ph.D. Thesis, University of St. Andrews (1996)

2 J.M. Catherall, G.H.C. New and P.M. Radmore, *Opt. Lett.* 7 ,319 (1982)

3 B.E. Bouma, and J.G. Fujimoto, *Opt. Lett.* **19** , 1756, (1994)

4 S. Aoshima, H. Itoh and Y. Tsuchiya, *IEEE J. Sel. Topics Quantum Electron.* **3,** 95 (1997)

5 R. Mellish, S.V. Chernikov, P.M.W. French and J.R. Taylor, *Elect. Lett.* **34,** 552 (1998)

6 P. Loza-Alvarez, D.T. Reid, M. Ebrahimzadeh, W. Sibbett, H. Karlsson, P. Henriksson, G. Arvidsson and F. Laurell in Digest of Conference on Lasers and Electro-optics, (Optical Society of America, Washington D.C. 1998) paper CthCC2 also submitted *Appl. Phys. B*

7 K. Tamura, L.E. Nelson, H.A. Haus and E.P. Ippen, *Appl. Phys. Lett.* **64,** 149 (1994)

8 M.E. Fermann, A. Galvanauskas, G. Sucha and D. Harter, *Appl. Phys. B* **65,** 259 (1997)

Appendix I: *Stepping Model of the Linear Cavity Synchronously-modelocked Laser with Coherent Photon Seeding (Turbo-pascal 6)*

```
{$R+}    { Enable range checking  }
□
□
uses□
 Intgt1, Dos, Crt;
□

□
{
□
**********************************CONSTANTS**************************
}

const

   { Program Control Parameters }
   savenum=20;    {save file every 20 round trips}
   beginning=0;   {start model at the first round trip (zero intracavity field & gain)}
   ending=9500;   {finish model after 9500 simulated round trips}
   code='lag';    {codename for model run}
   initrun=0;     {flag to 'reset' model for the first round trip}


   Calcsize=5;    {Runge-Kutta integration size}

   { Mesh Control}
   Meshsize=2500;  {No. of field points in the mesh}
   Tmin=-2.5e-10;   {Simulation runs from –250ps to}
   Tmax=2.5e-10;    {+250ps  where 0ps is the pumping pulse peak}
   DeltaT=(Tmax-Tmin)/Meshsize;  {calculates mesh spacing}

   { Fundamental Constants }
   h=6.626e-34; {Planck's IQ}
   c=2.998e+8;  {speed of cheese}
   root10=3.1622777;



□
```

```
{ NaCl Parameters }
□
EmissionCS=8.5e-21;  {stimulated emission cross section of gain medium}
□
AbsorptionCS=9.2e-21; {absorption cross section of gain}
AmpMax=5;             {Maximum value of small signal gain}
Lifetime=150E-9;      {upper state lifetime of gain}
PumpLambda=1.064e-6; {Pumping wavelength}
SignalLambda=1.5e-6;  {laser wavelength}

k1=EmissionCS*PumpLambda/(h*c);
k3=EmissionCS*SignalLambda/(h*c);

{ Model Parameters }
Refl=0.83333; {Reflectivity of bandwidth restricting etalon plates}
Loss=0.262;  {Loss in cavity excluding O/C}
octrans=0;   {Intensity transmittivity of O/C }
m1dist=0.05; { Distance from gain to curved endmirror in metres }
TotalLength=1.82; { Total Slave Length in metres}
CavityLength=TotalLength-m1dist-(DeltaT*Meshsize)*c; { Remaining Length of
cavity}


{ Main Cavity Mismatch Control }
Mismatchstart=-14; {start at -2.8ps=14} {Eff=-0.8ps} {mismatch measured in
mesh intervals}
Mismatchshiftrate=500; {Main cavity mismatch changed every 500 trips}
Mismatchshiftamount=2; {Shift by 2 mesh intervals every 500 trips}

{ Seeding Control }
Startseeding=1000; {seed after 1000th trip}
Seedinglevel=1e-5; { (amplitude seed level) Square this for initial intensity seeding
level }
Seedingadvancestart=450;  {Seed 90ps in advance (450 mesh intervals)}

{ Seeding Level Adjustment }
Seedlevelinc=20000; {Increase seeding level every 20000th trip (never increase in
this model)}
Seedinc=1; {Seeding Level Increase Factor (square for intensity) }

{ Seeding Advance Adjustment }
Seedingdelayrate=0; {Shift of 0ps ADVANCE every seedshiftrate trips }
Seedshiftrate=20000; {shift every 20000th trip (effectively disabled in this run)}


{ Pump Pulse Control Parameters }
Pumpwidthstart=90e-12;    {Width FWHM in seconds}
AbsPumpPeakstart=3.45e+13; {peak power of pump pulse if it was 1ps long}
Pumpwidthinc=0; {0ps increase in pump width}
Pumpwidthincrate=20000; {every 20000 trips (effect. disabled for this run)}
```

```
□
   { Stochastic Noise Control Parameters }
   noisy=1; { flag which controls if noise is on (1) or off (0) }
   tcoh=31.7e-15; {inverse fluorescence linewidth }
   Noisefactor=0.23; { mean noise amplitude }
   Scoh=Noisefactor; {used if noise is switched off: this constant value is used}

{
**********************************VARIABLES**************************
}
var
  OldnoiseI,OldnoiseR : Float ;
  Seedf : Float ;
FileName,numb : String;
 count,Seedingadvance,Mismatch : integer ;
 OutFile,cons : text;
 Ampend1,Ampend2 : Float;
 ExVR2,ExVI2 : Float ;
 Pumppeak,Pumpwidth : Float ;
 LowerLimit, UpperLimit : Float;
 XInitial : Float;
 NumIntervals : integer;
 NumReturn : integer;
 zipno : integer;
 TValues : Shortvect;
 XValues : Shortvect;
 Error : byte;
 run : integer;
 VRU : TNvector;              {These are all the electric}
 VIU : TNvector;              {field values on the mesh}
 VR2 : TNvector;              {calculated at different parts of}
 VI2 : TNvector;              {the simulated laser cavity}
 VR4 : TNvector;
 VI4 : TNvector;
 AmplificationU : TNvector;   {gain medium amplification values on a mesh}

{$F+}

□
{
□
```

```
!!!
```

```
end; { function Gain1Pass}
□
{
□
-------------------------------------------------------------------------------
}
□
function Gain2Pass(T, X : Float) : Float;  {2nd pass without pump}
□
{differential equation of small signal gain}
{includes: }
{ i)gain decrease from stimulated emission due to laser pulse}
{ ii)gain decrease from spontaneous emission}
□

begin
□
 Gain2Pass := -k3*(exp(X)-1)*Intensity(t)
□
          -X/LifeTime
□

□
end; { function Gain2Pass}
□
{
□
-------------------------------------------------------------------------------
□
}
□
function Decay(Value,Time:float) : float;   {Calculate decay of amplification inTime
interval}
begin
   Decay:=Value*exp(-Time/Lifetime);
end;
{
-------------------------------------------------------------------------------
}

Procedure Calcnewfield1; {recalcs mesh field values due to 1st pass thro' gain with
pump}

Var MeshI:integer;
  Phi,SI,SR,OldnoiseI,OldnoiseR:Float;

Begin

for MeshI:=1 to meshsize do begin
```

```
{ Real part of field }
 VRU^[MeshI]:=VRU^[MeshI]*exp((AmplificationU^[MeshI]-Loss)/2);
        { Effect of gain,loss}

{ Imaginary part of field }
 VIU^[MeshI]:=VIU^[MeshI]*exp((AmplificationU^[MeshI]-Loss)/2);
  { Effect of gain,loss}

if (noisy=1) then begin   {Adds spontaneous noise if flag is set}
     phi:=2*pi*random(65535)/65535;
    SI:=OldnoiseI*exp(-DeltaT/Tcoh)-
NoiseFactor*sqrt(AmplificationU^[MeshI])*sin(phi);
    OldnoiseI:=SI;
    SR:=OldnoiseR*exp(-
DeltaT/Tcoh)+NoiseFactor*sqrt(AmplificationU^[MeshI])*cos(phi);
    OldnoiseR:=SR;
   end
   else begin  {if flag not set, a constant background field is added instead}
     SR:=Scoh*sqrt(AmplificationU^[MeshI]);
     SI:=0;
   end;

        VRU^[MeshI]:=VRU^[MeshI]+SR;
        VIU^[MeshI]:=VIU^[MeshI]+SI;
 end; {loop}
end; { Calcnewfield1 }
{
-------------------------------------------------------------------------------
}

Procedure Calcnewfield2; {as Calcnewfield1 but for the gain without the pump pulse}

Var MeshI:integer;
  Phi,SI,SR,OldnoiseI,OldnoiseR:Float;

Begin

for MeshI:=1 to meshsize do begin

 { Real part of field }
 VR2^[MeshI]:=VRU^[MeshI]*exp((AmplificationU^[MeshI]-Loss)/2);
        { Effect of gain,loss}

 { Imaginary part of field }
 VI2^[MeshI]:=VIU^[MeshI]*exp((AmplificationU^[MeshI]-Loss)/2);
  { Effect of gain,loss}

if (noisy=1) then begin
     phi:=2*pi*random(65535)/65535;
```

```
    SI:=OldnoiseI*exp(-DeltaT/Tcoh)-
NoiseFactor*sqrt(AmplificationU^[MeshI])*sin(phi);
    OldnoiseI:=SI;
    SR:=OldnoiseR*exp(-
DeltaT/Tcoh)+NoiseFactor*sqrt(AmplificationU^[MeshI])*cos(phi);
    OldnoiseR:=SR;
   end
   else begin
     SR:=Scoh*sqrt(AmplificationU^[MeshI]);
     SI:=0;
   end;

        VR2^[MeshI]:=VR2^[MeshI]+SR;
        VI2^[MeshI]:=VI2^[MeshI]+SI;

  end; {loop}
end; { Calcnewfield2 }
{
-------------------------------------------------------------------------
}
```

Procedure Calc1; {Iterative procedure to simulate effect of pump pulse and circulating laser pulse 1st pass through the gain medium using a Runge-Kutta algorithm to solve the differential equation}

```
Var
 MeshI : Integer;

begin

For MeshI:=1 to meshsize do
begin
NumIntervals:=MeshI;
XInitial:=Ampend2*run;
Lowerlimit:=Tmin;
Upperlimit:= Tmin+Numintervals*DeltaT;

If (MeshI>Calcsize) then begin
NumIntervals:=Calcsize; {Runge-Kutta size (uses this many previously calculated
points on the mesh)}

Lowerlimit:= (Tmin+MeshI*DeltaT)-DeltaT*Calcsize; {limits of equation}
Upperlimit:= Lowerlimit+Calcsize*DeltaT;

XInitial:=AmplificationU^[MeshI-Calcsize]; {Initial value for algorithm}
end;

  Integrate(LowerLimit,Upperlimit, XInitial, NumIntervals,
            NumIntervals, TValues, XValues, Error, @Gain1Pass);
{Runge-Kutta routine from Mathbox package}
```

```
{ NOTE: @ sign above points to the userfunction }


 AmplificationU^[MeshI]:=XValues[NumIntervals];

end; {Loop MeshI}

CalcNewField1; {calls routine to calculate the effect of new gain values on field}

Ampend1:=Decay(AmplificationU^[Meshsize],2*m1dist/3e+8);
{Final amplification value is calculated from effect of the delay to endmirror on last
value}
end; { Procedure Calc1 }
{
--------------------------------------------------------------------------------
}
Procedure Calc2; {As for procedure Calc1 above but without the pumping pulse}

Var
 MeshI : Integer;

begin

For MeshI:=1 to meshsize do
begin
NumIntervals:=MeshI;
XInitial:=Ampend1;
Lowerlimit:=Tmin;
Upperlimit:= Tmin+Numintervals*DeltaT;

If (MeshI>Calcsize) then begin
NumIntervals:=Calcsize;

Lowerlimit:= (Tmin+MeshI*DeltaT)-DeltaT*Calcsize;
Upperlimit:= Lowerlimit+Calcsize*DeltaT;

XInitial:=AmplificationU^[MeshI-Calcsize];
end;



  Integrate(LowerLimit,Upperlimit, XInitial, NumIntervals,
```

```
                NumIntervals, TValues, XValues, Error, @Gain2Pass);
{  NOTE: @ sign above points to the userfunction }


 AmplificationU^[MeshI]:=XValues[NumIntervals];
if (MeshI/100=int(MeshI/100)) then writeln(code,Count,' Pass2 ',MeshI,'
Amp=',AmplificationU^[MeshI]);


end; {Loop MeshI}

CalcNewField2;
Ampend2:=Decay(AmplificationU^[Meshsize],2*cavitylength/3e+8);

end; { Procedure Calc2 }

{
--------------------------------------------------------------------------------
}

Procedure Filter1;  {simulates effect of 1st pass thro' etalon in a linear cavity}

Var MeshI:integer;

begin
 for MeshI:=1 to meshsize do begin
 VRU^[MeshI]:=(1-Refl)*VR2^[MeshI]+Refl*VRU^[MeshI-1];
 VIU^[MeshI]:=(1-Refl)*VI2^[MeshI]+Refl*VIU^[MeshI-1];
 end;
 end;
{
--------------------------------------------------------------------------------
}

Procedure Filter2; {simulates effect of 2nd pass thro' etalon in a linear cavity}

Var MeshI:integer;

begin
 for MeshI:=1 to meshsize do begin
 VR4^[MeshI]:=(1-Refl)*VRU^[MeshI]+Refl*VR4^[MeshI-1];
 VI4^[MeshI]:=(1-Refl)*VIU^[MeshI]+Refl*VI4^[MeshI-1];
 end;
 end;
{
--------------------------------------------------------------------------------
}
```

```
Procedure Output_Coupler; {simulates loss in field due to output coupling}

Var MeshI:integer;

begin
 for MeshI:=1 to meshsize do begin
 VRU^[MeshI]:=sqrt(1-octrans)*VRU^[MeshI];
 VIU^[MeshI]:=sqrt(1-octrans)*VIU^[MeshI];
 end;
end;
{
-------------------------------------------------------------------------------
}

Procedure Cavity_Mismatch; {Simulates the mismatch which exists between pump +
slave lasers}
Var MeshI,Index:Integer;
   ExVR4,ExVI4:Float;

begin

{Clear all mesh points for a +ve mismatch}

for Index:=1 to Mismatch do begin
   VRU^[Index]:=0;
   VIU^[Index]:=0;
end;


ExVR4:=VR4^[Meshsize];
ExVI4:=VI4^[Meshsize];

for MeshI:=1 to Meshsize do begin

If (Mismatch>0) then {if a positive mismatch condition is detected}
begin

If (Meshsize-MeshI>Mismatch) then {check that calc. will not run outside of mesh
size}
begin
 VRU^[MeshI+Mismatch]:=VR4^[MeshI]; { Effect of cavity length mismatch }
 VIU^[MeshI+Mismatch]:=VI4^[MeshI]; { Effect of cavity length mismatch }
end

end  { +ve Mismatch}
else begin   {-ve mismatch condition}
if ((MeshI+abs(Mismatch))<=Meshsize) then {check that calc. will not run outside of
mesh size}
begin
```

```
 VRU^[MeshI]:=VR4^[MeshI+abs(Mismatch)]; { Effect of - cavity length mismatch
}
 VIU^[MeshI]:=VI4^[MeshI+abs(Mismatch)]; { Effect of - cavity length mismatch }
end
else begin {if a –ve mismatch runs out of values, the last field value to be calculated is
reproduced}
 VRU^[MeshI]:=ExVR4;
 VIU^[MeshI]:=ExVI4;
end; {-ve mismatch in range}

end; {Mismatch test}
end; {Loop}

end; {Mismatch-Cavity}

{
--------------------------------------------------------------------------------
}
Procedure Seed; {simulates addition of seeding pulse back onto main laser pulse}
Var MeshI:integer;
ExVR2,ExVI2:Float;
begin
ExVR2:=VR2^[Meshsize];
ExVI2:=VI2^[Meshsize];
write ('ARSE'); {message informing user that seeding is applied ok.}
For MeshI:=1 to Meshsize-Seedingadvance do begin
{ Add coherent seeding }

VRU^[MeshI]:=VRU^[MeshI]+Seedf*VR2^[MeshI+Seedingadvance];
VIU^[MeshI]:=VIU^[MeshI]+Seedf*VI2^[MeshI+Seedingadvance];
{An attenuated replica is added in advance of the main field: the replica is taken from
a field value calculated earlier in the round trip to simulate the linear cavity which was
used in practice though this makes no difference to the final result whatsoever}

□
end; {seedLoop}
□

{Because seeding is similar to a –ve mismatch, the final calculated field value is used
to 'fill in' the missing field points in the following loop:}
□
For MeshI:=Meshsize-Seedingadvance to Meshsize do begin
VRU^[MeshI]:=VRU^[MeshI]+Seedf*ExVR2;
VIU^[MeshI]:=VIU^[MeshI]+Seedf*ExVI2;
end; {fillin loop}
end; {Procedure}

{
--------------------------------------------------------------------------------
}
```

```
procedure Initialize(var LowerLimit   : Float;          {Resets all variables at start of
model}
                var UpperLimit   : Float;
                var XInitial     : Float;
                var NumIntervals : integer;
                var Error        : byte);
               var    Index          : integer;

begin

 LowerLimit := 0;
 UpperLimit := 0;
 XInitial := 0;
 NumIntervals := 0;
 Error := 0;
 for Index:=0 to Meshsize do
  begin
   VRU^[Index]:=0;
   VIU^[Index]:=0;
   VR4^[Index]:=0;
   VI4^[Index]:=0;
   VR2^[Index]:=0;
   VI2^[Index]:=0;
   AmplificationU^[Index]:=0;
  end;

end; { procedure Initialize }
{
------------------------------------------------------------------------------
}

 Procedure loadoldfield(Filename : string);  {loads in a previously calculated mesh of
field and amplitude values to continue a model running after stopping}

□
Var Index : integer;
□
   Infile : Text;
□

□
Begin
□
    assign(Infile,Filename);
    reset(Infile);
 for Index:=0 to Meshsize do
    begin
    read(Infile,VRU^[Index]);
    read(Infile,VIU^[Index]);
```

```
   read(Infile,Ampend2);
end; {loop}
   close(Infile);
end; {LoadOldField}

{
--------------------------------------------------------------------------------
}

Procedure SaveField(Filename : string);  {saves the mesh of field and gain values to
disk}
Var      Index : integer ;
        Outfile : text ;
        zipnum,Cmdline : string;
begin
   Assign(Outfile,Filename);
   Rewrite(Outfile);
 For Index:=0 to Meshsize do
begin
   writeln(Outfile,VRU^[Index]);
   writeln(Outfile,VIU^[Index]);
   writeln(Outfile,AmplificationU^[Index]);

end; {loop}
   Close(Outfile);
end; {Savefield}

{
--------------------------------------------------------------------------------
}

Procedure Calc;  {performs 1 round trip of the linear laser cavity}
begin
   Calc1;            {1st pass thro' gain element with a pump pulse}
   Calc2;            {2nd pass thro' gain element w/o a pump pulse}
   Filter1;          {1st pass thro' bandwidth restricting element}
   Output_Coupler;    {field loss due to an output coupler}
   Filter2;          {2nd pass thro' bandwidth restricting etalon}
   Cavity_Mismatch;    {shift field values on mesh to simulate a mismatch}
If (count>=StartSeeding) then Seed; {if requested add CPS signal to field}
end;

{
--------------------------------------------------------------------------------
}
```

```
{**********************************MAIN
ROUTINE*****************************}

begin { MAIN }

   run:=initrun;

{Reset all arrays used}

   New(VRU);

   New(VIU);

   New(VI2);

   New(VR2);

   New(VR4);

   New(VI4);
   New(AmplificationU);

   ClrScr;

{initialize all variables}

   Seedingadvance:=Seedingadvancestart;

   Mismatch:=Mismatchstart;

   Randomize;

 Initialize(LowerLimit, UpperLimit, XInitial, NumIntervals, Error);

Seedf:=Seedinglevel;
LowerLimit:=Tmin;
Upperlimit:=Tmax;
XInitial:=0;
OldnoiseI:=0;
OldnoiseR:=0;
Pumpwidth:=Pumpwidthstart;
Pumppeak:=AbsPumppeakstart/(Pumpwidth*1e+12);

If run=0 then begin {resets variables if this is the start of a new model run and
performs a special 1st round trip simulation with all vars reset}
```

```
count:=0;

{ Reset all variables: }
 Initialize(LowerLimit, UpperLimit, XInitial, NumIntervals, Error);

Xinitial:=0;
Calc; { perform one cavity round trip }
   str(count,Numb);
Filename:=code+Numb+'.dat';
run:=1;

   Savefield(Filename);  {saves initialised 1st round trip}
end; {If No run}

{simulation loop starts here}
for count:=beginning to ending do
begin
If count<>0 then begin

{check if the model parameters need to be changed}
If ((count/Seedshiftrate)=int(count/Seedshiftrate)) then
Seedingadvance:=Seedingadvance+seedingdelayrate;
If ((count/Mismatchshiftrate)=int(count/Mismatchshiftrate)) then
Mismatch:=Mismatch+Mismatchshiftamount;
If  ((count/Seedlevelinc)=int(count/Seedlevelinc)) then
  Seedf:=Seedf*Seedinc;
If  ((count/Pumpwidthincrate)=int(count/Pumpwidthincrate)) then begin
   Pumpwidth:=Pumpwidth+Pumpwidthinc;
   Pumppeak:=AbsPumpPeakStart/(Pumpwidth*1e+12);
end;
end;
str(count,Numb);
Filename:=code+Numb+'.dat';
if (count/savenum=int(count/savenum)) then {reloads field values if a save has just
been performed}
loadoldfield(Filename);
Ampend2:=Decay(AmplificationU^[Meshsize],CavityLength*2/3e+8);
XInitial:=Ampend2;

Calc; {a cavity round trip is simulated}
   str(count+1,Numb);
Filename:=code+Numb+'.dat';
if ((count+1)/savenum=int((count+1)/savenum))then
   Savefield(Filename); {periodically saves the calculated mesh values}

end; {loop}


end. { MAIN }
```

Appendix II: *ABCD Model for Self-Modelocked Three-mirror Lasers (Mathcad 7)*

V. Magni, G. Cerullo, S. De Silvestri, and A. Monguzzi, *J. Opt. Soc. Am. B* **12**, 476 (1995)

Modelling of 3 mirror Cr:YAG KLM resonator Brewster with astigmatism

Wavelength

$$\lambda := 1550 \cdot 10^{-9}$$

Mirror angle

$$\theta := 25 \cdot \text{deg}$$

Refractive Index

$$n_{YAG} = 1.81$$

Crystal length

$$l := 20 \cdot 10^{-3}$$

Resonator components (dimensions in m, Siegman style matrices)

Flat endmirror

$$Roc_{M1} := \infty$$

$$M1 := \begin{bmatrix} 1 & 0 \\ -\frac{2}{Roc_{M1}} & 1 \end{bmatrix}$$

Long arm

$$L_{arm1} := 700 \cdot 10^{-3}$$

$$Arm1 := \begin{bmatrix} 1 & L_{arm1} \\ 0 & 1 \end{bmatrix}$$

Angled folding mirror (treat sagittal and tangential elements separately)

$$Roc_{M3} := 75 \cdot 10^{-3}$$

$$M3_{sag} := \begin{bmatrix} 1 & 0 \\ -\frac{2}{\left(\frac{Roc_{M3}}{\cos(\theta)}\right)} & 1 \end{bmatrix}$$

$$M3_{tan} := \begin{bmatrix} 1 & 0 \\ -\frac{2}{Roc_{M3} \cdot \cos(\theta)} & 1 \end{bmatrix}$$

Crystal to angled folding mirror separation

$$Short1(a) := \begin{bmatrix} 1 & a \\ 0 & 1 \end{bmatrix}$$

Brewster surface from air into a dielectric medium

$$\text{Brin}_{sag} := \begin{bmatrix} 1 & 0 \\ 0 & 1 \end{bmatrix}$$

$$\text{Brin}_{tan} := \begin{bmatrix} n_{YAG} & 0 \\ 0 & \frac{1}{n_{YAG}} \end{bmatrix}$$

Propagate in xtal to position ζ mm

$$\zeta := \frac{l}{2}$$

initially set to xtal centre

$$\text{Xtl}_{\zeta}(\zeta) := \begin{bmatrix} 1 & \frac{\zeta}{n_{YAG}} \\ 0 & 1 \end{bmatrix}$$

Propagate through rest of xtal starting from position ζ

$$\text{Xtl}_{l}(\zeta) := \begin{bmatrix} 1 & \frac{l-\zeta}{n_{YAG}} \\ 0 & 1 \end{bmatrix}$$

Brewster surface from a dielectric medium into air

$$\text{Brout}_{sag} := \begin{bmatrix} 1 & 0 \\ 0 & 1 \end{bmatrix}$$

$$\text{Brout}_{tan} := \begin{bmatrix} \frac{1}{n_{YAG}} & 0 \\ 0 & n_{YAG} \end{bmatrix}$$

Crystal to curved retroflecting end-mirror separation

$$\text{sh2}(a,b) := b - a - l$$

$$\text{Short2}(a,b) := \begin{bmatrix} 1 & \text{sh2}(a,b) \\ 0 & 1 \end{bmatrix}$$

Curved retroflecting end-mirror

$$\text{Roc}_{M4} := 50 \cdot 10^{-3}$$

$\phi := 0$ used at normal incidence

$$M4_{sag} := \begin{bmatrix} 1 & 0 \\ -\frac{2}{\left(\frac{\text{Roc}_{M4}}{\cos(\phi)}\right)} & 1 \end{bmatrix}$$

$$M4_{tan} := \begin{bmatrix} 1 & 0 \\ -\frac{2}{\text{Roc}_{M4} \cdot \cos(\phi)} & 1 \end{bmatrix}$$

Special case for a curved end-mirror
when a round trip terminates at this mirror is
to treat it as a mirror of half its actual strength

$$NM4 := \begin{bmatrix} 1 & 0 \\ -\frac{1}{Roc_{M4}} & 1 \end{bmatrix}$$

Starting from position ζ in the crystal, we calculate the round trip matrices in sag. and tan. planes by multiplying all cavity element matrices together

$$RT1_{tan}(\zeta,a,b) := Xtl_1(\zeta)\cdot Brin_{tan}\cdot Short2(a,b)\cdot M4_{tan}$$

$$RT2_{tan}(\zeta,a,b) := Short2(a,b)\cdot Brout_{tan}\cdot Xtl_{\zeta}(1)\cdot Brin_{tan}\cdot Short1(a)$$

$$RT3_{tan}(\zeta,a,b) := M3_{tan}\cdot Arm1\cdot M1\cdot Arm1\cdot M3_{tan}\cdot Short1(a)\cdot Brout_{tan}\cdot Xtl_{\zeta}(\zeta)$$

$$RoundTrip_x(\zeta,a,b) := RT1_{tan}(\zeta,a,b)\cdot RT2_{tan}(\zeta,a,b)\cdot RT3_{tan}(\zeta,a,b)$$

x refers to tan. plane from now on

$$RT1_{sag}(\zeta,a,b) := Xtl_1(\zeta)\cdot Brin_{sag}\cdot Short2(a,b)\cdot M4_{sag}$$

$$RT2_{sag}(\zeta,a,b) := Short2(a,b)\cdot Brout_{sag}\cdot Xtl_{\zeta}(1)\cdot Brin_{sag}\cdot Short1(a)$$

$$RT3_{sag}(\zeta,a,b) := M3_{sag}\cdot Arm1\cdot M1\cdot Arm1\cdot M3_{sag}\cdot Short1(a)\cdot Brout_{sag}\cdot Xtl_{\zeta}(\zeta)$$

$$RoundTrip_y(\zeta,a,b) := RT1_{sag}(\zeta,a,b)\cdot RT2_{sag}(\zeta,a,b)\cdot RT3_{sag}(\zeta,a,b)$$

y refers to sag. plane from now on

Must extract the ABCD elements from the 2 matrices

$$A_x(\zeta,a,b) := RoundTrip_x(\zeta,a,b)_{0,0}$$

$$B_x(\zeta,a,b) := RoundTrip_x(\zeta,a,b)_{0,1}$$

$$C_x(\zeta,a,b) := RoundTrip_x(\zeta,a,b)_{1,0}$$

$$D_x(\zeta,a,b) := RoundTrip_x(\zeta,a,b)_{1,1}$$

$$A_y(\zeta,a,b) := RoundTrip_y(\zeta,a,b)_{0,0}$$

$$B_y(\zeta,a,b) := RoundTrip_y(\zeta,a,b)_{0,1}$$

$$C_y(\zeta,a,b) := RoundTrip_y(\zeta,a,b)_{1,0}$$

$$D_y(\zeta,a,b) := RoundTrip_y(\zeta,a,b)_{1,1}$$

The Magni model also requires the one way trip matrices from ζ in xtal to the two cavity end-mirrors to be calculated.

$$Trip_{M1.x}(\zeta,a,b) := M1\cdot Arm1\cdot M3_{tan}\cdot Short1(a)\cdot Brout_{tan}\cdot Xtl_{\zeta}(\zeta)$$

$$Trip_{M1.y}(\zeta,a,b) := M1\cdot Arm1\cdot M3_{sag}\cdot Short1(a)\cdot Brout_{sag}\cdot Xtl_{\zeta}(\zeta)$$

$$A_{1.x}(\zeta,a,b) := Trip_{M1.x}(\zeta,a,b)_{0,0}$$

$$B_{1.x}(\zeta,a,b) := Trip_{M1.x}(\zeta,a,b)_{0,1}$$

$$C_{1.x}(\zeta,a,b) := Trip_{M1.x}(\zeta,a,b)_{1,0}$$

$$D_{1.x}(\zeta,a,b) := Trip_{M1.x}(\zeta,a,b)_{1,1}$$

$$A_{1.y}(\zeta,a,b) := Trip_{M1.y}(\zeta,a,b)_{0,0}$$

$$B_{1.y}(\zeta,a,b) := Trip_{M1.y}(\zeta,a,b)_{0,1}$$

$$C_{1.y}(\zeta,a,b) := Trip_{M1.y}(\zeta,a,b)_{1,0}$$

$$D_{1.y}(\zeta,a,b) := Trip_{M1.y}(\zeta,a,b)_{1,1}$$

For the one way trip to the curved end-mirror use the special 'half mirror' element

$$\text{Trip}_{M2.x}(\zeta,a,b) := NM4\cdot Short2(a,b)\cdot Brout_{tan}\cdot Xtl_1(\zeta)$$

$$\text{Trip}_{M2.y}(\zeta,a,b) := NM4\cdot Short2(a,b)\cdot Brout_{sag}\cdot Xtl_1(\zeta)$$

$$A_{2.x}(\zeta,a,b) := \text{Trip}_{M2.x}(\zeta,a,b)_{0,0}$$

$$B_{2.x}(\zeta,a,b) := \text{Trip}_{M2.x}(\zeta,a,b)_{0,1}$$

$$C_{2.x}(\zeta,a,b) := \text{Trip}_{M2.x}(\zeta,a,b)_{1,0}$$

$$D_{2.x}(\zeta,a,b) := \text{Trip}_{M2.x}(\zeta,a,b)_{1,1}$$

$$A_{2.y}(\zeta,a,b) := \text{Trip}_{M2.y}(\zeta,a,b)_{0,0}$$

$$B_{2.y}(\zeta,a,b) := \text{Trip}_{M2.y}(\zeta,a,b)_{0,1}$$

$$C_{2.y}(\zeta,a,b) := \text{Trip}_{M2.y}(\zeta,a,b)_{1,0}$$

$$D_{2.y}(\zeta,a,b) := \text{Trip}_{M2.y}(\zeta,a,b)_{1,1}$$

These expressions give the stability parameters separately in the sag. and tan. planes
Overall cavity is only stable if S.x and S.y both lie within -1 to +1 range

$$S_x(\zeta,a,b) := \frac{A_x(\zeta,a,b)+D_x(\zeta,a,b)}{2}$$

$$S_{x.F}(a,b) := S_x\left(\frac{1}{2},a,b\right)$$

The stability parameters
are independent of z so we
calculate them here

$$S_y(\zeta,a,b) := \frac{A_y(\zeta,a,b)+D_y(\zeta,a,b)}{2}$$

$$S_{y.F}(a,b) := S_y\left(\frac{1}{2},a,b\right)$$

Trapezium rule is used to calculate the integral in the Magni model

$$F_{trap.x}(\zeta,a,b) := \left[\sqrt{\left|\frac{B_x(\zeta,a,b)}{B_y(\zeta,a,b)}\right|}\cdot\left(B_{1.x}(\zeta,a,b)\cdot D_{1.x}(\zeta,a,b)\cdot S_{x.F}(a,b)+B_{2.x}(\zeta,a,b)\cdot D_{2.x}(\zeta,a,b)\right)\right]\Big/ B_x(\zeta,a,b)^2$$

$$Sum_{\delta.1.x}(N,a,b) := \left[F_{trap.x}\left(\frac{1}{2\cdot N},a,b\right)+F_{trap.x}\left(1-\frac{1}{2\cdot N},a,b\right)+2\cdot\sum_{i=1}^{N-1}F_{trap.x}\left[\frac{1}{N}\cdot\left(\frac{1}{2}+i\right),a,b\right]\right]\cdot\frac{1}{(N)\cdot 2}$$

$$F_{trap.y}(\zeta,a,b) := \left[\sqrt{\left|\frac{B_y(\zeta,a,b)}{B_x(\zeta,a,b)}\right|}\cdot\left(B_{1.y}(\zeta,a,b)\cdot D_{1.y}(\zeta,a,b)\cdot S_{y.F}(a,b)+B_{2.y}(\zeta,a,b)\cdot D_{2.y}(\zeta,a,b)\right)\right]\Big/ B_y(\zeta,a,b)^2$$

$$Sum_{\delta.1.y}(N,a,b) := \left[F_{trap.y}\left(\frac{1}{2\cdot N},a,b\right)+F_{trap.y}\left(1-\frac{1}{2\cdot N},a,b\right)+2\cdot\sum_{i=1}^{N-1}F_{trap.y}\left[\frac{1}{N}\cdot\left(\frac{1}{2}+i\right),a,b\right]\right]\cdot\frac{1}{(N)\cdot 2}$$

These equations give the Kerr Lens sensitivity factor defined by d=(1/2w*dw/dp)p=0 at the curved retroflecting end mirror

$$\delta_{1.x}(N,a,b) := \text{if}\left[\left(\left|S_{x.F}(a,b)\right| \le 1\right)\cdot\left(\left|S_{y.F}(a,b)\right| \le 1\right), -\frac{1}{n_{YAG}}\cdot\left(\frac{1-S_{y.F}(a,b)^2}{1-S_{x.F}(a,b)^2}\right)^{\frac{1}{4}}\cdot \text{Sum}_{\delta.1.x}(N,a,b), 0\right]$$

$$\delta_{1.y}(N,a,b) := \text{if}\left[\left(\left|S_{y.F}(a,b)\right| \le 1\right)\cdot\left(\left|S_{x.F}(a,b)\right| \le 1\right), -\frac{1}{n_{YAG}}\cdot\left(\frac{1-S_{x.F}(a,b)^2}{1-S_{y.F}(a,b)^2}\right)^{\frac{1}{4}}\cdot \text{Sum}_{\delta.1.y}(N,a,b), 0\right]$$

For the Kerr Lens sensitivity calculated at end of crystal (closest to M2) we must first calculate matrix for propagation from curved mirror to inside xtal face.

$$\text{Trip}_{M1.Xtl.x}(a,b) := \text{Brin}_{tan}\cdot\text{Short2}(a,b)\cdot NM4$$

$$A_{M1.Xtl.x}(a,b) := \text{Trip}_{M1.Xtl.x}(a,b)_{0,0}$$

$$B_{M1.Xtl.x}(a,b) := \text{Trip}_{M1.Xtl.x}(a,b)_{0,1}$$

$$\text{Trip}_{M1.Xtl.y}(a,b) := \text{Brin}_{sag}\cdot\text{Short2}(a,b)\cdot NM4$$

$$A_{M1.Xtl.y}(a,b) := \text{Trip}_{M1.Xtl.y}(a,b)_{0,0}$$

$$B_{M1.Xtl.y}(a,b) := \text{Trip}_{M1.Xtl.y}(a,b)_{0,1}$$

Must also calculate linear spot size on curved end mirror

$$\text{RTrip1}_{M1.x}(a,b) := NM4\cdot\text{Short2}(a,b)\cdot\text{Brout}_{tan}\cdot\text{Xtl}_{\zeta}(1)\cdot\text{Brin}_{tan}\cdot\text{Short1}(a)\cdot\text{M3}_{tan}\cdot\text{Arm1}\cdot M1$$

$$\text{RTrip2}_{M1.x}(a,b) := \text{Arm1}\cdot\text{M3}_{tan}\cdot\text{Short1}(a)\cdot\text{Brout}_{tan}\cdot\text{Xtl}_{\zeta}(1)\cdot\text{Brin}_{tan}\cdot\text{Short2}(a,b)\cdot NM4$$

$$\text{RTrip}_{M1.x}(a,b) := \text{RTrip1}_{M1.x}(a,b)\cdot\text{RTrip2}_{M1.x}(a,b)$$

$$\text{RTrip1}_{M1.y}(a,b) := NM4\cdot\text{Short2}(a,b)\cdot\text{Brout}_{sag}\cdot\text{Xtl}_{\zeta}(1)\cdot\text{Brin}_{sag}\cdot\text{Short1}(a)\cdot\text{M3}_{sag}\cdot\text{Arm1}\cdot M1$$

$$\text{RTrip2}_{M1.y}(a,b) := \text{Arm1}\cdot\text{M3}_{sag}\cdot\text{Short1}(a)\cdot\text{Brout}_{sag}\cdot\text{Xtl}_{\zeta}(1)\cdot\text{Brin}_{sag}\cdot\text{Short2}(a,b)\cdot NM4$$

$$\text{RTrip}_{M1.y}(a,b) := \text{RTrip1}_{M1.y}(a,b)\cdot\text{RTrip2}_{M1.y}(a,b)$$

$$A_{M1.x}(a,b) := \text{RTrip}_{M1.x}(a,b)_{0,0}$$

$$B_{M1.x}(a,b) := \text{RTrip}_{M1.x}(a,b)_{0,1}$$

$$C_{M1.x}(a,b) := \text{RTrip}_{M1.x}(a,b)_{1,0}$$

$$D_{M1.x}(a,b) := \text{RTrip}_{M1.x}(a,b)_{1,1}$$

$$A_{M1.y}(a,b) := \text{RTrip}_{M1.y}(a,b)_{0,0}$$

$$B_{M1.y}(a,b) := \text{RTrip}_{M1.y}(a,b)_{0,1}$$

$$C_{M1.y}(a,b) := \text{RTrip}_{M1.y}(a,b)_{1,0}$$

$$D_{M1.y}(a,b) := \text{RTrip}_{M1.y}(a,b)_{1,1}$$

test for stability

$$S_{M1.x.F}(a,b) := \left|\frac{A_{M1.x}(a,b)+D_{M1.x}(a,b)}{2}\right|$$

$$S_{M1.y.F}(a,b) := \left|\frac{A_{M1.y}(a,b)+D_{M1.y}(a,b)}{2}\right|$$

These equations calculate the linear spot size from a round trip matrix for a stable resonator:

$$w_{1.L.x}(a,b) := \text{if}\left[S_{M1.x.F}(a,b)\le 1,\ \left(\frac{\lambda}{\pi}\right)^{\frac{1}{2}}\cdot\frac{\left(\left|B_{M1.x}(a,b)\right|\right)^{\frac{1}{2}}}{\left[1-\left(\frac{A_{M1.x}(a,b)+D_{M1.x}(a,b)}{2}\right)^2\right]^{\frac{1}{4}}},10^{-10}\right]$$

If unstable, 1e-10 is returned as spot size (zero would cock up a division later)

$$w_{1.L.y}(a,b) := \text{if}\left[S_{M1.y.F}(a,b)\le 1,\ \left(\frac{\lambda}{\pi}\right)^{\frac{1}{2}}\cdot\frac{\left(\left|B_{M1.y}(a,b)\right|\right)^{\frac{1}{2}}}{\left[1-\left(\frac{A_{M1.y}(a,b)+D_{M1.y}(a,b)}{2}\right)^2\right]^{\frac{1}{4}}},10^{-10}\right]$$

$$\omega_{1.L.x}(a,b) := w_{1.L.x}(a,b)^2$$

$$\omega_{1.L.y}(a,b) := w_{1.L.y}(a,b)^2$$

These equations from Magni then give the Kerr lens sensitivity inside the xtal

$$\delta_{M1.Xtl.x}(N,a,b) := \text{if}\left[\left(S_{M1.x.F}(a,b)\le 1\right)\cdot\left(S_{M1.y.F}(a,b)\le 1\right),\ \frac{A_{M1.Xtl.x}(a,b)^2-\left(\lambda\cdot\frac{B_{M1.Xtl.x}(a,b)}{\pi\cdot\omega_{1.L.x}(a,b)}\right)^2}{A_{M1.Xtl.x}(a,b)^2+\left(\lambda\cdot\frac{B_{M1.Xtl.x}(a,b)}{\pi\cdot\omega_{1.L.x}(a,b)}\right)^2}\cdot\delta_{1.x}(N,a,b),0\right]$$

$$\delta_{M1.Xtl.y}(N,a,b) := \text{if}\left[\left(S_{M1.x.F}(a,b)\le 1\right)\cdot\left(S_{M1.y.F}(a,b)\le 1\right),\ \frac{A_{M1.Xtl.y}(a,b)^2-\left(\lambda\cdot\frac{B_{M1.Xtl.y}(a,b)}{\pi\cdot\omega_{1.L.y}(a,b)}\right)^2}{A_{M1.Xtl.y}(a,b)^2+\left(\lambda\cdot\frac{B_{M1.Xtl.y}(a,b)}{\pi\cdot\omega_{1.L.y}(a,b)}\right)^2}\cdot\delta_{1.y}(N,a,b),0\right]$$

As an example, we calculate the rate of change of spot size in the xtal in the sag and tan planes as we move the angled folding mirror whilst keeping the separation from the xtal to the curved end-mirror constant. (figure 5.20 in chapter 5)

$$k := 0..200$$

We take 200 values of xtal position from 31.5 to 33.5 mm from the angled folding mirror

$$a_k := 30.5+\frac{2\cdot k}{200}$$

We define the separation from the curved end-mirror to xtal as (c) and keep it fixed equal to the end-mirror ROC. This keeps both sag and tan foci at the xtal end

$$c := -50$$

$$b(a) := a + c + 1 \cdot 10^{3}$$

Hence calculate the overal mirror separation (inc. xtal) as (a) varied

$$w_{1.L.x_k} := w_{1.L.x}\left(a_k \cdot 10^{-3}, b\left(a_k\right) \cdot 10^{-3}\right)$$

Calculate spot size on the curved end-mirror as a test to see if this actually works

$$w_{1.L.y_k} := w_{1.L.y}\left(a_k \cdot 10^{-3}, b\left(a_k\right) \cdot 10^{-3}\right)$$

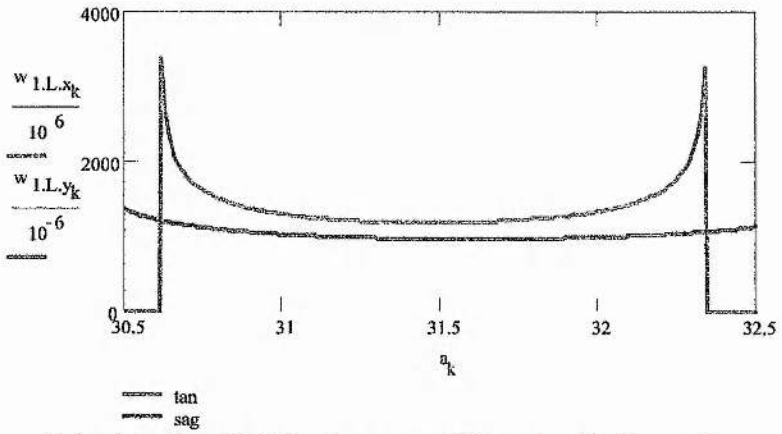

Calculate the KLS for these conditions inside the xtal:

$$\delta_{M1.Xtl.y_k} := \delta_{M1.Xtl.y}\left(20, a_k \cdot 10^{-3}, b\left(a_k\right) \cdot 10^{-3}\right)$$

$$\delta_{M1.Xtl.x_k} := \delta_{M1.Xtl.x}\left(20, a_k \cdot 10^{-3}, b\left(a_k\right) \cdot 10^{-3}\right)$$

And plot them out

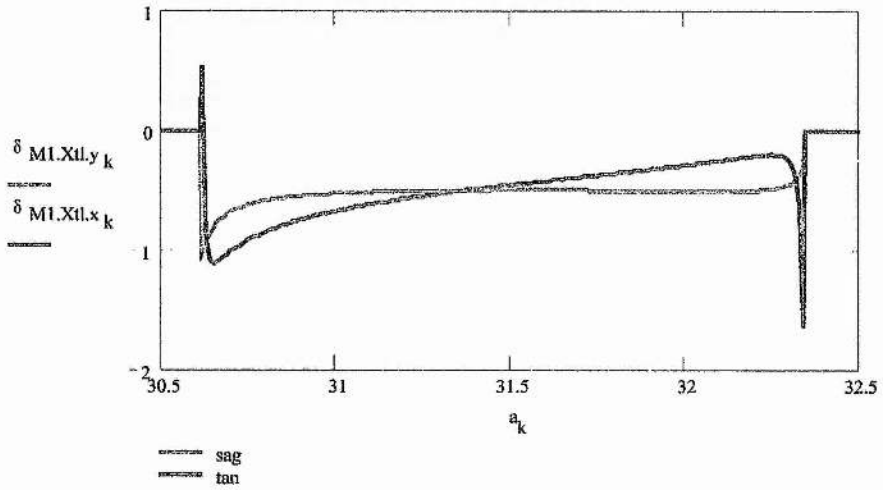

By varying the xtal location for the earlier round trip calculation, we can examine the beam profile inside the laser crystal:

$$w_{\zeta,x}(\zeta,a,b) := \text{if}\left(\left|\frac{A_x(\zeta,a,b)+D_x(\zeta,a,b)}{2}\right|<1,\left(\frac{\lambda}{\pi}\right)^{\frac{1}{2}}\cdot\frac{\left(|B_x(\zeta,a,b)|\right)^{\frac{1}{2}}}{\left[1-\left(\frac{D_x(\zeta,a,b)+A_x(\zeta,a,b)}{2}\right)^2\right]^{\frac{1}{4}}},10^{-10}\right)$$

$$w_{\zeta,y}(\zeta,a,b) := \text{if}\left(\left|\frac{A_y(\zeta,a,b)+D_y(\zeta,a,b)}{2}\right|<1,\left(\frac{\lambda}{\pi}\right)^{\frac{1}{2}}\cdot\frac{\left(|B_y(\zeta,a,b)|\right)^{\frac{1}{2}}}{\left[1-\left(\frac{D_y(\zeta,a,b)+A_y(\zeta,a,b)}{2}\right)^2\right]^{\frac{1}{4}}},10^{-10}\right)$$

Operate in the centre of stability from the plot above (a=31.5mm)

$a := -31.5$

Take 50 slices through the crystal

$\zeta := 0, \frac{1}{50} .. 1$

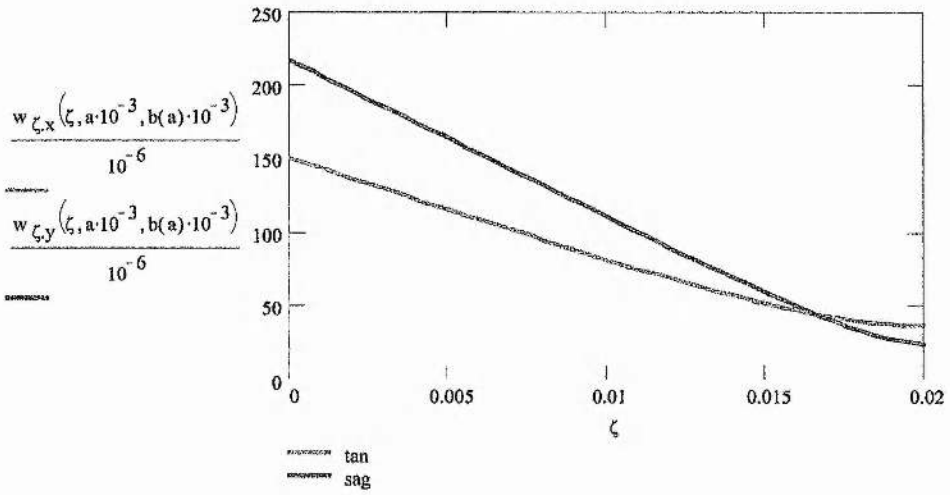

Finally we'll create a contour plot of the Kerr-lens sensitivity on the curved retroflecting end-mirror as both the mirror separation and rod position are varied in the tangential plane.

$a := 26.5\cdot10^{-3}$

Start rod displaced at 26.5mm from angled folding mirror

$b := (100.5)\cdot10^{-3}$

and a mirror separation of 100.5mm

$Rapidity1 := -0.5\cdot10^{-3}$

Move rod in steps of 1/2 mm

$$Rapidity2 := 0.05 \cdot 10^{3}$$

and change mirror separation in steps of 1/20mm

$$i := 0..40$$

Take 40 rod positions

$$j := 0..40$$

and 40 mirror separations

$$Tangential_{i,j} := \delta_{1.x}(20, a + i \cdot Rapidity1, b + j \cdot Rapidity2)$$

Create a 40x40 matrix of KLS values

but cap the greatest value to +/- 1 to create a clearer contour plot

$$Clipped_{i,j} := if\left(|Tangential_{i,j}| \le 1, Tangential_{i,j}, 1 \cdot \frac{Tangential_{i,j}}{|Tangential_{i,j}|}\right)$$

And here's the result! (figure 5.21 in Chapter 5):

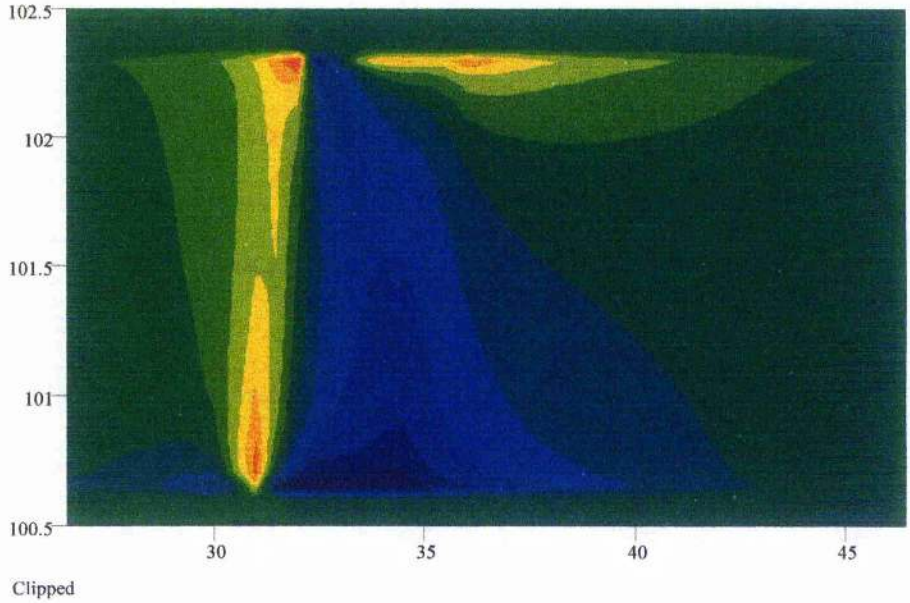

Appendix III: *Kostenbauder Model to Examine Dispersive Cavities (Mathcad 7)*

A.G. Kostenbauder, *IEEE J. Quantum Electron.* **26**, 1148 (1990)

G.J. Valentine 26/9/98 All units default to microns / femtoseconds

Speed of light in a vacuum

$c := 299792458 \cdot 10^{6} \cdot 10^{-15}\ \mu m\ fs^{-1}$

Reference wavelength

$\lambda_0 := 1.51\ \mu m$

$f_0 := \frac{c}{\lambda_0}$

$mm \equiv 10^{3}$

No. slices in each beam calculation

$VV := 100$

$V := 0 .. VV$

First define all the cavity element matrices

Endmirrors

$$M1 := \begin{bmatrix} 1 & 0 & 0 & 0 \\ 0 & 1 & 0 & 0 \\ 0 & 0 & 1 & 0 \\ 0 & 0 & 0 & 1 \end{bmatrix}$$

$M2 := M1$

Folding mirrors

$$M3 := \begin{bmatrix} 1 & 0 & 0 & 0 \\ \frac{-2}{ROC_{M3} \cdot \cos(\theta_{M3})} & 1 & 0 & 0 \\ 0 & 0 & 1 & 0 \\ 0 & 0 & 0 & 1 \end{bmatrix}$$

$$M4 := \begin{bmatrix} 1 & 0 & 0 & 0 \\ \frac{-2}{ROC_{M4} \cdot \cos(\theta_{M4})} & 1 & 0 & 0 \\ 0 & 0 & 1 & 0 \\ 0 & 0 & 0 & 1 \end{bmatrix}$$

Now define the six cavity spaces

$$d1(V) := \begin{bmatrix} 1 & \frac{V}{VV}\cdot space1 & 0 & 0 \\ 0 & 1 & 0 & 0 \\ 0 & 0 & 1 & 0 \\ 0 & 0 & 0 & 1 \end{bmatrix}$$

$$d2(V) := \begin{bmatrix} 1 & \frac{V}{VV}\cdot space2 & 0 & 0 \\ 0 & 1 & 0 & 0 \\ 0 & 0 & 1 & 0 \\ 0 & 0 & 0 & 1 \end{bmatrix}$$

$$d3(V) := \begin{bmatrix} 1 & \frac{V}{VV}\cdot space3 & 0 & 0 \\ 0 & 1 & 0 & 0 \\ 0 & 0 & 1 & 0 \\ 0 & 0 & 0 & 1 \end{bmatrix}$$

$$d4(V) := \begin{bmatrix} 1 & \frac{V}{VV}\cdot space4 & 0 & 0 \\ 0 & 1 & 0 & 0 \\ 0 & 0 & 1 & 0 \\ 0 & 0 & 0 & 1 \end{bmatrix}$$

$$d5(V) := \begin{bmatrix} 1 & \frac{V}{VV}\cdot space5 & 0 & 0 \\ 0 & 1 & 0 & 0 \\ 0 & 0 & 1 & 0 \\ 0 & 0 & 0 & 1 \end{bmatrix}$$

$$d6(V) := \begin{bmatrix} 1 & \frac{V}{VV}\cdot space6 & 0 & 0 \\ 0 & 1 & 0 & 0 \\ 0 & 0 & 1 & 0 \\ 0 & 0 & 0 & 1 \end{bmatrix}$$

space1 to space6 are defined later when the whole cavity is constructed

Define the dispersive element types now
First consider the laser crystal (Cr4+:YAG)

Change gain element material here

Use the Sellmeier expansion for YAG

$A := 2.08745$

$B := 1.2081$

$C := 0.02119$

$D := 17.2049$

$E := 1404.45$

$$n_{yag}(f_0) := \sqrt{A + \frac{B \cdot \left(\frac{c}{f_0}\right)^2}{\left(\frac{c}{f_0}\right)^2 - C} + \frac{D \cdot \left(\frac{c}{f_0}\right)^2}{\left(\frac{c}{f_0}\right)^2 - E}}$$

The gain element is termed n.gain(f.0) from now on

$$n_{gain}(f_0) := n_{yag}(f_0)$$

Change prism material here

Fused silica (SiO_2) Sellmeier data

$$n_{SiO2}(f_0) := \sqrt{1 + \frac{6.6347244310^{-1} \cdot \left(\frac{c}{f_0}\right)^2}{\left(\frac{c}{f_0}\right)^2 - (6.6517661310^{-2})^2} + \frac{4.4064791810^{-1} \cdot \left(\frac{c}{f_0}\right)^2}{\left(\frac{c}{f_0}\right)^2 - (1.1501507610^{-1})^2} + \frac{8.9900706110^{-1} \cdot \left(\frac{c}{f_0}\right)^2}{\left(\frac{c}{f_0}\right)^2 - 9.9031680^2}}$$

The prism refractive index is termed n.p(f.0)

$$n_p(f_0) := n_{SiO2}(f_0)$$

Group velocity of reference
pulse in gain material

$$v_{g.gain}(f_0) := \frac{c}{n_{gain}(f_0) + f_0 \cdot \frac{d}{df_0} n_{gain}(f_0)}$$

Construct a matrix which describes the effect of the brewster surface into the gain

Internal angle to normal at entrance

$$\psi_{gain} := \operatorname{atan}\left(\frac{1}{n_{gain}(f_0)}\right)$$

Howdy Ho

Internal angle to normal at exit

$$\phi_{gain} := 0$$

$$m_{\psi.gain} := \frac{\cos(\psi_{gain})}{\sqrt{1 - n_{gain}(f_0)^2 \cdot \sin(\psi_{gain})^2}}$$

$$m_{\phi.gain} := \frac{\sqrt{1 - n_{gain}(f_0)^2 \cdot \sin(\phi_{gain})^2}}{\cos(\phi_{gain})}$$

$$A := m_{\phi.gain} \cdot m_{\psi.gain}$$

$$B := 0$$

$$C := 0$$

$$D := \frac{1}{m_{\phi.gain} \cdot m_{\psi.gain}}$$

$$E := 0$$

$$F := -\left[\left(\frac{d}{df_0} n_{gain}(f_0)\right) \cdot \frac{(\tan(\phi_{gain}) + \tan(\psi_{gain}))}{m_{\phi.gain}}\right]$$

$$G := -\left(\frac{d}{df_0} n_{gain}(f_0)\right) \cdot m_{\psi.gain} \cdot \frac{(\tan(\phi_{gain}) + \tan(\psi_{gain}))}{\lambda_0}$$

$$H := 0$$

$$I := 0$$

X defines the orientation of the Brewster rod and is either -1 or +1.

$$BRinGAIN(X) := \begin{bmatrix} A & B & 0 & E \\ C & D & 0 & F\cdot\frac{|X|}{X} \\ G\cdot\frac{|X|}{X} & H & 1 & I \\ 0 & 0 & 0 & 1 \end{bmatrix}$$

Define a matrix which describes the effect of the brewster surface out of the gain

Internal angle to normal at entrance

$$\psi_{gain} := 0$$

Internal angle to normal at exit

$$\phi_{gain} := -\operatorname{atan}\left(\frac{1}{n_{gain}(f_0)}\right)$$

$$m_{\psi.gain} := \frac{\cos(\psi_{gain})}{\sqrt{1 - n_{gain}(f_0)^2\cdot\sin(\psi_{gain})^2}}$$

$$m_{\phi.gain} := \frac{\sqrt{1 - n_{gain}(f_0)^2\cdot\sin(\phi_{gain})^2}}{\cos(\phi_{gain})}$$

$$A := m_{\phi.gain}\cdot m_{\psi.gain}$$

$$B := 0$$

$$C := 0$$

$$D := \frac{1}{m_{\phi.gain}\cdot m_{\psi.gain}}$$

$$E := 0$$

$$F := -\left[\left(\frac{d}{df_0}n_{gain}(f_0)\right)\cdot\frac{(\tan(\phi_{gain}) + \tan(\psi_{gain}))}{m_{\phi.gain}}\right]$$

$$G := -\left(\frac{d}{df_0}n_{gain}(f_0)\right)\cdot m_{\psi.gain}\cdot\frac{(\tan(\phi_{gain}) + \tan(\psi_{gain}))}{\lambda_0}$$

$$H := 0$$

$$I := 0$$

X defines the orientation of the Brewster rod and is either -1 or +1.

$$\text{BRoutGAIN}(X) := \begin{bmatrix} A & B & 0 & E \\ C & D & 0 & F\cdot\frac{|X|}{X} \\ G\cdot\frac{|X|}{X} & H & 1 & I \\ 0 & 0 & 0 & 1 \end{bmatrix}$$

Now we only have the dispersive slab of material left in the middle

$$A := 1$$

$$B_V := \frac{d_{gain}\cdot\frac{V}{VV}}{n_{gain}(f_0)}$$

$$C := 0$$

$$D := 1$$

$$l_V := -\left(\frac{d}{df_0}v_{g.gain}(f_0)\right)\cdot\frac{d_{gain}\cdot\frac{V}{VV}}{v_{g.gain}(f_0)^2}$$

$$\text{GAINLUMP}_V := \begin{bmatrix} A & B_V & 0 & 0 \\ C & D & 0 & 0 \\ 0 & 0 & 1 & l_V \\ 0 & 0 & 0 & 1 \end{bmatrix}$$

Define the whole Brewster rod for the trip from M2 to M1 as follows

$$\text{NLP} := \text{BRoutGAIN}(-1)\cdot\text{GAINLUMP}_{VV}\cdot\text{BRinGAIN}(-1)$$

It is only necessary to redefine elements which have no mirror plane for correct dispersion
treatment i.e. for a prism rod, NLP=PLN:

Define the whole Brewster rod for the trip from M1 to M2 as follows

$$\text{PLN} := \text{BRoutGAIN}(1)\cdot\text{GAINLUMP}_{VV}\cdot\text{BRinGAIN}(1)$$

A prism type rod would have X of opposite signs and NLP=PLN, the orientation depending on other prisms in the cavity

Now define bits of the rod going in & out enabling the beam to be examined inside the rod

This goes into the rod to point V

$$GAINPLVin_V := GAINLUMP_V \cdot BRinGAIN(1)$$

This goes from point V to outside the rod

$$GAINPLVout_V := BRoutGAIN(1) \cdot GAINLUMP_V$$

Define the input Brewster surface of the prisms

$$\psi_1 := \operatorname{atan}\left(\frac{1}{n_p(f_0)}\right)$$

$$\phi_1 := 0$$

$$m_{\psi.1} := \frac{\cos(\psi_1)}{\sqrt{1 - n_p(f_0)^2 \cdot \sin(\psi_1)^2}}$$

$$m_{\phi.1} := \frac{\sqrt{1 - n_p(f_0)^2 \cdot \sin(\phi_1)^2}}{\cos(\phi_1)}$$

Group velocity of reference pulse in prism material

$$v_g(f_0) := \frac{c}{n_p(f_0) + f_0 \cdot \frac{d}{df_0} n_p(f_0)}$$

$$A := m_{\phi.1} \cdot m_{\psi.1}$$

$$D := \frac{1}{m_{\phi.1} \cdot m_{\psi.1}}$$

$$B := 0$$

$$C := 0$$

$$E := 0$$

$$F := -\left[\left(\frac{d}{df_0} n_p(f_0)\right) \cdot \frac{(\tan(\phi_1) + \tan(\psi_1))}{m_{\phi.1}}\right]$$

$$G := -\left(\frac{d}{df_0} n_p(f_0)\right) \cdot m_{\psi.1} \cdot \frac{(\tan(\phi_1) + \tan(\psi_1))}{\lambda_0}$$

$$H := 0$$

$$I := 0$$

$$BRinPRISM(X) := \begin{bmatrix} A & B & 0 & E \\ C & D & 0 & F\cdot\frac{|X|}{X} \\ G\cdot\frac{|X|}{X} & H & 1 & I \\ 0 & 0 & 0 & 1 \end{bmatrix}$$

Define the output Brewster surface of the prisms

$$\psi_1 := 0$$

$$\phi_1 := \operatorname{atan}\left(\frac{1}{n_p(f_0)}\right)$$

$$m_{\psi.1} := \frac{\cos(\psi_1)}{\sqrt{1 - n_p(f_0)^2\cdot\sin(\psi_1)^2}}$$

$$m_{\phi.1} := \frac{\sqrt{1 - n_p(f_0)^2\cdot\sin(\phi_1)^2}}{\cos(\phi_1)}$$

$$A := m_{\phi.1}\cdot m_{\psi.1}$$

$$C := 0$$

$$B := 0$$

$$D := \frac{1}{m_{\phi.1}\cdot m_{\psi.1}}$$

$$E := 0$$

$$F := -\left[\left(\frac{d}{df_0}n_p(f_0)\right)\cdot\frac{(\tan(\phi_1) + \tan(\psi_1))}{m_{\phi.1}}\right]$$

$$G := -\left(\frac{d}{df_0}n_p(f_0)\right)\cdot m_{\psi.1}\cdot\frac{(\tan(\phi_1) + \tan(\psi_1))}{\lambda_0}$$

$$H := 0$$

$$I := 0$$

$$BRoutPRISM(X) := \begin{bmatrix} A & B & 0 & E \\ C & D & 0 & F\cdot\frac{|X|}{X} \\ G\cdot\frac{|X|}{X} & H & 1 & I \\ 0 & 0 & 0 & 1 \end{bmatrix}$$

Now we only have the dispersive slab of material left in the middle

Path length in prism1

$$d_{prism1} := 2 \cdot mm$$

$$A := 1$$

$$B_V := \frac{d_{prism1} \cdot \frac{V}{VV}}{n_p(f_0)}$$

$$C := 0$$

$$D := 1$$

$$l_V := -\left(\frac{d}{df_0} v_g(f_0)\right) \cdot \frac{d_{prism1} \cdot \frac{V}{VV}}{v_g(f_0)^2}$$

$$PRISMLUMP1_V := \begin{bmatrix} A & B_V & 0 & 0 \\ C & D & 0 & 0 \\ 0 & 0 & 1 & l_V \\ 0 & 0 & 0 & 1 \end{bmatrix}$$

Path length in prism2

$$d_{prism2} := 2 \cdot mm$$

$$A := 1$$

$$B_V := \frac{d_{prism2} \cdot \frac{V}{VV}}{n_p(f_0)}$$

$$C := 0$$

$$D := 1$$

$$l_V := -\left(\frac{d}{df_0} v_g(f_0)\right) \cdot \frac{d_{prism2} \cdot \frac{V}{VV}}{v_g(f_0)^2}$$

$$PRISMLUMP2_V := \begin{bmatrix} A & B_V & 0 & 0 \\ C & D & 0 & 0 \\ 0 & 0 & 1 & l_V \\ 0 & 0 & 0 & 1 \end{bmatrix}$$

Can create prisms from these elements

$$Prism1 := BRoutPRISM(P1O) \cdot PRISMLUMP1_{VV} \cdot BRinPRISM(P1O)$$

$$Prism2 := BRoutPRISM(P2O) \cdot PRISMLUMP2_{VV} \cdot BRinPRISM(P2O)$$

As with the gain element, need to examine beam through prism bulk by sectioning

$$P1Vin_V := PRISMLUMP1_V \cdot BRinPRISM(P1O)$$

$P1Vout_V := BRoutPRISM(P1O) \cdot PRISMLUMP1_V$

$P2Vin_V := PRISMLUMP2_V \cdot BRinPRISM(P2O)$

$P2Vout_V := BRoutPRISM(P2O) \cdot PRISMLUMP2_V$

Laser cavity defined here:

Must declare the number of elements in our cavity and which element numbers involve propagation through a medium n>1

Total no. elements

$NN := 13$

Declare the prism element numbers

$\Omega_{P1} \equiv 3$

$\Omega_{P2} \equiv 11$

Declare the gain element number

$\Omega_{gain} \equiv 7$

This cavity <u>MUST</u> begin and end with a PLANE mirror: for 3-mirror cavities etc. use a plane mirror next to the curved end-mirror with doubled ROC

begin with the plane mirror M1

then have a gap to the prism (this gap is element d1(V))

$space1 \equiv 75 \cdot mm$

We define the 1st prism orientation (Prism1)

$P1O \equiv -1$

Next we have the gap from the prism to the folding section (use element d2(V))

$space2 \equiv 70 \cdot mm$

Then define the parameters for the first folding mirror (M3)

$ROC_{M3} \equiv 75 \cdot mm$

$\theta_{M3} \equiv 3 \cdot deg$

Gap between M3 and the nonlinear element (use d3(V))

$space3 \equiv 47.3 \cdot mm$

Define the length of the gain element (NLP/PLN) as defined earlier

$d_{gain} \equiv 23 \cdot mm$

gap between gain and the 2nd folding mirror M4 (d4(V))

space4 ≡ 38.61·mm

2nd folding mirror (M4)

$ROC_{M4} \equiv 75 \cdot mm$

$\theta_{M4} \equiv 25 \cdot deg$

Gap between M4 and the 2nd prism (d5(V))

space5 ≡ 170·mm

define the orientation of Prism2

P2O ≡ −1

and then there's the gap between the 2nd prism and the plane endmirror d6(V)

space6 ≡ 20·mm

Cavity completed with a plane endmirror (M2)

All the cavity elements are entered into this vector in the order in which they appear
This is a highly asymmetric 4 mirror cavity with a prism placed in each cavity arm a la Aoshima

$$Elements_V := \begin{bmatrix} M1 \\ d1(V) \\ Prism1 \\ d2(V) \\ M3 \\ d3(V) \\ NLP \\ d4(V) \\ M4 \\ d5(V) \\ Prism2 \\ d6(V) \\ M2 \\ 0 \\ 0 \\ 0 \\ 0 \\ 0 \\ 0 \\ 0 \end{bmatrix}$$

Extract the elements from the vector into matrix elements Ω.
The elements are constructed as: $\Omega_{\text{element no. , position in element (0-->100)}}$

$$u := 1 .. NN$$
$$\Omega_{u,V} := \left(Elements_V\right)_{u-1}$$

One way trip from M2 to M1 containing ALL elements

$$M2M1 := \prod_{k=1}^{NN} \Omega_{k,VV}$$

"Flip" the Brewster rod before propagating in the opposite direction

$$\Omega_{\Omega\ gain,V} := PLN$$

Confuse people who attempt to understand this codswallop by introducing a pointless subscript Θ:
(This does actually have some historical use, but I've forgotten what exactly)

$$QQ := NN - 1$$
$$Q := 1 .. QQ$$
$$\Theta_Q := Q$$

These two expressions allow the beam to be followed in *free space* only
BVO takes use from the element being examined to the rest of the cavity
BVI takes us back into the element being probed to finish off at the starting point

$$BVO_{Q,V} := \Omega_{\Theta_Q,VV-V}$$

$$BVI_{Q,V} := \Omega_{\Theta_Q,V}$$

Note: *the model returns a "cavity unstable" condition if attempting to propagate in a mirror.*
This condition is trapped later.

Need to define propagation through materials for which n>1 separately (i.e. gain element and prisms):

$$BVO_{\Omega\ gain,V} := GAINPLVout_{VV-V}$$

$$BVI_{\Omega\ gain,V} := GAINPLVin_{V}$$

$$BVO_{\Omega\ P1,V} := P1Vout_{VV-V}$$

$$BVI_{\Omega\ P1,V} := P1Vin_{V}$$

$$BVO_{\Omega\ P2,V} := P2Vout_{VV-V}$$

$$BVI_{\Omega\ P2,V} := P2Vin_{V}$$

This takes us from the 'probed' element to endmirror M2

$$BVM2_{Q} := \prod_{k=NN}^{\Theta_Q + 1} \Omega_{k,VV}$$

This takes us from mirror M1 to the element in which the beam profile is to be examined

$$BM1V_{Q} := \prod_{k=\Theta_Q - 1}^{1} \Omega_{k,VV}$$

$$Z := 0..VV$$

This expression gives an entire cavity round trip starting and finishing in element number Q at position Z

$$RoundTrip_{Q,Z} := BVI_{Q,Z} \cdot \left[BM1V_{Q} \cdot \left[M2M1 \cdot \left[BVM2_{Q} \cdot \left(BVO_{Q,Z} \right) \right] \right] \right]$$

Extract the round trip matrix elements:

$$\begin{bmatrix} A_{Q,Z} & B_{Q,Z} & o_{Q,Z} & E_{Q,Z} \\ C_{Q,Z} & D_{Q,Z} & o_{Q,Z} & F_{Q,Z} \\ G_{Q,Z} & H_{Q,Z} & o_{Q,Z} & I_{Q,Z} \\ o_{Q,Z} & o_{Q,Z} & o_{Q,Z} & o_{Q,Z} \end{bmatrix} := RoundTrip_{Q,Z}$$

Ray spacing around ref. ray

$$\Delta\lambda := 10 \cdot 10^{-3}\ \mu m$$

$$\Delta f := \frac{c \cdot \Delta\lambda}{\lambda_0^{\,2}}$$

Input pulse time delay
(relative to reference pulse)

$$t_{in} := 0\ fs$$

Input pulse centre frequency
(relative to reference pulse)

$$\Delta f_{in} := -\Delta f$$

Displacement of ray from ref.

$$x_{in_{Q,z}} := -\Delta f_{in} \cdot \frac{\left(-E_{Q,z} + D_{Q,z} \cdot E_{Q,z} - F_{Q,z} \cdot B_{Q,z}\right)}{\left(-C_{Q,z} \cdot B_{Q,z} + 1 - D_{Q,z} - A_{Q,z} + A_{Q,z} \cdot D_{Q,z}\right)}$$

Slope of ray wrt ref.

$$\theta_{in_{Q,z}} := \Delta f_{in} \cdot \frac{\left(F_{Q,z} + C_{Q,z} \cdot E_{Q,z} - A_{Q,z} \cdot F_{Q,z}\right)}{\left(-C_{Q,z} \cdot B_{Q,z} + 1 - D_{Q,z} - A_{Q,z} + A_{Q,z} \cdot D_{Q,z}\right)}$$

Relative delay

$$\delta\tau_Q := \frac{G_{Q,vv} \cdot x_{in_{Q,vv}} + H_{Q,vv} \cdot \theta_{in_{Q,vv}}}{\Delta f_{in}} + I_{Q,vv}$$

NOTE: problems may occur if the element number (Q) used in the following expressions is not an empty space element (change if the final answer is shite)
Simulate 5 pulses (ref pulse=third) all equally spaced

$$\tau_1 := -2 \cdot \Delta f \cdot \delta\tau_2$$

$$\tau_2 := -\Delta f \cdot \delta\tau_2$$

$$\tau_4 := \Delta f \cdot \delta\tau_2$$

$$\tau_5 := 2 \cdot \Delta f \cdot \delta\tau_2$$

$$K := \frac{\tau_1 - 8 \cdot \tau_2 + 8 \cdot \tau_4 - \tau_5}{12 \cdot 2 \cdot \pi \cdot \Delta f}$$

The GVD for this laser cavity is:

$$K = -935.388\ \ fs^2$$

Can also calculate the spot size through the cavity:

$$beam_{Q,Z} := \text{if}\left[\left|\frac{A_{Q,Z}+D_{Q,Z}}{2}\right| \le 1, \left(\frac{\lambda 0}{\pi}\right)^{\frac{1}{2}} \cdot \frac{\left(|B_{Q,Z}|\right)^{\frac{1}{2}}}{\left[1-\left(\frac{A_{Q,Z}+D_{Q,Z}}{2}\right)^2\right]^{\frac{1}{4}}}, 0\right]$$

Count through all the cavity elements in variable 'e'

$e := 2 .. QQ$

And count the space through all the elements in variable 'w'

$w := 1 .. VV \cdot (QQ - 1)$

Calc. position in cavity of calculated spot size in mm

$$pos_{e,Z} := \left[\sum_{\varepsilon=1}^{e-1}\left[\left[\frac{\left(\Omega_{\Theta_\varepsilon,VV}\right)}{mm}\right]_{0,1}\right]\right] + \left[\left[\frac{\left(\Omega_{\Theta_e,VV}\right)}{mm}\right]_{0,1} \cdot \frac{Z}{VV}\right]$$

$$BEAMZ_{Z+(e-2)\cdot VV} := pos_{e,Z}$$

Join all calculated intracavity spot size results together, checking first that the element in question has physical space

$$BEAM_{Z+(e-2)\cdot VV} := \begin{cases} beam_{e-1,VV} & \text{if } \left(\Omega_{\Theta_e,VV}\right)_{0,1} = 0 \\ beam_{e,Z} & \text{otherwise} \end{cases}$$

do. with rays

$$RAY2X_{Z+(e-2)\cdot VV} := \begin{cases} x\,in_{e-1,VV} & \text{if } \left(\Omega_{\Theta_e,VV}\right)_{0,1} = 0 \\ x\,in_{e,Z} & \text{otherwise} \end{cases}$$

Can now plot the tangential beam profile through the cavity

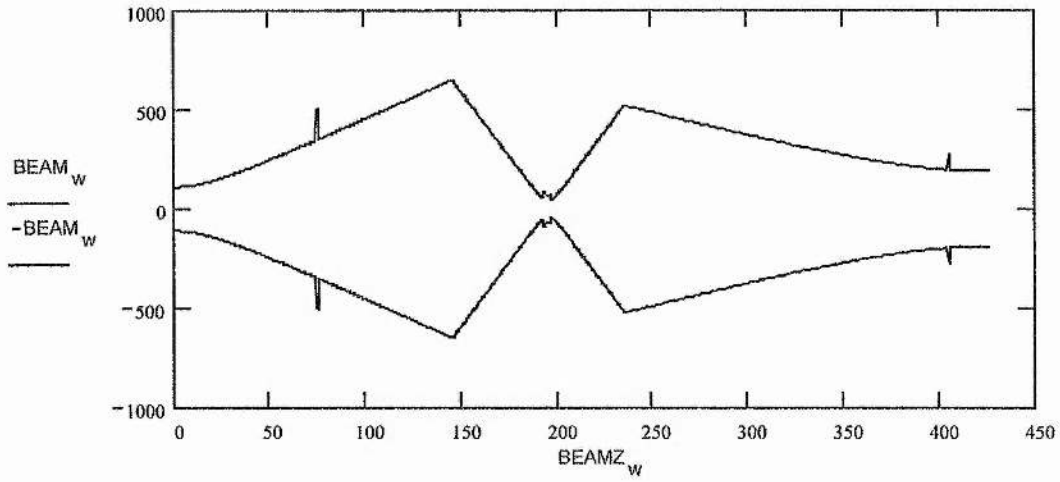

And plot the rays at +/- $\Delta\lambda$ from a reference ray

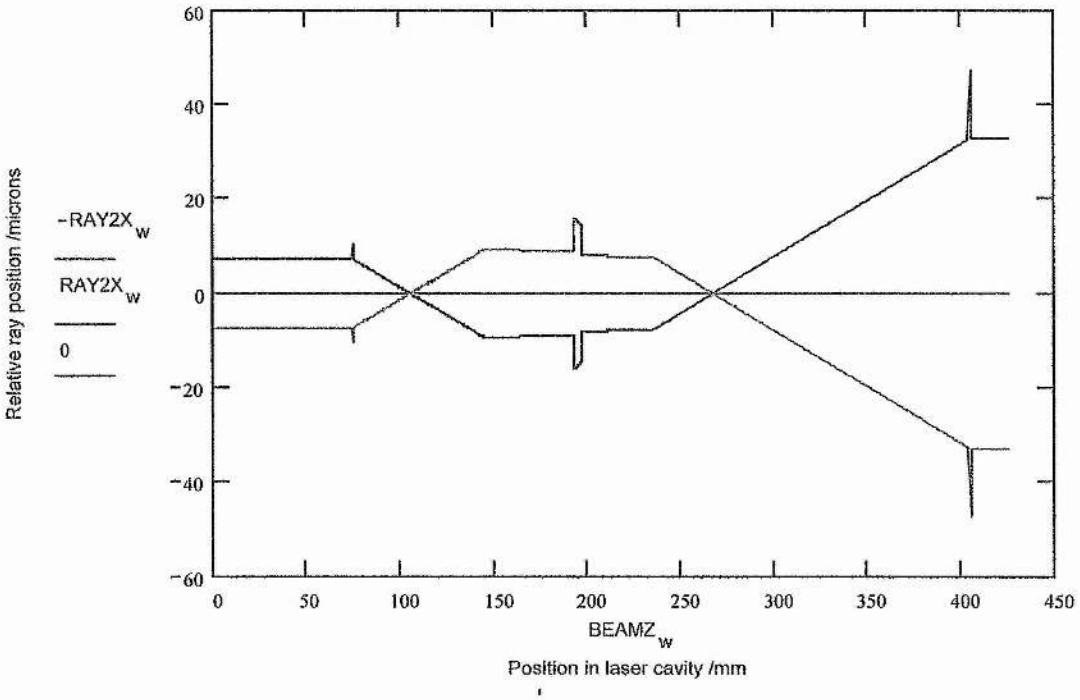

Can arbitrarily place the reference ray at the 1/e2 point in the beam profile

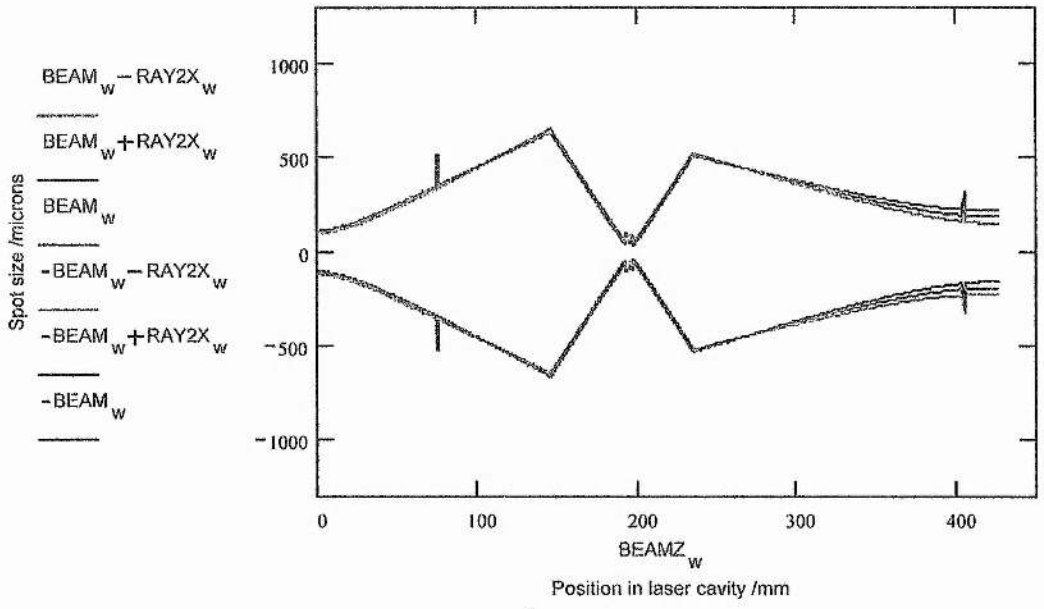

Publications

Coherent Photon Seeding Applied to the Synchronously Modelocked NaCl:OH Color-center Laser

G.J. Valentine, G.T. Kennedy and W. Sibbett, in Digest of 'Conference on Lasers and Electro-optics', (Optical Society of America, Washington D.C., 1995), paper CThI38

Passive stabilisation of Synchronously Modelocked Colour-centre Lasers via Coherent Photon Seeding

G.J. Valentine, G.T. Kennedy and W. Sibbett, in Digest of 'Twelfth UK National Quantum Electronics Conference' (QE12), Southampton 1995, paper P2-1

All-solid-state, Compact, Self-modelocked, Cr^{4+}:YAG Laser

G.J. Valentine, G.T. Kennedy and W. Sibbett, in Digest of 'European Conference on Lasers and Electro-optics', (Optical Society of America, Washington D.C., 1996), paper CFF6

Novel Resonator Designs for Low-Threshold Self-Modelocking

G.J. Valentine, M.P. Critten, G.T. Kennedy, J.M. Hopkins, P, Loza-Alvarez and W. Sibbett, in Digest of 'Conference on Lasers and Electro-optics', Vol. 11 of 1997 OSA Technical Digest Series (Optical Society of America, Washington D.C., 1997), paper CMI1

Low-threshold, High Repetition Rate, Self-modelocked Cr^{4+}:YAG Lasers

G.J. Valentine and W. Sibbett, in Digest of 'Conference on Lasers and Electro-optics', (Optical Society of America, Washington D.C., 1998), paper CTuM47

Ultralow-pump-threshold, Femtosecond Cr^{3+}:LiSAF Laser Pumped by a Single Narrow-stripe AlGaInP Laser Diode

G.J. Valentine, J.M. Hopkins, P, Loza-Alvarez, G.T. Kennedy, W. Sibbett, D. Burns, A. Valster, *Opt. Lett.* **22**, 1639 (1997)

Acknowledgements

I would like to thank my supervisor, Prof. Wilson Sibbett, for his encouragement throughout this project and for giving me the opportunity to complete this research within his group. I am grateful to Dr. Gordon Kennedy for showing me the ropes with all the solid-state lasers and his help on countless occasions. I also thank the other researchers from a bygone era working on colour-centre lasers in the darkness of 223B with whom I shared the unenviable task of dewar filling, in particular Pete Roberts (despite his torturous lab music taste) and Zengli Su.

I am grateful to all the members past and present who have made up the "Big W-Squad", in particular Bill Sleat for help with RF electronics and the avalanche-photodiode ECT machine, David Burns for importing some of his vast knowledge on everything and being a top scientist, and Matthew Critten, Jonny-Poko and Pablo for guiding me off torturous Cr^{4+} to the great Cr^{3+} stuff.

The assistance of the technical staff in the physics department has been essential throughout this work, in particular: Bob Mitchell for his diffusion pump and cryogenic expertise; Reg Gavine and Andy Barman for liquid nitrogen; Jimmy Lindsey for his precision micro-machining of countless crystal mounts and bases; and Ian McLaren in stores for giving me various odds and sods (sometimes willingly).